

Highly-Stretchable and High-Performance  
Electronic Devices by Electronic Component  
Mounting Using Liquid Metal

液体金属を用いた電子素子実装による  
高伸縮・高性能な電子デバイス

February 2024

Takashi SATO

佐藤 峻



Highly-Stretchable and High-Performance  
Electronic Devices by Electronic Component  
Mounting Using Liquid Metal

液体金属を用いた電子素子実装による  
高伸縮・高性能な電子デバイス

February 2024

Research on Micro and Nano Engineering  
Department of Materials Science  
Graduate School of Fundamental Science and Engineering  
Waseda University

Takashi SATO

佐藤 峻



# Contents

Chapter 1	General Introduction .....	1
1.1	Background .....	1
1.1.1	Stretchable Electronic Devices .....	1
1.1.2	Electronic Component Mounting for Stretchable Electronic Devices.....	2
1.1.3	LM for Electronic Component Mounting.....	3
1.2	Previous Studies.....	4
1.2.1	Stretchable Electronic Devices using Organic and Inorganic Materials.....	4
1.2.2	Stress Concentration around Rigid Electronic Components.....	9
1.2.3	Electronic Component Mounting for Stretchable Electronics .....	11
1.2.4	Low-Melting-Point Metals .....	13
1.2.5	Interface between LMs and SMs .....	19
1.2.6	Highly Accurate Measurement Method of Contact Resistance .....	21
1.3	Objective.....	25
1.4	Novelty.....	29
1.5	Thesis Structure .....	31
Chapter 2	Temporary Stability of Contact Resistance of Liquid Metal .....	33
2.1	Introduction.....	33
2.2	Contact Resistance for Contact Procedures .....	36
2.2.1	Study of Contact Resistance for Contact Procedures .....	36
2.2.2	Device Fabrications .....	39
2.2.3	Measurement Methods .....	47
2.2.4	Measurement Results of Contact Resistance for Contact Procedures .....	50

---

*Contents*


---

2.3	Time-Dependent Change in Contact Resistance.....	54
2.3.1	Evaluation Method of Time-Dependent Change in Contact Resistance.....	55
2.3.2	Time-Dependent Change in Contact Resistance.....	55
2.3.3	Measurement Results of Alloy Formation on Solid Metal Surface .....	57
2.4	Conclusions.....	63
 Chapter 3 High-Accuracy Measurement Method for Contact Resistance .....		64
3.1	Introduction.....	64
3.2	Measurement Accuracy for Voltage Detection Location.....	66
3.2.1	Device Fabrications .....	67
3.2.2	Results and Discussion .....	71
3.3	Measurement Accuracy for Current Applied Location .....	74
3.3.1	Simulation Methods.....	75
3.3.2	Simulation Results.....	81
3.3.3	Device Fabrication for Measurements.....	84
3.3.4	Measurement Results.....	88
3.4	Conclusions.....	92
 Chapter 4 Stretch Tolerance of Electronic Component Mounting Using Liquid Metal ..		94
4.1	Introduction.....	94
4.1.1	Stretch Tolerance of Mounting Method Using Liquid Metal and Its Challenges .....	94
4.1.2	Objective and Contents for Demonstration of Stretch Tolerance .....	96
4.2	Stretch Tolerance of Liquid Metals as EIMs.....	97
4.2.1	Methods .....	97
4.2.2	Results and Discussion .....	102
4.3	Stretch Tolerance of Wiring without Components.....	107
4.3.1	Methods .....	108
4.3.2	Results and Discussion .....	112
4.4	Stretch Tolerance of Wiring with Components .....	117
4.4.1	Methods .....	118

4.4.2	Results and Discussion .....	121
4.5	Demonstration of Stretchable Electronic Devices .....	131
4.5.1	Device Fabrications .....	131
4.5.2	Results and Discussion .....	134
4.6	Conclusions.....	136
Chapter 5	Conclusions .....	139
5.1	Overall Summary .....	139
5.2	Future Prospect .....	142
5.2.1	Application for Conventional Mounting Methods.....	142
5.2.2	Impacts on Science and Industry .....	142
5.2.3	Development of Proposed Mounting Method .....	143
Appendix A	Fabrication Procedures.....	145
Appendix B	Measurement Conditions.....	148
Appendix C	Letters .....	150
References	.....	152
Achievements	.....	167
Acknowledgements	.....	174





# Chapter 1      General Introduction

## 1.1      Background

---

### 1.1.1      Stretchable Electronic Devices

This study proposed a method for mounting an electronic component on a stretchable circuit substrate using liquid metal (LM) and demonstrated highly stretchable and high-performance electronic devices. Recently, environmental problems such as global warming and the decrease in mineral resources have become increasingly severe. In response, concepts such as “sustainable society,” “sustainable development goals,” and “carbon neutrality” have been proposed worldwide. To realize such a society, it is important to develop electronic devices that are closely related to people's lives. For example, the reduction of power consumption, toughening, and expansion of application range are required. Consequently, stretchable electronic devices have garnered significant attention. High stretchability and performance are important for stretchable electronic devices. High stretchability, including high breaking strain and high stretch tolerance, is required to expand the applications of stretchable electronic devices. For example, when such device is applied to human skin, stretchability of approximately 100% is required because human skin stretches by up to 70%. Regarding electronic devices, similar to conventional non-deformable electronic

devices, high electrical performance is required, such as low power consumption, high sensor sensitivity, and stable resistance.

The ideal device configuration for electrical performance includes rigid, high-performance electronic components mounted on stretchable metal wiring. Surface-mounted devices (SMDs), such as integrated circuit (IC) chips, chip light-emitting diodes (LEDs), and MEMS sensors, exhibit high electrical performance and various types, making them highly accessible and versatile. They have been utilized in conventional non-stretchable electronic devices such as smart phones and computers. Stretchable metal wiring exhibits excellent electrical performance, such as high conductivity and low resistance change. Stretchable structures, such as kirigami and serpentine, allow a hard metal substrate to stretch as a whole structure via local bending and torsion deformation. Another advantage is the low resistance change during stretching.

### 1.1.2 Electronic Component Mounting for Stretchable Electronic Devices

However, when SMDs are mounted on stretchable metal wiring for electrical performance, the stress concentration causes the rigid components around the components to break. Hence, three factors are considered for the electrical interface material (EIM) that connects the components to the wiring: (1) high-stretch tolerance, (2) low resistance, and (3) low mounting temperature. EIM is a material such as solder or conductive adhesive used to connect components and wiring. (1) The flexible connection between wiring and electronic components relieves stress concentration around the component and provides high stretchability. (2) Low resistance between the components and wiring is also important to minimize power consumption and measurement noise. The resistance between the electronic components and wiring is the combined resistance of the volume resistance of the EIM and the contact resistance ( $R_c$ ) between the EIM and component or wiring. (3) Low temperatures are required for mounting because several materials utilized for stretchable substrates, such as polyurethane and polyolefin, have low heat resistance below 60°C or 70°C.

A eutectic solder (Sn: 63%, Pb: 37%) is mainly employed as the conventional EIM. Among conventional EIMs, solders exhibit the lowest volume resistivity ( $1.5 \times 10^{-7} \Omega\text{m}$ ) and contact resistivity ( $\rho_c$ ) ( $10^{-8} \Omega\text{m}^2$ ). Here, the  $\rho_c$  is  $R_c$  per unit contact area. However, solders requires a high mounting temperature (>183°C) for melting, and they exhibit low stretch tolerance owing to their high stiffness. Ag-based conductive paste is utilized as an alternative EIM to solders. Conductive pastes can be classified into two types: sintering/drying and curing. Here, this paper focuses on Ag-based conductive pastes that can be employed

without heating. Although sintering/drying-type pastes have a low volume resistivity ( $>10^{-7} \Omega\text{m}$ ), they exhibit a low stretch tolerance. Curing-type pastes have high volume resistivities ( $10^{-5} \Omega\text{m}$ ); however, they may exhibit high stretch tolerance. In addition, both types of pastes exhibit high  $\rho_c$  ( $>10^{-7} \Omega\text{m}^2$ ) owing to their high viscosity. Hence, these conventional EIMs are unsuitable for low-temperature mounting because of their low resistance and high stretch tolerance. Therefore, this study considered utilizing LM as an EIM. Here, LM is defined as a metal with melting point below  $30^\circ\text{C}$  from the perspective of low mounting temperature.

### 1.1.3 LM for Electronic Component Mounting

This study proposed the use of LMs as EIMs for high stretch tolerance and low  $R_c$ . The proposed method was inspired by the author's experience in electronic component mounting and his encounter with LM during his study abroad. During the course of his undergraduate and master's courses, the author studied electronic component mounting using contact pressure. This study elucidated the importance of  $R_c$  and stretch tolerance for mounting. In addition, the author learned about LM during his study under Associate Professor Hashimoto at Singapore University of Technology and Design during his master's course. Associate Professor Hashimoto's group utilized Ga-based LM as a stretchable conductor for stretchable sensors and antennas. In contrast, the author's mounting experience inspired him to employ LM as an EIM. However, it was unclear whether low  $R_c$  and high bonding force could be obtained when LM was utilized with rigid components and wiring.

As a liquid at below  $30^\circ\text{C}$ , Ga-based LMs exhibit several excellent properties. Note that mercury is also liquid at room temperature; however, is not discussed here owing to its toxicity. Ga-based LMs are comprised of Ga, In, and Sn. LMs exhibit low volume resistivity (galinstan:  $0.297 \text{ m}\Omega\cdot\text{mm}$ )[1], which is almost identical to that of metallic materials (Cu:  $0.0168 \text{ m}\Omega\cdot\text{mm}$ )[2]. They are highly stretchable ( $\geq 500\%$  strain)[3], [4] because they exist in liquid form at room temperature owing to their low melting points ( $-19$ – $29^\circ\text{C}$ ). In addition, LMs exhibit low viscosity ( $2 \text{ mPa}\cdot\text{s}$ ), low toxicity[5], and negligible vapor pressure[6], [7]. In previous studies, LMs have been employed as conductors in stretchable electronic devices, such as stretchable wirings[3], [4], flexible sensors[8], [9], flexible antennas[10]–[12], flexible actuators[13]–[15], flexible gas barrier films[16], and integrated devices with chip LEDs[17], temperature sensors[18], [19], acceleration sensors[18], and thermoelectric generators[20].

In contrast, Ga-based LMs require more investigation before they can be applied as EIMs. They exhibit a high surface tension ( $534.6 \text{ mN/m}$ )[21], and an oxide layer tends to form on their surfaces[22]–[28]. Ga-

based LMs have been reported to form alloys with several solid metals (SMs) over time, and these alloys improve the wettability of LMs[21], [29]–[39]. Therefore, it is possible that their  $R_c$  is high and changes over time. Moreover, the stretch tolerance of LM when adopted as an EIM by placing it between rigid components and wiring may be low because of the low adhesiveness owing to the oxide layer or high surface tension. Furthermore, the effect of electronic component mounting using LMs on the deformation of stretchable wiring remains unclear. Therefore, this study investigates the  $R_c$  and stretch tolerance of the proposed mounting method using LM.

## 1.2 Previous Studies

---

### 1.2.1 Stretchable Electronic Devices using Organic and Inorganic Materials

Recently, stretchable electronic devices such as stretchable sensors, displays, and antennas have garnered significant attention[40]–[46]. As illustrated in Figure 1.1(a), when such stretchable electronic devices are attached to a human joint, high stretchability of more than 100% of the device strain is required. Under bending deformation, the maximum strains obtained on the skin were 42%, 45%, and 63% at the finger, wrist, and elbow, respectively[47]. Considering these skin attachable devices, the kinesiology tapes exhibit more than 180% stretchability (Air Through Premium, J-Road Sports, Tokyo, Japan), and stretchable fabrics can be stretched more than 100% strain[48]–[51]. High electrical performance, such as low power consumption, low resistance change, and high sensing sensitivity, are also required for highly accurate biometric monitoring. Figure 1.1(b) classifies conventional studies on stretchable electronic devices into two types: (1) devices using electronic components made of stretchable organic materials, such as organic LEDs (OLEDs) and organic transistors[41], [44], [52]–[54]. (2) Devices integrating rigid, high-performance electronic components, such as LEDs and micro-electro-mechanical system (MEMS) sensors on stretchable circuit substrates[40]–[43], [45], [46], [55]–[57]. Several researchers have studied the enhancement of electrical properties, such as conductivity and mobility, of devices using electronic components with organic materials (Figure 1.1(b-i)). For instance, organic transistors, LEDs, and solar cells that utilize organic materials provide flexibility for electronic devices[41], [44], [52], [53]. However, their electrical performance is not comparable to that of metals and semiconductors made of inorganic materials. However, this study attempted to improve the stretchability of electronic devices using rigid electronic components comprising inorganic materials (Figure 1.1(b-ii)). Hence, as illustrated in Figure

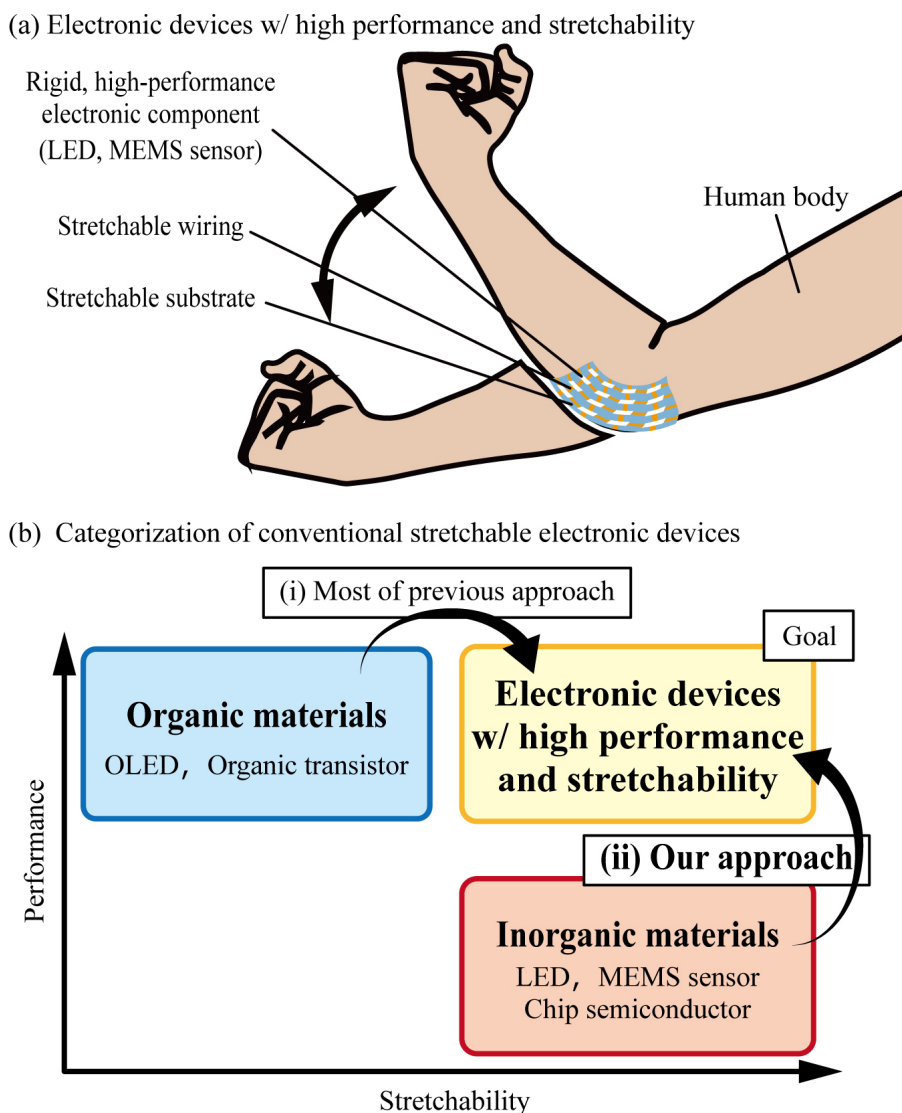


Figure 1.1 Approaches for electronic devices with high performance and stretchability. (a) Schematic of stretchable electronic device with high performance and stretchability using rigid high-performance electronic components. (b) Categorization of previous stretchable electronic devices.

1.2(b), the approach[43], [45], [46], [58]–[60] for realizing stretchable electronic devices utilizing conventional rigid electronic components made of semiconductors or metals for electronic components and stretchable metal wiring for wiring provides several advantages in the current case study. In other words, rigid, small electronic components, and flexible electronic devices are the most promising. Hence,

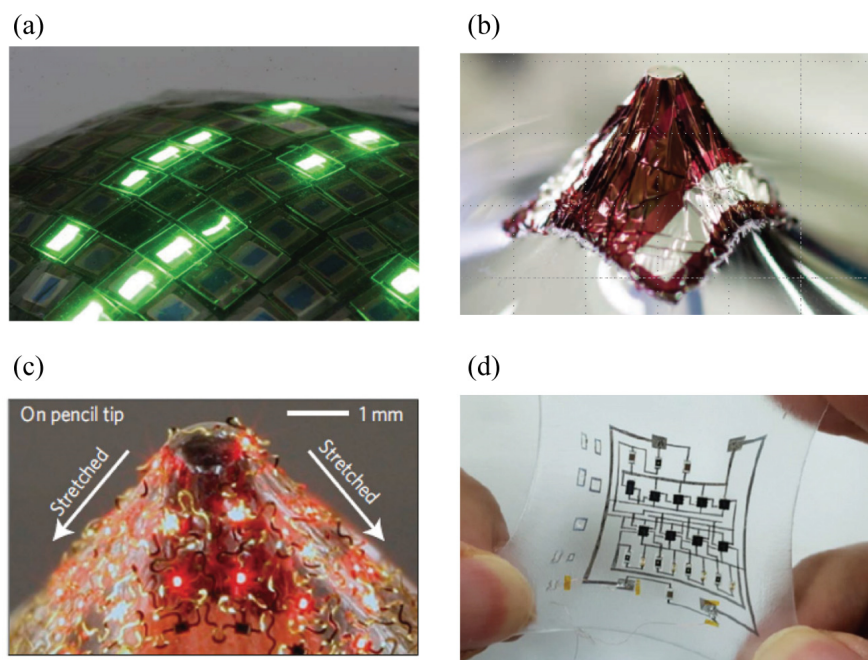


Figure 1.2 Stretchable electronic devices using (a), (b) organic materials[54], [53]; (c), (d) inorganic materials[46], [57]. Reproduced with permission from [54] Copyright 2012, Springer Nature; [53] Copyright 2009, Springer Nature; [46] Copyright 2010, Springer Nature.

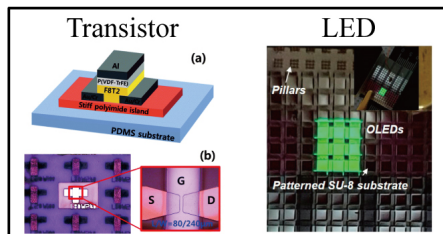
the combination of a rigid but small electronic component and stretchable wiring can realize a highly stretchable and highly functional flexible electronic device.

As shown in Figure 1.3, there are two types of rigid electronic components: thin-film devices[61]–[70], such as thin-film transistors, thin-film sensors, and thin-film LEDs, and SMDs such as chip LEDs, chip ICs, and chip sensors. This study focuses on stretchable hybrid electronic devices that include SMDs mounted on stretchable wiring, from the perspectives of versatility, availability, and reliability. The packages of SMDs are primarily made of plastic, ceramics, or metal, and their Young's modulus is several GPa or higher (epoxy resin: 3 GPa).

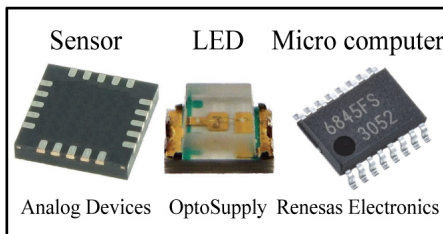
High conductivity ( $\approx$ metals), stretchability ( $>100\%$ ), and reliability due to low resistance changes are critical for stretchable wiring in stretchable hybrid electronic devices. As presented in Table 1.1, improved based on the previous paper[71], stretchable wirings in stretchable hybrid electronic devices can be divided into two types: those utilizing materials with inherent stretchability, and those employing hard, non-stretchable materials with stretchable shapes[71]. Stretchable wiring utilizes materials with inherent

## Categorization of electronic components

## (a) Thin-film components

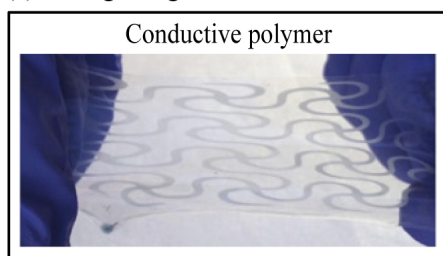


## (b) SMDs



## Categorization of stretchable wiring

## (c) Wiring using stretchable materials



## (d) Wiring using stretchable structures

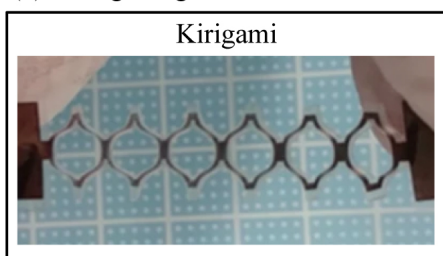


Figure 1.3 Categorization of electronic components: (a) thin-film components[68],[67] and (b) SMDs. Categorization of stretchable wirings: (c) wings using stretchable materials such as conductive polymers[73]. (d) Wiring using stretchable structures such as kirigami[59] structures. Reproduced with permission from [68] Copyright 2013, Royal Society of Chemistry; [67] Copyright 2020, American Chemical Society; [79] Copyright 2017, American Association for the Advancement of Science; [59] Copyright 2019, Springer Nature.

stretchability such as ionic liquids ( $>1 \times 10^3\%$ )[72], [73], LMs ( $>1 \times 10^3\%$ )[4], [74]–[76], conductive polymers ( $8 \times 10^2$ – $8 \times 10^3\%$ )[77]–[80], carbon nanotubes (CNTs;  $3 \times 10^2\%$ )[81], and elastic conductors ( $1 \times 10^2$ – $4 \times 10^2\%$ )[54], [82]–[85]. However, their conductivity is significantly lower than that of wirings with rigid materials owing to their natural low conductivity or structure with conductive particles mixed with stretchable binder materials. For instance, ionic liquids ( $1 \times 10^{-3}$  S/cm), LMs ( $3 \times 10^4$  S/cm)[3], [4], conductive polymers ( $1 \times 10^{-1}$ – $1 \times 10^3$  S/cm) [86], carbon nano tubes ( $1 \times 10^3$  S/cm), and elastic conductors ( $1 \times 10^2$ – $7 \times 10^4$ )[87], [88]. Regarding reliability, these wirings are limited because wiring resistance increases with the stretching of the materials. In contrast, wirings using rigid metal materials, such as copper and gold, with stretchable structures exhibit high conductivities ( $4 \times 10^5$  S/cm)[43], [45], [46], [58], [59], [89], [90]. These wirings also exhibit relatively high stretchability owing to various stretchable

Table 1.1 Structures and Materials for conventional stretchable wirings.

Materials and structures		Conductivity (S/cm)	Stretchability (%)	Ref. No.
Materials	Ionic liquid	$1 \times 10^{-3}$	$>1 \times 10^3$	[72],[73]
	Ga-based LMs	$3 \times 10^4$	$>1 \times 10^3$	[4],[74]-[76]
	Conducting polymer	$1 \times 10^{-1} - 1 \times 10^3$	$8 \times 10^2 - 8 \times 10^3$	[77]-[80]
	Carbon nanotubes	$1 \times 10^3$	$3 \times 10^2$	[81]
	Elastic conductors	$1 \times 10^2 - 7 \times 10^4$	$1 \times 10^2 - 4 \times 10^2$	[54],[82]-[85]
Structures	Serpentine	$4 \times 10^5$	$2 \times 10^1 - 2 \times 10^3$	[91]-[94]
	Mesh	$4 \times 10^5$	$2 \times 10^1 - 1 \times 10^3$	[95]-[98]
	Microcracks	$4 \times 10^5$	$3 \times 10^1 - 4 \times 10^2$	[99]-[102]
	Longitudinal wave	$4 \times 10^5$	$2 \times 10^1 - 4 \times 10^2$	[103]-[106]
	Kirigami	$4 \times 10^5$	$5 \times 10^1 - 1 \times 10^3$	[59], [107]
	Origami	$4 \times 10^5$	$3 \times 10^1 - 4 \times 10^2$	[108]-[110]

structures, such as serpentine structures ( $2 \times 10^1 - 2 \times 10^3\%$ )[91]-[94], mesh structures ( $2 \times 10^1 - 1 \times 10^3\%$ )[95]-[98], microcracks ( $3 \times 10^1 - 4 \times 10^2\%$ )[99]-[102], longitudinal waves ( $2 \times 10^1 - 4 \times 10^2\%$ )[103]-[106], kirigamis ( $5 \times 10^1 - 1 \times 10^3\%$ )[59], [107], and origamis ( $3 \times 10^1 - 4 \times 10^2\%$ )[108]-[110]. Here, stretchability is limited when the wiring is embedded in an elastomer substrate, because the elastomer suppresses the out-of-plane deformation of these structures. Another benefit of this wiring is that the change in wiring resistance during stretching is significantly lower than that of wiring with stretchable materials because the material itself was not stretched. In general, the adoption of metal-stretchable wiring is desirable in terms of performance and reliability.

Conventional flexible electronic devices use polyimide and other heat-resistive materials to withstand



high mounting temperatures. Considering their application to the skin, it is desirable to employ vinyl chloride, polyurethane, or polyolefins, which are utilized as base materials for adhesive plasters, as substrates because of their stretchability and biocompatibility. However, these materials exhibit significantly low heat resistance, and high temperatures during mounting have become a problem. Hence, the author infers that stretchable flexible electronic devices with high stretchability and functionality can be realized by combining a rigid electronic component using semiconductors and metal materials, a stretchable metal wiring component using metal materials, and a substrate using polyurethane and other materials with high stretchability and biocompatibility.

### 1.2.2 Stress Concentration around Rigid Electronic Components

Conventional stretchable hybrid electronic devices that integrate rigid SMDs with stretchable metal wiring often experience wiring failures around the electronic components owing to the strain and stress differences. In general, when rigid electronic components fabricated from semiconductors or metal materials are employed in electronic devices, EIMs are utilized to establish connections between the electronic components and metal wiring. Conventional rigid electronic devices employ EIMs with low volume resistivity, such as solder, to minimize the electrical resistance between the electronic components and wiring, thereby reducing power consumption and heat generation. Conventional solders, commonly employed as EIMs, exhibit stiffness values of approximately 35 GPa (37% Sn, 63% Pb) and 41.6 GPa (96.5% Sn, 3% Ag, 0.5% Cu) for leaded and lead-free solders, respectively. Flexible conductive pastes exhibit stiffness values of 225 MPa (SX-ECA48, Cemedine, Tokyo, Japan), 900 MPa (AA07, Fujikura Kasei, Tokyo, Japan), and 50 MPa (XA-819A, Fujikura Kasei, Tokyo, Japan). Regarding stretchable metal wiring, a trade-off exists between stretchability and breaking stress, characterized by a decrease in breaking stress as breaking strain increases. Therefore, the obtained tensile stiffness of the highly stretchable metal wiring was lower than that of the conventional EIM. For instance, the Young's modulus values of stretchable metal wirings with kirigami structures are 0.3 MPa[107] and 0.1 MPa[111]. When a device in which electronic components are mounted on stretchable metal wiring via soldering or conductive adhesion is stretched, the connected areas of the wiring are fixed to the electronic components, and the strain is almost zero, whereas other areas of the wiring are stretched; hence, the strain difference between the connected areas and other areas in the wiring is substantial.

As illustrated in Figure 1.4, conventional studies on the stretchable resistance of mounting areas employing stiff EIMs have progressively addressed strain disparities between connected wiring regions

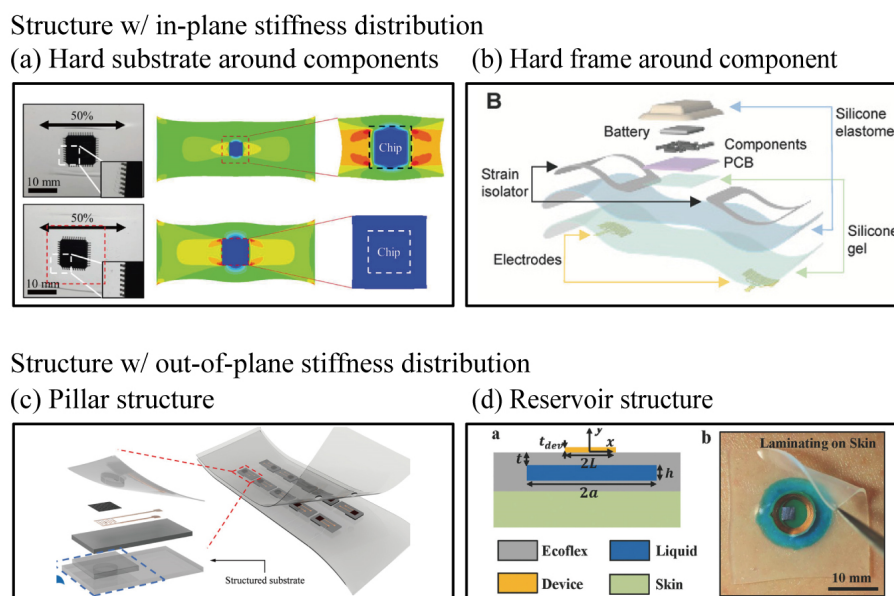


Figure 1.4 Previous studies conducted on reducing strain differences around rigid components via the continuous stiffness distribution of substrates. For structures with in-plane stiffness distributions, (a) hard substrate around components [124] and (b) hard frame around components [121]. For structures with out-of-plane stiffness distributions, (c) pillar structures under components [128] and (d) reservoir structure filled with liquid under components [133]. Reproduced with permission from [124] Copyright 2019, John Wiley and Sons; [126] Copyright 2021, John Wiley and Sons; [128] Copyright 2019, John Wiley and Sons; [133] Copyright 2016, John Wiley and Sons.

and other areas by gradually establishing the stiffness distribution of the wiring and substrate, thereby mitigating local strain differences [112]. This can be divided into two main approaches: one entails increasing the board stiffness distribution around the device in stages and the other involves separating the deformation between the board and device mounting area. For substrates with an in-plane stiffness distribution, the primary approach is to progressively increase the substrate stiffness around electronic components. For example, the stiffness of the substrate under the component increases in stages [11], [113]–[125] (Figure 1.4 (a)), the area around the component is covered with hard frames [126], and hard areas are fabricated under the component in the shape of a fish bone [127] (Figure 1.4 (b)).

A structure also exists in which the elements are placed on pillars of the substrate [128]–[131] (Figure 1.4 (c)) or covered with a hard shell [132], and the substrate stiffens increasingly the closer it is

perpendicular to the covered element with a continuous stiffness distribution in the out-of-plane direction. In studies that separated the deformation of the substrate from that of the mounting section, a liquid reservoir was positioned between the electronic component mounting area and substrate to separate the uniform deformation of the substrate from that around the component, allowing the wiring around the mounting area to deform naturally[55], [133] (Figure 1.4(d)). These approaches to reducing strain differences are effective when the device strain is negligible; however, they are not suitable for reducing strain differences when the device strain is significant because they require a multistep stiffness distribution and a substantial graduated area to reduce the strain. In contrast, this study proposes the use of EIMs with lower stiffness than stretchable metal wiring for the connection between the stretchable metal wiring and rigid electronic components. By employing this method, the connected area of the wiring could be stretched by applying a stretching pattern. Therefore, the difference in strain between the connected area of the wiring and other areas can be minimized, and the author infers that highly stretchable and high-performance electronic devices can be realized.

### 1.2.3 Electronic Component Mounting for Stretchable Electronics

To mount electronic components on stretchable wiring, the following three points are crucial: (1) low mounting temperature, (2) low electrical resistance between the electronic components and electrodes, and (3) high stretch tolerance. The low mounting temperature allows the use of materials with high stretchability and biocompatibility but low heat resistance (60–70°C) as substrates, such as polyurethane, polyvinyl chloride, and polyolefins [40]. Furthermore, low resistance results in low power consumption, low heat generation, and high sensing accuracy. Here, resistance refers to the composite resistance of the EIM's volume resistance and the  $R_c$  between the EIM and components or wiring. Hence, the low volume resistivity and low  $R_c$  of the EIM are required for low resistance. Furthermore, the stretch tolerance of the EIM allows the connected area of the wiring to stretch, reducing the strain difference in the wiring. Consequently, the stretchability of the stretchable electronic devices is improved. To stretch the connected area of the wiring, the tensile stiffness of the EIM must be less than that of the wiring, and the breaking strain of the EIM must be higher than that of the wiring (by several hundred percent).

Solders are the most prevalent EIM in electronic devices that do not exhibit conventional deformability. Various solder compositions exist, including eutectic, lead-free, and low-melting-point solders. The typical composition of eutectic solder is 63 mass% lead (Pb) and 37 mass% tin (Sn), and its melting point is 183°C. The Sn-Ag-Cu-based solder, as a prevalent Pb-free solder contains 96.5 mass% Sn, 3 mass% Ag, and 0.5%

Cu, with a melting point of 220°C, which is higher than that of eutectic solders. The Sn-In-based solder, as a typical low-melting point solder, contains 48 mass% Sn and 52 mass% In and exhibits a melting point of 139°C, which is lower than that of eutectic solder but higher than that of substrates with low heat resistance. These solders exhibit a low volume resistivity ( $10^{-7} \Omega\text{m}$ ) and low  $\rho_c$  ( $10^{-8} \Omega\text{m}^2$ ). In addition, they have a high Young's modulus of several tens of GPa; hence, they exhibit low stretchability, whereas they exhibit a high bonding force to the metal substrate by forming an alloy between the metal wiring and themselves. Hence, although solders exhibit superior electrical properties, they are not suitable for EIM in stretchable electronic devices owing to their high mounting temperature and low stretch tolerance.

Recently, conductive adhesives have been utilized as EIM alternatives to solders. Conductive adhesives comprise conductive fillers and base resins, and their properties, including their conductivity, curing temperature, and Young's modulus, vary significantly depending on the amount of conductive filler and type of base resin adopted. Ag is primarily utilized as a conductive filler owing to its low volume resistivity of  $1.6 \times 10^{-8} \Omega\text{m}$ . Other conductive fillers are also employed, including metal powders, such as Cu and Ni, and carbon-based materials, such as graphite and CNTs. Ag-based conductive adhesives that can be utilized without heating are the focus of this study for low mounting temperatures. Ag-based conductive adhesives are classified into sintering/drying and curing types. Sintering or drying-type adhesives exhibit low volume resistivity values, such as  $8.0 \times 10^{-7} \Omega\text{m}$  (D-500, Fujikura Kasei, Tokyo, Japan) and  $7.0 \times 10^{-6} \Omega\text{m}$  (D-362, Fujikura Kasei, Tokyo, Japan), because the solvent between their fillers are evaporated. However, their stretch tolerance is low owing to their high Young's modulus. In contrast, the cure-type Ag-based conductive adhesives exhibit high volume resistivity values, such as  $5 \times 10^{-5} \Omega\text{m}$  (CN-7120, Kaken Tec, Osaka, Japan),  $1.5 \times 10^{-5} \Omega\text{m}$  (SX-ECA48, Cemedine, Tokyo, Japan), and  $3.5 \times 10^{-5} \Omega\text{m}$  (No solder, Elephantech, Tokyo, Japan). However, their stretch tolerance is higher than that of sintering- or drying-type adhesives because the binder resin cures and remains intact after mounting. For both types of adhesives, the actual contact area between the adhesive and components or wiring is negligible, and the  $R_c$  is high ( $>10^{-7} \Omega\text{m}^2$ ) owing to the high viscosity of the adhesive. Accordingly, solder and conductive adhesives are unsuitable as EIMs for stretchable electronic devices because they cannot achieve both low mounting temperature ( $<60^\circ\text{C}$ ), low volume resistivity ( $<10^{-7} \Omega\text{m}$ ), low  $\rho_c$  ( $<10^{-9} \Omega\text{m}^2$ ), and high stretch tolerance. To address this problem, this study proposes the application of Ga-based LM as an EIM for mounting electronic components without heating. The Ga-based LM can be utilized as an EIM at low temperatures ( $-19$ – $25^\circ\text{C}$ ), as it exhibits low volume resistivity ( $2.9 \times 10^{-7} \Omega\text{m}$ )[9] and high stretch tolerance. However, its  $R_c$  may be high owing to the presence of an oxide layer on the LM surface.

Table 1.2 Melting points of metals and eutectic alloys

Alloyed elements	Element A (at%)	Element B (at%)	Element C (at%)	Melting point (°C)
Hg	100	0	0	-38.8
Ga	100	0	0	29.8
In	100	0	0	156.6
Sn	100	0	0	231.9
Ga/In	85.8	14.2	0	15.4
Ga/Sn	91.7	8.3	0	21.0
Ga/Ag	96.4	3.6	0	26.0
Ga/In/Sn	78.3	14.9	6.8	-19

#### 1.2.4 Low-Melting-Point Metals

Here, metals with melting points below 30°C are focused on from the perspective of low mounting temperature. As a liquid at below 30°C room temperature, Ga-based LMs exhibit several remarkable properties. Note that although mercury is also liquid at below -38.8°C, it is not discussed here owing to its toxicity. In addition, low-melting-point metals and alloys based on alkali metals are not included owing to their fundamentally different nature (i.e. pyrophoricity etc.). Ga-based LMs include Ga alone, E-GaIn (Ga:85.8 at%, In:14.2 at%), which is Ga mixed with In, and galinstan (Ga:78.3 at%, In:14.9 at%, Sn 6.8at%), which is Ga mixed with In and Sn. As presented in Table 1.1, improved based on the previous papers[22], Ga-based LMs have low melting points, for instance, 29.8°C, 15.4°C, and -19°C for Ga, E-GaIn, and galinstan, respectively (Figure 1.5(a))[22], [134]. Ga, In, and Sn form LM alloys with different atomic number ratios and exhibit different melting points. For example, the phase diagram of the Ga-In binary system of Ga and In is illustrated in Figure 1.5(b)[134]. The melting point further decreases when alloys are formed by adding Sn (Figure 1.5(c))[22]. Ga-based LMs exhibit low volume resistivity[1], [22], low melting point, low viscosity (2 mPa·s), low toxicity[5], negligible vapor pressure[7], [135], and high surface tension[21]. In a nitrogen atmosphere at 28°C with oxygen and moisture levels below 0.5 ppm, the surface tensions of E-GaIn and galinstan are 624 and 534 mN/m, respectively, which are one order of

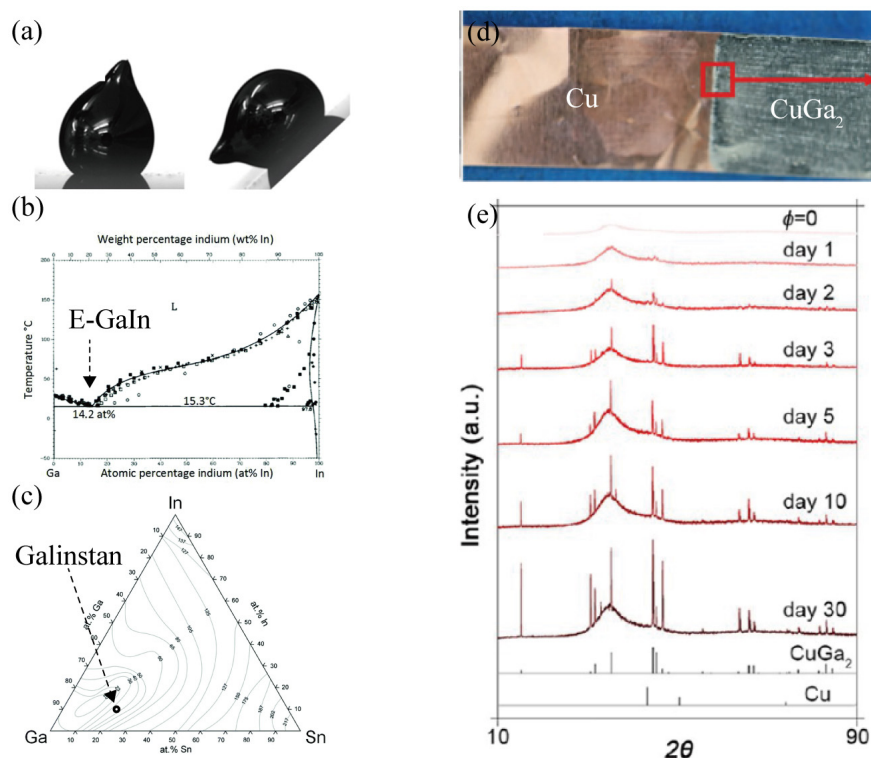


Figure 1.5 Properties of Ga-based LMs. (a) Retention of non-spherical shape by oxide layer on LM surface and adhesion to solid surface by oxide layer on LM surface[28]. (b) phase diagram of the Ga-In binary system[134] (c) Liquidus projection for Ga-In-Sn system[22]. (d) Alloy formation on SM surface in contact with LM[37]. (e) Progression of alloy formation over time[35]. Reproduced with permission from [28] Copyright 2017, Elsevier; [134] Copyright 2007, Springer Nature; [22] Copyright 2018, Royal Society of Chemistry; [37] Copyright 2018, Royal Society of Chemistry; [35] Copyright 2017, American Chemical Society.

magnitude higher than that of water (72 mN/m)[7], [21]. Their contact angles were also high, i.e., 127.6°, 129.8°, and 140.3° on bare-glass, cytop-coated, and Teflon-coated glass substrates in air, respectively[136].

A nitride layer (GaN) forms on LMs in special environments, such as during sonication in a nitrogen atmosphere[6], while an oxide layer ( $\text{Ga}_2\text{O}_3$ ) forms primarily in air[23]–[28]. Regarding the formation of the oxide layer, after an initial oxide monolayer has formed within a few milliseconds, its growth proceeds slowly until it reaches a critical thickness (typically several nanometers)[22]. The volume resistivity of the oxide layer was estimated to be  $10^6 \Omega\text{m}$ [137], and the resistance of the oxide layer changed with the

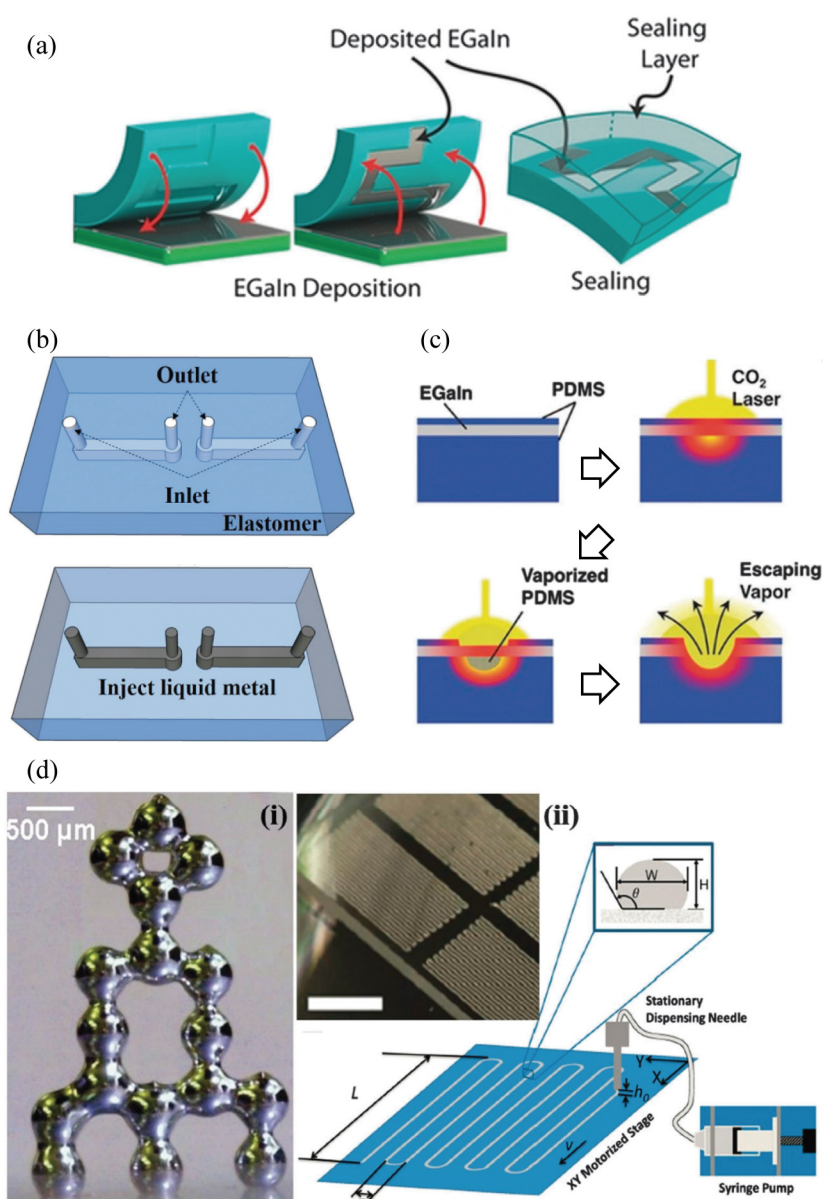


Figure 1.6 Patterning techniques of Ga-based LMs (a) Lithography-enabled processes[143]. (b) injection[7]. (c) subtractive[144]. (d) additive[145], [146]. Reproduced with permission from [143] Copyright 2014, John Wiley and Sons; [7] Copyright 2015, Royal Society of Chemistry; [144] Copyright 2014, John Wiley and Sons; [145] Copyright 2014, John Wiley and Sons; [146] Copyright 2013, John Wiley and Sons.

duration of the exposure of the Ga-based LMs to air. The oxide layer also reduced the surface tension of

Table 1.3 Patterning methods of Ga-based LMs.

Methods	Dimension	Substrate	Line width	Ref. No.
Transferring	2D	Elastomer	$\approx 2 \mu\text{m}$	[143]
Microchannel	2D, 3D	PDMS, elastomer	$\approx 100 \mu\text{m}$	[7]
Reactive wetting	2D	Metal patterns	$\approx 2 \mu\text{m}$	[18]
Laser irradiation	2D	PDMS	5–100 $\mu\text{m}$	[144]
Extrusion	2D, 3D	Silicon, glass, PDMS	$\approx 30 \mu\text{m}$	[145],[146]
Printing	2D, 3D	Glass, PET, PDMS, human skin	$< 1 \mu\text{m}$	[144]

the Ga-based LM. The oxide layer behaves like an elastic body until the surface stress exceeds 500–600 mN/m. When the pressure was further increased, the oxide layer broke, and the LM inside overflowed. The oxide layer causes LM to adhere to several solid surfaces. Ga-based LMs and several SMs form SM alloys over time[29]–[39], although some SMs such as stainless steel, nickel, and chromium do not easily form alloys [138]–[140], and Ga-based LMs with an oxide layer can wet the alloy[29]–[39]. Ga-based LMs exhibit higher adhesion to alloys than to pure metals[35]. For alloys between Cu and Ga ( $\text{CuGa}_2$ )[31], [33], [38], [141], [142], the thickness of the alloy layer is several tens of micrometers[31], [34]. The alloy layer was softer than that of the pure metal layer. For example, Young's modulus of  $\text{CuGa}_2$  is approximately 70 GPa, which is lower than that of Cu (130 GPa)[143].

Figure 1.6 and Table 1.3 show various LM patterning methods for device fabrication. LM patterning can be divided into four major categories: 1) lithography-enabled [144], 2) injection[7], 3) subtractive[18], [145], and 4) additive[146]–[148] patterning. In lithography-enabled patterning, an LM pattern is fabricated using a stencil or mold fabricated by lithography. As illustrated in Figure 1.5(a), imprint lithography transfers the LM by pressing an elastomer mold onto the LM spread on the substrate, and patterns with a 2- $\mu\text{m}$  line width, 1- $\mu\text{m}$  pitch, and submicron thickness can be produced[144]. Patterns with a 200- $\mu\text{m}$  line width and 100- $\mu\text{m}$  pitch can be fabricated[149], [150]. In selective-wetting patterning, the LM is placed on a substrate with both wettable and non-wettable areas, and the LM is patterned only on wettable areas[26], [151], [152]. In injection patterning, as illustrated in Figure 1.6(b), the LM is mainly injected from the inlet of the channel utilizing a syringe[7], [46], [73]. The LM injected into the channel



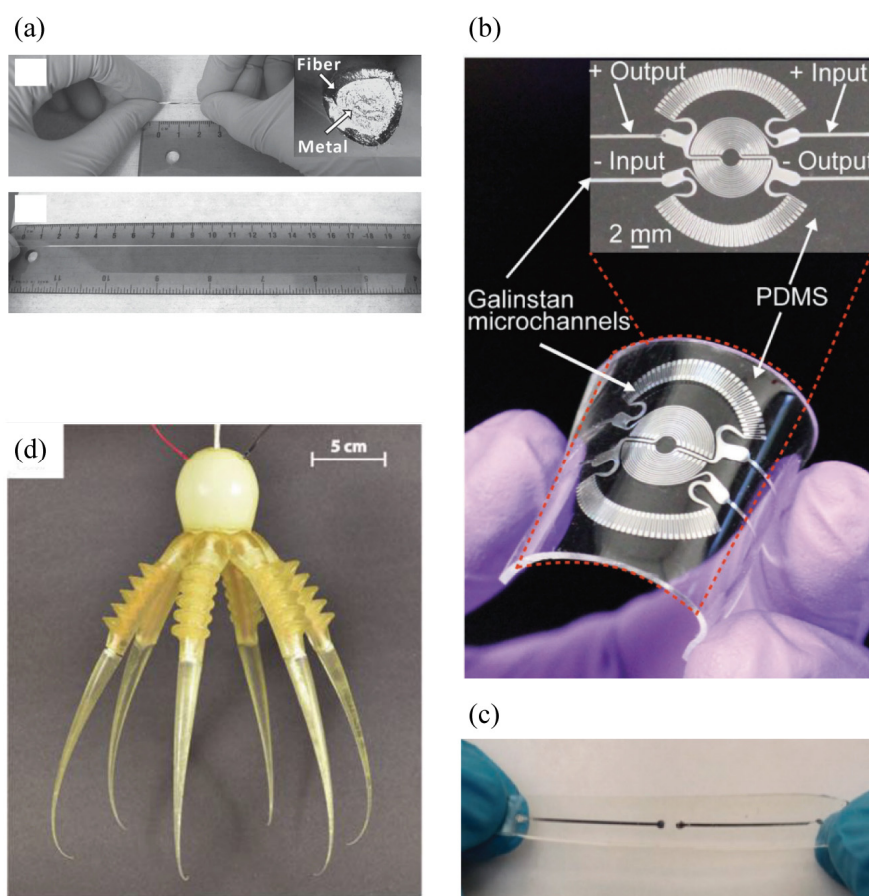


Figure 1.7 Conventional studies using Ga-based LMs. (a) Stretchable interconnect[4]. (b) flexible pressure sensor[9]. (c) flexible antenna[10]. (d) flexible actuator[13]. Reproduced with permission from [4] Copyright 2013, John Wiley and Sons; [9] Copyright 2017, John Wiley and Sons; [13] Copyright 2018, John Wiley and Sons; [10] Copyright 2009, John Wiley and Sons; [13] Copyright 2018, Mary Ann Liebert.

adheres to the channel wall via an oxide layer and is then stabilized. Other methods include filling the channel with LM using Laplace pressure, potential difference, and pressure difference owing to vacuum conditions[46], [153]. Direct patterning via a laser is primarily utilized for patterning via the subtraction process, as illustrated in Figure 1.6(c) A thin polydimethylsiloxane (PDMS) layer was placed over the LM layer on the PDMS substrate, and the PDMS was eliminated utilizing a CO<sub>2</sub> laser to discard the LM in that area[145]. Other methods include moving the LM using capillary force[154]. In patterning via additive processing, a conventional method involves printing the LM directly onto a substrate. As illustrated in

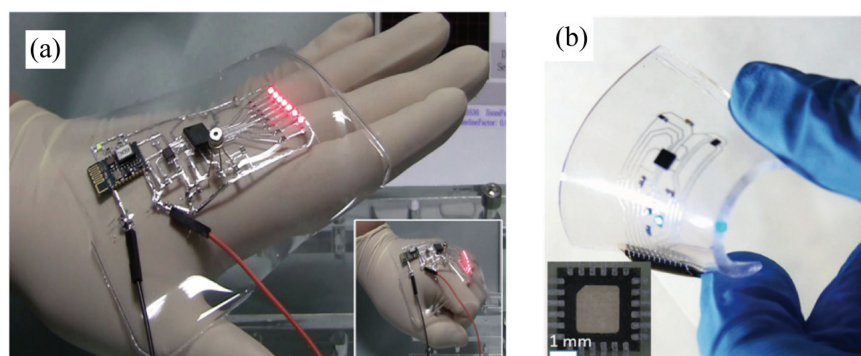


Figure 1.8 Demonstration devices for mounting electronic components on interconnections of Ga-based LMs[19], [18]. Reproduced with permission from [19] Copyright 2015, John Wiley and Sons; [18] Copyright 2018, John Wiley and Sons.

Figure 1.6(d), patterning was conducted by discharging the LM from the nozzle of a syringe onto the substrate. Direct printing enables both 2D [146] and 3D patterning[147]. The fabrication of freestanding structures up to 10 mm in height has been reported using 3D patterning. In direct printing of these LMs, the shape is maintained by utilizing an oxide layer formed on the surface of the LM after dispensing. Based on these techniques, LMs were utilized as stretchable and deformable conductors in stretchable electronic devices such as stretchable wirings[3], [4], flexible sensors[8], [9], flexible antennas[10], [11], and flexible actuators[13], as illustrated in Figure 1.7. Devices were also demonstrated to integrate chip LEDs[17], [155], temperature sensors[18], [19], acceleration sensors[18], and thermoelectric generators[20], as illustrated in Figure 1.8. However, the high  $R_c$  of the oxide layer on the surface of Ga-based LMs becomes a problem when the Ga-based LM is in contact with rigid electronic components.

As a highly stretchable EIM, it exhibits excellent potential because of its zero stiffness owing to its liquid nature. This allows the wiring connected area to be stretched without being constrained by the EIM, which increases the strain in the connected area of the wiring and minimizes the strain difference. The stiffness of the LM as an EIM is always lower than the tensile stiffness of the wiring regardless of the wiring structure or material. Hence, LM can be applied to various types of stretchable metal wiring and exhibits high applicability. The LM exhibited a high stretchability and low tensile stiffness when placed solely within the elastomer. However, when an LM is utilized as an EIM, certain concerns emerge regarding the effect of surrounding electronic components and wiring on the deformation of the LM. In addition, because the substrate strain is lower around the rigid component, the positioning of the element

and wiring may affect the strain distribution in the wiring. As expected, it was unclear whether the wiring section was stretched. If the tensile stiffness of the stretched substrate is higher than that of the wiring, substrate deformation dominates wiring deformation. Because the tensile stiffness of the LM is lower than that of the substrate, the connected areas where the LM is located experience more strain than the other areas, which may trigger new strain differences in the wiring. The effect of the stretchability structure on the electrical connection of the connected area of the wiring is unknown; however, it may suggest a tradeoff with the resistance to stretch tolerance.

### 1.2.5 Interface between LMs and SMs

When an LM is utilized in contact with a rigid electronic component, the high  $R_c$  owing to the oxide layers on the surface of the LM constitutes a problem. In general, the  $R_c$  between two conductors is expressed as the combined resistance of the concentration and film resistance. The  $R_c$  between the LM and SM is high because the volume resistivity of the oxide layer of the LM is as high as  $10^6 \Omega\text{m}$ , and the concentration resistance is also high because the LM with an oxide layer has poor wettability. In previous studies, chemical treatments using acids, bases, and inert atmospheres and physical treatments utilizing direct heating or  $\text{CO}_2$  lasers have been primarily employed to eliminate oxide layers from the surface of LMs. The wettability of the LMs was evaluated by measuring the contact angle between the LMs and SMs [30], [38], [156]. The wettability of the LM on SM was improved by spraying HCl or NaOH vapor on the LM after contact with the LM and SM in air [18], [136], [157]. In the inkjet and spray printing of LMs, the formation of oxide layers on the surface of LM particles is suppressed by mixing a small amount of aqueous NaOH solution in the LM [158]. To prevent the LM in the microfluidic channels from adhering to the channel walls due to the oxide layers, the oxide layer was discarded by the HCl vapor via the gas permeability of PDMS [23]. However, chemical treatments using acids and bases are problematic because they can damage the substrate material and are harmful to the human body. As illustrated in Figure 1.9(c), chemical treatments that employ an inert atmosphere have been investigated, where LM and SM are brought into contact within a nitrogen atmosphere [21], [159], [160]. A study utilizing a glove box to determine the contact angle of LM in a nitrogen atmosphere revealed that when the oxygen concentration was between 0.2% and 20.9%, an oxide layer promptly formed on the surface of the LM droplet, thereby indicating an aspherical shape. At oxygen concentrations exceeding 20 ppm, although the droplets transitioned to a spherical shape, they exhibited gel-like properties rather than liquid behavior. In contrast, droplets with an oxygen concentration of 1 ppm or less exhibited a liquid-like behavior and a spherical

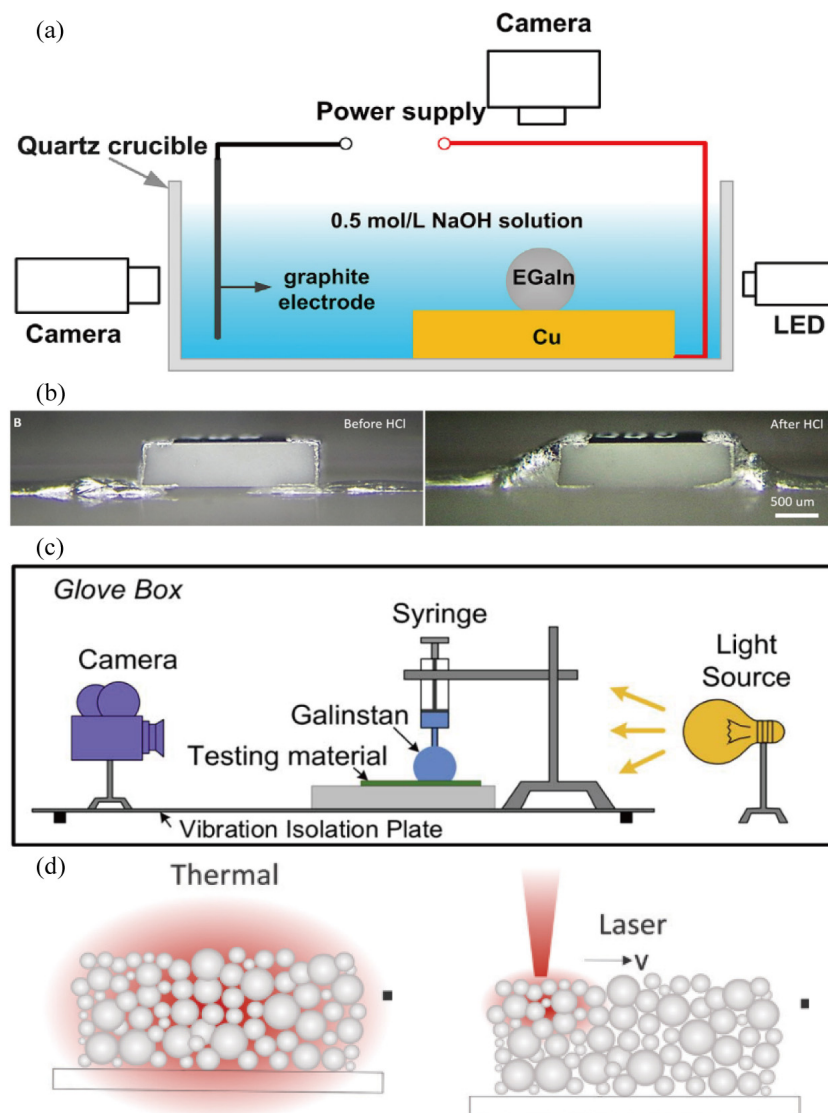


Figure 1.9 Conventional methods for discarding the oxide layer on an LM surface by utilizing (a) NaOH solution[30]; (b) HCl vapor[18]; (c) nitrogen atmosphere[21]; and (d) heat and CO<sub>2</sub> laser[2]. Reproduced with permission from [30] Copyright 2019, Elsevier; [18] Copyright 2018, John Wiley and Sons; [21] Copyright 2011, IEEE; [2] Copyright 2019, Royal Society of Chemistry.

shape. As illustrated in Figure 1.9(d), physical treatment via direct heating or a CO<sub>2</sub> laser eliminated the oxide layer via sintering[1]. Regarding the oxide layer elimination of LM nanoparticles, both laser and thermal sintering apply thermal energy to the LM to rupture the oxide layer on the surface by thermal

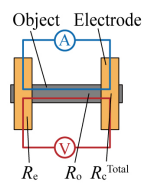
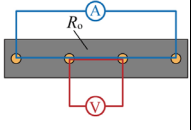
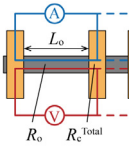
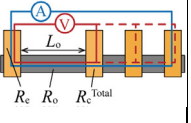
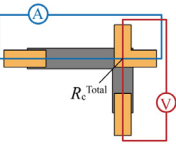
stress to obtain electrical conductivity. During thermal sintering, the generated thermal stress is negligible. Conversely, laser sintering produces significantly higher thermal stress, enabling the elimination of a broader range of oxide layers.

However, these treatments damage the substrates and require expensive equipment such as draft chambers, gloveboxes, and lasers. When an LM is in contact with a rigid electronic component in a stretchable flexible electronic device, the oxide layer must be discarded without damaging the substrate or requiring expensive equipment. The conventional  $R_c$  is altered owing to the contact between the LM and SM. It is considered that oxide layer formation can be suppressed by bringing the LM into contact with the SM before the oxide layer reforms. In addition, because vacuuming typically enhances the adhesion between liquids and solids in contact, it could potentially augment the adhesion between LM and SM. The  $R_c$  between the LM and materials such as carbon nanotubes, ionic liquids[161], [162], Ag-based conductive paste[163], [164], and chip resistors has been studied. However, the impact of the contact procedure on the  $R_c$  between the LM and material remains uninvestigated. Furthermore, although the  $R_c$  may be unstable over time owing to alloying, the change in  $R_c$  after a long time are yet to be studied.

### 1.2.6 Highly Accurate Measurement Method of Contact Resistance

Accurate measurement of the  $R_c$  of LMs is necessary to improve the electrical performance and applicability of stretchable electronic devices by mounting electronic components using LMs, and to better understand the interface between LMs and solid components. The  $R_c$  of LMs is typically measured using standard resistance measurement methods, such as the four-probe method[18], [163]–[167], as shown in Table 1.4. However, the high conductivity, oxide layer on the surface, and high surface tension of LMs complicate the accurate measurement of  $R_c$ , and high-precision measurement methods are yet to be investigated. Conventionally, the transfer length method (TLM)[168]–[172] and cross-bridge Kelvin resistor (CBKR)[173] method have been established for measuring  $R_c$ . In addition, three-point probe method was also used for simplicity of measurement configurations[174], [175], while electrode resistance ( $R_e$ ) cannot be ignored when  $R_c$  is lower than  $R_e$ . In the  $R_c$  measurement of LMs, the LMs are placed in the channel or directly on the substrate to maintain the LM shape. The shape of the placed LM is difficult to control because of its high surface tension and the oxide layer on its surface. Hence, the TLM is suitable for  $R_c$  measurement because it can simultaneously measure the sheet resistance of the object ( $R_{sho}$ ) and  $R_c$  even if the cross-sectional shape of the object is unknown. Therefore, this paper presents a high-precision method for measuring the  $R_c$  of an LM via TLM. In  $R_c$  measurements, there are two types of contact

Table 1.4 Characterization of conventional  $R_c$  measurement methods.

	Four-probe	Four-point probe method	TLM	Three-point probe	CBKR
Configuration					
Measured resistance	$R = R_o + R_c + R_c^{\text{Total}}$	$R = R_o$	$R = R_o + R_c^{\text{Total}}$	$R = R_o + R_c + R_c^{\text{Total}}$	$R = R_c^{\text{Total}}$
Obtaining of $R_c^{\text{Total}}$	Sbtracting calculated $R_o$ and $R_c$ from $R$	-	Sbtracting experimentally obtained $R_o$ from $R$	Sbtracting experimentally obtained $R_o$ and calculated $R_c$ from $R$	Measured value
Ref. No.	[1], [18], [163]–[167]	JIS H 0602-1995, JIS K 7194-1994	[168]–[172]	[174], [175]	[173]

methods between the object and measurement terminal: point and surface contacts. Surface contact was utilized to measure  $R_c$ . Regarding surface contact, electrodes must be fabricated on the object before measurement. The measured resistance ( $R$ ) includes  $R_{\text{sho}}$  and  $R_c$ ; hence,  $R_{\text{sho}}$  and  $R_c$  can be simultaneously obtained. In contrast, point contact is utilized to measure the  $R_{\text{sho}}$  value of an object, such as in the four-point probe method. The contact area at the point of contact is significantly negligible, which allows us to disregard  $R_c$ . Because the measured  $R$  includes only  $R_{\text{sho}}$ ,  $R_{\text{sho}}$  is solely obtained and not  $R_c$ . For  $R_{\text{sho}}$  measurements alone, point contact is a more suitable approach due to its simplicity, as it eliminates the need for prior electrode fabrication on the object. Here, surface contact was utilized as the primary method for measuring the  $R_c$  value of the LM.

In TLM, multiple metal electrodes are brought into contact with the object. Current ( $I$ ) is applied to the outermost electrode, the voltage ( $V$ ) between the adjacent electrodes is measured, and  $R$  is obtained by dividing the applied  $I$  by the measured  $V$ . The measured resistance  $R (=V/I)$  between adjacent electrodes is the combined resistance of the resistance of the object ( $R_o$ ) and contact area ( $R_c^{\text{Total}}$ ). Technically,  $R_c^{\text{Total}}$  may encompass the volume resistance of the object or electrode at the contact area in addition to the resistance  $R_c$  at the interface. During the conventional  $R_c$  measurement,  $R_c^{\text{Total}}$  is considered to be  $R_c$  because the  $R_c$  is high, and the volume resistance of the semiconductor object or electrode in the contact

area is sufficiently low to be disregarded.  $R$  was measured for different object lengths ( $L_o$ ), i.e., the distance between the electrodes.  $R_o$  is proportional to  $L_o$  when the cross-sectional area of an object is constant. In this case, the relationship between  $L_o$  and  $R$  is linearly approximated. The sheet resistance of the object is experimentally obtained from the slope of an approximately straight line. The  $R_c^{\text{Total}}$  value is obtained as the Y-intercept of the linear approximation ( $R_c^{\text{Total}} = \text{Y-intercept}/2$ ), even if  $R_{\text{sho}}$  is unknown.

In TLM, two factors are crucial for achieving highly accurate  $R_c$  measurement: 1) all applied current should pass through the interface between the object and the electrode; 2) modeling and simulation should be performed considering the current-density distribution. The  $R_c$  component in the measured resistance  $R$  is  $R_c \times I_i/I$ , where  $I$  and  $I_i$  denote the applied current and current passing through the interface between the object and electrode, respectively. For highly accurate  $R_c$  measurements, the total  $R_c$  component must be incorporated into the measured value; hence, all applied currents are required to pass through the interface ( $I_i = I$ ). Modeling and simulation should be conducted with the dimensions that align with the current density distribution within the device for measurement. Two-dimensional models and simulations are simpler than three-dimensional models; however, 2D models cannot be utilized when the current density in the device has a 3D distribution. The conventional TLM assumes that the sheet resistance of the metal electrode ( $R_{\text{she}}$ ) ( $\text{Cu}: 10^{-3} \Omega \square$ ) is negligibly low compared to the sheet resistance of the object ( $R_{\text{sho}}$ ). This is because  $R_c$  measurements primarily target materials with high sheet resistance, such as semiconductors, graphene, and conductive pastes ( $>10^2 \Omega \square$ ). Based on this assumption, previous studies [168] and the ISO standard (ISO 16525-2:2014) state that current should be applied to the outer electrode, as illustrated in Figure 1.10(a) and (b). The current applied to the outer electrode flows through the object, and the entire applied current passes through the interface between the object and electrode and flows into the electrode at the contact area between the electrode and object. The current in the electrode passes through the interface again and returns to the object. Based on this assumption, the current density of the device was modeled as a 2D distribution model (transmission line model) [168] and simulated in 2D via the finite element method (FEM) [169] because the electrodes were equipotential, as illustrated in Figure 1.10(c) and (d).

In contrast, when the LM is the object, the LM's sheet resistance ( $10^{-2}$  to  $10^{-4} \Omega \square$ ) is comparable to that of the metal electrode ( $10^{-3} \Omega \square$ ). Hence, the conventional TLM assumption of neglecting  $R_{\text{she}}$  can trigger problems. Specifically, when applying current to the outer electrode following the conventional TLM, only a part of the applied current may pass through the interface between the electrode and the object ( $I_i \ll I$ ). In this case, only a small part of  $R_c$  is included in the measured resistance  $R$ , resulting in low measurement

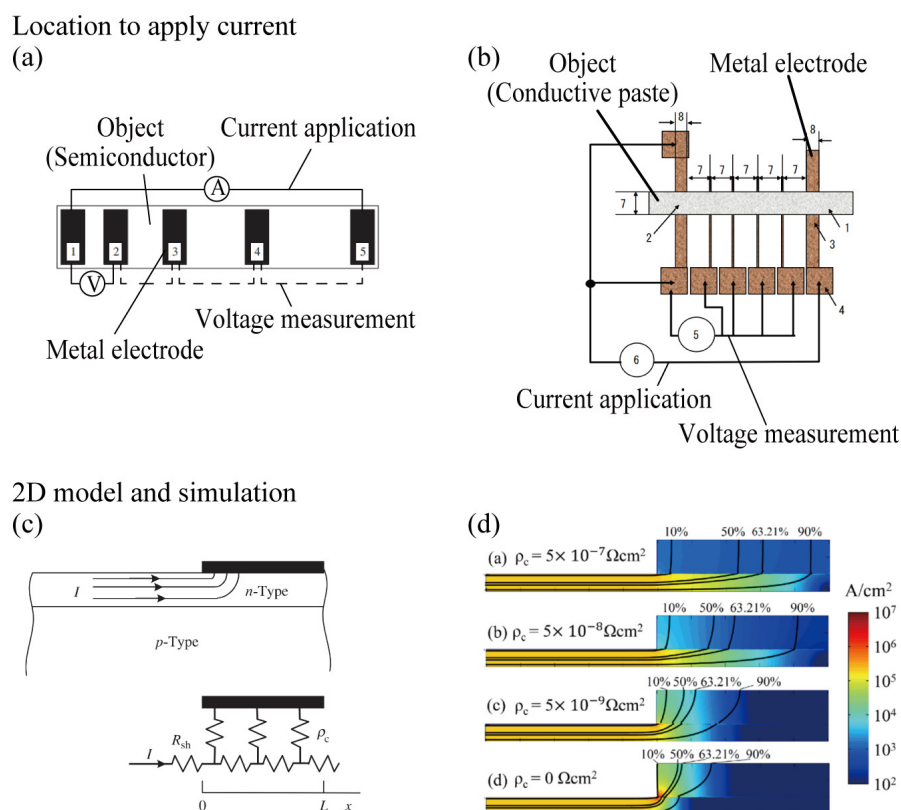


Figure 1.10 Conventional TLM for measuring the  $R_c$  of an object with high sheet resistance, such as semiconductor, graphene, and conductive paste. Location for applying current for (a) semiconductor[168] and (b) conductive paste (ISO 16525-2:2014). Two-dimensional (c) model[168] and (d) simulation[169] of current density distribution in TLM measurement. Reproduced with permission from [168] Copyright 2005, John Wiley and Sons; [169] Copyright 2015, IOP Publishing.

accuracy. In addition, because the electrodes are not equipotential, the current density may exhibit a 3D distribution. Here, conventional 2D models and simulations cannot be employed. To make  $I_i = I$  even for an object with low sheet resistance, the current must be applied to each measurement electrode. By employing this current application method,  $I_i = I$  can be obtained regardless of the sheet resistance ratio ( $R_{sho}/R_{she}$ ) or contact resistivity ratio ( $\rho_c/R_{she}$ ). However, the number of connections doubled. In addition, because current is applied to the electrodes perpendicular to the object, the current density becomes a 3D distribution, requiring a 3D simulation. Hence, a trade-off exists in applying current to each measurement



electrode. The trade-offs represent the improvement in measurement accuracy and complications. Therefore, it is necessary to investigate whether a simple conventional TLM can be applied to objects with low sheet resistance, such as LM.

The effectiveness of the improved TLM in measuring the  $R_c$  of the LM should also be investigated. In addition, for high accuracy, the simulated and measured  $R_c$  values should be compared to obtain the  $R_c$ . Technically, the  $R_c^{\text{Total}}$  includes the volume resistance of the object or electrode at the contact area in addition to the resistance  $R_c$  at the interface. For the conventional objects, such as semiconductor, graphene, and conductive pastes,  $R_c^{\text{Total}}$  is considered  $R_c$  because the  $R_c$  is high and the volume resistance of the object or electrode in the contact area is sufficiently low compared to  $R_c$  to be ignored. However, the  $R_c$  between the LM and metal electrode is considered lower than that between a conventional object and the metal electrode because of the  $R_c$  between the metals. In this case, the volume resistance of the object and electrode in the contact area cannot be ignored, and  $R_c^{\text{Total}} \neq R_c$ . Therefore,  $R_c^{\text{Total}}$  can be obtained from the intersection of  $R_c^{\text{Total}} = Y\text{-intercept}/2$  obtained via measurements and  $R_c^{\text{Total}}$  simulated by swinging the  $\rho_c$ . In previous studies,  $R_c$  was obtained via FEM simulation alone when the actual contact area between the object and electrode and the formation of a surface layer on the object and electrode were known. However, the  $R_c$  values of LMs are difficult to obtain via FEM simulations alone because the formation of an oxide layer on the LMs and actual contact area are unknown.

### 1.3 Objective

This study proposed an electronic component mounting method utilizing LM and evaluated its  $R_c$  and stretch tolerance to realize a highly stretchable and high-performance electronic device. In the evaluation of  $R_c$ , the temporal stability of  $R_c$  due to the contact procedure of LM and alloy formation on the metal electrode surface was investigated. Furthermore, highly accurate measurement of the LM's  $R_c$  was proposed via TLM considering the current density distribution. The stretch tolerance of the LM as an EIM was investigated. Furthermore, the stretch tolerance of stretchable metal wiring on which electronic components were mounted utilizing LM was investigated. Finally, this study presented stretchable electronic devices with electronic components mounted using LM.

Regarding the  $R_c$  of LM, it is necessary to achieve low  $R_c$  without damaging the substrate or expensive equipment. Here, the  $R_c$  for the contact procedures between the LM and metal electrodes was investigated. The three contact procedures were compared to physically rupture the oxide layer on the LM surface. First,

the LM was positioned in a reservoir fabricated between Cu electrodes by injection. The oxide layer on the surface of the LM would be ruptured by the injection of the LM, and the formation of the oxide layer would be suppressed. Next, after the LM and metal electrode were in contact with each other, depressurization was applied. It was hypothesized that the oxide layer on the metal electrode would rupture under reduced pressure when the LM metal was pressed against the microscopic irregularities of the metal electrode surface. These contact procedures were compared with a procedure in which the metal electrode was placed on an LM, on which an oxide layer was sufficiently formed beforehand. Furthermore, because the LM forms alloys with the metal electrode, this study measured the time-dependent change in the  $R_c$  of the LM. To elucidate the contribution of alloy formation to the change in  $R_c$ , this study verified the alloy formation on the Cu electrode surface via morphological observation and compositional analysis. It was determined that the  $R_c$  of LM was reduced to 1/10 or less by injection and depressurization, and the contact procedures of LM were intended to physically rupture the oxide layer. Furthermore, it was inferred that the  $R_c$  of the LM decreased to the same order of magnitude after a long time. The presence of alloys on the metal electrode surfaces in contact with the LM over time revealed a change in  $R_c$  due to alloying. Overall, the reduction in  $R_c$  without damaging the substrate or expensive equipment expands the range of materials utilized as stretchable substrates and significantly benefits the development of stretchable electronics.

Furthermore, a highly accurate measurement method for  $R_c$  between the LM and metal electrodes was proposed. This method addresses the limitations of conventional  $R_c$  measurement methods, which typically focus on TLM, the current application method, and current density distributions. The current density distribution was simulated utilizing FEM for two current application methods: (1) the current was applied to the outer electrodes following the conventional TLM and (2) the current was applied to each measuring electrode following the improved TLM. When current is applied to the outer electrode, the entire applied current passes through the interface between the object and metal electrode in conventional objects with high sheet resistance, such as semiconductors and conductive pastes. Because the fundamental assumption of the conventional TLM, that the entire applied current passes through the interface, remains valid, it is evident that employing the conventional TLM for measurement is appropriate. In contrast, only a part of the applied current passed through the interface when the object exhibited low sheet resistance, such as the LM. The assumption of conventional TLM is not valid; hence, the conventional TLM should not be utilized for the measurement. In addition, the current density was two-dimensionally distributed for all sheet resistances of the objects. Therefore, it is evident that 2D models and simulations can be employed

following the conventional TLM.

However, when the current was applied to each measuring electrode, all the applied current passed through the interface, regardless of the sheet resistance of the object or the  $R_c$  between the object and metal electrode. The current density exhibited a 3D distribution for all the objects with sheet resistance. Therefore, for objects with high sheet resistance, a 2D simulation of the current density distribution, based on the conventional TLM, is recommended for simplicity. In contrast, for objects with low sheet resistance, applying current to the outer electrode reduces the measurement accuracy. Hence, current must be applied to each measuring electrode, and the current density distribution should be simulated in 3D. Furthermore, TLM measurements of the LM and metal electrodes were performed for the two measurement methods of the current application, and the accuracy of the measurements was evaluated by comparing the 3D simulations and measurements. When current was applied to the outer electrodes, the simulated and measured resistances did not intersect when the  $\rho_c$  was swept. Hence, it is clear that the measurement of an object with low sheet resistance, such as LM, is impossible when current is applied to the outer electrode. However, when current was applied to each measuring electrode, the simulated and measured resistance values obtained by altering the  $\rho_c$  had an intersection point, and the  $R_c$  could be obtained. Therefore, it is evident that  $R_c$  can be measured by applying current to each measuring electrode and simulating the current density distribution in 3D for objects with low sheet resistance such as LMs. The improved TLM could measure the same level of  $R_c$  as the solder with the lowest  $R_c$  in the conventional EIM; hence, the measurement accuracy is sufficient for practical use.

Next, this study studied the stretch tolerance of stretchable electronic devices in which electronic components were mounted using an LM. First, the stretch tolerance of the LM as an EIM was evaluated. The samples were fabricated by mounting SMDs using a solder, flexible conductive adhesive, and LM between non-stretchable metal wirings, and sealing them with elastomers. The effects of the stretchability of the EIM and the bonding force between the EIM and metal wiring or electronic components on the stretch tolerance of the EIM are discussed. The Young's modulus of the conductive adhesive was lower than that of the solder; however, the conductive adhesive peeled off from the metal wiring at a lower strain than that of the solder. Nevertheless, although the Young's modulus of the solder is higher than that of the adhesive, the bonding force of the solder is very high because an alloy layer is formed between the metal wiring or electronic components and the solder. This indicates that the stretchability of the EIM and the bonding force between the EIM and stretchable metal wiring and electronic components impact the stretch tolerance of the EIM. In addition, the LM utilized as an EIM exhibited stretch tolerance more than 12

times higher than that of solder or conductive adhesive. This indicates that the LM exhibits both high stretchability and high bonding force. Technically, the peeling of an EIM is determined by peeling and bonding forces. Conventional EIMs, such as solder and conductive adhesives, are solids; hence, the tensile force is converted into a peel force. However, the LM is a liquid; therefore, the peel force is considered to be affected by the surface tension, and the stretched LM attempts to recover its spherical shape. Peeling is considered to be suppressed because the peeling force caused by the surface tension is lower than the adhesive force of the LM on the metal electrode or electronic component. In summary, the LM exhibits excellent performance as an EIM for stretchable electronic devices.

Furthermore, the effect of the EIM on the stretch tolerance of the stretchable metal wiring was investigated. The stretch tolerance of stretchable metal wiring with electronic components mounted using different EIMs was determined. First, the maximum stretch tolerance of the stretchable wiring was obtained. The study considered that the maximum stretch tolerance of wiring can be achieved when the stiffness and strain distributions in the wiring are uniform. To evaluate the stretchability of the kirigami-structured stretchable metal wiring, a sample was fabricated, sealed with an elastomer, and subjected to a tensile test. Subsequently, the stretch tolerance of kirigami-structured stretchable wiring with electronic components mounted utilizing paste solder and LM was determined. The effect of the kirigami structure on the electrical connection was also studied by positioning the structure in the connected area of the wiring. The stretchable metal wiring with electronic components mounted with solder and LM exhibited 0.14 times and 0.79 times higher stretch tolerance than stretchable metal wiring without electronic components, respectively. This indicates that the high stretch tolerance of the EIM can enhance the stretch tolerance of wiring. To further enhance the stretchable wiring tolerance, it is necessary to address the breakage of the substrate around the component. Moreover, it was observed that the electrical performance remained intact even when slits were introduced in the connected region of the wiring. This is because the kirigami structure's ability to stretch uniformly stems from the bending deformation of each beam, which maintains a constant contact area between the LM and the wiring. Finally, stretchable electronic devices were fabricated by mounting chip resistors and chip LEDs on stretchable metal wiring with a kirigami structure. The device exhibited a negligible resistance change during stretching, and stable electrical connections were obtained for each component. This demonstrates that highly stretchable and high-performance electronic devices can be realized by mounting electronic components using LM. In summary, utilizing the LM as an EIM contributed to the development of stretchable electronic devices by significantly enhancing the stretch tolerance of wiring and expanding the device configuration and range

of applications.

## 1.4 Novelty

This study presents four novel contributions:

- 1) A novel device configuration is proposed utilizing an LM exclusively for connecting stretchable wiring to electronic components to significantly enhance the stretchability and performance of stretchable electronic devices.
- 2) The study focuses on the  $R_c$  between the LM and either the components or the wiring. Accordingly, the  $R_c$  was studied for contact procedures to physically rupture the oxide layer and for time-dependent alloying.
- 3) An  $R_c$  measurement method is specifically proposed for materials with low sheet resistance, such as LM, considering the current density distribution.
- 4) This study addresses the breakage around the rigid component caused by the stress concentration and proposes utilizing LM as an EIM to improve the stretch tolerance of the mounting area.

1) The novel feature of the proposed stretchable electronic device is the configuration in which the LM is exclusively utilized to connect the electronic components and stretchable metal wirings. Stretchable electronic devices utilizing LMs can comprise wirings and functional parts fabricated using LMs alone. Hybrid configurations comprising LM, rigid high-performance electronic components, and metal wirings have advantages relative to electrical performance. Although the high stretchability and high conductivity of LMs have garnered significant attention in the past, in such a configuration in which rigid components are mounted using LMs, both the conductivity and stretchability of the LMs and the  $\rho_c$  and stretch tolerance of the component mounting area are important. Ga-based LMs have garnered considerable attention because they exhibit higher conductivities than those of SMs. However, the high  $R_c$  at the interface with the SM remains uninvestigated and was closely evaluated in this study.

2) The novelty in the evaluation of the temporal stability of  $R_c$  of LM is its focus on the  $R_c$  between LM and SM and elucidating the change in  $R_c$  by the contact procedures for the physical rupture of the oxide layer and by alloying over time. Acids, bases, inert atmospheres, and CO<sub>2</sub> lasers have been proposed to discard the oxide layer of LMs. These conventional methods damage stretchable substrates and require expensive equipment. To reduce  $R_c$  without damage, this study investigated the physical rupture of oxide layers by injection, depressurization, and vibration, including the suppression of oxide layer formation by

pre-placing the liquid. It was inferred that  $R_c$  could be reduced to 1/10 by contact procedures for rupturing the oxide layer. Furthermore, Ga-based LMs form alloys with metal substrates, and their wettability can be improved by alloying. Hence, the time-dependent change in  $R_c$  and the effect of alloying were studied. This study determined that  $R_c$  decreased to the same value and was saturated over time by the alloy formation on the metal electrode surface in contact with the LM.

3) Another novel feature of the proposed  $R_c$  measurement is that the  $R_c$  of a low sheet resistance, such as LM, is measured accurately by considering the current density distribution. The conventional TLM has been utilized to measure the  $R_c$  of materials with high sheet resistance, such as semiconductors, and the sheet resistance of metal electrodes is sufficiently lower than that of other objects. Accordingly, the conventional TLM assumes that all the applied current passes through the interface between the object and electrode and flows two-dimensionally in the devices. However, when a conventional TLM is applied to the LM, the sheet resistance of the LM is almost the same as that of the electrode. Hence, this study determined that a part of the applied current passed through the interface and flowed three-dimensionally, making it impossible to measure  $R_c$ . In addition, this study successfully measured  $R_c$  by altering the current application position and simulating the 3D current density distribution.

4) For the final novelty, we investigated the stretch tolerance of the electronic component mounting area and proposed the use of an LM for component mounting. Previous stretchable electronic studies have focused on the stretchability and conductivity of wiring, and several stretchable materials and structures have been proposed accordingly. However, the incorporation of rigid components in these devices introduces a susceptibility to breakage around the components, arising from the stress concentration induced by the disparity in stiffness and strain. This study proposes to mount electronic components on wiring with a stretchable kirigami structure up to the wiring edges using a highly stretchable material (LM). The proposed method suppressed the differences in the strain and stiffness within the wiring and improved its stretch tolerance. The mounting utilizing an LM achieved strain=3/12 wiring stretch, which was 7.4 times higher than that achieved using a conventional solder.

Regarding the impact on science and industry, in addition to being a basic research for elucidating the factors that determine  $R_c$  from the perspectives of interface science and materials science, this study also applied a research to demonstrate stretchable electronic devices. If highly stretchable and high-performance electronic devices can be realized utilizing LMs with low  $R_c$  based on the elucidated factors, it would be of immense industrial significance. This study will pave the way for a novel hardware field dedicated to the development of high-performance, highly stretchable electronic devices, addressing a

pressing industrial need. In addition, the mounting technology utilizing an LM exhibits a substantial industrial ripple effect because it can be applied to any type of functional component and sensor. Specifically, it can be applied to bio-monitoring sheets attached to the skin as an adhesive bandage to measure body temperature and pulse, electronic circuit skin attached to the entire body of a communication-type robot, and clothing-embedded displays that can arbitrarily switch the displayed information.

## 1.5 Thesis Structure

---

This study proposes a method for mounting electronic components on stretchable circuit substrates utilizing an LM and presents highly stretchable, high-performance electronic devices. To achieve this objective, the  $R_c$  and stretch tolerance of the LM utilized as an EIM were studied. As shown in Figure 1.11, this paper is organized as follows.

**Chapter 1 General Introduction:** The background, problems, and inspiration of the proposed method are described. Subsequently, previous studies are categorized, and the challenges of the proposed method are explained. Finally, the purpose and features of this study are presented.

**Chapter 2 Temporary Stability of Contact Resistance of LM:** The  $R_c$  of the investigated LM was studied as the electrical performance of LM as an EIM. The time-dependent change in  $R_c$  was measured. This study identified changes in  $R_c$  for the contact procedures to physically rupture the oxide layer and time-dependent alloy formation. The relatively low  $R_c$ , one or two orders of magnitude higher than that of a conventional solder, was achieved by LM as an EIM.

**Chapter 3 High-Accuracy Contact Resistance Measurement Method :** A highly accurate measurement method for the of  $R_c$  value of the investigated LM was developed to elucidate the factors governing  $R_c$  and identify conditions for achieving low  $R_c$  values. When the conventional  $R_c$  measurement method was applied to the LM, only part of the applied current flowed through the interface, and the  $R_c$  could not be measured. Furthermore, the  $R_c$  measurement was achieved by altering the current application position and analyzing the 3D current density distribution.

**Chapter 4 Stretch Tolerance of Electronic Component Mounting using LM:** The electrical performance of the LM utilized as an EIM is presented in Chapters 2 and 3. In Chapter 4, the high stretch tolerance of the LM as an EIM is investigated. The stretch tolerance of EIMs in stretchable electronic devices is determined by their stretchability and bonding force. Furthermore, it was inferred that the

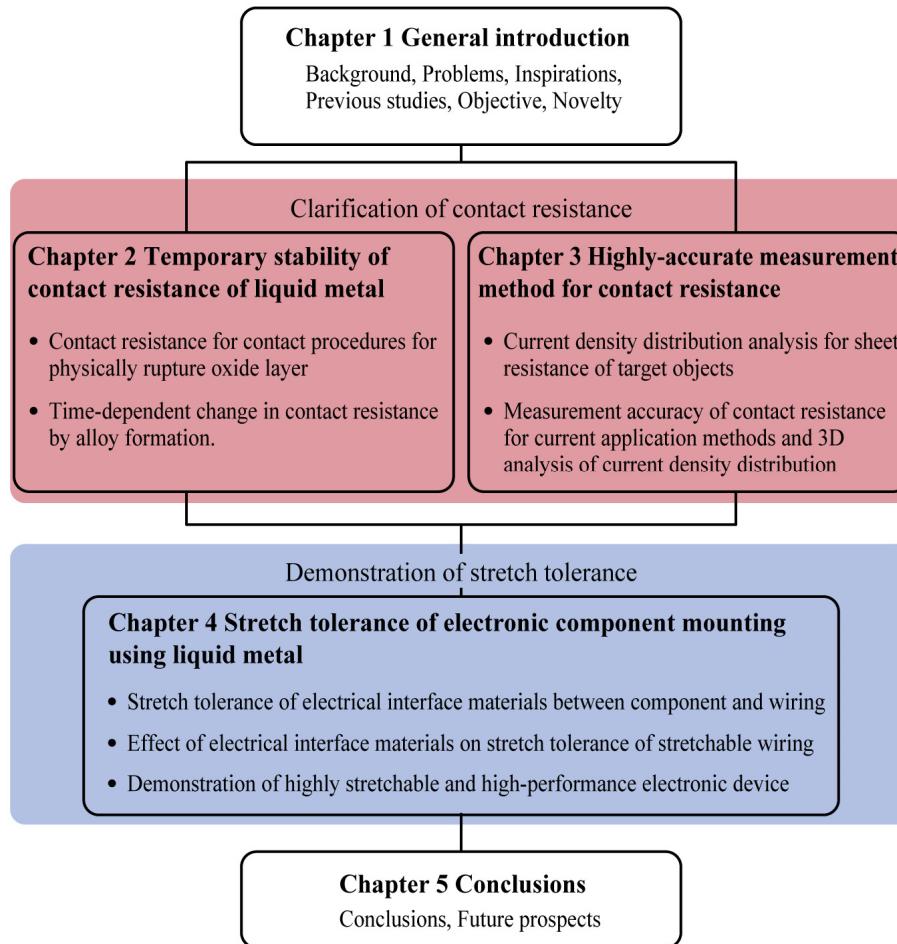


Figure 1.11 Thesis structure.

stretchable EIMs, such as LM, can significantly improve the stretch tolerance of wiring. Accordingly, a stretchable LED display was fabricated, and its high stretchability and performance were demonstrated.

**Chapter 5 Conclusions:** Chapters 2–4 demonstrate the low  $R_c$  and high stretch tolerance of the LM-based mounting method, which resulted in the realization of highly stretchable and high-performance electronic device. Finally, the potential impact of this device on academic research and the industry is discussed.



## Chapter 2      Temporary Stability of Contact Resistance of Liquid Metal

### 2.1      Introduction

---

Flexible electronic connections between rigid components and electrodes are crucial in stretchable electronic devices and thin-film devices[40]–[46]. To mount electronic components in such devices, three factors are required: (1) low mounting temperature, (2) low resistance between electronic components and electrodes, and (3) high stretch tolerance. Low-temperature mounting enables the use of substrates with high elasticity, biocompatibility, but limited heat resistance, such as polyurethane, vinyl chloride, and polyolefin (60–70°C)[40]. Furthermore, low resistance is required for low electricity consumption and low Joule heating in electronic devices. In conventional stretchable and non-stretchable electronic devices, a material placed between the components and electrodes, called EIM, is typically utilized. The resistance is the combined resistance of the EIM volume resistance and  $R_c$  between the EIM and component or electrode. Furthermore, an EIM with stretch tolerance connects the components and stretchable interconnects flexibly and improves the stretchability and flexibility of the stretchable electronic devices. Solders (63% tin, 37% lead by weight), which are typically utilized for conventional EIM, exhibit low

volume resistivity ( $1.5 \times 10^{-7} \Omega\text{m}$ ) and low  $\rho_c$ , i.e., the  $R_c$  per unit contact area ( $10^{-8} \Omega\text{m}^2$ ). However, solders require a high mounting temperature ( $>183^\circ\text{C}$ ) and exhibit low stretch tolerance. An Ag-based conductive paste is a conventional low-temperature EIM. Ag-based conductive pastes can be classified into two types: sintering/drying and curing types, and some Ag-based conductive pastes do not require heating. Here, this study consider the Ag-based conductive pastes that can be utilized without heating. In the Ag-based conductive pastes of the sintering/drying type, the solvent is evaporated; hence, although they can achieve a low volume resistivity of  $8.0 \times 10^{-7} \Omega\text{m}$  (D-500, Fujikura Kasei, Tokyo, Japan) or  $7.0 \times 10^{-6} \Omega\text{m}$  (D-362, Fujikura Kasei, Tokyo, Japan), respectively, they exhibit low stretch tolerance. In the Ag-based conductive pastes of the curing type, the binder resin is cured and retained after mounting; hence, although they exhibit high volume resistivities of  $5 \times 10^{-5} \Omega\text{m}$  (CN-7120, KAKEN TECH, Osaka, Japan),  $1.5 \times 10^{-5} \Omega\text{m}$  (SX-ECA48, CEMEDINE, Tokyo, Japan), and  $3.5 \times 10^{-5} \Omega\text{m}$  (No solder, Elephantech, Tokyo, Japan), they may exhibit high stretch tolerance. In addition, both types of pastes exhibit high  $\rho_c$  ( $>10^{-7} \Omega\text{m}^2$ ) owing to their high viscosity. Hence, these conventional EIMs are unsuitable for low-temperature mounting with low resistance and high stretch tolerance. This study proposes employing Ga-based LMs as EIMs to mount electronic components without heating. The Ga-based LMs can be utilized at low temperatures ( $<25^\circ\text{C}$ ) as EIM, exhibit a low volume resistivity ( $2.9 \times 10^{-7} \Omega\text{m}$ )[1], and have a potential for high stretch tolerance. However, the  $\rho_c$  may be high owing to an oxide layer present on the surface.

Ga-based LMs exhibit low volume resistivity, low melting point, low viscosity (2 mPa·s), low toxicity[5], and negligible vapor pressure[7], [135]. A nitride layer (GaN) forms on the LMs under specific environmental conditions, such as during sonication in a nitrogen atmosphere[6], while an oxide layer ( $\text{Ga}_2\text{O}_3$ ) forms primarily in air[23]–[28]. Regarding the formation of the oxide layer, after an initial oxide monolayer has formed within a few milliseconds, its growth progresses slowly until it reaches a critical thickness (typically several nanometers)[22]. The volume resistivity of the oxide layer is estimated to be  $10^6 \Omega\text{m}$ [137], and the resistance of the oxide layer changes with the exposure duration of the Ga-based LMs to air. The oxide layer also exhibits poor wettability for metallic materials[23]–[28], [176]. The Ga-based LMs and several SMs form alloys over time[29]–[39], although some SMs such as stainless steel, nickel, and chromium do not readily form alloys[138]–[140], and the Ga-based LMs with the oxide layer wet the alloy[29]–[39]. Previously, LMs have been utilized as stretchable and deformable conductors in stretchable electronic devices, such as stretchable interconnects[3], [4], flexible sensors[8], [9], flexible antennas[10], [11], flexible actuators[13], devices to integrate chip light-emitting diodes (LEDs)[17],

[155], temperature sensors[18], [19], acceleration sensors[18], and thermoelectric generators[20]. However, the high  $R_c$  of the oxide layer on the surface of the Ga-based LMs constitutes a problem when the Ga-based LM is utilized in contact with rigid electronic components.

Previously, chemical treatments involving hydrochloric acid (HCl)[177], sodium hydroxide (NaOH)[136], electrolytes[178], a nitrogen atmosphere[21], and physical treatments involving heat such as direct heating and CO<sub>2</sub> laser treatments[1] have been investigated to reduce the effect of the oxide layer on LMs. However, these treatments, damage the substrates and require expensive equipment such as draft chambers[167], gloveboxes, and lasers. The  $R_c$  between the LMs and materials, such as carbon nanotubes, ionic liquids[161], [162], Ag-based conductive pastes[163], [164], and chip resistors, has been studied; however, the change in the  $R_c$  via the contact methods involving the LMs and materials remains unexplored. Furthermore, the  $R_c$  may not remain constant over time owing to alloying. However, the change in the  $R_c$  after a long duration has also not been investigated.

Low  $R_c$  should be achieved without additional processes or equipment that can damage the substrate. Consequently, this study investigated the effect of the oxide layer on the  $R_c$  via the contact methods of Ga-based LMs (galinstan) and a copper film. As its objective, this study focused on the behavior of an electroplated Cu electrode whose roughness  $R_a$  was of a submicron order[166]. This substrate was selected because it is typically utilized as an electrode and interconnect in conventional rigid and flexible electronic devices. Galinstan was positioned after the placement of a Cu film layer, to suppress the formation of the oxide layer. The sample was further degassed in a vacuum to enhance the connection between the Cu film and Ga. These contact methods were compared with the positioned of the Cu film on a prepositioned galinstan on which the oxide layer grew. Here, the  $R_c$  would be affected by the oxide layer thickness, alloying, metal material, surface roughness, etc. Regarding the oxide layer and alloying, the  $R_c$  immediately after making contact would be primarily affected by the oxide layer; however, the time-dependent change in the  $R_c$  would be impacted by both the oxide layer and alloying, which is difficult to separate from each other. Hence, this study measured the  $R_c$  and its time-dependent change. Alloy formation on the Cu film surface was also verified via morphological observation and elemental analysis to elucidate the contribution of alloy formation to the change in  $R_c$ . The obtained results suggest that as an EIM, galinstan achieved low and temporally stable  $R_c$  over time in the case of the galinstan positioned after the Cu film and application of vacuum. The difference in the initial  $R_c$  emerging from the different contact methods eventually reduced owing to alloy formation. In general, the reduction in  $R_c$  without damage to the substrates or the requirement of expensive equipment expands the range of materials utilized

as substrates, which benefits the development of stretchable electronics.

## 2.2 Contact Resistance for Contact Procedures

---

In Section 2.2, a method is presented for mounting electronic components using an LM and the  $R_c$  of the LM relative to the contact procedures is investigated. The LM forms an oxide layer on its surface, which can increase the  $R_c$  between the LM and electronic components or wiring. However, conventional methods for discarding the oxide layer cause damage to the substrate and require expensive equipment. Therefore, to eliminate the oxide layer without damage, this study compared the  $R_c$  between an LM (galinstan) and SM (Cu film) by adopting different procedures; in the L-S method, the SM (S) is placed after the LM (L) to allow sufficient oxide layer formation. In the S-L method, the LM is injected into the liquid reservoir after the SM to physically rupture the oxide layer. In the S-L-V method, the sample prepared by the S-L method is vacuumed (V) for further oxide layer destruction. After 1 day, the contact resistivities ( $\rho_c$ ) were  $5.7 \times 10^{-7} \Omega\text{m}^2$ ,  $3.3 \times 10^{-7} \Omega\text{m}^2$ , and  $0.3 \times 10^{-7} \Omega\text{m}^2$  for the L-S, S-L, and S-L-V methods, respectively. These results indicate that the contact procedure of the LM attempted to break the oxide layer changes of  $\rho_c$  to 1/10. Accordingly, this study verified that physically rupturing the oxide layer is potentially highly effective in reducing the  $R_c$  of the LM without damage.

### 2.2.1 Study of Contact Resistance for Contact Procedures

Figure 2.1 presents a schematic of the method for mounting electronic components utilizing the proposed LM. In this mounting method, a Ga-based LM is placed between the stretchable metal wiring on the stretchable substrate and rigid electronic component, and sealed with a stretchable material to electrically and mechanically connect them. Utilizing LM with low volume resistivity, low mounting temperature, and high stretchability as an EIM allows the reduction of power consumption and heat generation and utilization of materials with low heat resistance as substrates. Furthermore, stress concentration around the electronic component is minimized, and highly stretchable and high-performance electronic devices can be realized. In contrast, when LM is utilized as an EIM, the oxide layer formed on the surface of the LM increases  $R_c$ ; however, it is difficult to discard the oxide layer without damaging the substrate or utilizing expensive equipment. In addition, although LM tends to form alloys with SM over time, the change in  $R_c$  over time and its factors are yet to be comprehensively studied. Alloying of LM

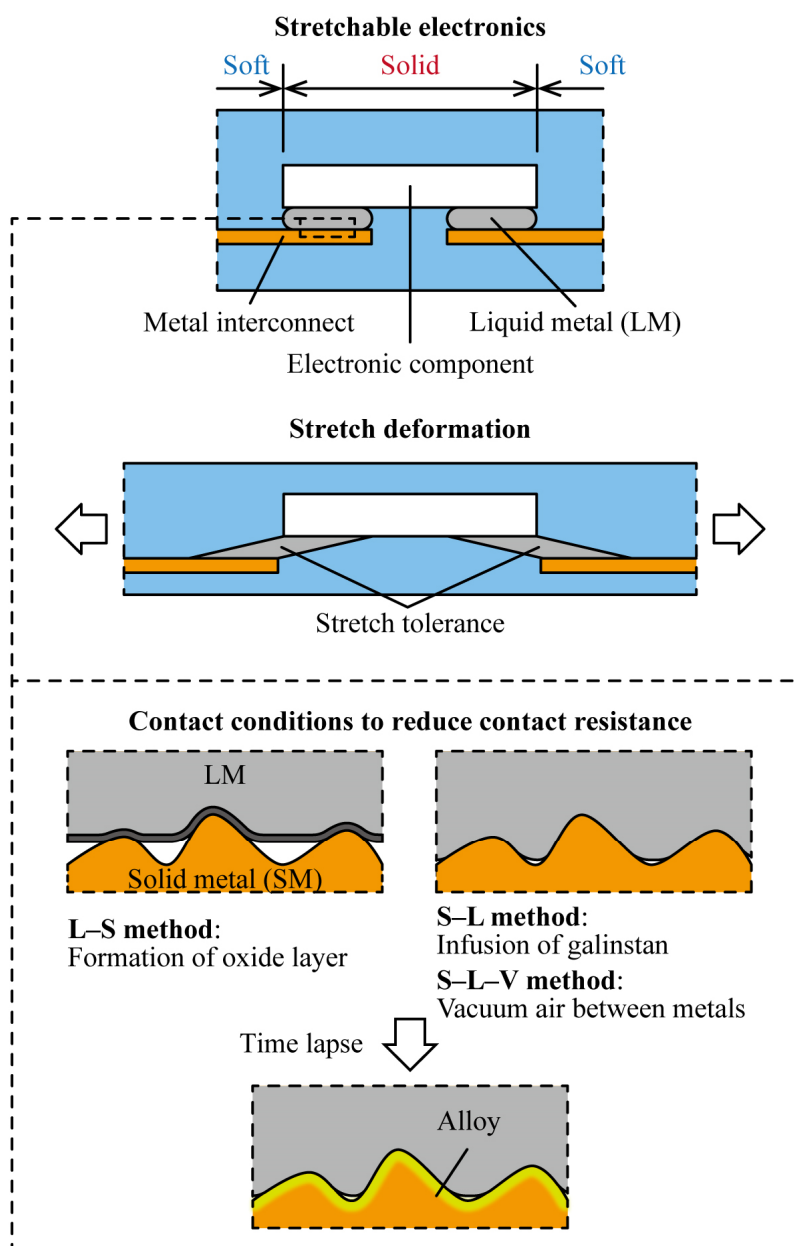


Figure 2.1 Schematic of electronic component mounting method using LM.

with SMs can lead to the embrittlement of electronic components and SM wiring. Although LM exhibits high elongation resistance, the change in resistance to the elongation deformation of the LM as an EIM is unknown. In addition, because LM is liquid, unlike other EIMs, it requires encapsulation during mounting, which may complicate the mounting process and structure. Hence, several challenges exist when utilizing

Table 2.1 Contact procedures of LM and SM and their purposes.

Purpose	L-S	S-L	S-L-V	S-IPA-L	S-L-heat	S-IPA-L-heat	plasma-S-L	L-S-sonication
Fig. No.	2.4(a)	2.4(b)	2.4(c)	2.6(a)	2.6(b)	2.6(c)	2.6(d)	2.6(e)
Form oxide layer	✓ Leave in air	-	-	-	-	-	-	-
Rupture oxide layer	-	✓ Injection	✓ Injection vacuum	✓ Injection	✓ Injection	✓ Injection	✓ Injection	✓ Sonication
Accerate alloying	-	-	-	-	✓ Heat	✓ Heat	-	-
Improve wettability	-	-	-	✓ IPA	✓ Alloying	✓ Alloying	✓ Plasma	-

LM as an EIM. Nevertheless, reliable electrical connection (low  $R_c$  with temporal stability) and high stretch tolerance are considered crucial for the EIMs of stretchable electronic devices. In this chapter, the  $R_c$  between LM and SM is evaluated.

Table 2.1 shows the proposed contact procedures and their purposes. First, Ga-based LM and SM were contacted by three different contact procedures to compare the contact  $R_c$  between the LM and SM. In the L-S method, the SM is placed after the LM to form a sufficient oxide layer. In the S-L method, the LM is injected into the liquid reservoir after the SM to physically rupture the oxide layer. It is assumed that the injection repeatedly destroys and re-forms the oxide layer on the surface of the LM, and that the LM contacts the SM before the oxide layer re-forms, thereby inhibiting the formation of the oxide layer. For further physical rupture of the oxide layer in the S-L-V method, the sample prepared by the S-L method was vacuumed. It is assumed that air between the LM and SM is eliminated via vacuuming, and the oxide layer is ruptured when the SM is pressed against the surface roughness of the SM. Furthermore, in the solid-isopropyl alcohol (IPA)-liquid method, to fill the reservoir with LM, after placing the SM, the IPA is injected into the liquid reservoir, and then the LM is injected into the liquid reservoir. The LM is injected into the IPA to prevent it from being oxidized in the reservoir. In the solid-liquid-heat method, devices

fabricated by the S-L method are heated to promote alloy formation between LM and SM at high temperatures. In the solid-IPA-liquid-heat method, IPA is utilized to prevent the oxidation of the SM in the air in the reservoir. The devices fabricated by the solid-IPA-liquid method were heated to promote alloying between the SM and LMs. In the plasma-solid-liquid method, the SM surfaces were treated with O<sub>2</sub> plasma to improve the wettability of the SM, and then the LM and SM were brought into contact by the S-L method. In the liquid-solid-sonication method, devices fabricated by the L-S method were subjected to ultrasonic vibration. This study hypothesized that the vibration would destroy the oxide layer on the surface of the LM. This study determined the  $R_c$  of the devices fabricated by the aforementioned connection methods.

### 2.2.2 Device Fabrications

To compare the  $R_c$  between LM and SM via the contact procedures, a device was fabricated to measure the  $R_c$  between the LM and SM, as illustrated in Figure 2.2. Here, galinstan (Changsha Rich Nonferrous Metals, Hunan, China)[179], which is prevalent among Ga-based LMs because of its low melting point (-19°C), was employed as the LM material. A Cu electrode was utilized as the SM material. Cu is typically employed as a wiring and electrode material in both flexible- and conventional-hard-electronic devices. Table 2.2-Table 2.5 present the properties of materials employed in the samples. The Cu electrode comprises two layers: a 25- $\mu\text{m}$  thick polyimide layer and an 8- $\mu\text{m}$  thick electroplated Cu layer (Metaroyal, Toray Advanced Materials Korea, Seoul, Korea)[180]. In the device for measuring  $R_c$ , two Cu electrodes for connecting to the measuring device and a PDMS sheet (Silgard 184, Dow Chemical, MI, US)[181] with a liquid reservoir filled with galinstan were positioned between two glass substrates. Two devices were positioned between the pair of glass substrates. It was assumed that the compressive deformation of the PDMS when sandwiched between the glass substrates would fill the gap between the LM and SM metals in the reservoir and make them stick together, thereby improving contact reproducibility. PDMS, an elastic material, rather than a rigid material, was utilized as the material for the liquid reservoir. The liquid reservoir has no outlet because air in the reservoir permeates the PDMS when LM is injected. Devices fabricated via the contact procedure, in which IPA is injected into the liquid reservoir before the LM is injected into the reservoir, have an outlet for the IPA. When the two Cu electrodes are in contact with the top surface of the LM in the reservoir, the current flows in a U-shape through the galinstan, resulting in a non-uniform current density and making it difficult to accurately calculate the volume resistivity of the LM. However, the volume resistance of galinstan in a reservoir, which is estimated via

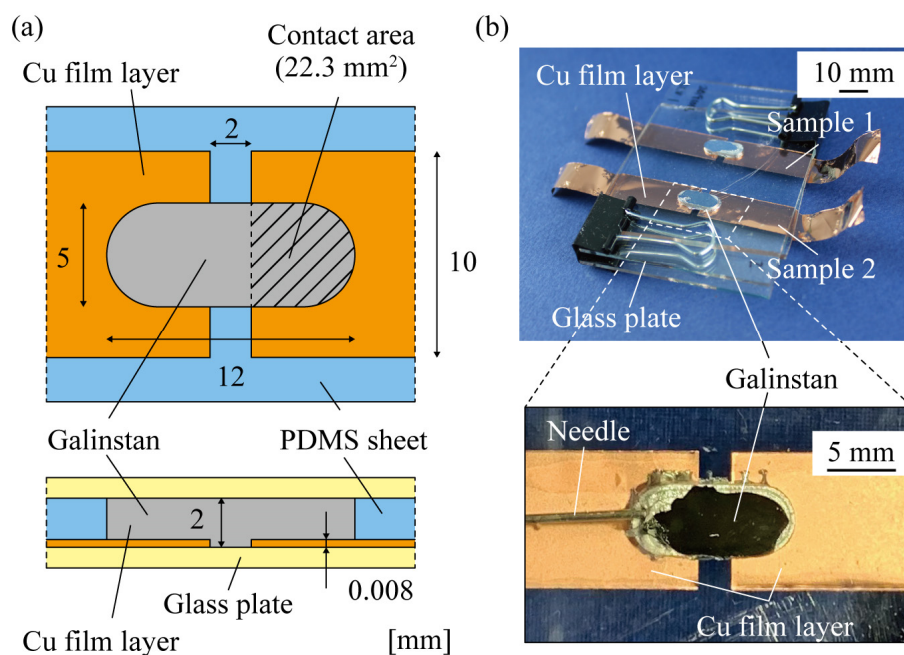


Figure 2.2 Sample to measure the  $R_c$  between galinstan and copper (Cu) electrode. (a) Schematic illustrations and (b) Optical images of the samples.

the volume resistivity of galinstan, is more than one order of magnitude smaller than the  $\rho_c$ . Hence, the effect of non-uniform current density in the galinstan and at the interface between the galinstan and Cu electrode on the  $R_c$  is considered negligible. Here, a device with two Cu electrodes in contact with LM in a reservoir was fabricated. The Cu electrodes were 50-mm long, 10-mm wide, and 0.008-mm thick. The reservoir was 12-mm long, 5-mm wide, and 2-mm thick, and the radius of curvature of the corners of the reservoir was 5 mm. Cu electrodes were positioned at 2-mm intervals on both sides of the reservoir. The apparent contact area between the galinstan and Cu electrode was 22.3 mm<sup>2</sup>, as illustrated in the hatched area in Figure 2.2(a). The galinstan's volume resistance decreased as the galinstan's thickness increased relative to the Cu electrode. The study also considered increasing the  $R_c$  between the galinstan and Cu electrode by decreasing the apparent contact area between them. However, if the apparent contact area is negligible, the wettability between galinstan and PDMS or the Cu electrode is insufficient and the galinstan does not fill the corners of the liquid reservoir; hence, the apparent contact area may be smaller than the actual apparent contact area, making it difficult to accurately calculate  $R_c$ . Therefore, the contact area between the galinstan and Cu electrode was set to the aforementioned dimensions.



Table 2.2 Properties of galinstan used for samples.

Properties	Galinstan	Ref. No.
Purchase	Changsha Rich Nonferrous Metals, Hunan, China	[179]
Composition	Ga:78.3 at%, In:14.9 at%, Sn 6.8at%	[179]
Purity	99.99	[179]
Melting Point	-19°C	[22]
Conductivity	$3.46 \times 10^6$ S/m (at 20°C)	[22]
Viscosity	0.0024 Pa·s (at 20°C)	[22]
Surface tension	534.6 mN/m (at 20°C)	[21]

Table 2.3 Properties of Cu electrode used for samples.

Properties	Cu electrode (Cu-polyimide layers)	Ref. No.
Purchase	Metaroiyal, Toray Advanced Materials Korea, Seoul, Korea	-
Thickness	Cu:8 $\mu$ m, Polyimide: 25 $\mu$ m	-
Conductivity	$5.96 \times 10^7$ S/m (at 20°C)	[3]
Fabrication	Electroplating	-
Surface roughness	$R_a < 1 \mu\text{m}$	[166]
Young's modulus	Cu: 130 GPa, Polyimide: 2.5 GPa	[143],[180]

In addition, as illustrated in Figure 2.3, a sample with a galinstan placed between the chip resistor (RK73ZW2HTTE, KOA, Nagano, Japan)[182] and Cu electrode was fabricated. The study demonstrated that the proposed contact procedure for reducing  $R_c$  could be applied for mounting components on the device. In the sample, a chip resistor was embedded in a PDMS sheet. Reservoirs were fabricated in the PDMS sheet between the chip resistor and Cu electrode. Galinstan was positioned in the reservoir via the L-S, S-L, S-L-V methods. The electrodes of the chip resistors were coated with Sn. For comparison, we also fabricated a device in which chip resistors were mounted with conductive paste (D-500, Fujikura Kasei, Tokyo, Japan), which exhibits the lowest  $\rho_c$  in conventional non-heat mounting. Figure 2.3(a) presents an overview of a device with chip resistors mounted using galinstan and conductive paste. Figure 2.3(b) presents an optical image of the device. To demonstrate the effectiveness of the contact procedure in reducing  $R_c$ , the entire device resistance was measured.

Table 2.4 Properties of silicone rubber used for samples.

Properties	Silicone rubber (PDMS)	Ref. No.
Purchase	Silgard 184, Dow Chemical, MI, US	[181]
Material	Polydimethylsiloxane (PDMS)	[181]
Young's modulus	6.7 MPa	[181]
Curing	48 h (at 25°C), 10 min (at 150°C)	[181]

Table 2.5 Properties of chip resistors used for samples.

Properties	Chip resistor (RK73Z)	Ref. No.
Purchase	RK73ZW2HTTE, KOA, Tokyo, Japan	[182]
Type	Thick film resistors	[182]
Resistance	<50 mΩ	[182]
Electrode	Sn plating on Ni plating	[182]
Chip dimensions	Length 5 mm, Width 2.5 mm, Thickness 0.6 mm	[182]
Electrode dimensions	Length 0.65 mm, Width 2.5 mm	[182]

The procedure for fabricating a PDMS sheet with a liquid reservoir is presented below. A mold with the same dimensions as the liquid reservoir was fabricated by acrylonitrile butadiene styrene using a thermal melt lamination (FDM) 3D printer (X-pro, Qidi Technology, China). This mold was glued to the bottom of a 100-mm petri dish. To fabricate a PDMS sheet with uniform thickness, it is important to reduce the inclination of the flat plate as described below. A mold of the same height as the liquid reservoir was fabricated with an FDM-3D printer and attached to the bottom of the petri dish. Subsequently, uncured PDMS was poured into the petri dish such that it was higher than the mold, and a PDMS sheet of uniform thickness was fabricated by placing a flat plate on top of the PDMS and pressing it against the 3D printed mold. The silicone rubber base and hardener were mixed at a mass ratio of 10:1 and mixed using a mixer (ARE-312, THINKY, Tokyo, Japan). When placing a flat plate on the PDMS, the plate was tilted and gradually flattened to prevent air bubbles from being retained. PDMS was left for 24 h to cure, and then cut into sheet shapes with a scalpel. Cu electrodes were cut out with a cutter knife using a ruler and an oil-based marker. The copper substrate was treated with flux (NS30, Nihon Superior, Osaka, Japan) before assembly. The galinstan was stored in a sealed shipping container. Syringes were utilized to position the

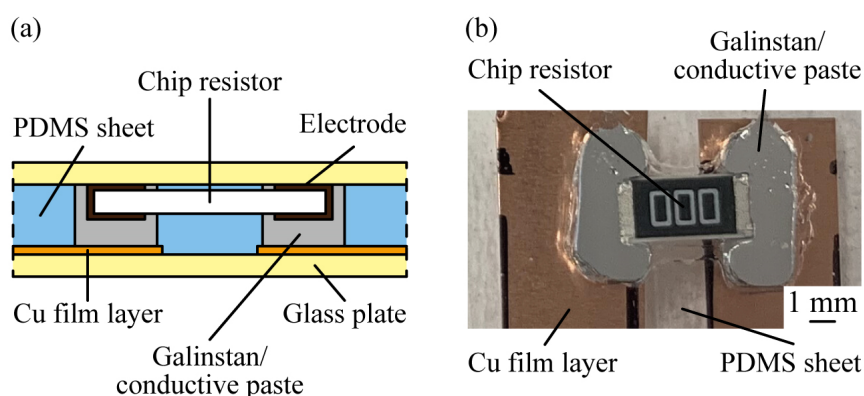


Figure 2.3 Sample for mounting a chip resistor utilizing LMs and conductive paste as an EIM.  
 (a) Schematics and (b) Optical image of the sample.

galinstan. The syringe was employed to take the galinstan out of the container, and the container was closed immediately after opening. The syringe was utilized several times with the needle attached, and when the galinstan in the syringe was exhausted, the galinstan was sucked out of the container again. The syringe containing the galinstan was stored in air until its next use. The syringe needles were replaced with new ones each time because they were prone to clogging due to the oxidation of the Ga.

Figure 2.4(a)–(c) present the procedure for fabricating devices to measure the  $R_c$  between LM and SM via the L-S, S-L, and S-L-V methods, respectively. In the L-S method, the galinstan was placed in a reservoir fabricated in a PDMS sheet on a glass substrate, as illustrated in Figure 2.4(a-i) and left in air. Subsequently, 24 h after placement, two Cu electrodes were positioned on top of the galinstan with a gap between them, and the glass substrate was placed between them and fixed (Figure 2.4(a-i)). The Cu electrodes were aligned using tweezers (Figure 2.4(a-ii)). In the S-L method, two Cu electrodes were placed on both sides of the reservoir in the PDMS sheet and fixed between two glass substrates, as illustrated in Figure 2.4(b-i). Galinstan was then injected into the reservoir using a stainless steel G22 needle and a 5-ml syringe (Figure 2.4(b-ii)), and the needle was removed after the reservoir was full (Figure 2.4(b-iii)). The needle was inserted between the PDMS sheet and glass substrate on the opposite side of the Cu electrode to prevent the galinstan from sticking to the Cu electrode. In the S-L-V method, devices fabricated via the S-L method were placed in a vacuum desiccator (VE-ALL, As one, Osaka, Japan) at  $-0.08$  MPa (gauge pressure) and removed after 24 h, as illustrated in Figure 2.4(c).

Figure 2.5 illustrates the procedure for placing a certain amount of galinstan to fill the reservoir via the

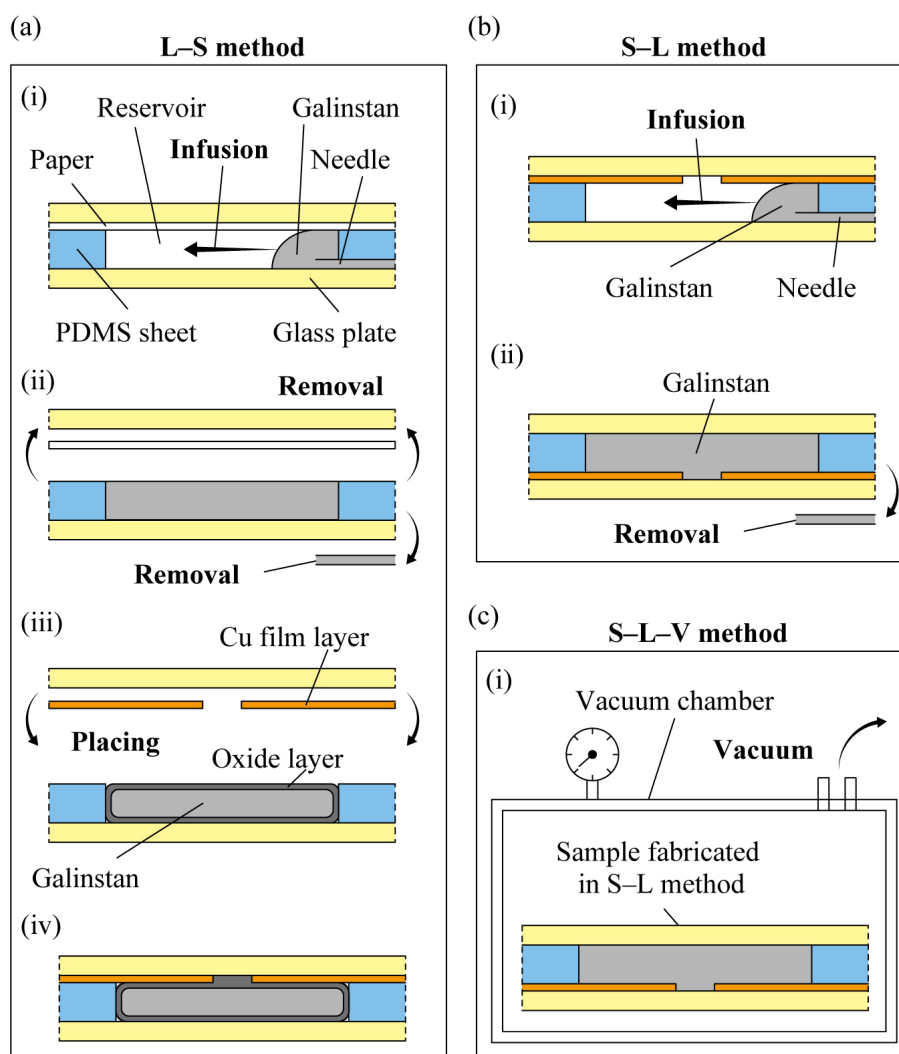


Figure 2.4 Fabrication procedures of samples via (c) L-S; (d) S-L; (e) S-L-V methods.

L-S method. A PDMS sheet with a reservoir and a piece of paper are fixed between two glass substrates (Figure 2.5(a)). The piece of paper was placed between the PDMS sheet and one of the glass substrates to prevent the galinstan from sticking to the glass substrates and altering the Ga's volume. A needle and syringe were utilized to inject the galinstan into the reservoir, and the needle was removed after the reservoir was full (Figure 2.5(b) and (c)). Finally, the glass substrate and piece of paper were removed (Figure 2.5(d)). The syringe needle was inserted between the PDMS sheet and glass substrate on the opposite side of the piece of paper. During injection, the PDMS sheet deformed and covered the gap between the PDMS sheet and glass substrate where the needle was inserted. If galinstan adheres to the

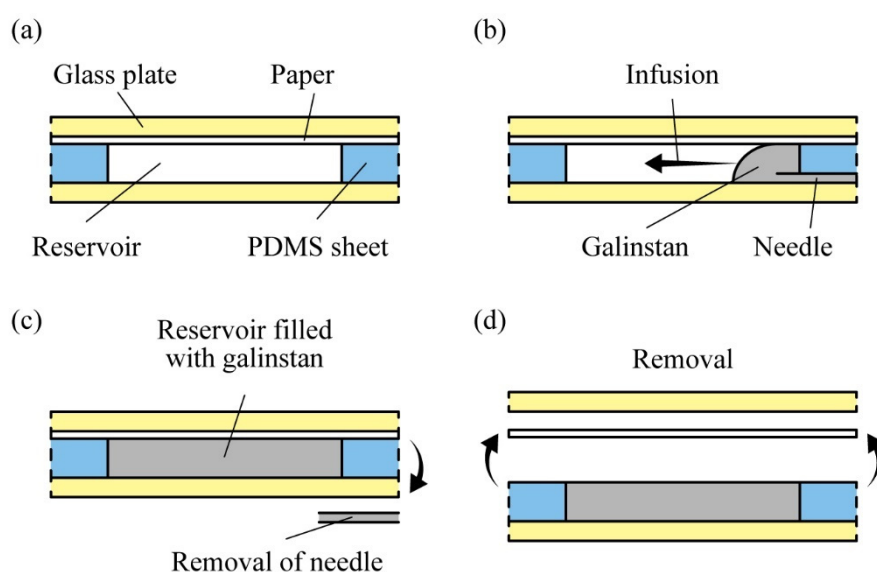


Figure 2.5 Fabrication procedures for placing galinstan in a reservoir in the L-S method. (a) A piece of paper was placed on a PDMS sheet to prevent the galinstan from adhering to a glass plate, and they were sandwiched by two glass plates. (b) galinstan was then injected into the reservoir with a syringe and needle. (c) After the reservoir was filled out, the needle was removed. (d) The upper glass plate and piece of paper were removed.

outside of the needle, it would leak through the outer wall of the needle during injection. Hence, the needle was wiped with an IPA-soaked Kimwipe after each injection.

Figure 2.6 illustrates the fabrication procedures of the  $R_c$  measurement devices via the solid-IPA-liquid, solid-liquid-heat, solid-IPA-liquid-heat, plasma-solid-liquid, and liquid-solid-sonication methods. As illustrated in Figure 2.6(a), in the solid-IPA-liquid method, two Cu electrodes were placed on both sides of the reservoir in the PDMS sheet and fixed between two glass substrates (Figure 2.6(a-i)). Next, IPA was injected into the reservoir using a needle and syringe (Figure 2.6(a-ii)), and the needle was removed when the reservoir was full. Finally, another needle and syringe were utilized to inject galinstan into the reservoir (Figure 2.6(a-iii)), and the needle was removed after the reservoir was full (Figure 2.6(a-iii)). As illustrated in Figure 2.6(b), for the solid-liquid-heat method, devices fabricated by the S-L method were placed in an oven at 250°C and removed after 1 h. As illustrated in Figure 2.6(c), the solid-IPA-liquid-heat method, devices fabricated by the solid-IPA-liquid method were placed in an oven at 250°C and removed after 1 h. As illustrated in Figure 2.6(d), in the plasma-solid-liquid method, devices were prepared by the S-L

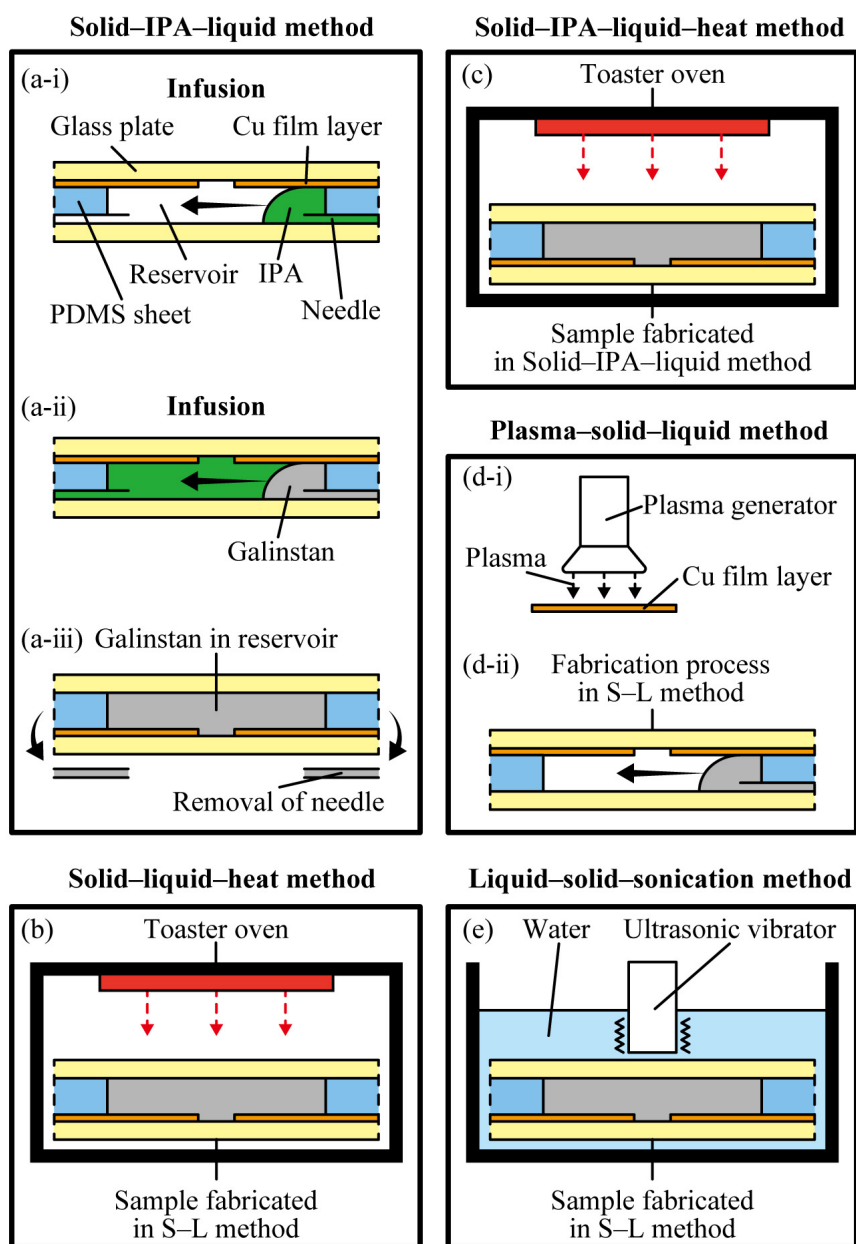


Figure 2.6 Fabrication processes of the device in the (a) Solid-IPA-liquid method; (b) Solid-liquid-heat method; (c) Solid-IPA-liquid-heat method; (d) Plasma-solid-liquid method; (e) Liquid-solid-sonication method.

method using Cu electrodes whose surface was plasma-treated for 1 min. As illustrated in Figure 2.6(e), for the liquid-solid-sonication method, devices fabricated by the L-S method were placed in a container of

water and vibrated using a portable ultrasonic cleaner (W20, Winten, Tokyo, Japan), and removed after 1 h.

### 2.2.3 Measurement Methods

As illustrated in Figure 2.7, this study measured the resistances of a sample via the four-terminal method using a digital multimeter (34420A, Keysight, CA, US). Detailed settings are presented in the Appendix B. The  $R_c$  [ $\Omega$ ] value was obtained by subtracting the volume resistances of the Cu electrode  $R_{SM}$  [ $\Omega$ ] and galinstan  $R_{LM}$  [ $\Omega$ ] from the measured resistance  $R$  [ $\Omega$ ] of the entire sample. The Cu electrode was connected to the measurement equipment using alligator clips. The Cu electrode was marked at 10-mm intervals, and two alligator clips were connected from both sides of the electrode at the same distance from the edge of the Cu electrode. Because the resistance of the device may fluctuate immediately after the commencing the resistance measurement, the resistance value presented on the display of the measurement device was read when the resistance value stabilized after 60 s from the start of measurement. The measurement speed of the digital multimeter was number of power line cycle (NPLC) = 1, and the applied voltage was 10 mV.

The resistance  $R$  [ $\Omega$ ] between the measurement terminals in Figure 2.7(b) can be expressed by Equation (2.1), considering that the two SM wiring are electrically connected by the LM in the reservoir.

$$R = R_{SM} + R_{LM} + R_c = \rho_{SM} \frac{l_{SM}}{w_{SM} t_{SM}} + R_{LM} + \rho_c \frac{1}{S_c} \quad (2.1)$$

$$R = R_{SM} + R_{LM} + R_c = \alpha_{SM} l_{SM} + R_{LM} + \rho_c \frac{1}{S_c} \quad (2.2)$$

where  $R_{SM}$  and  $R_{LM}$  denote the volume resistivity [ $\Omega$ ] of the solid and LMs, respectively, and  $R_c$  represents the interface resistivity [ $\Omega$ ].  $\rho_{SM}$ ,  $l_{SM}$ ,  $w_{SM}$ , and  $t_{SM}$  denote the volume resistivity [ $\Omega\text{m}$ ], (total) length, width, and thickness of the SM, respectively.  $\rho_{LM}$ ,  $l_{LM}$ ,  $w_{LM}$ , and  $t_{LM}$  represent the volume resistivity, (total) length, width, and thickness of the LM, respectively. As illustrated in Figure 2.8(a),  $\alpha_{SM}$  [ $\Omega\text{m}^{-1}$ ] denotes the resistance of SM per unit length, which is presented as the slope of the approximate straight line obtained and extrapolated on the relationship between  $l_{SM}$  and  $R$ .  $\rho_c$  [ $\Omega\text{m}^2$ ] and  $S_c$  [ $\text{m}^2$ ] denote the  $\rho_c$  and total contact area ( $2 \times 22.3 \text{ mm}^2 = 44.6 \text{ mm}^2$ ) between the galinstan and Cu electrode, respectively. Because  $R_{SM}$  is more than 10 times larger than  $R_c$  and  $R_{LM}$ , the  $R$  was measured at different  $l_{SM}$  values as in previous studies to accurately determine  $R_{SM}$  (Figure 2.6). Accordingly,  $\alpha_{SM} = 0.1761 \pm 0.0075 \text{ }\Omega\text{m}^{-1}$ , or  $R_{SM} =$

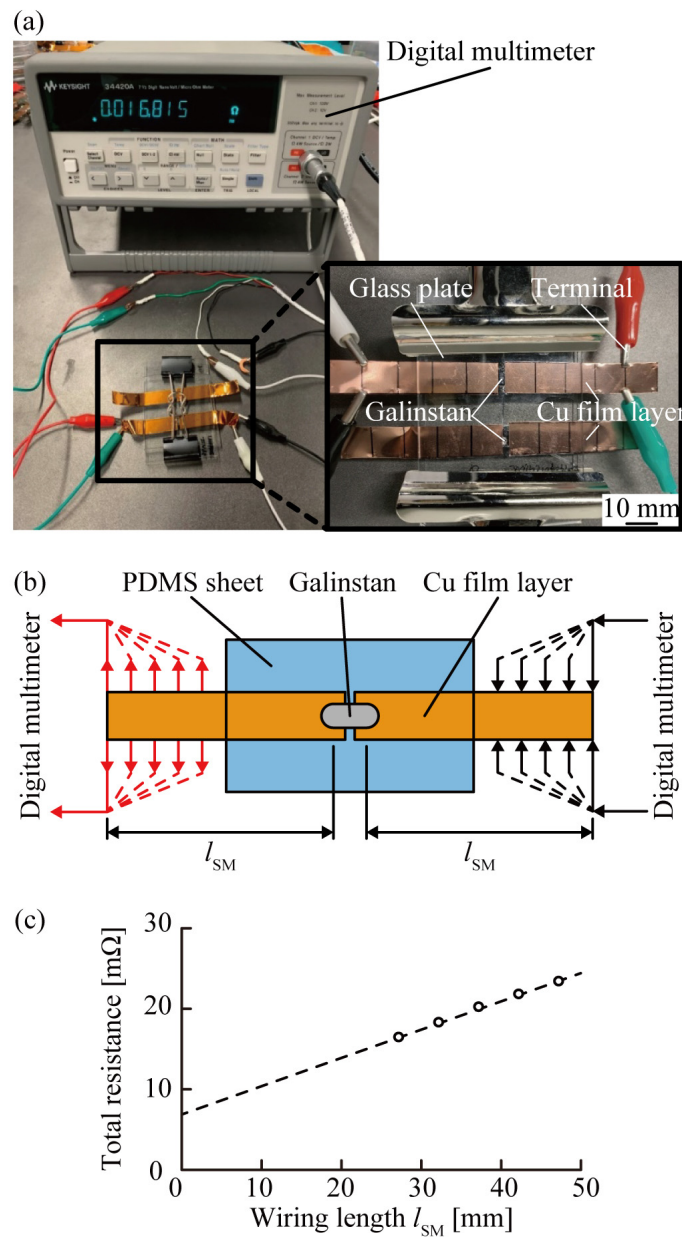


Figure 2.7 Measurement method for  $R_c$ . (a) Schematics of the change in position where the terminal contacted a Cu film layer and measurement of the total resistance of the sample. (b) Total resistance change for the length of a Cu film layer ( $l_{SM}$ ).

$16.73 \pm 1.01 \text{ m}\Omega$  was obtained for an  $l_{SM}$  of 95 mm. In contrast, because  $R_{LM}$  is more than 10 times lower than  $R_c$ ,  $R_{LM}$  was estimated from the literature value of the volume resistivity of galinstan and the



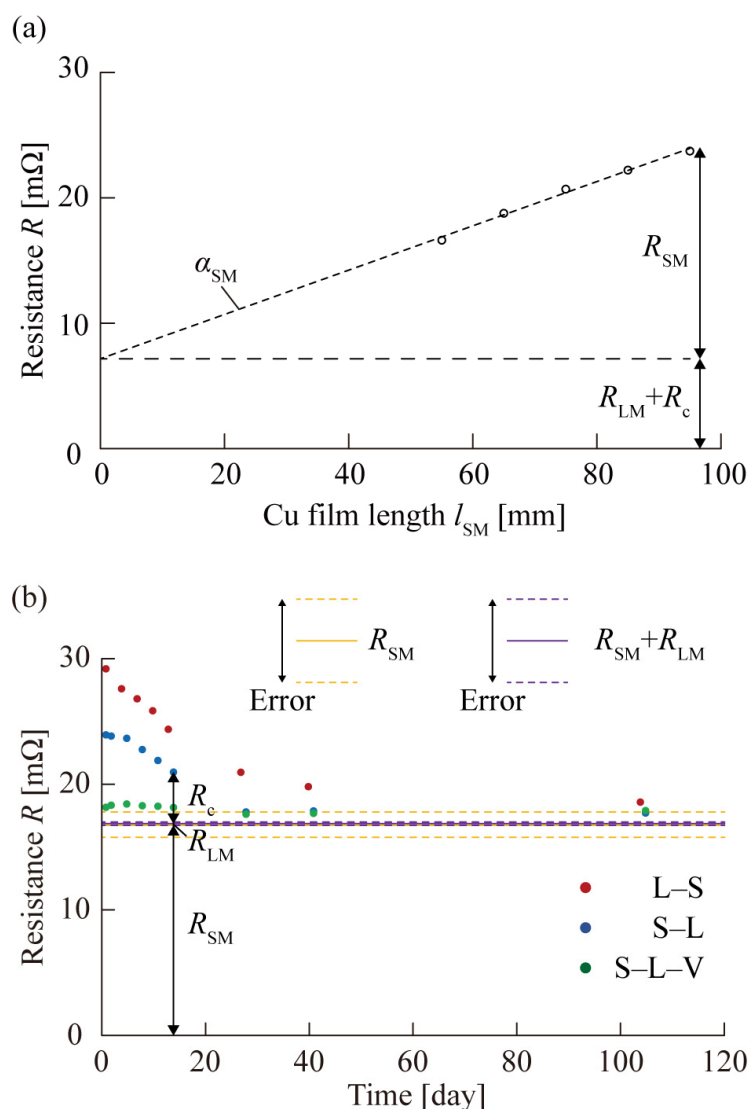


Figure 2.8 Breakingdown of the measured resistance  $R$  between an SM (galinstan) and LM (Cu electrode) achieved in the L-S, S-L, and S-L-V methods (Day 1) ( $N = 10$ ).

dimensions of the reservoir. The obtained result was  $R_{LM} = 0.17 \pm 0.13$  mΩ. Here, the values of  $R_c$  determined from  $R$  ranged from 0.75 to 12.31 mΩ, and the error between  $R_{SM}$  and  $R_{LM}$  was within 1.14 mΩ. Because  $R_{SM}$  and  $R_{LM}$  are identical across all experiments, their error difference is incorporated as an offset for all  $R_c$  values. Therefore, errors due to the  $R_{SM}$  and  $R_{LM}$  do not influence the time-dependent change in measurement of  $R_c$ . Figure 2.8(b) presents the actual measurement values of  $R$  and ratios of  $R_{SM}$ ,

$R_{LM}$ , and  $R_c$ . Finally,  $\rho_c$  was calculated by multiplying  $R_c$  with a  $S_c$  value of  $44.6 \text{ mm}^2$ .

#### 2.2.4 Measurement Results of Contact Resistance for Contact Procedures

Figure 2.9 presents the  $\rho_c$  for the L–S, S–L, and S–L–V methods on Day 1 from the contact between the galinstan and Cu electrode. The  $\rho_c$  in the S–L method was  $3.3 \times 10^{-7} \Omega\text{m}^2$ , which was lower by 42% than that achieved by the L–S method ( $5.7 \times 10^{-7} \Omega\text{m}^2$ ). In an unpaired  $t$ -tests for the L-S and S-L methods, a significant difference between them ( $t_{t\text{-test}}(10) = 2.27$ ,  $p_{t\text{-test}} = 0.04$ ). Here,  $t_{t\text{-test}}$  and  $p_{t\text{-test}}$  were  $t$ -value and  $p$ -value in the  $t$ -test, respectively. Moreover, the  $\rho_c$  in the S–L–V method was  $0.59 \times 10^{-7} \Omega\text{m}^2$ , which was further reduced by 82% relative to that in the S–L method. In an unpaired  $t$ -tests for the S-L and S-L-V methods, a significant difference between them ( $t_{t\text{-test}}(10) = 4.77$ ,  $p_{t\text{-test}} = 0.00$ ) Our mounting method that utilizes galinstan (S–L–V method) achieved low  $\rho_c$  ( $10^{-8} \Omega\text{m}^2$ ), which was one or two order of magnitude higher than that of a solder. Solders have one of the lowest  $\rho_c$  among conventional EIMs. The highest  $\rho_c$  of the L–S method among the three methods can be obtained by the contact between the Cu electrode and galinstan with a well-formed oxide layer on its surface. In contrast, the decrease in the  $\rho_c$  in the S–L method compared with that in the L–S method can be caused by the physical rupturing of the oxide layer on the galinstan surface by injection. In this case, the galinstan was brought into contact with the Cu electrode before reforming the oxide layer ruptured by injection. The further decrease in the  $\rho_c$  in the S–L–V methods compared with that in the S–L method can be caused by the physical rupture of the oxide layer on the galinstan surface by vacuuming. In this case, the galinstan was pressed against the Cu electrode surface, which exhibited microscopic roughness, by removing air between the galinstan and Cu electrode, resulting in the breakage of the oxide layer. This direct contact between the galinstan and Cu facilitated intimate atomic contact, leading to the formation of a stable Ga-Cu intermetallic compound ( $\text{GaCu}_2$ ) at the interface. The error bars representing standard deviations were  $2.8 \times 10^{-7} \Omega\text{m}^2$ ,  $2.8 \times 10^{-7} \Omega\text{m}^2$ , and  $2.8 \times 10^{-7} \Omega\text{m}^2$  for the L-S, S-L, S-L-V methods, respectively, The error bars were larger in the order of L-S, S-L, and S-L-V methods. Because the oxide layer is easily broken, its formation state of the oxide layer may vary depending on the shear stress and pressure at the time of contact. Hence, the L-S method, in which the oxide layer is well-formed, is considered to exhibit a large variation in  $R_c$ . Conversely, the reduced variation in the S-L and S-L-V methods suggests the rupture of the oxide layer. Overall, these results indicate that the contact procedures of the LM and SM aimed at physically disrupting the oxide layer on the LM surface result in a tenfold reduction in  $\rho_c$ . Therefore, this study verified that physically rupturing the oxide layer is potentially highly effective in reducing the  $R_c$  of the LM without damage.

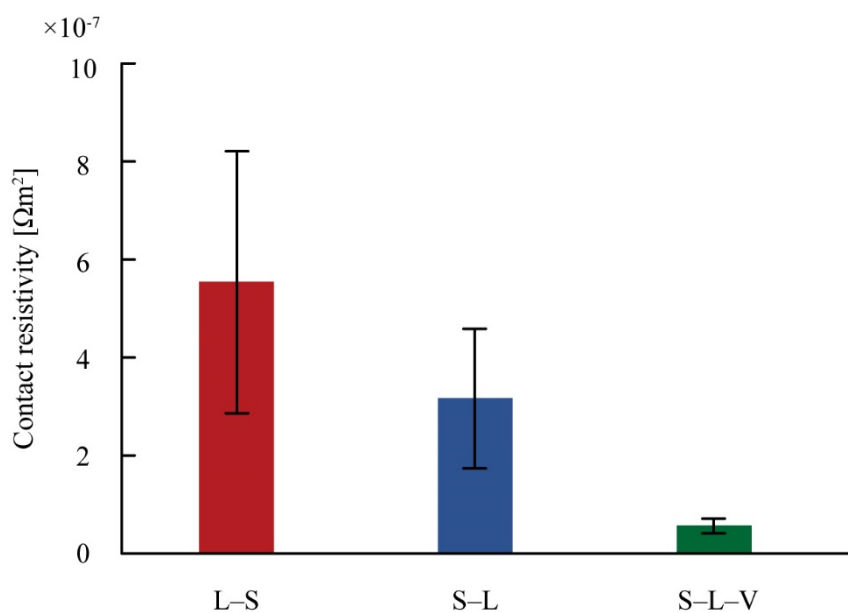


Figure 2.9 The  $\rho_c$  between an LM (galinstan) and SM (Cu electrode) achieved in the L-S, S-L, and S-L-V methods (Day 1) ( $N = 10$ ).

Figure 2.10(a) presents the measurement results of  $\rho_c$  for the solid-IPA-liquid, solid-liquid-heat, solid-IPA-liquid-heat, Plasma-solid-liquid, and liquid-solid-sonication methods. Figure 2.10(b) presents the enlarged graph on the vertical axis of the graph illustrated in Figure 2.10(a). The  $\rho_c$  for the solid-IPA-liquid method was  $2.1 \times 10^{-7} \Omega\text{m}^2$ , which was 36% lower than that achieved by the S-L method ( $3.3 \times 10^{-7} \Omega\text{m}^2$ ). This reduction in  $\rho_c$  can be caused by suppressing the formation of the oxide layer on the galinstan surface by covering the galinstan with IPA without espousing it to air. The  $\rho_c$  for the solid-liquid-heat method was  $0.094 \times 10^{-7} \Omega\text{m}^2$ , which was 97% lower than that achieved by the S-L method ( $3.3 \times 10^{-7} \Omega\text{m}^2$ ). This reduction in  $\rho_c$  can be triggered by the acceleration of the formation of the alloy between the Ga and Cu electrode by heating. The rapid formation of the alloy between the galinstan and Cu electrode can be observed in the morphology of the electrode surface. The surface of the Cu electrode was discolored to gray after 1 h heating from the contact of the galinstan and Cu electrode, while the surface of the Cu electrode was not discolored after 24 h for the S-L method. The  $\rho_c$  for the solid-IPA-liquid-heat method was  $0.12 \times 10^{-7} \Omega\text{m}^2$ , which was 96% lower than that achieved by the S-L method ( $3.3 \times 10^{-7} \Omega\text{m}^2$ ). The reduction in  $\rho_c$  can be caused by suppressing the formation of the oxide layer on the galinstan surface by covering the galinstan with IPA and accelerating the alloy formation by heating. In addition, the error bar,

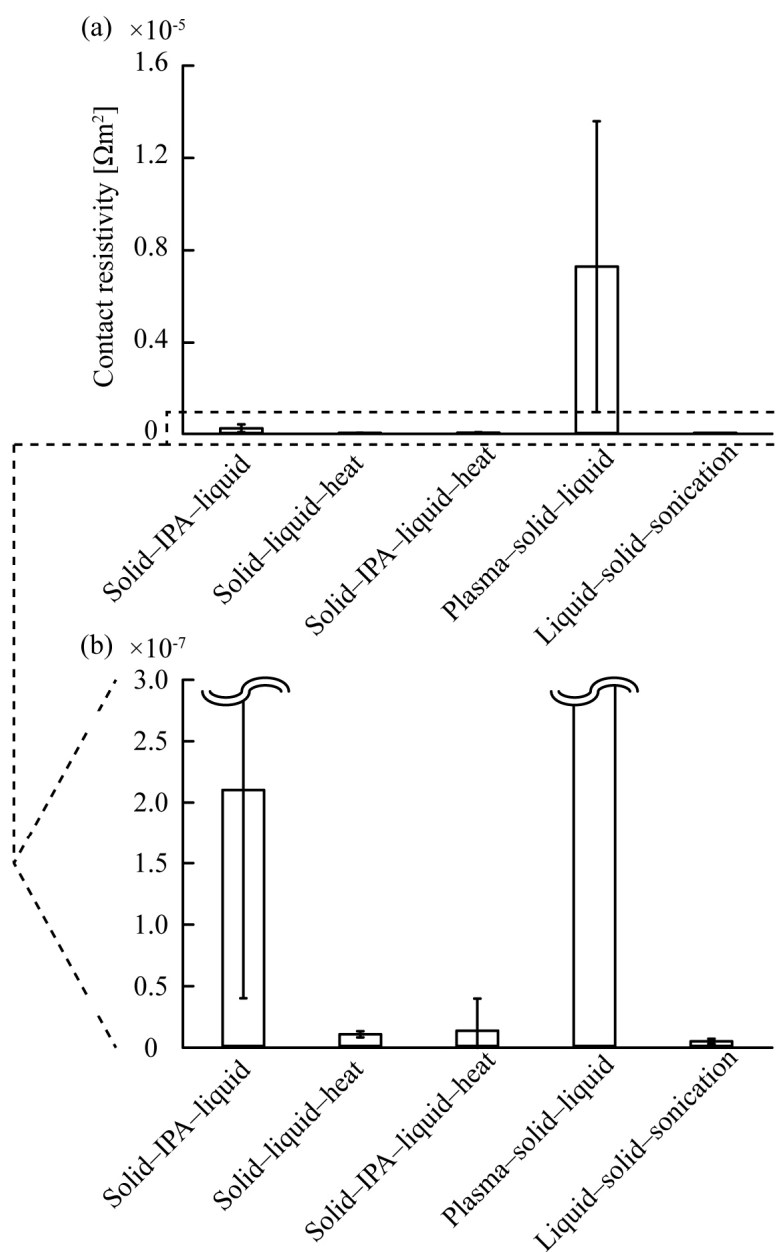


Figure 2.10 The  $\rho_c$  between galinstan and Cu electrode achieved in the Solid-IPA-liquid, Solid-liquid-heat, Solid-IPA-liquid-heat, Plasma-solid-liquid, and Liquid-solid-sonication methods (Day 1) ( $N = 4$ ).

standard deviation, of the  $\rho_c$  for the solid-IPA-liquid-heat method overlapped that for the solid-liquid-heat method. This result indicates that the acceleration of the alloying by heating reduces the  $\rho_c$  more than the

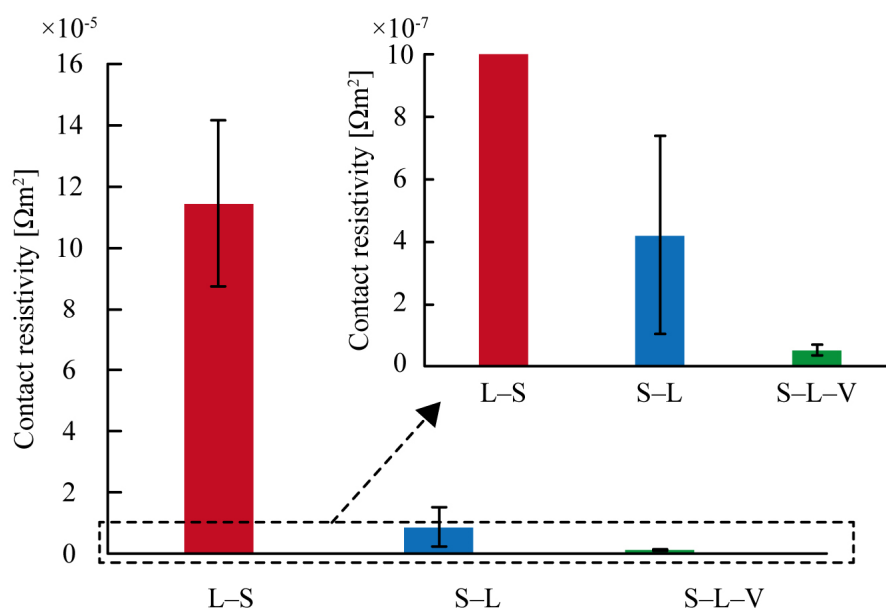


Figure 2.11 The  $\rho_c$  between an LM (galinstan) and SM (Sn electrode) achieved in the L-S, S-L, and S-L-V methods (Day 1) ( $N=6$ ).

covering galinstan with liquid. The  $\rho_c$  for the plasma-solid-liquid method was  $73 \times 10^{-7} \Omega\text{m}^2$ , which was 2112% higher than that achieved by the S-L method ( $3.3 \times 10^{-7} \Omega\text{m}^2$ ). The increase in  $\rho_c$  can be triggered by the formation of the oxide layer on the galinstan surface by plasma treatment. The electrode surface was discolored after the plasma treatment, which exhibit the formation of the oxide layer on the electrode surface. In the liquid-solid-sonication method, the oxide layer on the galinstan surface was deformed by the ultrasonic vibration of the device, and the galinstan penetrated into the microscopic irregularities on the copper foil surface, increasing the true contact area and minimizing the  $R_c$ . This is hypothesized to have decreased the  $R_c$ . The fact that the  $R_c$  remains low even after the ultrasonic vibration was terminated suggests that once the galinstan penetrates into the irregularities on the copper foil surface, the alloying of the copper foil surface progresses and wettability improves, thereby resulting in a decrease in  $R_c$ .

Furthermore, the applicability of the proposed method of reducing  $R_c$  by physically rupturing the oxide layer to metals other than Cu was studied, as shown in Figure 2.11. galinstan was contacted with a Sn electrode by the L-S, S-L, and S-L-V methods.  $\rho_c$  in the L-S, S-L, and S-L-V methods was  $1.14 \times 10^{-5} \Omega\text{m}^2$ ,  $8.40 \times 10^{-7} \Omega\text{m}^2$ , and  $1.01 \times 10^{-7} \Omega\text{m}^2$ , respectively. These results demonstrate that the reduction of  $R_c$  by physically rupturing the oxide layer is effective for metals other than Cu.

Finally, as illustrated in Figure 2.12, the L-S, S-L, and S-L-V methods were utilized to fabricate a chip

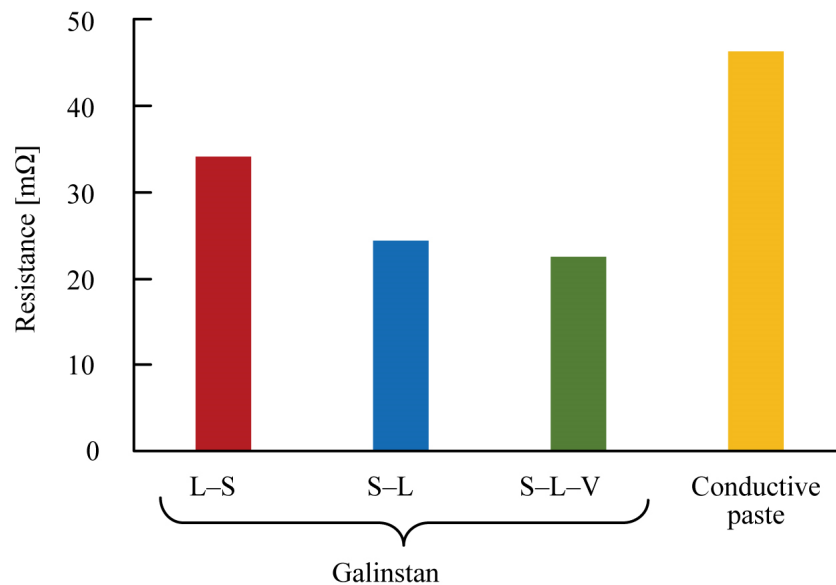


Figure 2.12 Resistance of the sample (via the L-S, S-L, and S-L-V methods) and conductive paste (Day 1) ( $N = 2$ ).

resistor. In addition, 12 h after fabrication, the resistance values of the entire device with chip resistors mounted by the L-S, S-L, and S-L-V methods were 34.3, 24.5, and 22.7 mΩ, respectively. The resistance of the device with chip resistors mounted using conductive paste was 46.5 mΩ. These results indicate that the same  $\rho_c$  trend changes for the three connection methods can be obtained when electronic components are mounted using galinstan as when galinstan and Cu film are connected. The LM mounting method (S-L-V method) succeeded in obtaining a  $\rho_c$  51.2% lower than that of the conductive paste. This result indicates that the LM mounting method (S-L-V method) can achieve low  $R_c$  between electrodes and LM, and also between electronic components and the LM.

### 2.3 Time-Dependent Change in Contact Resistance

The  $R_c$  between the galinstan and copper film under different contact procedures was compared, and the change in  $R_c$  over time was measured. In this section, the L-S, S-L, and S-L-V methods were focused on because of their simple mounting procedures and mounting temperature without heating. To investigate the effect of the oxide layer on the  $R_c$  after a long time, the morphological observation and elemental analysis of the copper film surface in contact with the LM were utilized to evaluate the alloy formation

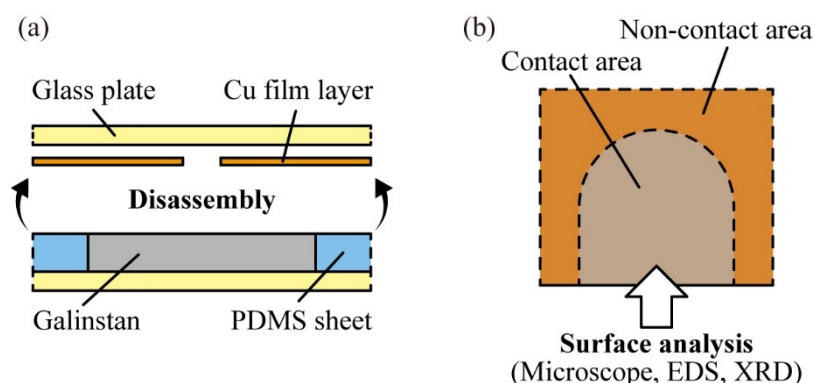


Figure 2.13 Surface analysis of the Cu film layer in contact with galinstan.

over time. It was determined that the effect of the oxide layer on the  $R_c$  disappeared after a long time, and the  $\rho_c$  decreased to the same order of  $10^{-8} \Omega\text{m}^2$  regardless of the contact procedure. The compositional analysis of the copper film surface demonstrated that after 133 days, the copper film surface turned gray and contained 11.1 at% Ga, indicating alloy formation on the copper film surface, which improved wettability and minimized  $\rho_c$ .

### 2.3.1 Evaluation Method of Time-Dependent Change in Contact Resistance

This study determined the change in  $R_c$  over time to investigate the effect of oxide layers on  $R_c$  after a long time. This study also observed the morphology of the SM surface in contact with the LM and verified the alloy formation on the SM surface via elemental analysis. To observe the morphology and measure the composition of the copper foil surface, the device for  $R_c$  measurement was disassembled after measuring the  $R_c$ , and the copper film was eliminated from the galinstan and wiped with a Kimwipe moistened with IPA (Figure 2.10(a)). The surface morphology of the copper film was then observed using a microscope (VW-9000, Keyence, Osaka, Japan), and the composition of the copper film surface was determined via energy dispersive spectrometry (EDS; JED-2300F, JEOL, Tokyo, Japan) and X-ray diffraction (XRD; SmartLab, Rigaku, Tokyo, Japan) (Figure 2.13(b)).

### 2.3.2 Time-Dependent Change in Contact Resistance

Figure 2.14 illustrates the time-dependent change in the  $\rho_c$  for the L-S, S-L, and S-L-V methods. In the L-S method, the  $\rho_c$  decreased by 86.1%, from  $5.7 \times 10^{-7} \Omega\text{m}^2$  (Day 1) to  $0.79 \times 10^{-7} \Omega\text{m}^2$  (Day 103).

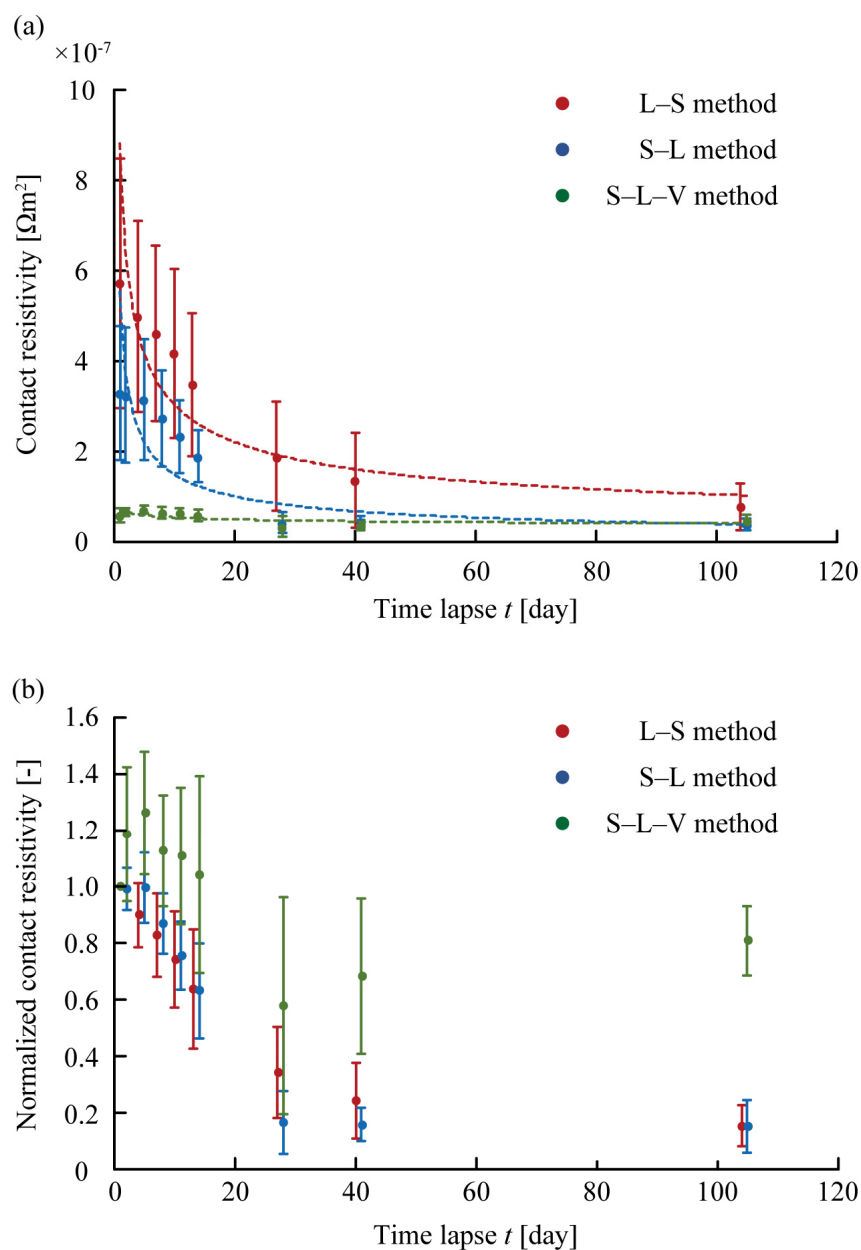


Figure 2.14 Time-dependent change in  $R_c$ . (a) Time-dependent change in the  $\rho_c$  for the L-S, S-L, and S-L-V methods ( $N=10$ ). (b) Time-dependent change in the normalized  $\rho_c$  for the L-S, S-L, and S-L-V methods ( $N=10$ )

In the S-L method, the  $\rho_c$  decreased by 88.2%, from  $3.3 \times 10^{-7} \Omega\text{m}^2$  (Day 1) to  $0.39 \times 10^{-7} \Omega\text{m}^2$  (Day 103). In the S-L-V method, the  $\rho_c$  decreased by 18.6%, from  $0.59 \times 10^{-7} \Omega\text{m}^2$  (Day 1) to  $0.48 \times 10^{-7} \Omega\text{m}^2$



(Day 103). In all three contact methods, the  $\rho_c$  decreased over time. This result indicates that low and stable  $\rho_c$  could be achieved via the mounting method using LMs (S–L–V method). The change in the  $\rho_c$  was negligible in the order of the S–L–V, S–L, and L–S methods. Furthermore, this study determined that the effect of the oxide layer reduced over time, and the  $\rho_c$  in all three methods reached the same order ( $10^{-8} \Omega\text{m}^2$ ) after a long period. Furthermore, the  $\rho_c$  barely decreased from Days 40 and 41 to Days 103 and 104, and the error bars completely overlapped. Hence, it was determined that the change in the  $\rho_c$  gradually decreased over time, and after Days 103 and 104, the  $\rho_c$  saturated. In addition, the change over time in  $R_c$  is considered to be triggered by chemical reactions such as the alloying of Cu and Ga to form  $\text{CuGa}_2$ . The formation of intermetallic phases usually follows a power law [142], [183]. Hence, this study extrapolated the change in  $\rho_c$  over time by plotted a power-law approximation curve for the L-S, S-L, and S-L-V methods,  $\rho_c = 9 \times 10^{-7}t - 0.460 [\Omega\text{m}^2]$ ,  $\rho_c = 6 \times 10^{-7}t - 0.567 [\Omega\text{m}^2]$ , and  $y = 7 \times 10^{-8}t - 0.121 [\Omega\text{m}^2]$ , respectively.  $t$  denoted the lapsed time [day]. These approximate curves are reliable because they cover the error bars of the measured values. This enabled the estimation of the  $\rho_c$  after a long time.

The normalized  $\rho_c$  of the L-S and S-L methods decreased from 1 to 0.2 from 24 h to Days 103 and 104 after fabrication. The normalized  $\rho_c$  of the L-S and S-L methods exhibited overlapping error bars indicating the standard deviation over the entire measurement range, indicating that the normalized contact resistivities of the two methods were almost identical. The normalized  $\rho_c$  of the S-L-V method decreased from 1 to 0.8 from 24 h to Day 104 after fabrication. This is because the ratio of the measurement error to the  $\rho_c$  in the S-L-V method is larger than those in the L-S and S-L methods owing to the lower  $\rho_c$  in the S-L-V method. This is attributed to the ratio of the measurement error to  $\rho_c$  being larger than that of the L-S and S-L methods owing to the lower  $\rho_c$  in the S-L-V method. It is considered that the  $\rho_c$  in the S-L-V method will decrease from 1 to 0.2 over time, similar to the L-S and S-L methods, by more accurate  $\rho_c$  measurement. The change in  $\rho_c$  with time is considered a significant factor in the change in  $\rho_c$ . Therefore, it is hypothesized that a common chemical reaction, such as the alloying of Cu and Ga to form  $\text{CuGa}_2$ , is behind the change in  $\rho_c$  over time, and that the chemical reaction alters the wettability of the copper film surface, causing the  $\rho_c$  to decrease. In addition, the slope of the change in  $\rho_c$  over time may differ depending on the difference in the initial value of the  $\rho_c$ , which is basically the difference in the initial true contact area.

### 2.3.3 Measurement Results of Alloy Formation on Solid Metal Surface

Figure 2.15 (a) and (b) present the optical images of the Cu film surfaces in the L–S, S–L and S–L–V

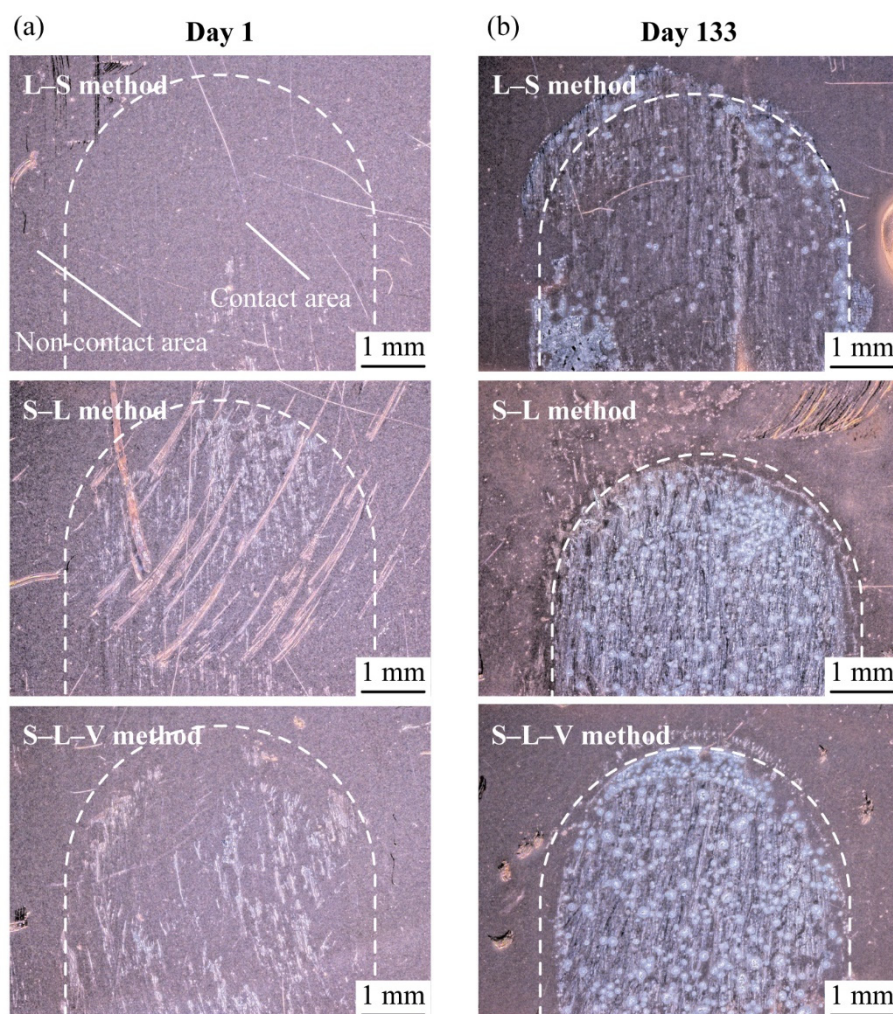


Figure 2.15 Optical images of the surface of Cu films in contact with galinstan in the L–S, S–L, and S–L–V methods (a) (Day 1) and (b) (Day 133).

methods (Days 1 and 133). The morphology of the contact area with galinstan did not change in the L–S method, and the contact area was partly discolored to light gray in the S–L and S–L–V methods (day 1) (Figure 2.15(a)). In contrast, the contact area was entirely discolored to light gray and partly discolored to dark gray for all three methods (day 133) (Figure 2.15(b)). This result suggested that the surface of the Cu film was discolored to gray over time, regardless of the contact methods used to apply the galinstan.

Figure 2.16(a) and (b) present the XRD patterns of the Cu film surface in contact with the galinstan in the L–S, S–L and S–L–V methods (Days 1 and 133). Figure 2.16(c) presents the XRD patterns of Cu ( $K_{\alpha}$ ,

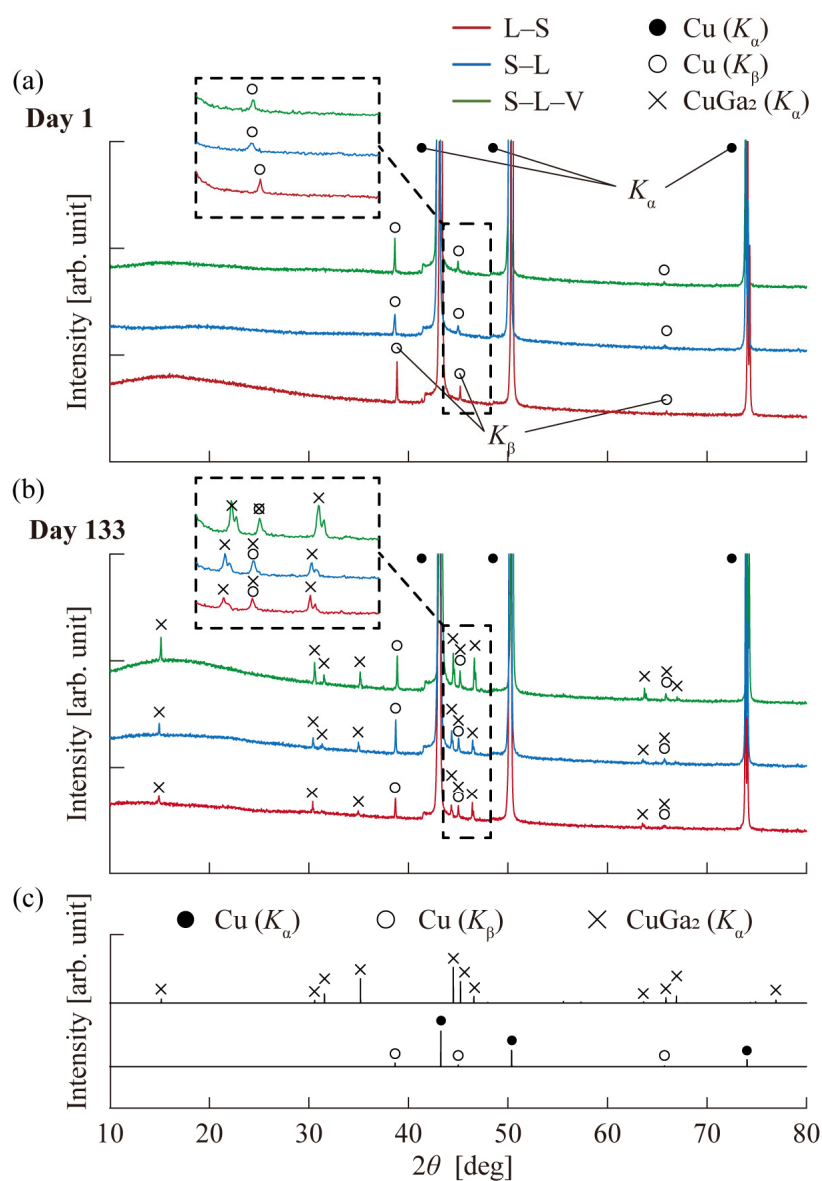


Figure 2.16 XRD patterns of the surface of a Cu film in the L-S, S-L, and S-L-V methods after (a) Day 1 and (b) Day 133. (c) XRD patterns of Cu ( $K_\alpha$ ,  $K_\beta$ ) and CuGa<sub>2</sub> ( $K_\alpha$ ).

$K_\beta$ ) and CuGa<sub>2</sub> ( $K_\alpha$ ), an alloy of Ga-based LM and Cu. Here,  $K_\alpha$  and  $K_\beta$  were K-alpha and K-beta emission lines, and  $\theta$  was the diffraction angle. On Day 1, Cu was primarily present on the Cu film surface, while CuGa<sub>2</sub> was not present in all three contact methods. However, on Day 133, CuGa<sub>2</sub> was present on the Cu film surface in addition to Cu in all three contact methods. Table 2.6 presents the composition of the contact

Table 2.6 Composition of surface of Cu film layer in contact with galinstan after 24 h and 133 days from fabrication.

Day	Contact procedures	Composition [at%]			
		Cu	Ga	In	Sn
1	L–S	BAL	0.0	0.0	0.0
	S–L	BAL	0.0	0.0	0.0
	S–L–V	BAL	0.0	0.0	0.0
133	L–S	BAL	0.9	0.0	0.0
	S–L	BAL	11.0	0.4	0.1
	S–L–V	BAL	14.4	0.7	0.4

area in the Cu film surfaces on Days 1 and 133. Only four elements, Cu, Ga, In, and Sn, which are the major elements in the contact between the Cu electrode and galinstan, were analyzed. Even if other elements were present, their effect would be negligible as they are considered to be lower than the minimum detectable amount of Sn. galinstan was detected in the contact area in any of the three methods on Day 1. However, galinstan was present in the contact area at 0.9 atom% in the L–S method, 11.0 atom% in the S–L method, and 14.4 atom% in the S–L–V method on Day 133. These XRD and EDS results suggested the formation of  $\text{CuGa}_2$  between galinstan and the Cu film over time. This study also confirmed via XRD and EDS analyses that the light gray discoloration of the Cu film surface in the S–L and S–L–V methods in Figure 2.15(a) was not an alloy but Cu. The lower  $\rho_c$  in the S–L and S–L–V methods than that in the L–S method may be related to the difference in the progression of alloying. Overall, this study determined that the  $\rho_c$  decreased as the alloying between galinstan and the Cu film progressed and the wettability between galinstan and the Cu film increased, which presumably contributed to the decrease in  $\rho_c$ . In addition, as other Ga-based LMs, such as pure Ga and E-GaIn, are also known to form  $\text{CuGa}_2$  with Cu, their  $R_c$  may decrease over time. In addition, the time required to reduce the  $\rho_c$  can be possibly decreased by increasing the temperature. In our preliminary experiment, a sample fabricated via the S–L method was heated at 200°C for 60 min, the  $\rho_c$  decreased to the order of  $10^{-8} \Omega\text{m}^2$ , and the Cu film surface was discolored to dark gray after 60 min. In the case of Cu electrodes with thicknesses of several

micrometers to several tens of micrometers, which are mainly used in conventional electronic devices, CuGa<sub>2</sub> is formed on the surface of the Cu electrode. Thus, the destruction of the electrode owing to alloying is not expected to be a problem after several months of use. In addition, because the Young's modulus of CuGa<sub>2</sub> is lower than that of the Cu electrode, the alloy on the Cu electrode surface is unlikely to delaminate during deformation of the stretchable electronic device.

Figure 2.17(a)–(c) present SEM images of the Cu electrode surface of the device employed in Figure 2.14 after 24 h of contact with Ga. No discoloration was observed on the Cu electrode surface 24 h after contact with galinstan in the SEM image using the L-S method. In contrast, the SEM images of the Cu electrode surfaces obtained via the S-L and S-L-V methods exhibited areas of discoloration and no discoloration. In the S-L method, there was a gray raised area within the discolored area. To determine the composition of the non-tarnish, tarnish, and gray-raised areas in the SEM image of the Cu electrode surface, the composition of the area after 24 h of SEM observation was measured by EDS, and the obtained results are presented in Figure 2.17(d). The surface compositions of the L-S, S-L, and S-L-V methods were very similar. The composition of the Cu electrode surface indicates that no CuGa<sub>2</sub> exists in the non-tarnish area, and that the gray-raised areas are galinstan because their composition is close to the mixing ratio of Ga. The discoloration region is considered to be CuGa<sub>2</sub>, because its composition differs from that of the gray-raised area. However, CuGa<sub>2</sub> and galinstan were not detected via the EDS and XRD analysis of the entire Cu electrode owing to their negligible amount. Figure 2.17(f)–(h) present the SEM images of the Cu electrode surface after 133 days in the device utilized in Figure 2.17 for measuring  $R_c$ . In the L-S, S-L, and S-L-V methods, there were gray-raised areas within the dark gray discoloration area on the Cu electrode surface. To examine the composition of the Cu electrode surface, the compositions of the dark-gray and light-gray discoloration areas and the gray-raised areas are presented in Figure 2.17(e). These compositions are nearly identical for the three contact procedures. The compositions of the dark-gray, light-gray, and gray-raised areas are considered to be CuGa<sub>2</sub>, trace amounts of CuGa<sub>2</sub>, and Ga, respectively. The composition of the dark gray region is close to that of CuGa<sub>2</sub> (Cu: 33.3 at%, Ga: 66.7 at%), thereby suggesting that the dark gray discoloration is CuGa<sub>2</sub> and the light gray discoloration is CuGa<sub>2</sub> in the early formation stage owing to the small proportion of Ga. Therefore, CuGa<sub>2</sub> is considered to have increased with the expansion of the dark-gray discoloration area.

In contrast, this result differs from the  $\rho_c$  of  $3.3 \times 10^{-7} \Omega\text{m}^2$  in the S-L method presented in Figure 2.17, which is 42% lower than the  $\rho_c$  of  $5.7 \times 10^{-7} \Omega\text{m}^2$  in the L-S method. This may be because the flow path of the acrylic sheet is not deformed in the device for high-precision measurement; hence, the liquid

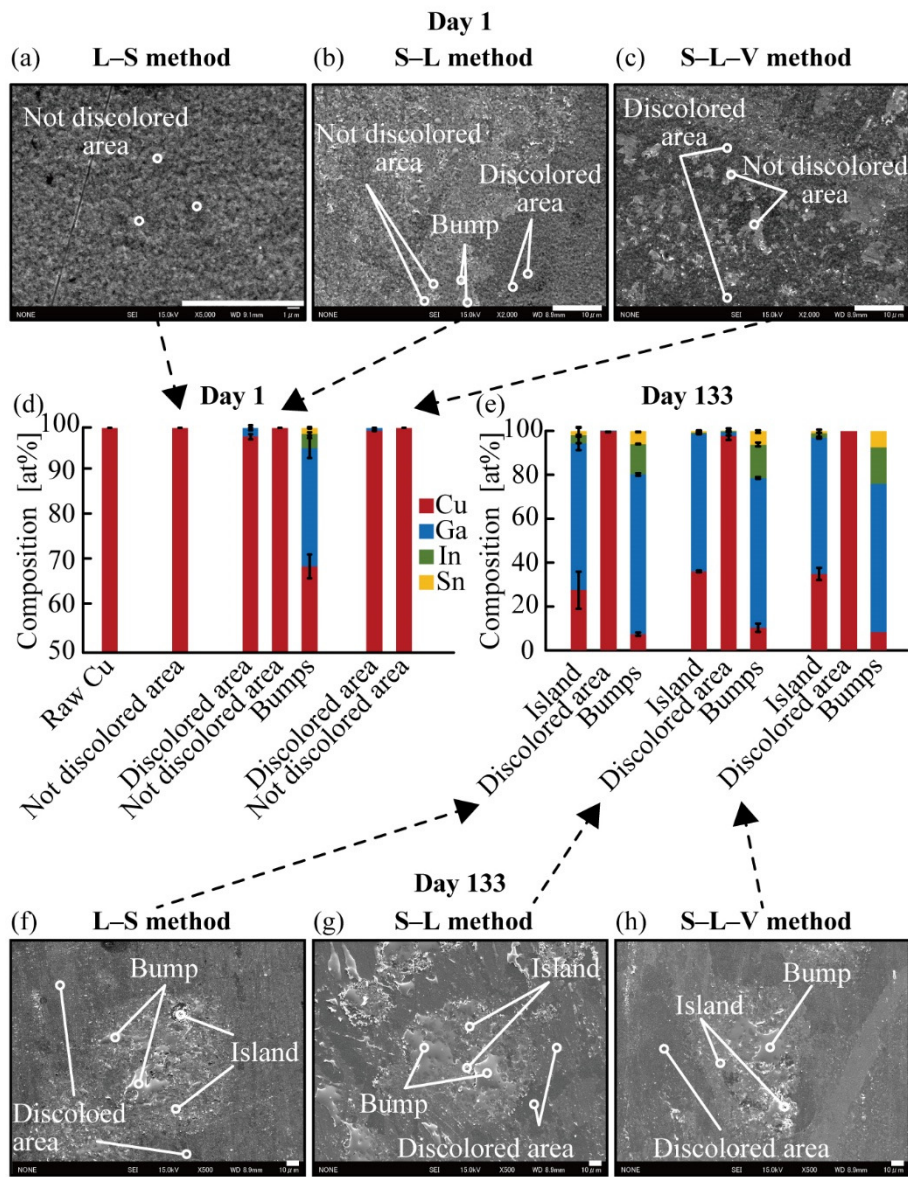


Figure 2.17 SEM images of the Cu films that were connected to galinstan in the (a) L-S; (b) S-L; and (c) S-L-V methods after 24 h and those in the (f) L-S, (g) S-L, and (h) S-L-V methods after 133 days. The scale bar intervals are 10  $\mu\text{m}$ . (d) Compositions of the discolored area, not-discolored area, and bumps in the three methods after 24 h. (e) Compositions of the islands, discolored area, and bumps in the three methods after five months.

reservoir is not deformed like the liquid reservoir of the PDMS sheet, and the effect of adhesion between

the galinstan and Cu electrode is not achieved, thereby resulting in the generation of minute gaps between the galinstan and Cu electrode, which may have minimized contact reproducibility. Therefore, it is considered that the  $R_c$  measurement with higher accuracy will be possible by studying the materials, shape, and fabrication method of the channel from the perspective of improving the reproducibility of contact between the LM and SM.

## 2.4 Conclusions

---

This study presents a method for mounting electronic components using Ga-based LMs with reduced  $\rho_c$  between the LM and a Cu electrode. Ga-based LMs exhibit low volume resistivity and low melting points, and they are utilized as electronic components such as interconnects and sensors in stretchable electronic devices. However, the high  $\rho_c$  of the oxide layer on the surface of Ga-based LMs constitutes a problem when the Ga-based LMs are employed in contact with rigid electronic components. To address this problem, this study investigated the effect of the oxide layer on  $\rho_c$  via the contact methods of the Ga-based LM (galinstan) and Cu film.

On Day 1, the contact resistivities were  $5.7 \times 10^{-7}$ ,  $3.3 \times 10^{-7}$ , and  $0.59 \times 10^{-7} \Omega\text{m}^2$  in the L-S, S-L, and S-L-V methods, respectively. It was determined that the  $\rho_c$  differs by approximately 10 times depending on the contact method. Furthermore, on Day 103, the  $\rho_c$  decreased to the same orders of  $10^{-8} \Omega\text{m}^2$ :  $0.79 \times 10^{-7}$ ,  $0.39 \times 10^{-7}$ , and  $0.48 \times 10^{-7} \Omega\text{m}^2$  in the L-S, S-L, and S-L-V methods, respectively. In addition,  $\text{CuGa}_2$  formed on the Cu film surface in contact with galinstan in all three contact methods (Day 133). To obtain low  $R_c$  immediately after contact, the S-L-V method had an advantage because of its low initial  $R_c$  and stable time variation of  $R_c$ . Whereas, the S-L-V method had a low yield rate due to leakage of LM during vacuuming. Thus, from the viewpoint of simplicity and applicability, the L-S and S-L methods can also be used. Overall, the proposed mounting method using galinstan allows us to achieve low  $R_c$  by a simple mounting method without chemicals or heating, whereby the range of materials utilized as substrates can be expanded and the stretchability of the device can be improved. Hence, new opportunities can be provided for the development of stretchable electronics.

# Chapter 3 High-Accuracy Measurement Method for Contact Resistance

## 3.1 Introduction

---

In stretchable electronic devices using Ga-based LMs, the  $R_c$  between the LM and metal electrodes, such as electronic components or wiring, is critical for achieving a low energy-consumption rate and high signal-to-noise ratio. The  $R_c$  measurement of LMs is typically employed to compare the  $R_c$  values of LMs for different contact conditions, e.g., materials and contact procedures, with those of conventional EIMs between electronic components and wiring, such as solders and conductive adhesives. Although the  $R_c$  values of LMs have been measured[18], [163]–[167], accurate measurement remains difficult, and accurate methods for measuring the  $R_c$  of LMs are yet to be developed. The TLM[168]–[172] and CBKR[173] methods are well-established methods for measuring  $R_c$ . To measure the  $R_c$  of LMs, the current-density distribution must be considered because LMs have the same  $R_{she}$  as metal electrodes. TLM is suitable for considering the current-density distribution because the distribution is two-dimensional.



Hence, this study studied the current distribution in the TLM to achieve high accuracy. There are two types of TLM measurements: point and surface contacts. Surface contact was utilized to measure  $R_c$ . The contact area between the object and electrode has a finite value required to include  $R_c$  in the measured  $R$ . Surface contact requires the fabrication of electrodes on the object before measurement. The measured  $R$  includes object sheet resistance ( $R_{\text{sho}}$ ) and  $R_c$ ; accordingly,  $R_{\text{sho}}$  and  $R_c$  can be obtained. In contrast, point contact is employed to measure the sheet resistance of the object  $R_{\text{sho}}$ . The contact area is sufficiently small to ignore  $R_c$ . The measured  $R$  includes only  $R_{\text{sho}}$ ; hence, although  $R_{\text{sho}}$  can be obtained,  $R_c$  cannot. Although only  $R_{\text{sho}}$  can be measured, point contact is beneficial for simplicity because it does not require electrode fabrication. Here, surface contacts were utilized to obtain  $R_c$ .

In the TLM, metal electrodes are brought into contact with an object, a current ( $I$ ) is applied to the outer electrodes, and the voltage ( $V$ ) between adjacent electrodes is determined. The measured resistance between adjacent electrodes  $R (=V/I)$  is the sum of  $R_o$  and  $R_c^{\text{Total}}$ . Generally,  $R_c^{\text{Total}}$  is considered as  $R_c$ .  $R$  is measured for different object lengths ( $L_o$ ), and the relationship between  $L_o$  and  $R$  is approximated linearly. The resistance in the contact area ( $R_c^{\text{Total}}$ ) is obtained as the Y-intercept of the linear approximation without knowing  $R_{\text{sho}}$ . Current should be applied to each measuring electrode to achieve high accuracy regardless of the sheet and  $R_c$ . In the TLM measurement in the ISO standard (ISO 16525-2:2014), current is applied to the outer electrodes for simplicity within a limited range of sheet and  $R_c$ . However, the conventional TLM may not be applicable because LMs exhibit low sheet resistance. Furthermore, the conventional TLM ignores the object and electrode resistances included in  $R_c^{\text{Total}}$ . However, the  $R_c$  between LMs and metal electrodes may be low; in this case, the electrode and object resistances cannot be ignored.

Specifically, when current is applied to the outer electrodes, the  $R_c$  component included in the measured  $R_c^{\text{Total}}$  is  $R_c \times I_i/I$ . Here,  $I_i$  represents the current passing through the interface between the electrode and object. For accuracy, all applied currents  $I$  must pass through the interface ( $I_i = I$ ), and all  $R_c$  components must be included in the measured  $R_c^{\text{Total}}$ . The current should be applied to each measuring electrode to achieve  $I_i = I$  regardless of the sheet-resistance ratio ( $R_{\text{sho}}/R_{\text{she}}$ ) and contact resistivity ratio ( $\rho_c/R_{\text{she}}$ ); however, this doubles the number of connections. Here, the  $\rho_c$  is the  $R_c$  per unit contact area. Conventional  $R_c$  measurements are typically utilized used for semiconductors and conductive pastes. Hence, the conventional TLM assumes that  $R_{\text{she}}$  (Cu:  $10^{-3} \Omega\Box$ ) is more negligible than  $R_{\text{sho}}$  (Si, graphene, conductive adhesive:  $>10^2 \Omega\Box$ ). In this case, current can be applied to the outer electrodes for simplicity because all the applied currents pass through the interface ( $I_i = I$ ) for both current application methods. In previous studies,  $R_c$  was obtained via FEM simulation alone when the real contact area between the object and

electrode and the formation of a surface layer on the object and electrode were known<sup>42</sup>. However, the  $R_c$  values of LMs are difficult to obtain via FEM simulations alone because the formation of an oxide layer on the LMs and actual contact area are unknown. Furthermore, the  $R_e$  and  $R_o$  included in  $R_c^{\text{Total}}$  cannot be ignored when  $R_c$  is lower than  $R_e$  or  $R_o$ . The measurement and simulation results should be compared to obtain  $R_c$ , ignoring  $R_e$  and  $R_o$ . However, the simulation of each measurement is computationally demanding. Hence, the conventional TLM assumes that  $R_c^{\text{Total}} \doteq R_c$  for semiconductors and conductive pastes. Under this assumption, current is applied to the outer electrodes, and  $R_c$  is solely obtained via measurements, based on the ISO standards (ISO 16525-2:2014) and a book cited by several papers on conventional TLMs. In contrast, because the  $R_{\text{sho}}$  of the LMs ( $10^{-2}$ – $10^{-4}$   $\Omega\Box$ ) is significantly the same as the  $R_{\text{she}}$ , only a part of the applied current may pass through the interface ( $I_i \ll I$ ) when current is applied to the outer electrodes. In this case, the  $R_c$  component included in  $R_c^{\text{Total}}$  is  $R_c \times I_i/I$ , which is undesirable for accuracy. Furthermore, the  $R_c$  between the LM and metal electrode may be lower than  $R_e$  and  $R_o$ , in which case the  $R_o$  and  $R_e$  included in  $R_c^{\text{Total}}$  cannot be ignored. Hence, for accuracy, the measured  $R_c^{\text{Total}}$  must not be regarded as  $R_c$ .

This study examined the current application methods for highly accurate TLM measurement of LMs (galinstan) and metal (Cu) electrodes. The current-density distribution was analyzed using FEM simulations for different current application methods. Furthermore, the  $R_c^{\text{Total}}$  between galinstan and Cu electrodes was measured for the current application methods. According to the simulation results,  $I_i/I$  was  $<10^{-1}$  for galinstan when current was applied to the outer electrodes. In contrast,  $I_i$  was equal to  $I$ , regardless of the sheet resistance and  $R_c$ , when current was applied to each electrode. Furthermore,  $\rho_c$  was obtained by comparing the measured  $R_c^{\text{Total}}$  and simulated  $R_c^{\text{Total}}$  for  $\rho_c$ . When current was applied to the outer electrodes, the measured  $R_c^{\text{Total}}$  of  $0.125 \pm 0.056$  m $\Omega$  and the simulated  $R_c^{\text{Total}}$  of 0.111 to 0.122 m $\Omega$  did not intersect, and  $\rho_c$  could not be obtained. In contrast, when the current was applied to each electrode, the measured  $R_c^{\text{Total}}$  of  $0.120 \pm 0.043$  m $\Omega$  and the simulated  $R_c^{\text{Total}}$  of 0.063 to 9.823 m $\Omega$  had an intersection. The obtained  $\rho_c$  was 0.115 m $\Omega\text{mm}^2$  (max: 0.185 m $\Omega\text{mm}^2$ , min: 0.030 m $\Omega\text{mm}^2$ ). The accuracy when current was applied to each electrode was better for practical use than the  $\rho_c$  of the solders ( $10^{-1}$  m $\Omega\text{mm}^2$ ).

### 3.2 Measurement Accuracy for Voltage Detection Location

---

In Section 2.2, this study investigated the voltage detection location in TLMs to measure the  $R_c$  of the LMs with high accuracy. Conventionally, TLM is typically utilized to measure the  $R_c$  of materials with

high sheet resistance, such as semiconductors and conductive pastes. Hence, it is assumed that the sheet resistance of the metal electrode is more negligible than that of the object. Specifically, the measured resistance is the combined value of the volume resistances of the object and metal electrodes and the  $R_c$  between the object and the electrode. However, the volume resistance of the metal electrodes is typically neglected. In this case, the electrodes can be regarded as equipotential; hence, the voltage can be measured anywhere on the electrodes. However, because the LM has the same sheet resistance as that of the metal electrode, the electrode resistance may not be negligible. In this case, it is necessary to consider where to measure the voltage, such that the electrode resistance is not included in the measured resistance. In addition, when measuring voltage across other electrodes, there is a concern that current may flow into unused electrodes between the measurement electrodes, resulting in measurement errors. Therefore, this section discusses the measurement accuracy of the TLM for different combinations of electrodes and voltage detection positions on the electrodes.

### 3.2.1 Device Fabrications

Figure 3.1 presents the schematic illustrations of a method for measuring the  $R_c$  between LMs and SMs via the TLM with high accuracy. As illustrated in Figure 3.1(a), the connection of measuring terminals was compared. In the one-sided connection, the sensing and source terminals of the four-probe method were connected to the same end of the electrodes. The measured  $R$  was expressed in Equation (3.1).

$$R = R_o + 2R_c + 2R_e = \alpha L_o + 2R_c + 2R_e. \quad (3.1)$$

Where  $R_e$  was electrode resistance. In contrast, in the two-sided connection, the sensing and source terminals were connected to both ends of the electrodes. The measured  $R$  is defined in Equation (3.2).

$$R = R_o + 2R_c = \alpha L_o + 2R_c. \quad (3.2)$$

This study compared the one- and two-sided connections to evaluate the effect of  $R_e$  and presented the measurement of  $R$  that does not include  $R_e$  by the two-sided connection. As illustrated in Figure 3.1(b), the study further compared the TLM measurement configurations: measuring the electrodes across the other electrodes or measuring the adjacent electrodes. Although the number of samples can be increased by measuring across electrodes, there is a concern that the current flowing through the unused electrode may cause an error in the estimation of  $R_o$ . Therefore, the TLM measurement results were evaluated with and without unused electrodes. Figure 3.2(c) presents a schematic illustrating the effect of unused electrodes

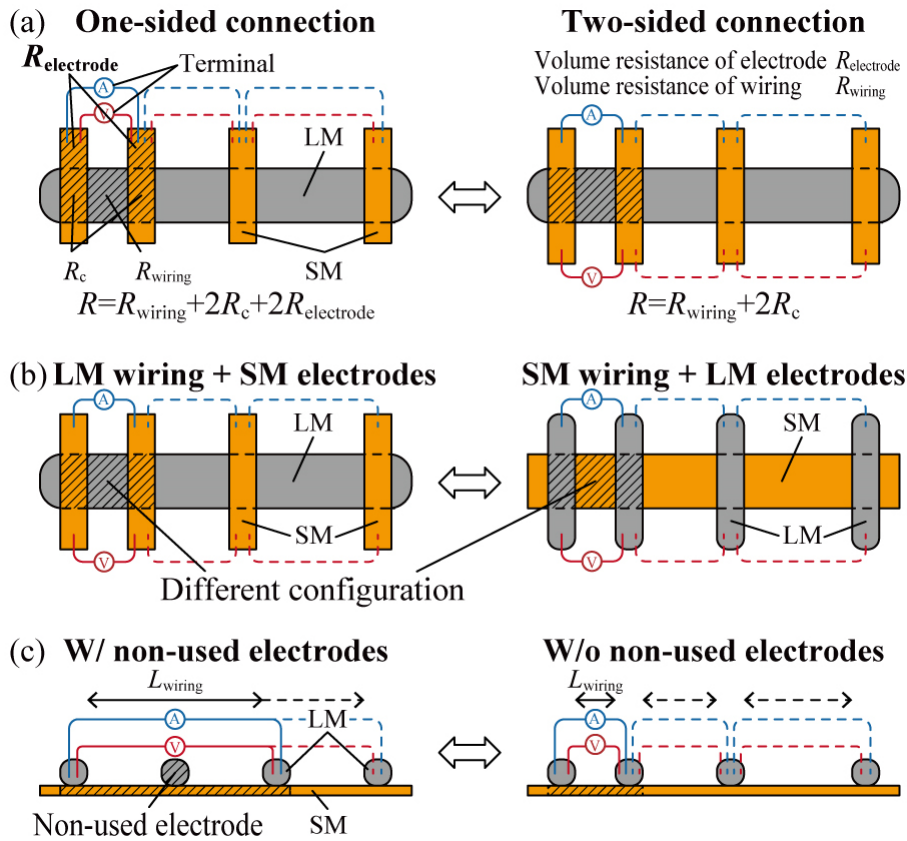


Figure 3.1 Schematics of measurement configuration for the highly accurate measurement of  $R_c$  between Ga-based LMs and SMs via TLM.

between measurement electrodes.

Figure 3.2 presents schematics and photographs of TLM measurement devices with LM wiring and SM electrodes (Figure 3.2(a)) and with SM wiring and LM electrodes (Figure 3.2(b)). This study employed galinstan (Changsha Rich Nonferrous Metals, Hunan, China) and a Cu substrate (Metaroyal, Toray Advanced Materials Korea, Seoul, Korea) as LM and SM materials, respectively. In the measurement device, galinstan contacted the Cu substrate. The Cu substrate was patterned into electrode or wiring shapes using a UV laser cutter. The conditions for laser cutting are presented in Appendix A. The galinstan filled a cutout in the polyethylene terephthalate (PET) substrate in the shape of the electrodes or wirings. Acrylic substrates sandwiched the PET substrate with cutouts filled with galinstan and the Cu substrate. This structure can seal LM without altering the surface condition of the Cu substrate. The copper substrate and galinstan were 0.008-mm and 1-mm thick, respectively. The electrodes and wiring were 1-mm wide,

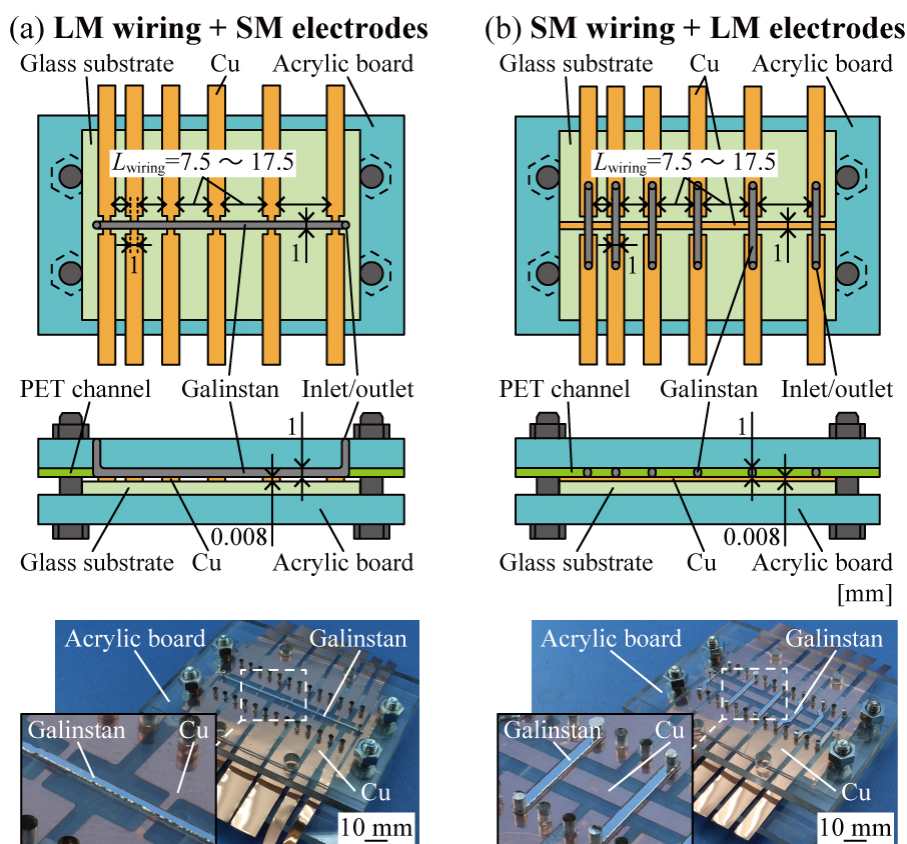


Figure 3.2 Schematic illustrations and photographs of TLM measurement devices with (a) LM (galinstan) wiring and SM (Cu) electrodes, (b) SM wiring and LM electrodes.

while the  $L_o$  was from 7.5 mm to 17.5 mm.

Since the  $R_c$  of LM may differ depending on the contact procedures, this section also studied the cause of the difference in TLM measurement results. Figure 3.3 shows an L-shaped device for measuring  $R_c$  at the same contact point with different measurement configurations. In the L-shaped device, two LM lines and two SM lines crossed each other. For the configuration with LM wiring and SM electrodes, one LM wiring and two SM electrodes were measured. For the configuration with SM wiring and LM electrodes, one SM wiring and two LM electrodes were measured. The copper substrate and galinstan were 0.008 mm thick and 1 mm thick, respectively. The electrodes and wiring were 1 mm wide, and  $L_o$  was 10 mm. The measured  $R$  is described as Equation (3.2).  $R_o$  was calculated from  $\alpha$  obtained from Figure 3.6 and  $L_o$ , and  $R_c$  is calculated by subtracting  $R_o$  from  $R$ .

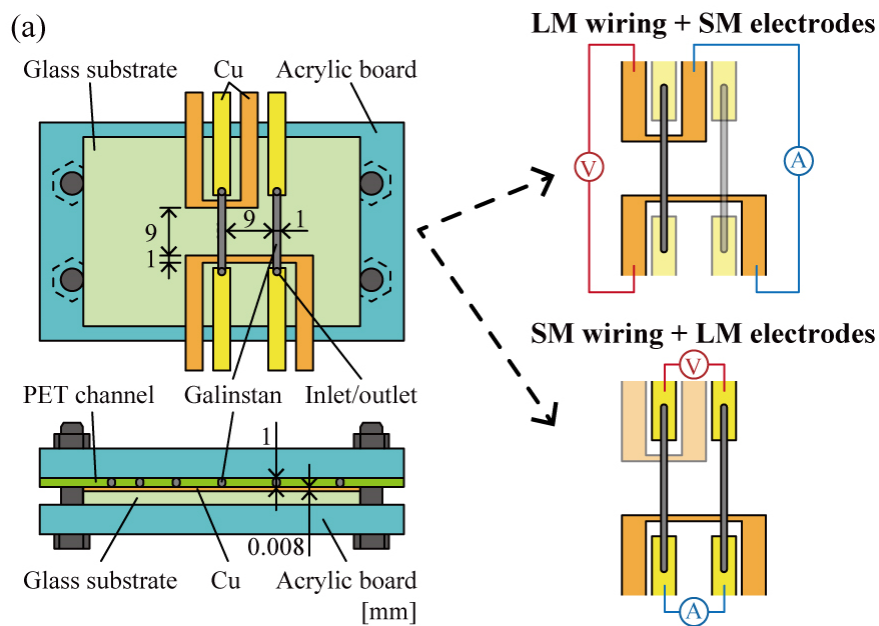


Figure 3.3 Schematic illustrations of L-shaped devices for measuring  $R_c$  at same contact point by different measurement configurations.

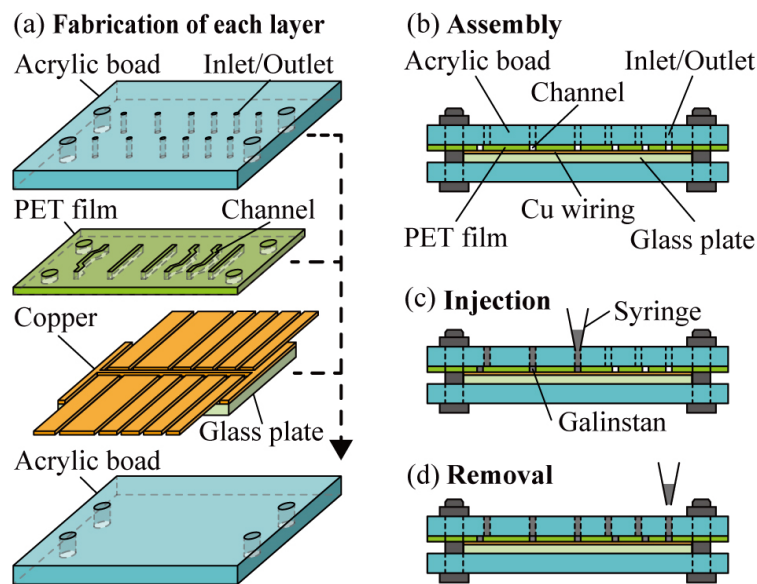


Figure 3.4 Schematics of the fabrication procedure of TLM measurement devices.

Figure 3.4 illustrates the fabrication process of the measurement devices. As presented in Figure 3.4 (a) and (b), two acrylic substrates, a PET substrate with cutouts, and a copper substrate were assembled and

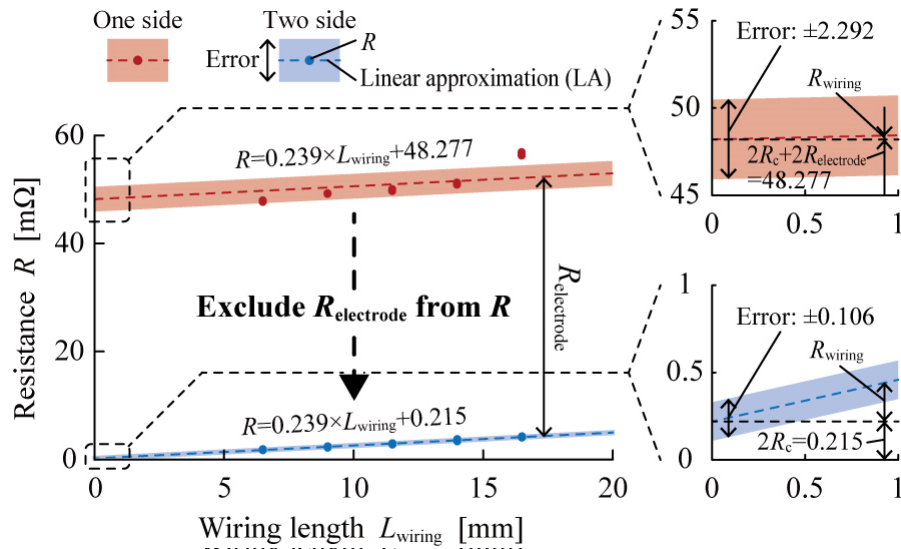


Figure 3.5 TLM measurement results for the voltage measurement terminal connections ( $N=4$ ).

fixed. The copper substrate was treated with flux (NS30, Nihon Superior, Osaka, Japan) before assembly. Then, as illustrated in Figure 3.4 (c) and (d), galinstan was injected with a syringe in the cutout and sealed. The resistance of the device  $R$  was measured with an ohm meter (RM3545, Hioki, Nagano, Japan) and a switch main frame (SW1002, Hioki, Nagano, Japan). The device had five different  $L_o$ s, and the resistance  $R$  was measured ten times for each  $L_o$ . An approximate straight line was drawn for the measurement result (200 plots) of the four devices, and the Y-intercept and its standard deviation were calculated. Detailed settings are presented in the Appendix B.

### 3.2.2 Results and Discussion

Figure 3.5 presents the TLM measurement results for connecting measuring terminals. Because this study used the same device for the one-sided and two-sided connections, the slope of the approximate straight line  $\alpha$  of Equations (1) and (2) was 0.239 mΩ/mm in both results. The measured  $\alpha$  was almost the same (-16.7%) as the  $\alpha$  of 0.279 mΩ/mm estimated from the conductivity and dimensions of the galinstan wiring. The Y-intercept ( $= 2R_c + 2R_c$ ) was  $48.277 \pm 2.292$  mΩ for the one-sided connection, while the Y-intercept ( $= 2R_c$ ) was  $0.215 \pm 0.106$  mΩ for the two-sided connection. The difference in Y-intercept between the one- and two-sided connections was 48.062 mΩ. The measured difference was almost the same (-0.8%) as the difference of 48.444 mΩ estimated from the conductivity and dimensions of the copper

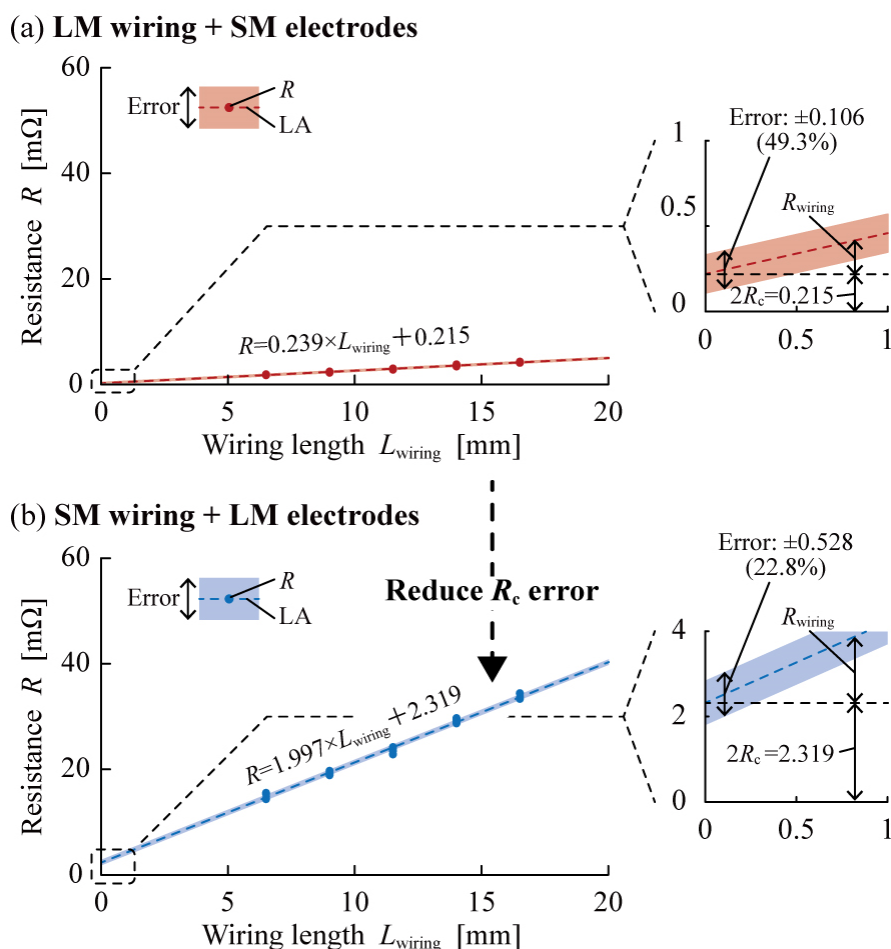


Figure 3.6 TLM measurement results of  $R_c$  on configurations with (a) LM wiring and SM electrodes, (b) SM wiring and LM electrodes ( $N = 4$ ).

electrode. Therefore,  $2R_c$  and  $2R_e$  were 0.215 m $\Omega$  and 48.062 m $\Omega$ , respectively. These results indicate that  $R_c$  cannot be ignored for the TLM measurement of LMs and SMs because  $R_c$  was higher than  $R_e$  by more than two orders of magnitude. Moreover, this study demonstrated that  $R$  could be measured without including  $R_c$  by the two-sided connection.

Figure 3.6 shows the TLM measurement results for the measurement configurations. The slope  $\alpha$  for the configuration of LM wiring and SM electrodes and that of SM wiring and LM electrodes were 0.239 m $\Omega$ /mm and 1.997 m $\Omega$ /mm, respectively. The measured  $\alpha$  for the configuration of SM wiring and LM electrodes was almost the same (-5.2%) as  $\alpha$  of 2.100 m $\Omega$ /mm estimated from the conductivity and



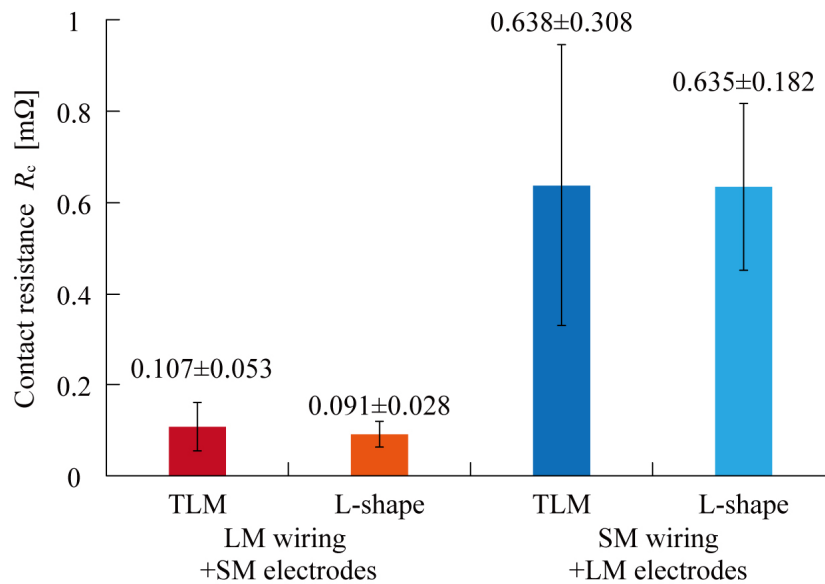


Figure 3.7  $R_c$  at same contact point by different measurement configurations.

dimensions of the copper wiring. The Y-intercept was  $0.215 \pm 0.106$  mΩ (error: 49.3%) for the configuration of LM wiring and SM electrodes. In contrast, Y-intercept was  $1.275 \pm 0.616$  mΩ (error: 48.3%) for the configuration of SM wiring and LM electrodes. These results show that  $R_c$  differed by six times for the configurations.

Figure 3.7(a) shows the  $R_c$  for the measurement configurations measured by L-shaped and TLM devices obtained from equation (4). For the configuration of LM wiring and SM electrodes,  $R_c$  in L-shaped devices was  $0.091 \pm 0.028$  mΩ, almost the same (-15.0%) as in the TLM devices. For the configuration of SM wiring and LM electrodes,  $R_c$  in L-shaped devices was  $0.635 \pm 0.182$  mΩ, almost the same (-0.5%) as in the TLM devices. These results show that the difference in  $R_c$  between configurations was due to the measurement configuration, not the fabrication process. The  $L_T$  for the configurations of LM wiring and SM electrodes and that of SM wiring and LM electrodes were  $0.449 \pm 0.221$  mm and  $0.319 \pm 0.154$  mm, respectively. Moreover, the  $\rho_c$  for the configurations of LM wiring and SM electrodes and that of SM wiring and LM electrodes were  $0.048 \pm 0.034$  mΩmm<sup>2</sup> and  $0.204 \pm 0.139$  mΩmm<sup>2</sup>, respectively. Therefore, this study found that the  $\rho_c$  for the configuration of SM wiring and LM electrodes was four times higher than that of LM wiring and SM electrodes. These results indicate that the measurement configuration of the TLM must be investigated more for the  $R_c$  measurement of LM.

Figure 3.8 presents the TLM measurement results for the unused electrode. The slope of the approximate

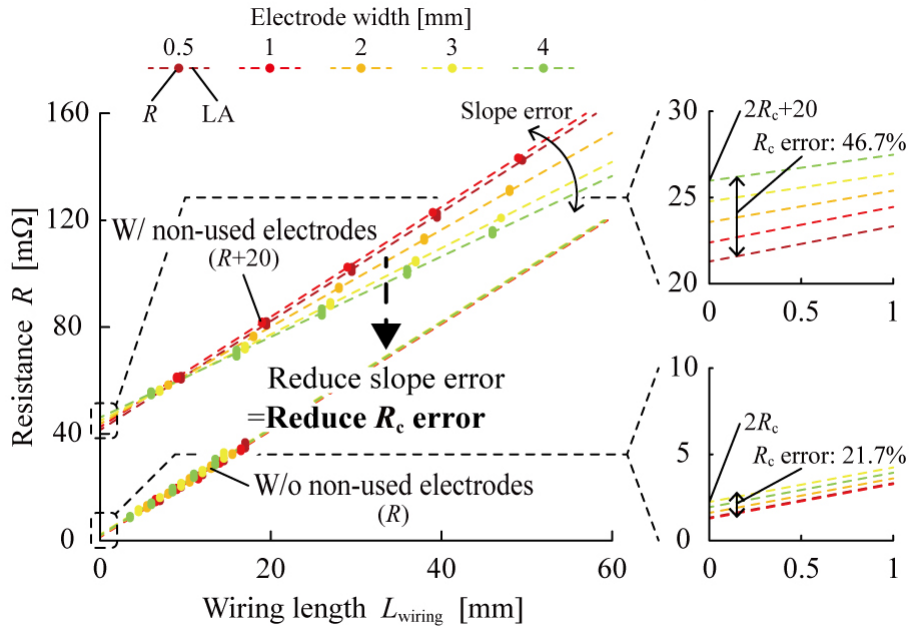


Figure 3.8 TLM measurement results with and without unused electrodes ( $N = 4$ ).

straight line without a non-used electrode was constant at  $1.997 \text{ m}\Omega/\text{mm}$ , while the slope of the approximate straight line with a non-used electrode decreased from  $2.043 \text{ m}\Omega/\text{mm}$  to  $1.510 \text{ m}\Omega/\text{mm}$  as the electrode width increased. This resulted in a  $R_c$  error of 21.7% for the case without the unused electrode, which was 53.5% lower than the  $R_c$  error (46.7%) for the case with the unused electrode. This result verifies that the  $R_c$  error can be reduced by measuring without an unused electrode.

### 3.3 Measurement Accuracy for Current Applied Location

LMs are utilized as stretchable conductors in various stretchable electronic devices. Moreover, such devices with Ga-based LMs have garnered considerable attention. This study presents a method for accurately determining the  $R_c$  between galinstan and Cu electrodes by considering the current-density distribution in TLM measurements. Conventional TLM measurements assume that the  $R_{\text{she}}$  is negligible compared with  $R_{\text{sho}}$ , such as Si. However, this assumption may be problematic because the  $R_{\text{sho}}$  of Ga-based LM is close to the  $R_{\text{she}}$ . Therefore, this study developed a method of applying current to each measuring electrode and compared it with the conventional method of applying current to the outer

electrodes. Obtained simulation results indicate that  $R_{\text{she}}$  cannot be ignored for galinstan, and the  $R_{\text{c}}^{\text{Total}}$  included  $<10\%$  of the  $R_{\text{c}}$  component when current was applied to the outer electrodes. In contrast,  $R_{\text{c}}^{\text{Total}}$  included the entire  $R_{\text{c}}$  component when current was applied to each electrode. Furthermore, it was determined that the volume resistances of the object and electrode included in  $R_{\text{c}}^{\text{Total}}$  cannot be ignored. Therefore, for accurate measurement, current must be applied to each electrode, and  $R_{\text{c}}$  must be determined from the intersections of the measured and simulated  $R_{\text{c}}^{\text{Total}}$ . The obtained  $\rho_{\text{c}}$  was  $0.115 \text{ m}\Omega\text{mm}^2$ . The maximum error was  $0.085 \text{ m}\Omega\text{mm}^2$ , which was lower than the  $\rho_{\text{c}}$  of the solders ( $>10^{-1} \text{ m}\Omega\text{mm}^2$ ) with the lowest  $\rho_{\text{c}}$  among the EIMs between the electronic components and wiring. This study provides valuable insight into the  $R_{\text{c}}$  measurement of LMs, along with new opportunities for the development of stretchable electronics using LMs.

### 3.3.1 Simulation Methods

Figure 3.9(a) presents a schematic of the TLM measurements. The conventional TLM assumes that  $R_{\text{she}}$  is negligible compared with  $R_{\text{sho}}$ . In this case, the current applied to the outer electrode completely passes through the interface between the electrode and object ( $I_i = I$ ), and the entire  $R_{\text{c}}$  component is included in the measured  $R_{\text{c}}^{\text{Total}}$ . Furthermore, assuming that  $R_{\text{o}}$  and  $R_{\text{e}}$  are negligible compared with  $R_{\text{c}}$ , the measured  $R_{\text{c}}^{\text{Total}}$  is regarded as  $R_{\text{c}}$ . Figure 3.9(b-i) presents a schematic of the TLM measurement for the LMs in which current is applied to the outer electrodes.  $R_{\text{sho}}$  may not be negligible compared with  $R_{\text{she}}$ . In this case,  $I_i < I$ , and part of the  $R_{\text{c}}$  component ( $R_{\text{c}} \times I_i/I$ ) is included in the measured  $R_{\text{c}}^{\text{Total}}$ . Figure 3.9(b-ii) presents a schematic of the TLM measurement for the LMs in which current is applied to each measuring electrode.  $I_i$  is equal to  $I$  regardless of the sheet resistance and  $\rho_{\text{c}}$ , and the entire  $R_{\text{c}}$  component is included in the measured  $R_{\text{c}}^{\text{Total}}$ . For both current application methods, the  $R_{\text{o}}$  and  $R_{\text{e}}$  included in  $R_{\text{c}}^{\text{Total}}$  are not negligible compared with the  $R_{\text{c}}$  of the LMs. Figure 3.10 presents the equivalent circuit diagrams of the TLM measurement for the different current application methods.

Figure 3.10 presents the equivalent circuit diagrams of the TLM measurements for the current application methods. In the contact region, the electrode and object are divided into  $2n$  small regions. Here, the electrode, object, and  $R_{\text{c}}$  in each small region are expressed as  $r_{\text{e}}$ ,  $r_{\text{o}}$ , and  $r_{\text{c}}$ , respectively. The current passing through the interface between the electrode and object in each small area is expressed as  $i_1, i_2, \dots, i_n$  ( $\geq 0$ ). The amount of current passing through the interface  $I_i$  at each condition by these equivalent circuit diagrams can be considered. When current is applied to the outer electrodes (Figure 3.10(a)),  $I_i = i_1 + i_2 + \dots + i_n$ . Accordingly, Equations (3.3) and (3.4) can be obtained from Loops 1 and 2 in Figure 3.10(a),

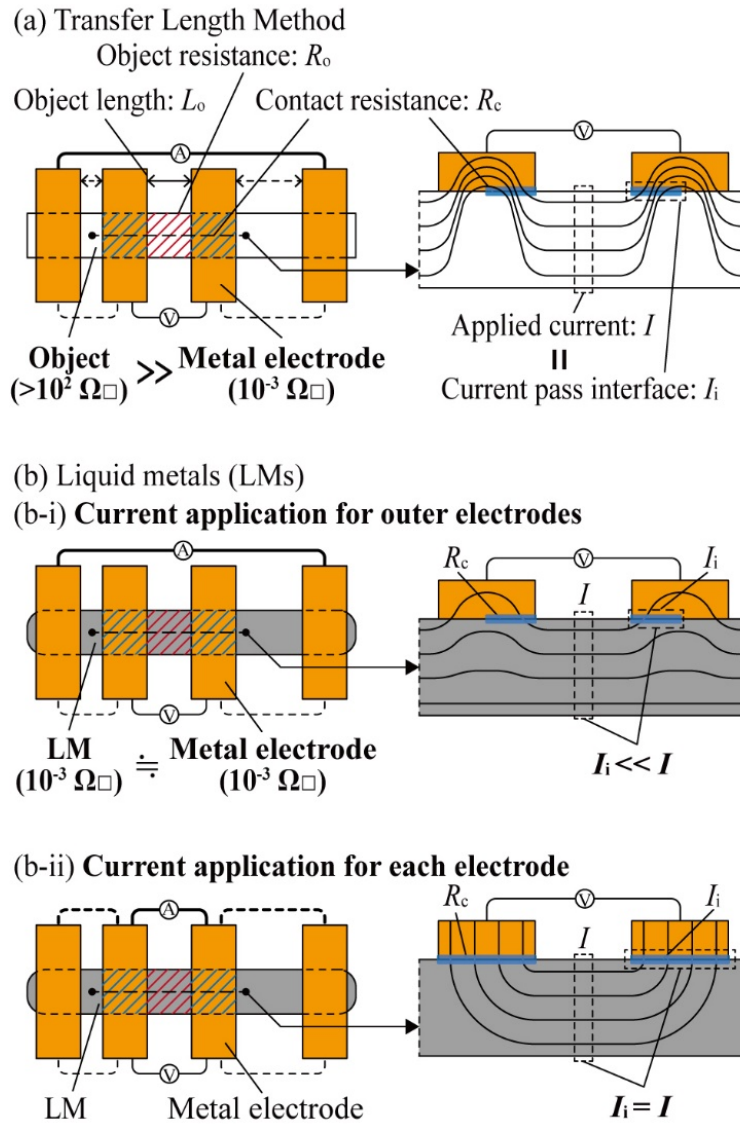


Figure 3.9 Schematic of  $R_c$  measurements of Ga-based LMs using the TLM. (a) Conventional TLM measurement, in which current is applied to the outer electrodes. (b) The TLM measurements of LMs in which current is applied to (b-i) the outer electrodes and (b-ii) each electrode.

respectively.

$$R_c i_1 + n r_e i_1 + (n-1) r_e i_2 + \dots + r_e i_n = n r_o I - n r_o i_1 - (n-1) r_o i_2 - \dots - r_o i_n \quad (3.3)$$

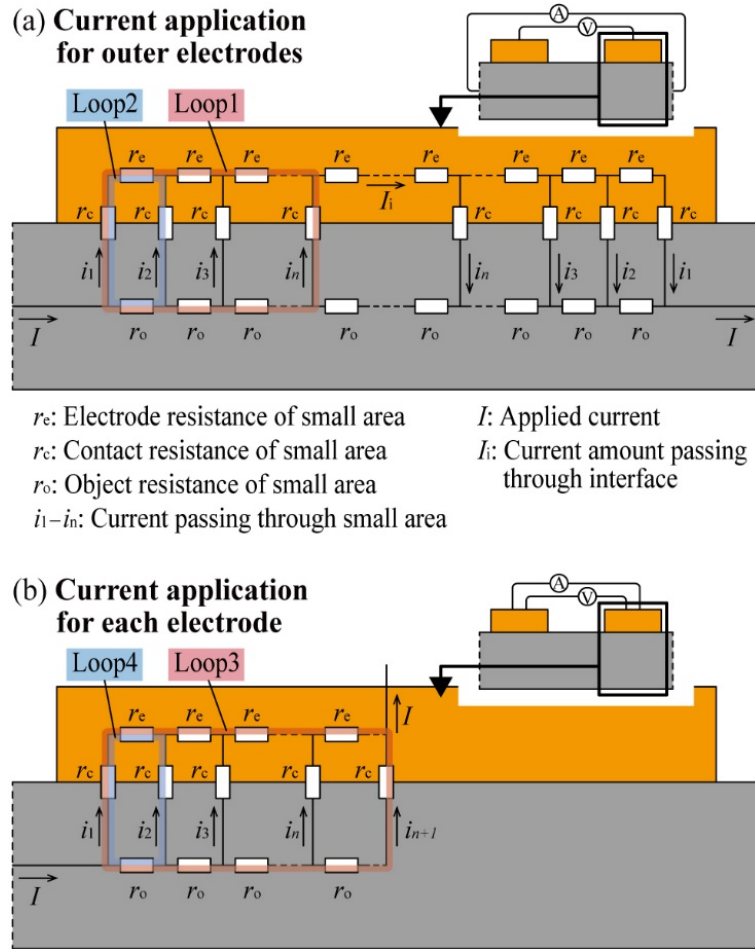


Figure 3.10 Equivalent circuit diagrams of TLM measurements in which current is applied to (a) the outer electrodes and (b) each electrode. (a) Amount of current passing through the interface between the electrode and object ( $I_i$ ) depends on the object, electrode, and  $R_c$ . (b) All the applied current ( $I$ ) passes through the interface regardless of the object, electrode, and  $R_c$ . For both current application methods, the object and electrode resistances included in the measured resistance in the contact area ( $R_c^{\text{Total}}$ ) cannot be ignored when  $R_c$  is low.

$$(r_c + r_e + r_o)i_1 - r_c i_2 - r_o I = 0 \quad (3.4)$$

In addition, Equations (3.3) and (3.4) are valid for Loops 1 and 2, respectively. When  $r_o$  is significantly higher than  $r_e$  and  $r_c$ ,  $i_1 = I$  and  $i_2 = i_3 = \dots = i_n = 0$  from Equation (3.4). In other words, the amount of

current passing through the interface  $I_i$  is equal to  $I$ . When  $r_e$  is significantly higher than  $r_o$  and  $r_c$ ,  $i_1 = i_2 = i_3 = \dots = i_n = 0$  from Equation (3.3). In other words, the amount of current passing through the interface  $I_i$  is equal to 0.

In contrast, when current is applied to each electrode (Figure 3.10(b)),  $I_i = i_1 + i_2 + \dots + i_n + i_{n+1}$ . Equation (3.5) and (3.4) from Loops 1 and 2 in Figure 3.10(b), respectively.

$$R_c i_1 + n r_e i_1 + (n-1) r_e i_2 + \dots + r_e i_n = n r_o I - n r_o i_1 - (n-1) r_o i_2 - \dots - r_o i_n + r_c i_{n+1} \quad (3.5)$$

When  $r_o$  is significantly higher than  $r_e$  and  $r_c$ ,  $i_1 = I$  and  $i_2 = i_3 = \dots = i_n = i_{n+1} = 0$  from Equation (3.4). In other words, the amount of current passing through the interface  $I_i$  is equal to  $I$ . When  $r_e$  is significantly higher than  $r_o$  and  $r_c$ ,  $i_1 = i_2 = i_3 = \dots = i_n = 0$  and  $i_{n+1} = I$  from Equation (3.5). In other words, the amount of current passing through the interface  $I_i$  is also equal to  $I$ . In conclusion, the following can be inferred from these equivalent circuit diagrams. In the configuration of the current application for the outer electrodes (Figure 3.10(a)), the amount of current passing through the interface  $I_i$  depends on the values of the object, electrode, and  $R_c$ . In particular, in the configuration of the current application for each electrode (Figure 3.10(b)), the amount of current passing through the interface  $I_i$  is always equal to  $I$  although the current distribution depends on the values of the object, electrode, and  $R_c$ .

Here, the current-density distribution for the current application methods was analyzed via TLM measurements based on FEM simulations. In addition,  $I_i/I$  was analyzed relative to the sheet-resistance ratio ( $R_{sho}/R_{she}$ ) and contact resistivity ratio ( $\rho_c/R_{she}$ ). The  $I_i/I$  for the  $R_{sho}$  of the LMs was compared with those of conventional objects, such as Si, graphene, and conductive adhesives. Furthermore, the  $R_c^{\text{Total}}$  between galinstan and Cu electrodes for the current application methods was measured using the TLM.  $P_c$ ,  $I_i/I$ , and  $R_c$  were obtained by comparing the FEM simulations with the measurement results. Accordingly, the measurement accuracies of the current application methods were compared. Although  $R_c^{\text{Total}}$  can be measured using several conventional methods, the results obtained from different methods cannot be compared. The  $R_c$  and  $R_o$  included in  $R_c^{\text{Total}}$  depend on the measurement configuration and dimensions of the devices.

Figure 3.11(a) presents the electrical contact model of the TLM measurement in which current was applied to the outer electrodes (COMSOL Multiphysics ver. 6.0, COMSOL, MA, USA). Two metal electrodes were placed in contact with the object. Current was applied uniformly to the cross section of one end of the object (hatched red). The cross section of the other end of the object (hatched green) was grounded. These current application conditions represented the situation in which current was applied to

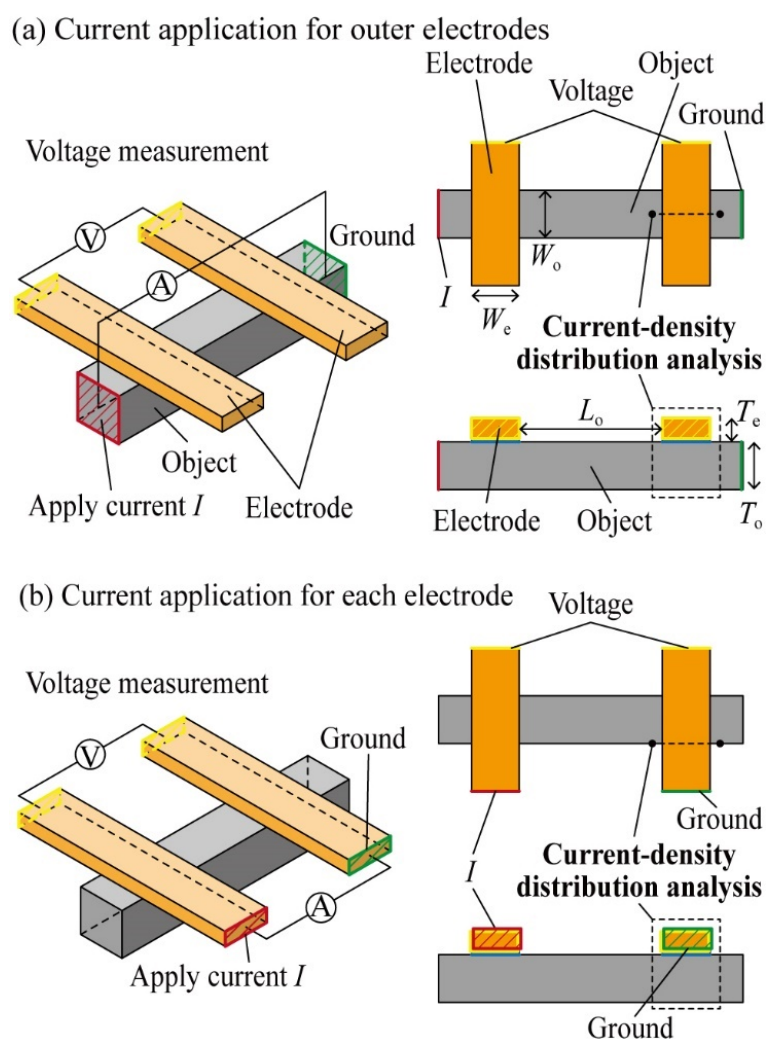


Figure 3.11 Electrical contact models for the simulation of the current-density distribution in TLM measurement using the FEM. Two metal electrodes are brought into contact with the object. The voltage difference between the two electrodes ( $V$ ) is measured.  $I_i$  is obtained by integrating the normal current density at the interface. (a) Model of current application to the outer electrodes. The current is applied uniformly to the cross sections of both ends of the object. The current-density distribution is analyzed at the central cross section of the object. (b) Model of the current application to each electrode. A current is applied to the ends of the electrodes, opposite the voltage measurement. The current-density distribution is analyzed on the same side of the object where the current was applied.

one of the outer electrodes and flew through the object toward the measuring electrodes and then toward

Table 3.1 Laplace equation and boundary conditions for the models in Figure 3.12.

Conditions	Current application to the outer electrodes	Current application to each measuring electrode
Inside the electrode	$\nabla^2\Phi_I=0$	$\nabla^2\Phi_{II}=0$
Inside the object	$\nabla^2\Phi_{II}=0$	$\nabla^2\Phi_{II}=0$
End of the electrode for $V$	$\Phi_I$	$\Phi_I$
End of the electrode for $I$	-	$\Phi_I=0$
End of the object	$\Phi_{II}=0$	-
Cross section of the object	$\Phi_{II}=\frac{V}{2}$	$\Phi_{II}=\frac{V}{2}$
Outer surfaces	$\frac{\partial\Phi}{\partial x}=\frac{\partial\Phi}{\partial y}=\frac{\partial\Phi}{\partial z}=0$	$\frac{\partial\Phi}{\partial x}=\frac{\partial\Phi}{\partial y}=\frac{\partial\Phi}{\partial z}=0$
Interface between the electrode and object	$J_z=-\frac{1}{\rho_1}\frac{\partial\Phi_I}{\partial z}=-\frac{1}{\rho_2}\frac{\partial\Phi_{II}}{\partial z}$ $\rho_c J_z = \Phi_{II}(Z = 0^-) = \Phi_I(Z = 0^+)$	$J_z=-\frac{1}{\rho_1}\frac{\partial\Phi_I}{\partial z}=-\frac{1}{\rho_2}\frac{\partial\Phi_{II}}{\partial z}$ $\rho_c J_z = \Phi_{II}(Z = 0^-) = \Phi_I(Z = 0^+)$

the other outer electrode. The interface between the object and electrodes was characterized by contact impedance in COMSOL. This contact condition provided a uniform  $\rho_c$  [ $\text{m}\Omega\text{mm}^2$ ]. In the transmission-line model, which was the basis of the TLM, the upper surface of the electrode was grounded such that the current completely passed through the interface. However, in conventional TLM measurements, the current applied to the outer electrodes flew from the object to the electrode and then back to the object. Therefore, the cross section of the end of the object hatched green was grounded in our model. Here, the potential distribution on the cross sections at the end of the measuring electrodes (hatched yellow) was considered uniform because the electrode length ( $L_e$ ) exceeded the object width ( $W_o$ ) and electrode width ( $W_e$ ). Hence, the difference between the average potentials on the cross sections of the ends of the measuring electrodes was obtained as  $V$ . This study analyzed the current-density distributions on the central cross section of the object, as depicted by the dotted line in Figure 3.11(a).  $I_i$  was obtained by integrating the normal current density at the interface between the object and electrodes. Figure 3.11(b)



presents the electrical contact model of the TLM measurement, in which current was applied to each measuring electrode. Two metal electrodes were brought into contact with the object. Current was applied uniformly to the cross section of one end of the electrode (hatched red), while the cross section of the other end (hatched green) was grounded. The difference between the average potentials on the cross sections of the opposite ends of the measuring electrodes (hatched yellow) was measured. The study also analyzed current-density distribution on the same side of the object where the current was applied, as depicted by the dotted line.  $I_i$  was obtained by integrating the normal current density at the interface.

The volume resistivity, thickness, length, and width of the object were  $\rho_o = 10^{-10} \Omega\text{m}$  to  $10^{-4} \Omega\text{m}$ ,  $T_o = 10 \mu\text{m}$ ,  $L_o = 10 \text{mm}$ , and  $W_o = 5 \text{mm}$ , respectively. The simulated  $R_c^{\text{Total}}$  was constant regardless of  $L_o$ , because the current density was uniformly distributed in the object between the measuring electrodes. Hence, any  $L_o$  value can be used in the simulation. The volume resistivity, thickness, length, and width of the metal electrodes were  $\rho_e = 10^{-8} \Omega\text{m}$ ,  $T_e = 5 \mu\text{m}$ ,  $L_e = 10 \text{mm}$ , and  $W_e = 5 \text{mm}$ , respectively.  $P_c$  ranged from  $10^{-12}$  to  $10^{-6} \Omega\text{m}^2$ .  $I_i$  was simulated for different values of the sheet-resistance ratio  $R_{\text{sho}}/R_{\text{she}}$  and contact resistivity ratio  $\rho_c/R_{\text{she}}$ .  $R_{\text{sho}}$  varied because the metal electrodes were in contact with objects with different  $R_{\text{sho}}$  values. In addition,  $\rho_c$  varied under the assumption that  $I_i$  decreased as  $\rho_c$  increased because the resistance along the current path increased. The model had tetrahedral meshes with maximum mesh size of  $4 \mu\text{m}$ . The Laplace equation and boundary conditions are summarized in Table 3.1, improved from the previous studies[169].  $J_z$  is the normal component of current density crossing the interface between the electrode and object, and  $\Phi_I$  and  $\Phi_{II}$  are the potentials in the contact area and the object, respectively.

### 3.3.2 Simulation Results

Figure 3.12(a) and (b) present the current-density distribution and current ratio  $I_i/I$  relative to the sheet-resistance ratio  $R_{\text{sho}}/R_{\text{she}}$  and contact resistivity ratio  $\rho_c/R_{\text{she}}$  when current was applied to the outer electrodes. As indicated by Figure 3.12(a-iii) and (a-iv), most of the applied current passed through the interface between the electrode and object ( $I_i \cong I$ ) for high  $R_{\text{sho}}/R_{\text{she}}$  values. The degree of current crowding around the interface edge decreased as  $\rho_c/R_{\text{she}}$  increased. In contrast, a negligible amount of applied current passed through the interface ( $I_i \ll I$ ) for low  $R_{\text{sho}}/R_{\text{she}}$  values, and  $I_i$  decreased slightly as  $\rho_c/R_{\text{she}}$  increased (Figure 3.12(a-i) and (a-ii)). Figure 3.12(b) demonstrates that  $I_i/I$  decreased from  $10^0$  to  $<10^{-2}$  as  $R_{\text{sho}}/R_{\text{she}}$  decreased from  $10^5$  to  $10^{-2}$  for all the  $\rho_c/R_{\text{she}}$  values. The decrease in  $I_i/I$  accelerated as  $\rho_c/R_{\text{she}}$  increased from  $10^{-9}$  to  $10^{-3}$ . In addition,  $I_i$  was equal to  $I$  for conventional objects such as Si ( $R_{\text{sho}} > 10^4 \Omega\Box$ ), graphene ( $R_{\text{sho}} > 10^3 \Omega\Box$ ), and conductive pastes ( $R_{\text{sho}} > 10^2 \Omega\Box$ ) for all  $\rho_c/R_{\text{she}}$  values. This

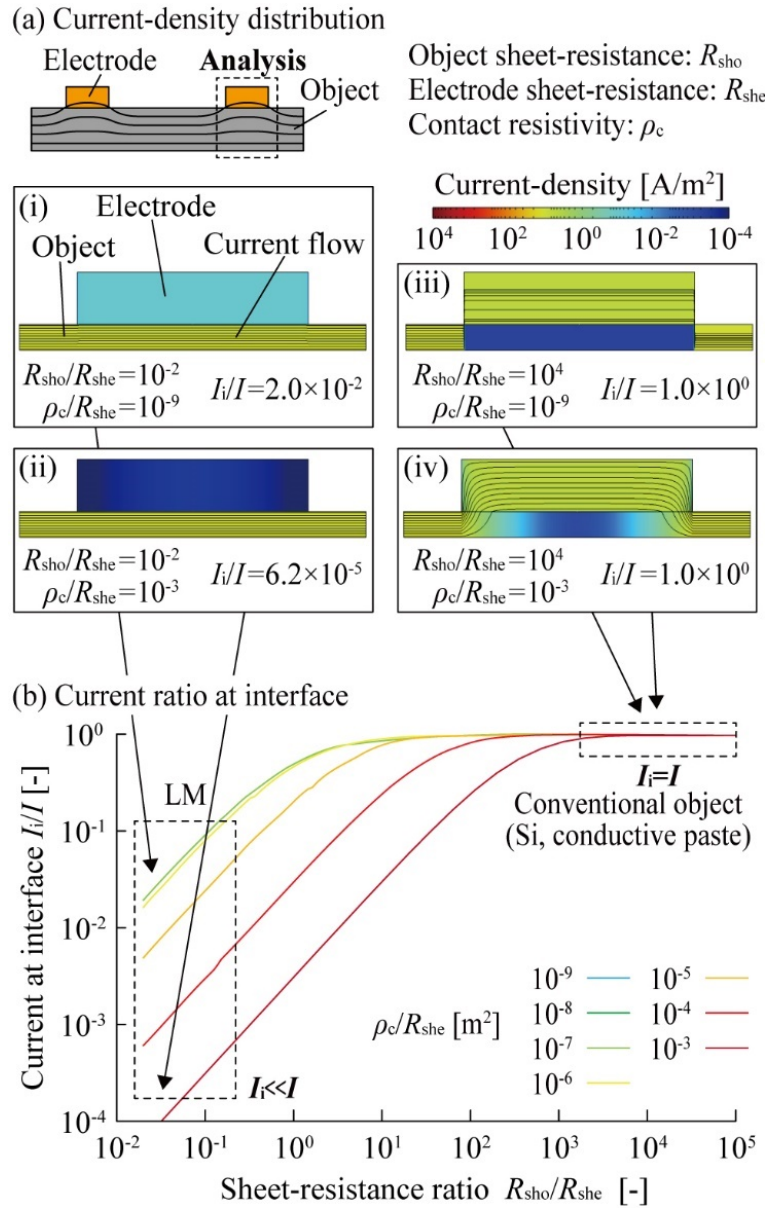


Figure 3.12 FEM simulation results for (a) the current-density distribution and (b) ratio of the current passing through the interface ( $I_i/I$ ) relative to the sheet-resistance ratio ( $R_{\text{sho}}/R_{\text{she}}$ ) and contact resistivity ratio ( $\rho_c/R_{\text{she}}$ ). Current was applied to the outer electrodes. The lines in the current-density distribution depict the current flow.  $I_i$  was equal to  $I$  for conventional objects (Si, graphene, conductive adhesive:  $R_{\text{sho}} > 10^2 \Omega\Box$ ). In contrast,  $I_i/I$  was  $< 10^{-1}$  for LMs ( $R_{\text{sho}} = 10^{-2}$  to  $10^0 \Omega\Box$ ).

result verifies that the assumptions in the TLM measurement that  $R_{\text{she}}$  is negligible relative to  $R_{\text{sho}}$  and that

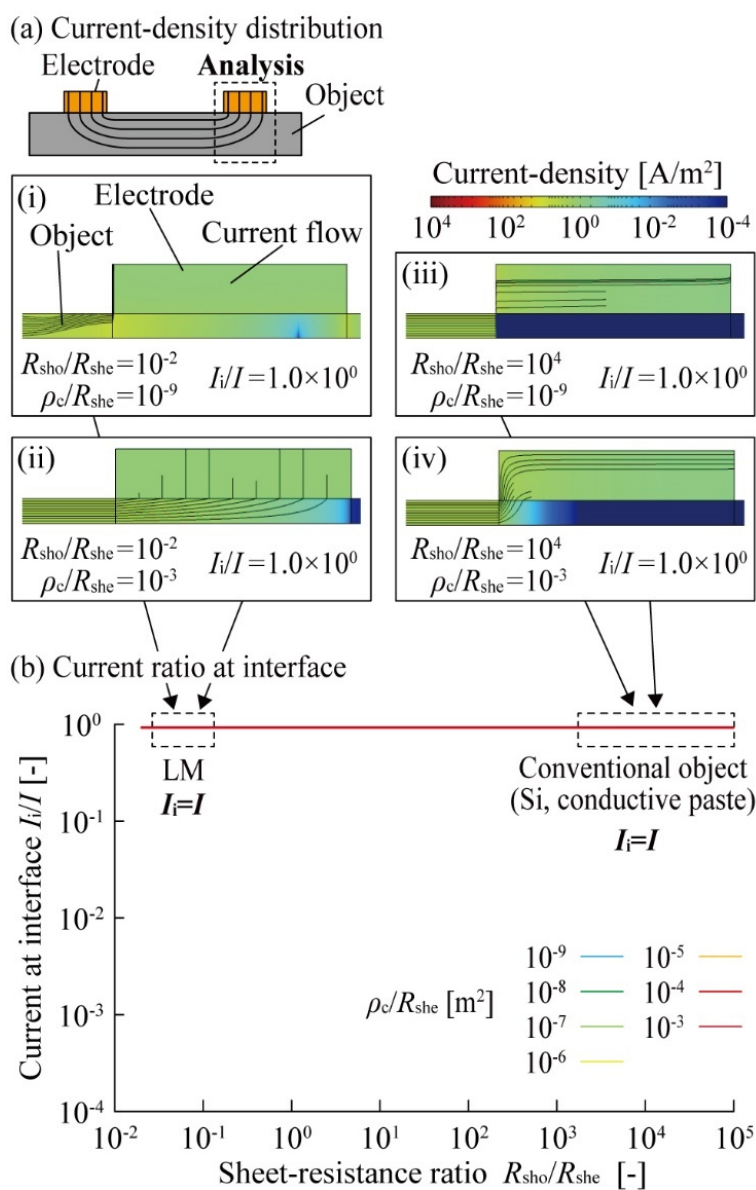


Figure 3.13 Simulation results of the (a) current-density distribution and (b)  $I_i/I$  for  $R_{\text{sho}}/R_{\text{she}}$  and  $\rho_c/R_{\text{she}}$ . Current is applied to each electrode.  $I_i$  is equal to  $I$  regardless of  $R_{\text{sho}}/R_{\text{she}}$  and  $\rho_c/R_{\text{she}}$ .

$I_i$  is equal to  $I$  are valid for conventional objects. In contrast,  $I_i/I$  was  $<10^{-1}$  for LMs ( $R_{\text{sho}} = 10^{-2}$  to  $10^0 \Omega \square$ ) and for all the  $\rho_c/R_{\text{she}}$  values. This result indicates that the assumptions that  $R_{\text{she}}$  is negligible compared to  $R_{\text{sho}}$  and that  $I_i$  is equal to  $I$  are invalid for LMs. In general, current application to the outer electrodes yields accurate measurements when  $R_{\text{sho}}/R_{\text{she}} > 10^3$ , because  $I_i$  is equal to  $I$  and the entire  $R_c$  component is included in  $R_c^{\text{Total}}$ . However, to ensure high accuracy, the current must not be applied to the outer electrodes

when  $R_{\text{sho}}/R_{\text{she}}$  is  $<10^3$ , because  $I_i < I$  and part of the  $R_c$  component is included in  $R_c^{\text{Total}}$ .

Figure 3.13 (a) and (b) present the current-density distribution and  $I_i/I$  relative to  $R_{\text{sho}}/R_{\text{she}}$  and  $\rho_c/R_{\text{she}}$  when current was applied to each electrode. As illustrated in Figure 3.13 (a), all the applied currents passed through the interface between the electrode and object, regardless of  $R_{\text{sho}}/R_{\text{she}}$  and  $\rho_c/R_{\text{she}}$ . The degree of current crowding around the interface edge decreased as  $R_{\text{sho}}/R_{\text{she}}$  decreased and  $\rho_c/R_{\text{she}}$  increased. Figure 3.13 (b) demonstrates that  $I_i$  was equal to the applied  $I$  for all the  $R_{\text{sho}}/R_{\text{she}}$  and  $\rho_c/R_{\text{she}}$  values when current was applied to each electrode. Therefore, to ensure high accuracy, the current should be applied to each electrode, because  $I_i = I$  and the entire  $R_c$  component is included in  $R_c^{\text{Total}}$ , regardless of  $R_{\text{sho}}/R_{\text{she}}$  and  $\rho_c/R_{\text{she}}$ . However,  $I_i = I$  and the entire  $R_c$  component is included in  $R_c^{\text{Total}}$  for both current application methods when  $R_{\text{sho}}/R_{\text{she}}$  is  $>10^3$ . For simplicity, current can be applied to the outer electrodes. Furthermore, regarding LMs, the current density exhibits a continuous distribution; hence, the  $R_c$  must be obtained from a comparison of simulations and measurements.

### 3.3.3 Device Fabrication for Measurements

Figure 3.14(a) and (b) present schematics and photographs of the TLM measurement devices. Galinstan (Changsha Rich Nonferrous Metals, Hunan, China) was employed as the LM material because it is prevalent owing to its low melting point ( $-19^\circ\text{C}$ ) among Ga-based LMs. Electroplated Cu with submicron surface roughness ( $R_a$ ) (Metaroyal, Toray Advanced Materials Korea, Seoul, Korea) was employed as the metal electrode material, in accordance with the ISO standard (ISO 16525-2:2014) for TLM measurements of conductive adhesives. Galinstan was brought into contact with a Cu substrate. The Cu substrate was patterned into electrode shapes using an ultraviolet laser cutter. The conditions for laser cutting are presented in Appendix A. Subsequently, cutouts on a polyethylene terephthalate (PET) substrate were filled with galinstan, and the resulting PET substrate and a Cu substrate were sandwiched between acrylic substrates. These measurement configurations were designed to ignore the effects of the wetting behavior of galinstan. Galinstan exhibits high surface tension and forms an oxide layer on its surface. Hence, the cross-sectional shape of galinstan is unknown if it is deposited on a substrate in the same manner as conventional TLM measurements. Therefore, a rectangular channel was filled with galinstan to determine the cross-sectional shape of the galinstan. Although the galinstan largely filled the channel, it may not have filled the corners of the channel, because of its wettability and the oxide layer. Consequently, to ignore the edge shape of the galinstan, the channel length exceeded the distance between the measuring electrodes. In addition, the structure could seal the galinstan without altering the surface conditions of the metal

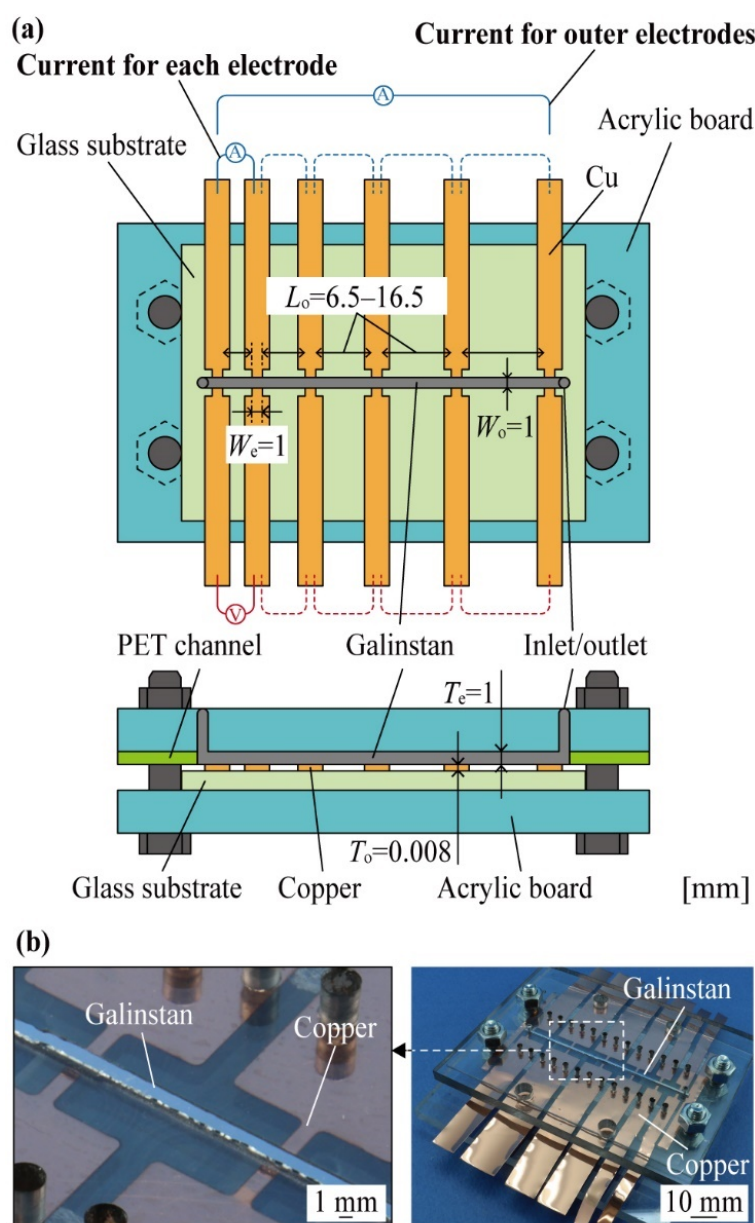


Figure 3.14 TLM measurement devices. (a) Schematics and (b) photographs of the devices. LM (galinstan) brought into contact with metal electrodes (Cu substrate). Current was applied to the outer electrodes or each electrode of the same device.

electrodes. The thickness, length, and width of the galinstan were  $T_o = 1$  mm,  $L_o = 7.5-17.5$  mm, and  $W_o = 1$  mm, respectively. The thickness and width of the Cu electrodes were  $T_e = 8$   $\mu\text{m}$  and  $W_e = 1$  mm, respectively.

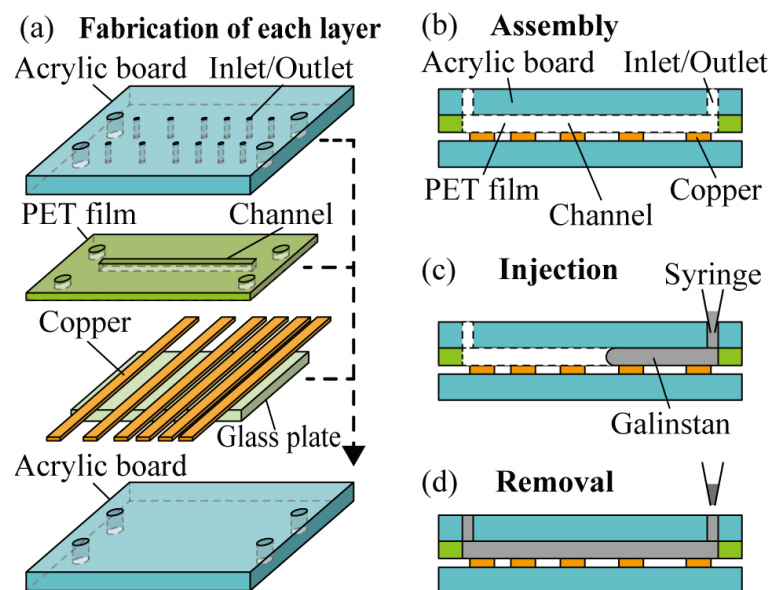


Figure 3.15 Fabrication procedures for the devices. (a), (b) Simple channel fabricated by sandwiching the PET substrate with a cutout and Cu substrate between acrylic substrates. (c), (d) Galinstan injected into the channel and sealed.

Figure 3.15 illustrates the fabrication process for the measurement devices. As presented in Figure 3.15(a) and (b), two acrylic substrates, a PET substrate with cutouts, and a Cu substrate, were assembled and fixed. Prior to the assembly, the Cu substrate was deoxidized using solder flux (NS-30, Nihon Superior, Osaka, Japan). The acrylic substrate was drilled to create the inlet and outlet for injecting galinstan into the cutouts. As illustrated in Figure 3.15(c) and (d), galinstan was injected into the cutouts using a syringe. The resistance of the device ( $R$ ) was measured using an ohm meter (RM3545, Hioki, Nagano, Japan). The measurement conditions were determined to ignore the time-dependent change in  $R$  during TLM measurements. For LMs, the TLM is typically used to measure the time-dependent change in  $R_c$  for different contact conditions, such as materials and contact procedures. The TLM measurement of LMs can be affected by alloying, Joule heating, electromagnetic interference, and ground loops. To ignore the effect of Joule heating, pulse currents were applied to the measuring electrodes for 200 ms by the SLOW2 mode. To ignore the effect of alloying, the duration of the TLM measurements was 150 s using an automatic switching machine (SW1002, Hioki, Nagano, Japan). To accurately measure the low resistance, the applied current  $I$  was as high as 1.5 A. In one measurement cycle,  $R$  was determined for five different  $L_o$  values

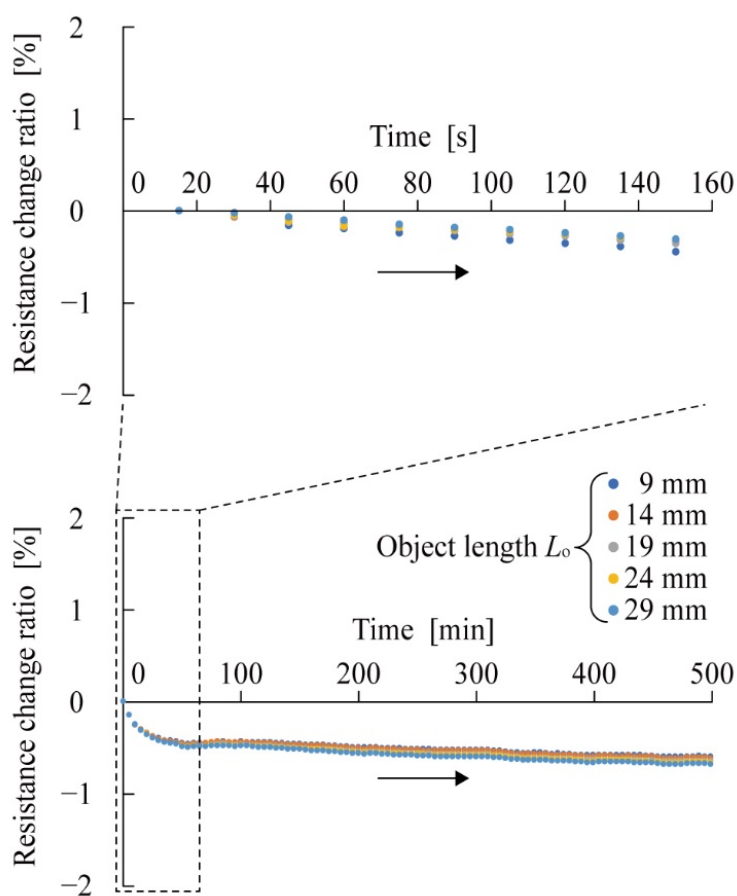


Figure 3.16 Time-dependent change in the measured resistance ( $R$ ) in the TLM measurement of galinstan and Cu electrodes. Current was applied to each electrode.  $R$  was reduced by 0.45% after 150 s and 0.68% after 500 min.

after 15 s had passed from the start of the measurement. This measurement cycle was performed 10 times consecutively (150 s). Here, the current was applied in a pulsed wave to neglect the increase in resistance due to heat generation. Figure 3.16 presents the time-dependent changes in  $R$ .  $R$  was reduced by 0.45% after 150 s of contact between the galinstan and Cu electrodes and by 0.68% after 500 min of contact. These results indicated that the effect of noise during the measurement was  $<0.45\%$  immediately after contact. Assuming measurement under various contact conditions, the effect of noise is  $<0.68\%$ , regardless of the time from contact to measurement. An approximate straight line was drawn for the measurement results (200 plots) of the four devices, and the Y-intercept was calculated. The simulation and measurement results were compared, and  $\rho_c$  was obtained from the intersections of the measured  $R_c^{\text{Total}}$  and the simulated

values for different  $\rho_c$ .  $I_i/I$  and  $R_c$  were calculated from the obtained  $\rho_c$ . The accuracy was evaluated from the error range of the obtained  $\rho_c$ . The measured  $R_c^{\text{Total}} = (R - R_o)/2$  was obtained from the Y-intercept ( $=2R_c^{\text{Total}}$ ) of the TLM results. The simulated  $R_c^{\text{Total}} = R_c \times I_i/I$  was obtained using the  $I_i/I$  and  $R_c$  from the simulations. In the simulations, the models presented in Figure 3.11 were employed. The channel width is adopted as the galinstan width, and the sheet resistance obtained experimentally from the slope of the TLM measurement results is adopted as that of the galinstan. Detailed settings are presented in the Appendix B.

### 3.3.4 Measurement Results

Figure 3.17(a) illustrates the relationship between  $L_o$  and the measured and simulated  $R = \alpha L_o + 2R_c^{\text{Total}}$  values when current was applied to the outer electrodes. The slope  $\alpha$  and Y-intercept ( $=2R_c^{\text{Total}}$ ) of the approximate line between  $L_o$  and the measured  $R$  were 0.243 m $\Omega$ /mm and 0.250 m $\Omega$ , respectively. Here, the  $R_{\text{sho}}$  of the galinstan obtained from the measured  $\alpha$  was  $2.43 \times 10^{-4}$   $\Omega$ . Figure 3.17(b) illustrates the relationship between  $L_o$  and the measured and simulated resistance in the contact area  $R_c^{\text{Total}} = (R - R_o)/2$ . The measured  $R_c^{\text{Total}}$  was  $0.125 \pm 0.056$  m $\Omega$ . In contrast, the simulated  $R_c^{\text{Total}}$  increased from 0.111 to 0.122 m $\Omega$  as  $\rho_c$  increased from  $10^{-4}$  to  $10^4$  m $\Omega\text{mm}^2$ . The measured and simulated  $R_c^{\text{Total}}$  did not intersect, and  $\rho_c$  could not be obtained. Figure 3.18 presents the simulated relationship between  $I_i/I$  and  $\rho_c$ .  $I_i/I$  decreased from 0.099 to 0.000 as  $\rho_c$  increased from  $10^{-4}$  to  $10^4$  m $\Omega\text{mm}^2$ .  $I_i$  was significantly lower than  $I$ , which reduced the slope of the simulated curve of  $R_c^{\text{Total}}$ , as illustrated in Figure 3.17(b). This simulation result indicates that  $R_{\text{she}}$  is not negligible compared with  $R_{\text{sho}}$  for LMs. Overall, it can be observed that the simulated values change negligibly when  $\rho_c$  is varied, as only a small fraction ( $<9.9\%$ ) of the applied current passes through the interface. Hence, the measured and simulated values did not intersect, and the measurement of  $R_c$  was impossible. Even if they intersect, the accuracy of the  $R_c$  obtained from the interface will be low, because the range of the simulated  $R_c^{\text{Total}}$  is lower than that of the measured  $R_c^{\text{Total}}$ .

Figure 3.19(a) illustrates the relationship between  $L_o$  and the measured and simulated  $R = \alpha L_o + 2R_c^{\text{Total}}$  when current was applied to each electrode. The slope  $\alpha$  and Y-intercept ( $=2R_c^{\text{Total}}$ ) of the approximate line between  $L_o$  and the measured  $R$  were 0.241 m $\Omega$ /mm and 0.239 m $\Omega$ , respectively. Here, the  $R_{\text{sho}}$  of the galinstan obtained from the measured  $\alpha$  was  $2.41 \times 10^{-4}$   $\Omega$ . Figure 3.19(b) presents the relationship between  $L_o$  and the measured and simulated resistances in the contact area ( $R_c^{\text{Total}} = (R - R_o)/2$ ). The measured  $R_c^{\text{Total}}$  was  $0.120 \pm 0.043$  m $\Omega$ . In contrast, the simulated  $R_c^{\text{Total}}$  increased from 0.063 to 9.823 m $\Omega$  as  $\rho_c$  increased from  $10^{-4}$  to  $10^1$  m $\Omega\text{mm}^2$ . The  $\rho_c$  at the intersection of the measured and simulated  $R_c^{\text{Total}}$  was 0.115 m $\Omega\text{mm}^2$  (min: 0.030 m $\Omega\text{mm}^2$ , max: 0.185 m $\Omega\text{mm}^2$ ). The  $R_c$  obtained using  $\rho_c$  was 0.230



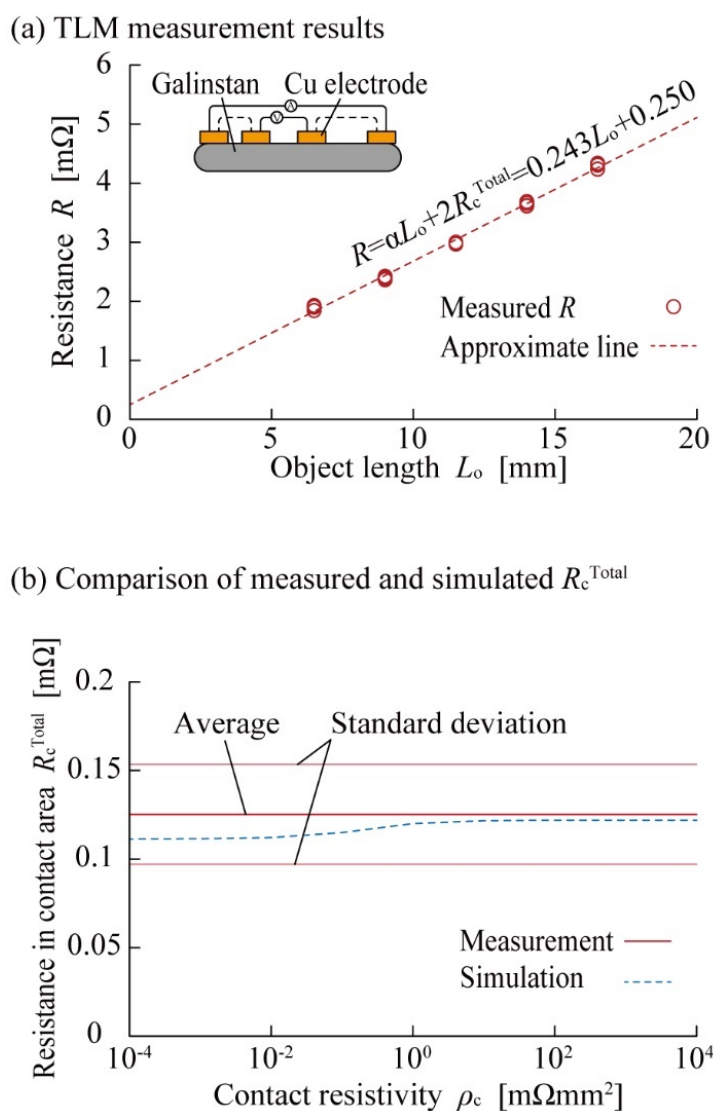


Figure 3.17 Measurement results for current application to the outer electrodes. (a) Relationship between  $L_o$  and  $R$  ( $N = 200$ ). (b) Relationship between  $\rho_c$  and resistance in the contact area ( $R_c^{\text{Total}} = (R - R_o)/2$ ).  $R_c^{\text{Total}}$  is given as Y-intercept/2 in the TLM measurement results. The  $R_c^{\text{Total}}$  for  $\rho_c$  was simulated via the FEM. The measured and simulated  $R_c^{\text{Total}}$  did not intersect, and  $\rho_c$  could not be obtained.

mΩ (min: 0.060 mΩ, max: 0.370 mΩ). These results indicate that  $R_c^{\text{Total}}$  is not equal to  $R_c$  even when a current is applied to each electrode. Therefore,  $R_c$  must be obtained via the intersection of the measured and simulated  $R_c^{\text{Total}}$  to achieve high accuracy. Figure 3.20 illustrates the simulated relationship between

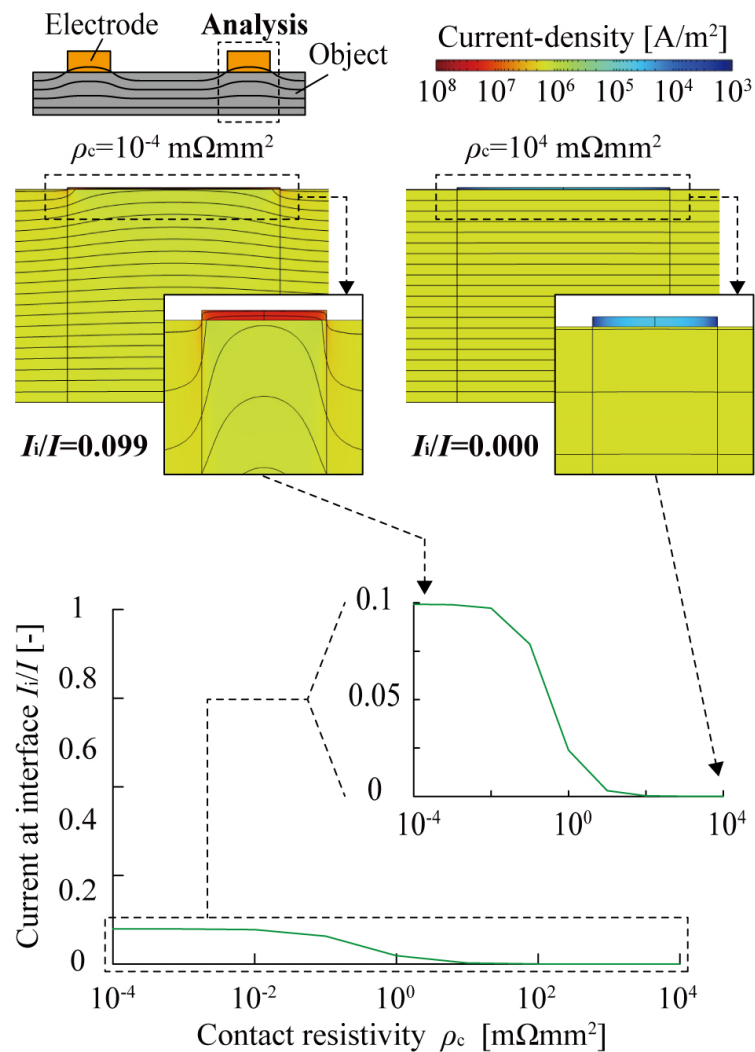


Figure 3.18 Simulation results for the current-density distribution and  $I_i/I$  for  $\rho_c$ .  $I_i/I$  was  $<0.1$ . Current was applied to the outer electrodes.

$I_i/I$  and  $\rho_c$ .  $I$  was equal to  $I$  regardless of  $\rho_c$ . This result indicates that  $I_i$  being equal to  $I$  increased the slope of the simulated curve of  $R_c^{\text{Total}}$  in Figure 3.19(b) compared with that in Figure 3.17(b), as well as the accuracy. Overall, it can be observed that the simulated values are significantly altered when  $\rho_c$  is varied because the entire applied current passes through the interface. Hence, the measured and simulated values intersected, and  $R_c$  can be measured. The  $R_c$  measurement of LMs is typically utilized to compare the  $\rho_c$  values of LMs with those of conventional EIMs. Solders exhibit the lowest  $\rho_c$  ( $>10^{-1}$  m $\Omega\text{mm}^2$ ) among conventional EIMs. The  $\rho_c$  of galinstan was 0.115 m $\Omega\text{mm}^2$  and the maximum  $\rho_c$  error was 0.085 m $\Omega\text{mm}^2$ .

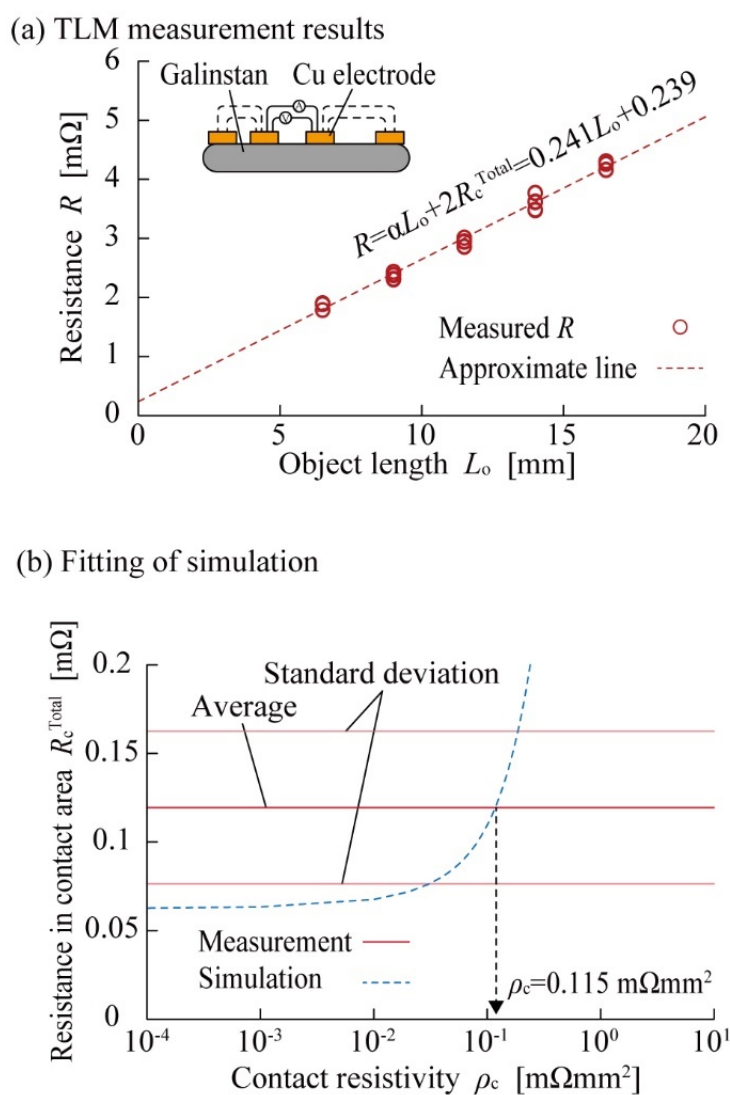


Figure 3.19 Measurement results for current application to each measuring electrode. (a) Relationship between  $L_o$  and  $R$  ( $N = 200$ ). Current was applied to each electrode. (b) Relationship between  $\rho_c$  and  $R_c^{\text{Total}} = (R - R_o)/2$ .  $R_c^{\text{Total}}$  is given as Y-intercept/2 in the TLM measurement results. The  $R_c^{\text{Total}}$  for  $\rho_c$  was simulated via the FEM. The  $\rho_c$  at the intersection of the measured and simulated  $R_c^{\text{Total}}$  was  $0.115 \text{ m}\Omega\text{mm}^2$  (min:  $0.030 \text{ m}\Omega\text{mm}^2$ , max:  $0.185 \text{ m}\Omega\text{mm}^2$ ).

The obtained  $\rho_c$  value was of the same magnitude as the solders.  $\rho_c$  close to that of the solders can be measured under the magnitude of the errors in the proposed method. Therefore, the proposed method is practical.

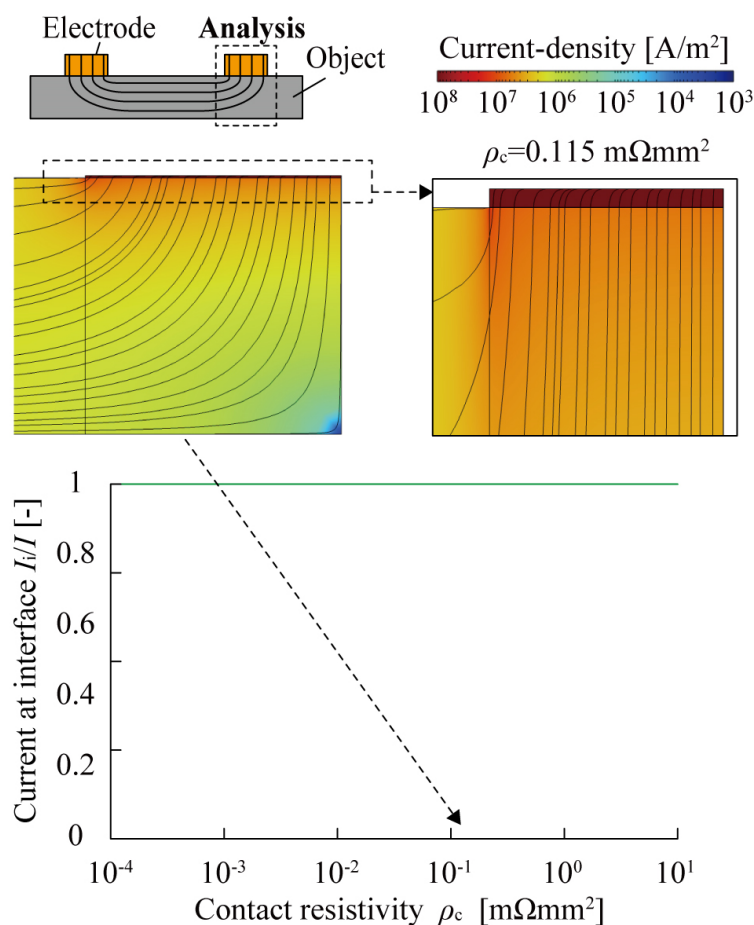


Figure 3.20 Simulation results for the current-density distribution and  $I_i/I$  for  $\rho_c$ .  $I_i$  was equal to  $I$  for all  $\rho_c$  values. Current was applied to each measurement electrodes.

### 3.4 Conclusions

This study investigated a measurement configuration for highly accurate measurement of the  $R_c$  between gallium-based LMs and SMs via TLM. First, the effect of  $R_e$  on TLM measurement was evaluated. From TLM measurement results for the connection of measurement terminals, it was determined that  $R_e$  cannot be ignored for the TLM measurement of LMs and SMs because  $R_e$  was higher than  $R_c$  by more than two orders of magnitude. It was also demonstrated that  $R$  could be measured without including  $R_e$  by the two-sided connection. In addition, it was inferred that  $R$  could be measured without including  $R_e$  by the two-sided connection. Furthermore, it was confirmed that  $R_c$  error can be reduced by measuring without unused

electrodes. Furthermore, this study investigated the measurement configurations of LMs and SMs. From the TLM measurement results for the configurations, it was determined that the  $R_c$  for the configuration of SM wiring and LM electrodes was six times higher than that of the LM wiring and SM electrodes.

The current-density distribution in the TLM measurement of galinstan was analyzed via FEM simulations, and a method for applying current to each measuring electrode for accurate resistance measurements was developed. The ratio of the current passing through the interface between the electrode and the object  $I_i/I$  was simulated for different values of  $R_{sho}/R_{she}$  and  $\rho_c/R_{she}$ . When current was applied to the outer electrodes,  $I_i$  was equal to  $I$  for conventional objects (Si, graphene, conductive adhesive:  $> 10^2 \Omega\Box$ ) for all the tested values of  $\rho_c/R_{she}$ , and the assumption in the conventional TLM was valid. However, it was inferred that  $I_i/I$  was  $< 10^{-1}$  for LMs ( $R_{sho} = 10^{-2}$  to  $10^0 \Omega\Box$ ) for all the  $\rho_c/R_{she}$  values, and the conventional assumption was invalid. In contrast, when current was applied to each electrode,  $I_i$  was equal to  $I$ , regardless of  $R_{sho}/R_{she}$  and  $\rho_c/R_{she}$ . Therefore, to ensure high accuracy, the current should be applied to each electrode because  $I_i$  is equal to  $I$  and the entire  $R_c$  component is included in  $R_c^{Total}$  regardless of  $R_{sho}/R_{she}$  and  $\rho_c/R_{she}$ . Furthermore,  $\rho_c$  was obtained by comparing the measured and simulated  $R_c^{Total}$  values. When current was applied to the outer electrodes, the measured  $R_c^{Total}$  was  $0.125 \pm 0.056 \text{ m}\Omega$ , and the simulated  $R_c^{Total}$  ranged from 0.111 to 0.122 m $\Omega$  for  $\rho_c$  values of  $10^{-4}$ – $10^4 \text{ m}\Omega\text{mm}$ . The measured and simulated  $R_c^{Total}$  did not intersect, and  $\rho_c$  could not be obtained. In contrast, when the current was applied to each electrode, the measured  $R_c^{Total}$  was  $0.120 \pm 0.043 \text{ m}\Omega$ , and the simulated  $R_c^{Total}$  ranged from 0.063 to 9.823 m $\Omega$  for  $\rho_c$  values of  $10^{-4}$ – $10^1 \text{ m}\Omega\text{mm}^2$ . The obtained  $\rho_c$  and maximum error were 0.115 m $\Omega\text{mm}^2$  and 0.085 m $\Omega\text{mm}^2$ , respectively, which is sufficient for practical use compared with the  $\rho_c$  of the solders ( $> 10^{-1} \text{ m}\Omega\text{mm}^2$ ). This study can help discover suitable electrode materials for LMs and provide novel avenues for the development of stretchable electronics using LMs.

# Chapter 4      Stretch Tolerance of Electronic Component Mounting Using Liquid Metal

## 4.1      Introduction

---

### 4.1.1      Stretch Tolerance of Mounting Method Using Liquid Metal and Its Challenges

**Stretch tolerance of mounting area:** In Chapter 4, the stretch tolerance of electronic component mounting using an LM is demonstrated. The wiring around the electronic components broke owing to the stress concentration caused by the difference in stiffness and strain in the stretchable electronic devices with rigid high-performance electronic components mounted on stretchable metal wiring. Stretchable connections between the components and wiring are critical for relieving stress concentration. In this study, a mounting method using LMs was proposed for achieving high stretch tolerance as shown in Figure 4.1. Ga-based LMs can provide high stretch tolerance as EIMs themselves, as they are liquid at room temperature. Furthermore, LM as an EIM can improve the stretch tolerance of stretchable wiring by reducing the difference in stiffness and strain on the wiring. Conventional EIMs, such as solders and conductive pastes, fix wiring under the components. Thus, there are differences in stiffness and strain in

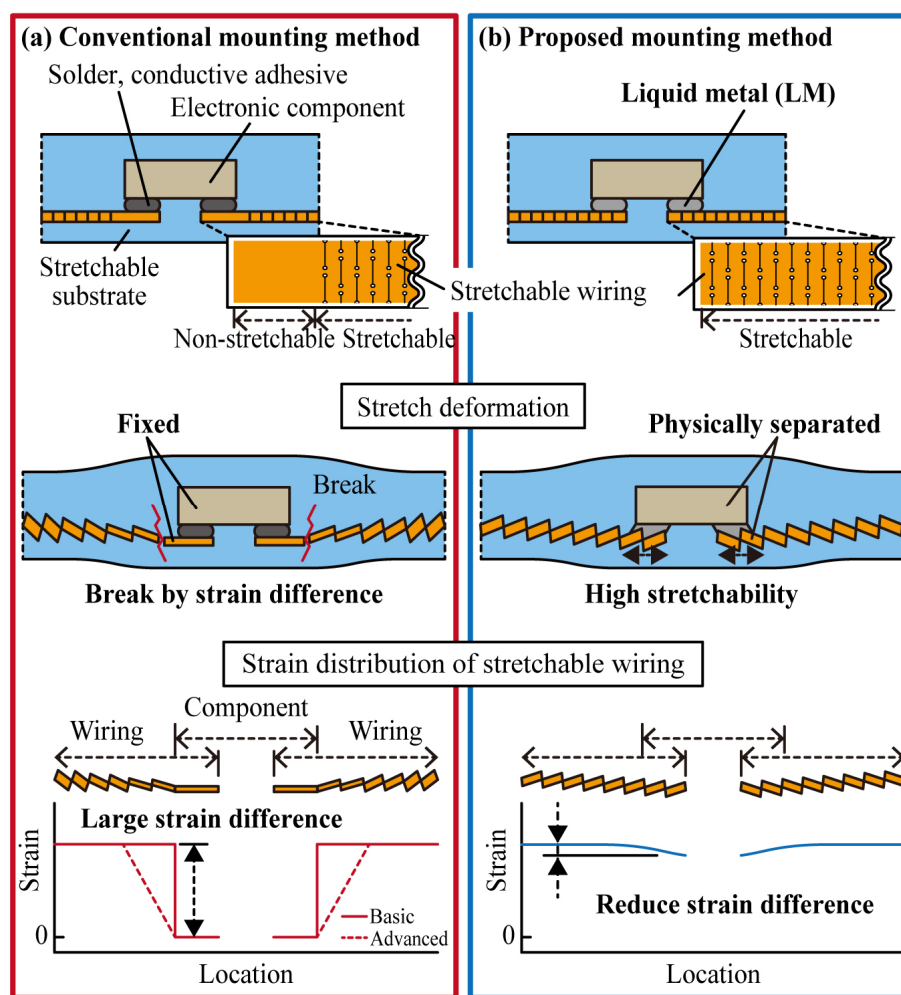


Figure 4.1 Schematic illustrating the effect of EIM stretchability on the stretch tolerance of stretchable wiring. (a) Under stretching deformation, rigid EIMs trigger strain differences in stretchable wiring because the connection area of wiring fixed by rigid EIM cannot stretch. (b) Stretchable EIMs, such as LMs, reduce strain differences on stretchable wiring and increase its stretch tolerance as connection area of wiring can stretch.

the wiring, and the wiring cannot achieve a high stretch tolerance. In contrast, the LM does not physically fix the components and wiring, but only electrically connects them. Thus, the wiring under the component can stretch when the component was mounted on the wiring with stretchable structure on the pads area of the wiring using LM. It was assumed that differences in stiffness and strain within the wiring would be eliminated, and that highly stretchable wiring tolerance would be achieved.

**Challenges in stretch tolerance:** Ga-based LMs have high surface tension and tend to form oxide layers on their surface. Thus, even if the LM itself has high stretchability (>500% stretch), the stretch tolerance may be lower than expected owing to delamination between components or wiring and the LM. Previously, the stretchability of the LM itself was evaluated for stretchable wiring, sensors, and antennas using the LM. However, when LMs are in contact with solid-state components such as electronic components or wiring, delamination between the LMs and the components or wiring may also affect the stretch tolerance; however, the stretch tolerance in such cases has not been investigated. In addition, there is a concern that the stretch tolerance of the wiring itself may be affected by differences in stiffness and strain at the ends of the wiring. However, the stretch tolerance of the wiring itself for the wiring end structures has not been investigated in detail. Furthermore, when SMDs are mounted on stretched wiring, the effect of the stretchability of the EIM on the stretch tolerance of the wiring is not clear. Additionally, the presence of rigid electronic components on the wiring may affect the strain distribution in the wiring during stretching. There is also a concern that the fabrication of a stretchable structure on the pad areas of wiring might increase the  $R_c$ , resulting in a trade-off between stretch tolerance and electrical performance.

#### 4.1.2 Objective and Contents for Demonstration of Stretch Tolerance

**Objective:** The objective of Chapter 4 is to evaluate the stretch tolerance of electronic component mounting using LMs, and to demonstrate the high stretchability of stretchable electronic devices by the mounting method using LMs. Thus, four contents were studied: 1) stretch tolerance of LM as an EIM itself, 2) stretch tolerance of stretchable wiring itself, 3) stretch tolerance of stretchable wiring with components mounted using LM, and 4) stretchability and performance of stretchable electronic devices fabricated using the proposed method.

**1) Stretch tolerance of LM as an EIM:** The stretch tolerance of the EIM itself was compared. In the sample, the chip resistors were mounted on non-stretchable metal wiring using an EIM and sealed with an elastomer. LM, paste solder, and flexible conductive adhesives were used as EIMs. In the tensile tests, the average stress, that is, the load divided by the cross-sectional area, and the sample resistance were measured to determine the strain in the mounting area. The breaking strain and hysteresis of the samples were analyzed based on the measurement results. In addition, the broken areas were observed and analyzed to investigate the effects of delamination at the interface between the EIM and the components or wiring and breakage within the components, wiring, or EIMs.

**2) Stretch tolerance of stretchable wiring:** The stretching tolerance of wiring to the end structures



of the wiring was evaluated. In the samples, stretchable metal wiring with a kirigami structure as a stretchable structure was embedded in an elastomer substrate. As wiring end structures, the separation of the wiring ends from the substrate for gripping and the fabrication of the stretchable structure to the pad areas of the wiring were studied. The average stress against the wiring strain was measured in the tensile test. The breaking strain and hysteresis of the samples were evaluated based on the measurement results. The strain distribution in the wiring was analyzed from the optical images of the wiring to evaluate the breaking locations.

**3) Stretch tolerance of stretchable wiring with components mounted using LM:** Stretch tolerance of the wiring with chip resistors mounted using the qn EIM was evaluated. In the sample, the SMD was mounted using an EIM on stretchable metal wiring with a kirigami structure and encapsulated with an elastomer substrate. The effect of the stretchable structure fabricated on the pad areas of the wiring on the stretch tolerance of the wiring was investigated. The average stress and sample resistance for the wiring strain were measured in the tensile test. The breaking strain and hysteresis of the samples were analyzed based on the measurement results. The strain distribution of the wiring was analyzed from optical images of the stretchable wiring to evaluate the breaking strain.

**4) Stretchability and performance of stretchable electronic devices:** The stretchability and performance of stretchable electronic devices with SMDs mounted on stretchable wiring using LMs were demonstrated. Chip LEDs and resistors were arrayed on stretchable metal wiring with a kirigami structure using LM, and the samples were sealed with elastomers. The change in the device resistance for the device strain was measured in the tensile test of the device with chip resistors. In the tensile test of the device with chip LEDs, the lighting of the LEDs was demonstrated under device strain.

## 4.2 Stretch Tolerance of Liquid Metals as EIMs

---

### 4.2.1 Methods

Figure 4.2 presents schematics and optical images of the device used to evaluate the stretch tolerance of the LM adopted as an EIM. Table 4.1-4-5 present the materials used in the samples. The surface-mounted component devices were mounted on non-stretchable metal wiring using LMs and embedded in an elastomeric substrate. Galinstan was selected because it has the lowest melting point among Ga-based LMs. A Cu thin-film rolled substrate (Nilaco, Tokyo, Japan)[184] was used for metal wiring. When

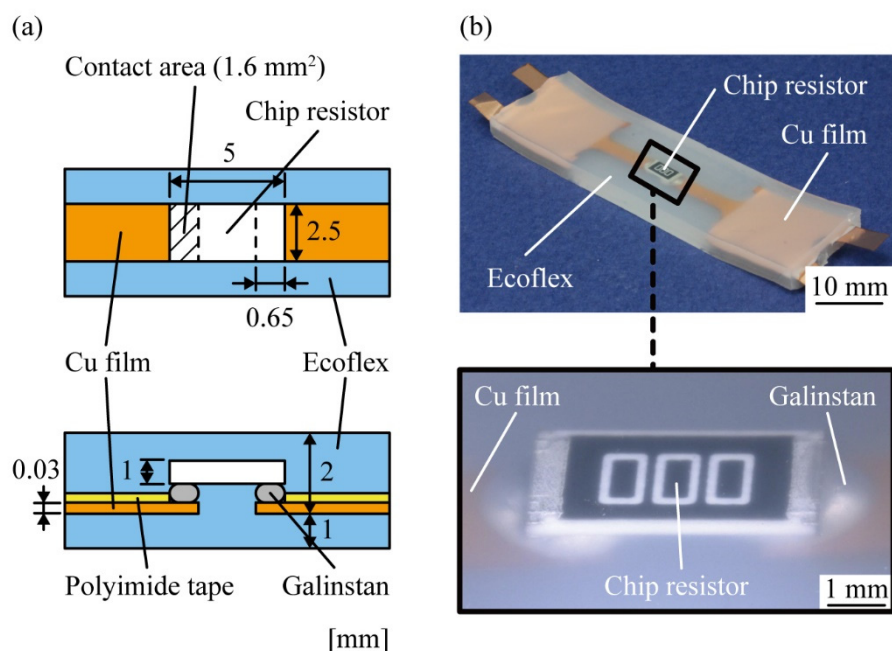


Figure 4.2 Measurement devices for mounting a chip resistor using galinstan for tensile test. (a) Schematics and (b) optical images of the devices.

evaluating the stretch tolerance of the EIM in this section, only the EIM should be deformed without breaking owing to the high tensile stiffness of the wiring section. A copper single-layer substrate with high tensile stiffness was utilized because high tensile loads are expected in tensile tests of samples with components mounted between non-stretchable wirings by solders or conductive adhesive. The thickness adopted is 0.03 mm, which is the wiring thickness typically utilized in conventional non-stretch electronic devices. Silicone rubber (Ecoflex 00-30, Smooth-On, PA, US)[185], one of the most stretchable elastomer materials, was employed as the elastomer substrate. Jumper chip resistors (RK73ZW2HTTE, KOA, Nagano, Japan) were utilized as the SMD. Jumper resistors with resistance  $<50\text{m}\Omega$  were adopted as the SMD elements to reduce the effect on device resistance and improve the accuracy of resistance change measurement via EIM. The electrode surface was then coated with tin. For comparison, the samples were mounted with paste solder (SMX-H05A, Sunhayato, Tokyo, Japan)[186], which required heating at  $200^\circ\text{C}$ , and a flexible conductive adhesive (CN-7120, Kaken Tec., Osaka, Japan)[187] cured at room temperature was also fabricated. This conductive paste was chosen because it can be cured at  $25^\circ\text{C}$  and because the binder resin is a thermoplastic resin with stretchability. The volume resistivity was approximately the same

Table 4.1 Properties of Cu wiring used for samples.

Properties	Cu wiring (Cu single layer)	Ref. No.
Purchase	Nilaco, Tokyo, Japan	[184]
Thickness	Cu:30 $\mu$ m	[184]
Conductivity	$5.96 \times 10^7$ S/m (at 20°C)	[3]
Fabrication	Rolling	[184]
Surface roughness	Ra < 1 $\mu$ m	[166]
Young's modulus	Cu: 130 GPa	[143]

Table 4.2 Properties of silicone rubber used for samples.

Properties	Silicone rubber (Ecoflex)	Ref. No.
Purchase	Ecoflex 00-30, Smooth-On, PA, US	[185]
Material	Silicone rubber	[185]
Young's modulus	1.3 MPa	[185]
Curing	4 h (at 25°C)	[185]

Table 4.3 Properties of chip resistor used for samples.

Properties	Chip resistor (MCR10)	Ref. No.
Purchase	MCR10EZPJ000, Rohm, Kyoto, Japan	[188]
Type	Thick film resistors	[188]
Resistance	<50 m $\Omega$	[188]
Chip dimensions	Length 2 mm, Width 1.25 mm, Thickness 0.55 mm	[188]
Electrode dimensions	Length 0.40 mm, Width 1.25 mm	[188]

as that of the other cured conductive pastes ( $5 \times 10^{-6} \Omega\text{m}$ ). The volume resistivity of galinstan is  $2.9 \times 10^{-7} \Omega\text{m}$ . The chip resistor was 1-mm thick, 5-mm long, and 2.5-mm wide; the electrodes were coated with Sn and were 0.65-mm long and 2.5-mm wide; the Cu thin film wiring was 0.03-mm thick and 2.5-mm wide, and the distance between the wiring was 2.5 mm. Curvature radius of 2 mm was introduced to prevent breakage due to stress concentration at the corners of the wiring roots during tension. The surfaces of the Cu thin film other than the contact area were covered with polyimide tape, and the contact area between the galinstan and Cu thin film was 1.6 mm<sup>2</sup> (hatching area in Figure 4.2). The injection volume

Table 4.4 Properties of solder used for sample.

Properties	Solder paste	Ref. No.
Purchase	SMX-H05A, Sunhayato, Tokyo, Japan	[186]
Composition	Sn: 63% and Pb: 37%	[186]
Melting point	183°C	[186]
Grain diameter	20-38 $\mu\text{m}$	[186]

Table 4.5 Properties of conductive adhesive used for samples.

Properties	Conductive adhesive	Ref. No.
Purchase	CN-7120, Kaken Tech, Osaka, Japan	[187]
Binder type	Thermoplastic resin	[187]
Conductivity	$5 \times 10^{-4} \Omega \text{ cm}$	[187]
Viscosity	27 Pa S	[187]
Curing	60 min (at 25°C) or 5 min (at 60°C)	[187]

of galinstan was 8  $\mu\text{L}$ , and the width and thickness of the silicone rubber were 2 and 3 mm, respectively.

Figure 4.3 illustrates the device fabrication procedure. First, a Cu substrate fixed on a weak adhesive sheet was cut using a UV laser-cutting machine. The conditions for laser cutting are presented in Appendix A. Because the surface of the elastomer substrate has adhesive properties, the Cu substrate was transferred onto the substrate. In addition, because the adhesive strength of the elastomer substrate was not significantly high, the adhesive strength of the weak adhesive tape was adjusted to be lower than that of the elastomer substrate for the transfer. The surface of the weak adhesive tape was roughened using a UV laser to reduce the adhesive strength. Next, the Cu substrate was transferred onto a 0.5-mm-thick elastomer substrate placed at the bottom of the mold. After the transfer, unnecessary parts other than wiring were discarded from the Cu substrate, and the Cu surface was fluxed to remove the oxide layer. Dispensers were utilized to place galinstan in the connected area of the wiring. A chip resistor was mounted on the LM. After the transfer, unnecessary parts other than wiring were removed from the Cu substrate, and the Cu surface was fluxed to eliminate the oxide layer. Galinstan was placed on the wiring connected area of wiring using a micropipette (P20, Gilson, WI). A chip resistor was mounted on the LM. For comparison, the paste solder was stencil-printed on a 1 mm  $\times$  2.5mm area connected to the wiring area using a mask. A simple stencil mask was fabricated by cutting a 0.5-mm thick PET substrate using a UV laser-cutting

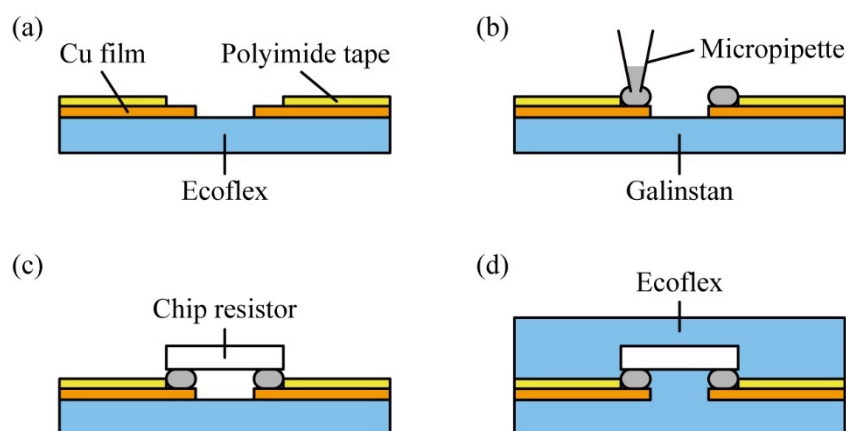


Figure 4.3 Fabrication processes of the device for tensile test. (a) Cu film interconnects were placed on an Ecoflex sheet. (b) Galinstan was placed on the Cu film interconnects using micro pipette. (c) Chip resistor was placed on galinstan. (d) Device was sealed with Ecoflex.

machine. The stencil mask was then heated at 200°C for 1 min to melt and then cured. In the sample mounted using the conductive adhesive, the conductive adhesive was stencil-printed on both ends of the wiring. The sample was left for 1 h to cure and obtain the conductivity. For each sample, the uncured elastomer was poured into a mold, and the mold was sealed with a lid to maintain a constant thickness. Details of the fabrication procedure for mixing and curing the elastomer are provided in the Appendix A. The elastomer substrate was mixed 1:1 with Liquids A and B, mixed in a mixer (ARE-310, Thinkey, Tokyo, Japan), depressurized to -0.09 MPa in a vacuum desiccator (VE-ALL, As One, Osaka, Japan) for 10 min, cured in an oven at 60°C for 1 h, and then cut from the mold.

Figure 4.4 presents a schematic of the measurement method. The sample was fixed on a motorized stage (FSA-0.5K2, IMADA, Aichi, Japan) and the tensile load was measured using a force gauge (ZTS-5N, IMADA, Aichi, Japan) while applying displacement in the extension direction. The elastomer substrate was fixed using a roll chuck because its thickness decreased during extension. The resistance of the sample was measured using a source meter (2614 B, Keithley, OH, US) with a four-terminal method to evaluate electrical stability and detect breakage. The EIM displacement was considered equal to the device displacement and the EIM strain was calculated by dividing the device displacement by the electrode length of the chip resistor (1.3 mm). The measurement commenced with the sample slackened slightly, and the load was reset to zero. The zero point was set when the load measured by the force gauge became larger than zero as the stage displacement increased. To synchronize the start time of the resistance

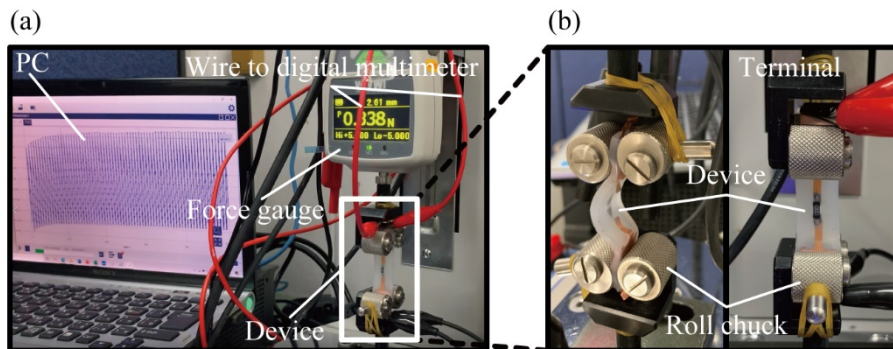


Figure 4.4 Experimental setup for tensile test.

measurement by the source meter and the load measurement by the force gauge, the control software for each was displayed on the computer and started simultaneously. The stage movement speed was maintained constant at  $10 \text{ mm/min} = 0.16 \text{ mm/s}$ , sufficiently slow compared to the measurement speed of the force gauge (10 fps) and the measurement speed of the source meter (2 fps) to reduce the accuracy loss due to the delay in the analysis start time and measurement speed of the measurement devices. First, the sample was pulled to measure the load and resistance to the strain. The increase in the resistance was utilized to detect a break, and the break strain of the EIM was determined from the stage displacement at that time. The resistance was measured via repeated stretching at a strain lower than the breaking strain. The stage speed was  $80 \text{ mm/min}$  for cyclic tests. The loading and unloading cycles were repeated continuously without stopping. Within one cycle,  $R_{\max}$  and  $R_{\min}$  were measured as a function of the number of cycles, where  $R_{\max}$  and  $R_{\min}$  denote the resistance at the maximum strain and 0% strain, respectively. To investigate the effect of aging on the stretching tolerance and resistance of LM as an EIM, samples were tensile tested 130 days after mounting to evaluate the initial resistance, the change in resistance to strain, and the change in resistance to repeated stretching. Detailed settings are presented in the Appendix B.

#### 4.2.2 Results and Discussion

Next, the electrical stability of the LM adopted as an EIM during stretching was evaluated. Figure 4.5 compares the resistance knowledge at 0% strain for the EIM types. Figure 4.5 illustrates the relationship between the strain and sample resistance with galinstan, solder, and conductive paste on Days 1 and 130. The strain was obtained from the length of the chip resistor electrode (1.3 mm). Under zero strain, the sample resistances with galinstan, solder, and conductive paste were 22.3, 19.4, and 677 mΩ, respectively,

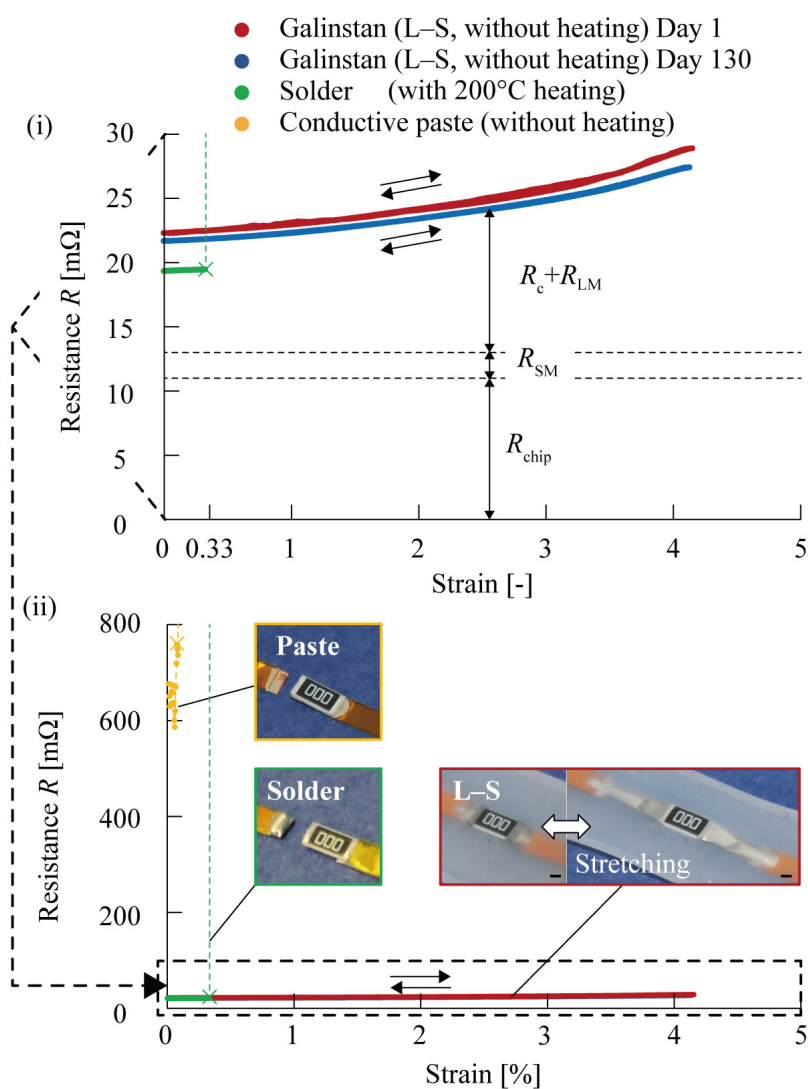


Figure 4.5 Relationship between strain and sample resistance on Days 1 and 130. Stretching speed was 10 mm/min. Insets present optical images of a sample during stretching deformation, and scale bars show 1 mm ( $N = 3$ ).

on Day 1 (Figure 4.5a-ii). This result indicates that galinstan can achieve low resistance, which is of the same order as that of the solder and is 96.7% lower than that of the conductive paste. The resistance in galinstan decreased by 2.8% on Day 130, approaching the resistance of the solder. Note that the degree of the decrease was smaller than that presented in Figure 4.5, owing to the resistance of the Cu film  $R_{SM}$  (2 m $\Omega$ ), chip resistor  $R_{chip}$  (11 m $\Omega$ ), and galinstan  $R_{LM}$  included in the measured resistance value (Figure

4.5(a-i)). In a complex circuit with multiple electronic components, the contribution of the  $R_c$  to the sample resistance is larger than that of a circuit consisting only of galinstan, Cu electrodes, and a chip resistor.

Figure 4.5 illustrates the relationship between the wiring strain and sample resistance for solder, conductive adhesive, and galinstan at Days 1 and 130 after mounting. For the sample mounted with solder, the sample resistance slightly increased from 19.4 m $\Omega$  to 19.5 m $\Omega$  as the wiring strain increased from 0% to 32.7%, resulting in a broken wire. For the sample mounted with conductive adhesive, the sample resistance increased from 677.4 m $\Omega$  to 736.6 m $\Omega$  and broke when the wiring strain increased from 0% to 7.3%. However, the sample resistance increased from 22.3 m $\Omega$  to 28.5 m $\Omega$  when the wiring strain was increased from 0% to 400% at Day 0 after mounting with the LM. The sample at Day 130 after mounting with LMs exhibited an increase in resistance from 21.7 m $\Omega$  to 27.4 m $\Omega$  as wiring strain increased from 0% to 400%, maintaining electrical connection at 400% strain.

Under stretching deformation, the sample with the solder and the conductive paste broke at the interface between the chip resistor and Cu film at 33% and 7.3% strains, respectively. Although the binder resin of the conductive paste possessed some stretchability, the conductive paste peeled off from the Cu film at a lower strain than in the case of the solder. In contrast, galinstan maintained an electrical connection up to 400% strain. The change ratios in the resistance at 100% strain were 2.9% and 4.0% on Days 1 and 130, respectively. The insets in Figure 4.5(a-ii) present the optical images of a sample during stretching deformation. The solder and conductive paste broke at the interface between the chip resistor and Cu films during the first stretching deformation. However, galinstan maintained an electrical connection between the chip resistor and the Cu films during stretching deformation on Days 1 and 130. This result indicates that galinstan can be utilized under a strain that is more than 1200% larger than the breaking strain of the solder and conductive paste. Overall, even when LM is placed between rigid electronic components and wiring as an EIM, the LM can be stretched by the deformation of the elastomeric substrate between the components and wiring, and it was determined that the LM exhibits high stretch tolerance as an EIM.

As illustrated in Figure 4.6, the factors for the resistance change during stretching were studied in the sample mounted with LMs. Possible factors include changes in the volume resistance of the LM and  $R_c$ . Assuming that the LM deforms uniformly in the tensile direction, the cross-sectional area of the LM is inversely proportional to its length in the tensile direction ( $L_{LM}$ ). Therefore, the resistance of the mounting area is a quadratic function of  $L$ , which is expressed as Equation (4.1).

$$R = AL_{LM}^2 + B \quad (4.1)$$



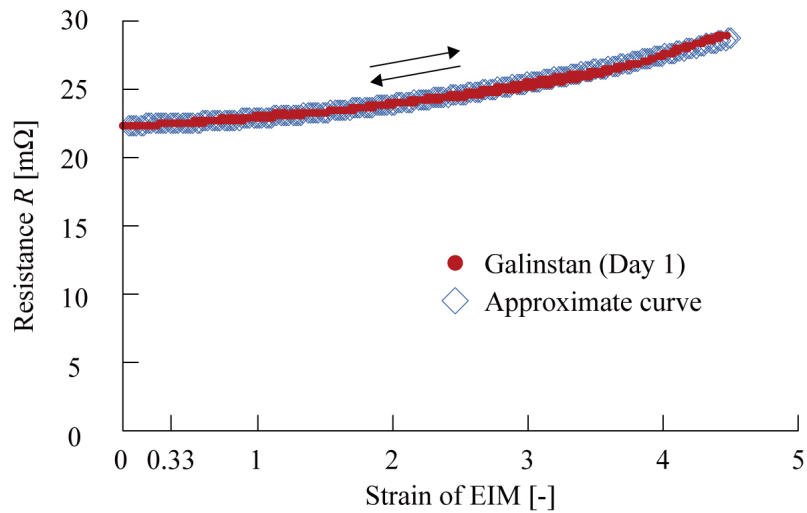


Figure 4.6 Relationship between strain and sample resistance for galinstan (Day 1) and approximate quadratic function curve.

Where A and B are the constants. A and B were obtained by fitting the quadratic function of  $L$  to the measured value of the sample resistance at Day 0 after mounting with the LM (Equation (4.2)).

$$R = 0.1740L_{LM}^2 + 22.318 \quad (4.2)$$

The coefficients of each order were obtained such that the standard deviation between the measured and estimated values was minimized. The standard deviation between the measured and estimated values was 0.147 mΩ, and the error was less than 0.66% compared with the measured value (>22.318 mΩ). Therefore, the change in resistance of the entire sample during stretching was primarily due to the change in the volume resistance caused by the stretching of the LM. The effects of interruption in the middle of the tension, separation of the electronic component, wiring from the EIM, and poor connections were almost negligible.

The EIM strain at the break point for each EIM type was compared in Figure 4.5. The solder and conductive adhesive tape broke at 32.7% and 7.3%, respectively. The solder exhibited a high adhesive strength owing to alloying with the Cu wiring and element electrode, and its Young's modulus was as high as 27.3 GPa; hence, the EC electrode peeled off from the component when stretched. In addition, because the adhesive was resin-based, it was more flexible than the solder. However, it was highly stretchable to the components and wiring; hence, it peeled off at the EIM and wiring interface during stretching. In

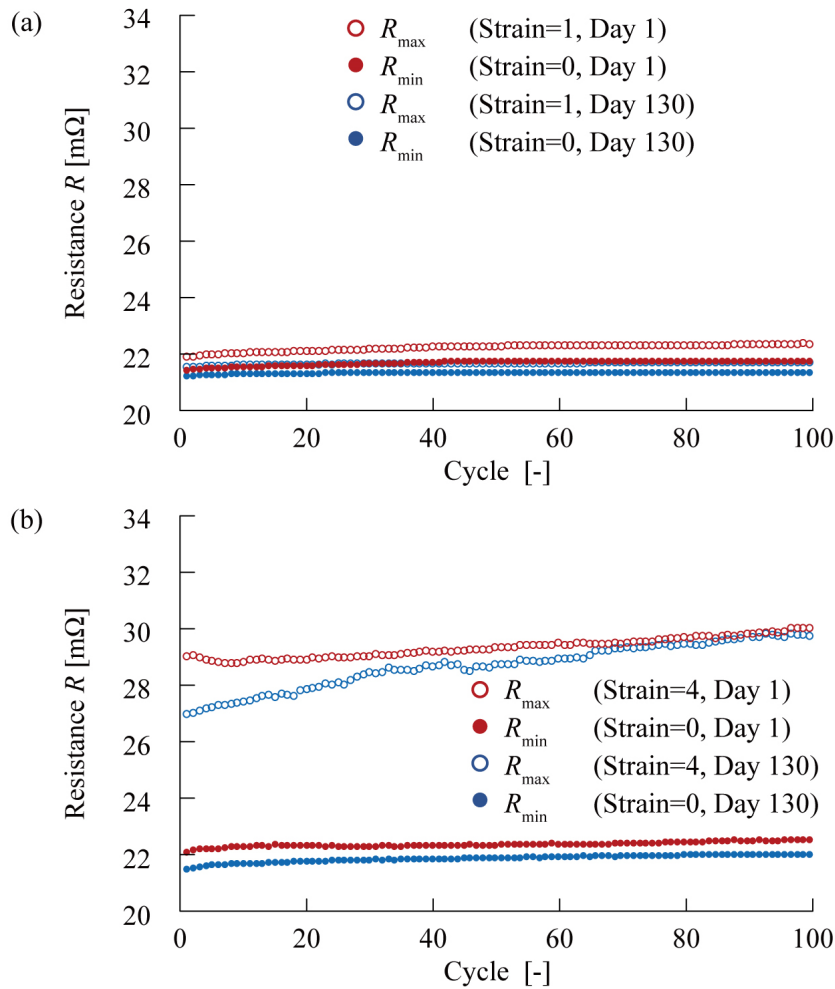


Figure 4.7 Relationship between the number of tensile cycles at maximum strain of 1 and 4 and the sample resistance on Days 1 and 130. Stretching speed was 20 mm/min ( $N=2$ ).

contrast, the LM mounting on Day 0 did not break even when stretched to 400%. This demonstrates that the LM mounting provides a highly stretchable tolerance that is 12 times higher than that of the conventional solder and adhesives. The graph also presents a sample stretched for 130 days after LM mounting. After 130 days of LM mounting, the sample did not break, even when stretched to 400%. This indicates that the LM maintains the same high level of stretching tolerance after 130 days immediately after mounting. As explained in the stiffness section of the LM sample, because the LM exhibits a stiffness of zero and the elastomer is the dominant deformation, the LM can be stretched to the breaking strain of the elastomer (500%).

Furthermore, the resistance  $R_{\max}$  at the maximum strain and  $R_{\min}$  at 0% strain of LM as the EIM were analyzed by the cyclic tensile test results on Days 0 and 130. As shown in Figure 4.7(a), after 100 stretching cycles on Day 1,  $R_{\min}$  increased by 1.6% from 21.4 m $\Omega$  to 21.8 m $\Omega$ , while  $R_{\max}$  increased by 2.2% from 21.9 m $\Omega$  to 22.4 m $\Omega$ . After 100 stretching cycles on Day 130,  $R_{\min}$  increased by 0.8% from 21.2 m $\Omega$  to 21.4 m $\Omega$ , while  $R_{\max}$  increased by 0.7% from 21.5 m $\Omega$  to 21.7 m $\Omega$ . These results indicate that the LM adopted as an EIM can be utilized with a resistance change of less than 2.2% even after stretching it 100 times at 100%, thus indicating that it has high stretch tolerance. As shown in Figure 4.7(b), after 400 stretching cycles on Day 1,  $R_{\min}$  increased by 2.0% from 22.1 m $\Omega$  to 22.5 m $\Omega$ , while  $R_{\max}$  increased by 3.5% from 29.1 m $\Omega$  to 30.0 m $\Omega$ . After 400 stretching cycles on Day 130,  $R_{\min}$  increased by 2.4% from 21.6 m $\Omega$  to 22.0 m $\Omega$ , while  $R_{\max}$  increased by 10.3% from 27.0 m $\Omega$  to 29.8 m $\Omega$ . These results indicate that LM as an EIM can be utilized with a resistance change of less than 10.3% even after stretching at 400% for 100 cycles, and that it has high stretch tolerance, although the resistance increase is slightly larger than that of 100% repeated stretching. The same level of stretch tolerance was maintained for 130 days. From the above, it was demonstrated that the galinstan mounting exhibits a high stretching tolerance that can be stretched repeatedly at more than 1200% of the breaking strain of the solder or conductive paste (400%). Overall, it was verified that the resistance value returns to the value before stretching when unloaded, and that the electrical performance is maintained even during repeated stretching because galinstan is liquid, its stiffness is zero, and the silicone rubber substrate is elastically deformed.

### 4.3 Stretch Tolerance of Wiring without Components

---

In Section 4.2, it was clarified that the LM as an EIM exhibits high stretchability. Therefore, by mounting components with LM, the wiring connected area can be stretched without being constrained by the EIM, which increases the strain in the wiring connected area and reduces the strain difference. Furthermore, the LM is highly stretchable owing to its liquid nature, and can continue to be stretched while the wiring is breaking. This implies that the wiring can be stretched to its maximum stretch tolerance. However, the effect on the strain distribution and stretch tolerance of wiring when connected area of wiring ends with LM as EIM remains unknown. The tensile stiffness of the LM is lower than that of the substrate. Therefore, if the tensile stiffness of the substrate is higher than that of the wiring, the deformation of the substrate will dominate the deformation of the wiring, and the connected area of wiring will experience a larger strain than the other areas, causing a strain difference at the boundary. The effect of the stretchable

structure in the connected area of wiring on the electrical connection is unknown. This may be a trade-off with stretch tolerance.

Hence, this section examines the wiring's stretch tolerance. In this section, stretchable metal wiring with a kirigami structure was utilized from the perspective of high stretchability and reliability. Stretchable wiring with a kirigami structure up to the connected area of wiring was encapsulated in an elastomer substrate. The wiring resistance and tensile load were measured against the strain in the wiring section by fixing and pulling the substrate outside the wiring. Stretch tolerance to repeated stretching was also measured. The wiring strain distribution was calculated from the amount of aperture in the kirigami structure and evaluated. Furthermore, the stretch tolerance of wiring to the connected area of wiring end was evaluated. First, the stretch tolerance of the fixed end and free end without electronic components were compared. At the fixed end, the wiring end is the connected area of wiring to the pad area for tension. At the free end, a cut is made between the wiring and the pad, and the two are connected by an LM, which are then sealed with elastomer. The effect of the presence or absence of a cutout in the connected area of wiring on the stretch tolerance of the wiring and on the electrical connection between the electronic component and wiring is also investigated. In addition, to investigate the effect of an electronic component on the wiring strain, the stretching tolerance was evaluated by altering the in-plane distance between the edge of the electronic component and wiring edge. Using paper-cut wiring optimized in the previous section in terms of stretch tolerance and electrical connection, samples connected between the electronic component and wiring area of wiring by LM were utilized to measure the load and sample resistance change in response to the wiring area of wiring strain. The change in sample resistance for repeated stretching deformation was also measured.

#### 4.3.1 Methods

A schematic of the stretch tolerance of wiring is presented in Figure 4.1 To improve the stretching tolerance of wiring by the wiring connection method, the stretching tolerance of the wiring itself without components should first be evaluated. The stretch tolerance of the wiring itself, which does not depend on the shape of the wiring ends or the fixing method, is considered to be the stretch tolerance under the condition of uniform strain and stiffness and uniform stress applied to the entire wiring. This stretch tolerance cannot be obtained with wiring where the connected area of wiring is rigid and does not stretch. In addition, when the connected area of wiring is fixed and stretched, the wiring strain in the fixed area becomes zero, making evaluation impossible. Hence, it is inferred that the original stretch tolerance of

wiring can be evaluated by adopting a test method in which the entire wiring, which has a kirigami structure up to the connected area and uniform tensile stiffness, is subjected to uniform strain. Almost all conventional stretching wiring has no stretchable structure in the connected area of wiring; hence, there is a difference in tensile stiffness within the wiring. In addition, although some studies have utilized the wiring as a stand-alone component, stretchable metal wiring is fragile. Therefore, in practical use, it is desirable to cover the wiring with an elastomer substrate, as electronic components are typically covered in general electronic devices. In this section, a stretchable structure is also provided in the connected area of wiring, and the wiring is embedded in the elastomer substrate. The substrate was held outside the wiring in the longitudinal direction and stretched to evaluate the breaking strain and tensile stiffness of the stretching wiring. Stretching tolerance was compared between the case in which the wiring connected area of wiring was fixed as before and the case in which the wiring and pads were separated. The effects of the presence or absence of a stretchable structure in the wiring connected area on the distribution of wiring strain, as well as the location of wiring breakage and wiring strain distribution under tension were investigated. The study verified whether uniform stiffness and uniform strain can be achieved by the wiring connection method.

Figure 4.8 presents a diagram and a photograph of the measurement device utilized to evaluate the stretch tolerance of stretchable metal wiring. Stretchable metal wiring with a kirigami structure was embedded in an elastomer substrate. The kirigami structure is a prevalent stretchable structure, in which the non-stretchable substrate is cut in alternating directions. When the tensile load is applied, each slit opens and the entire structure stretches. The kirigami structure exhibits high stretch tolerance and is easy to fabricate by cutting the substrate on a flat surface. Even if notches are made in the connected area of wiring, cutouts do not exist, making it easy to place LMs. Although it is difficult to place the LM on an elastomer substrate due to its high surface tension, it is easy to place LM on a metal electrode because it is relatively wettable against metal materials. The material employed for stretchable metal wiring is a two-layer substrate of Cu and polyimide (Metaroyal, Toray Advanced Materials Korea, Seoul, Korea), which is conventionally used as a flexible circuit substrate that can be bent. Cu is plated on the polyimide substrate. As in the previous section, silicone rubber (Ecoflex 00-30, Smooth-On, PA, US) with high stretchability was utilized as the elastomer substrate material, and the low-melting-point galinstan (Changsha Rich Nonferrous Metals, Hunan, China) was utilized as the LM. In the device, the stretchable copper wiring with a kirigami structure is 14-mm long and 2-mm wide; the wiring thickness is 0.008 mm for the Cu layer and 0.025 mm for the polyimide layer. The pads were 13-mm wide, and the distance

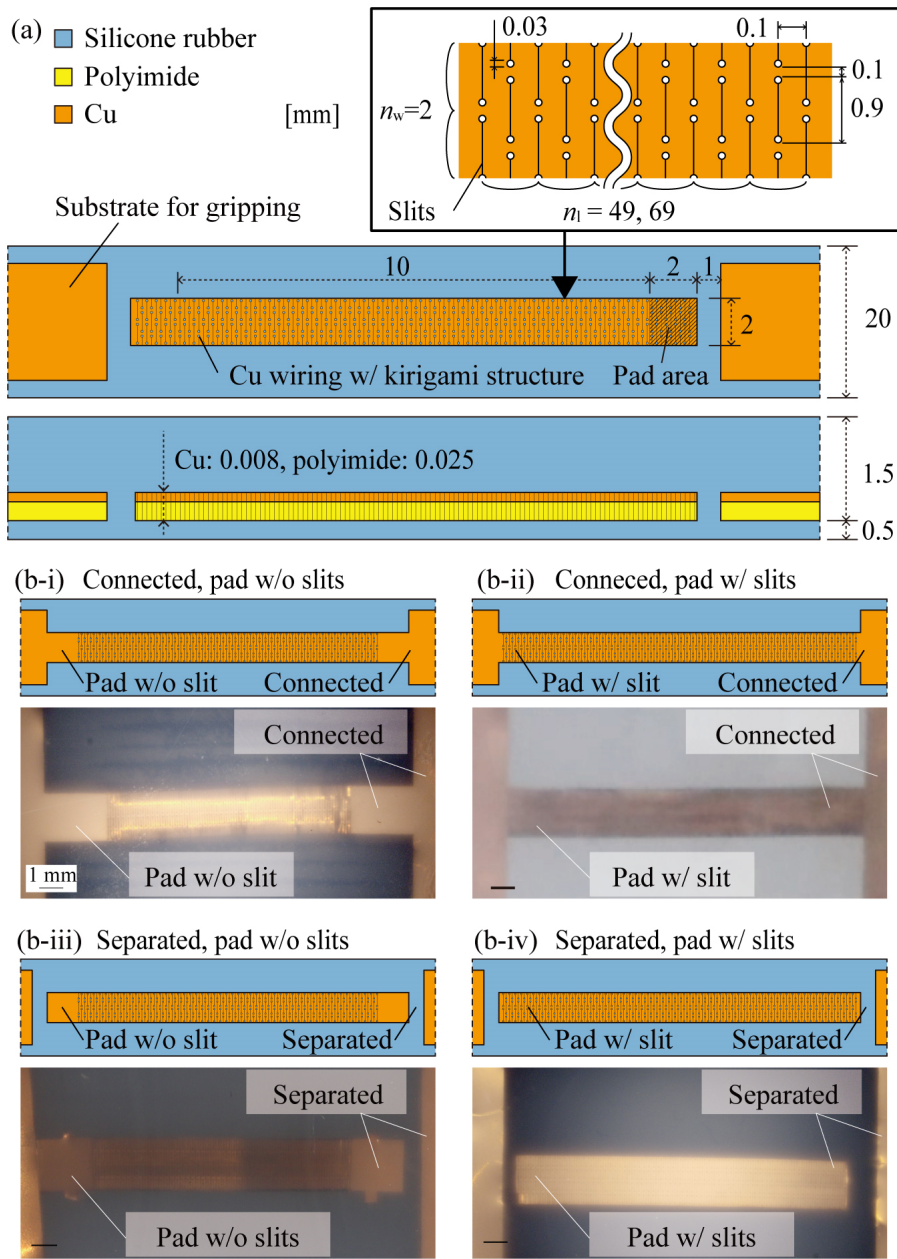


Figure 4.8 Tensile test samples in which stretchable Cu wiring ends were connected by different methods. (a) Schematics and (b) optical images of the sample.

between the pads and wiring was 1 mm. The elastomer substrate was 15-mm wide and 3-mm thick. Details of the kirigami pattern are presented in the inset. The objective of this study was not to improve the stretching tolerance of wiring by designing wiring patterns, but to investigate the effect of wiring connection methods on the stretching tolerance of existing wiring. Hence, the paper cut patterns follow

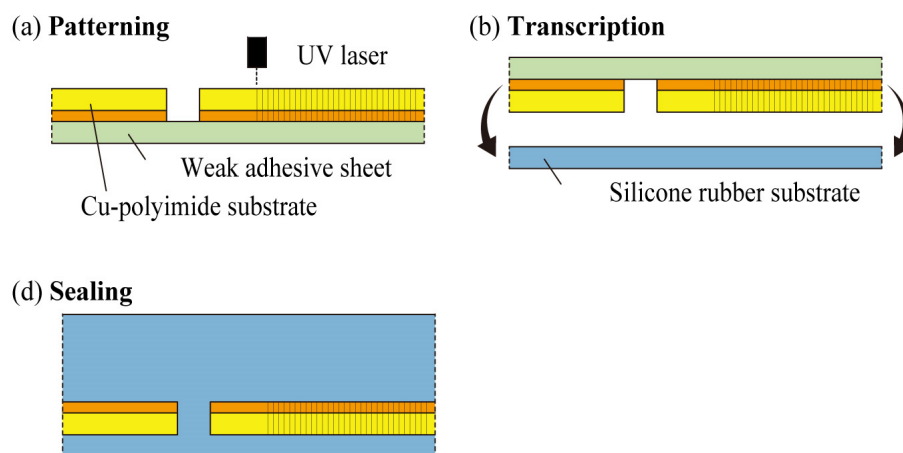


Figure 4.9 Fabrication processes of the sample for wiring tensile test. (a) Cu film was cut using UV laser cutter. (b) Cu film was placed on an Ecoflex sheet. (c) Sample was sealed with Ecoflex.

the previous studies. Among the conventional kirigami structures, a highly stretchable structure with a small cut pitch was utilized. The width of the cutout was 0.9 mm, the width of the leftover cutout was 0.01 mm, and the cutout spacing was 0.1 mm. The longitudinal period ( $n_L$ ) was set to  $n_L = 49$  for the pad areas without the kirigami structure and  $n_L = 69$  for the pad areas with the kirigami structure. Following previous studies, a circular hole with a 0.03-mm diameter was placed at the edge of the slit to alleviate the stress concentration at the edge of the slit when it was stretched. Figure 4.8 presents optical images of the stretchable metal wiring before encapsulation and the device after fabrication. As described in the previous section, the spot diameter of the UV laser cutting machine (OLMUV-355-5A-K, OPI, Saitama, Japan) was approximately 0.02 mm, and the width of the cut slit was also approximately 0.02 mm. The paper cut patterns were all neatly processed.

Figure 4.9 illustrates the device fabrication procedure. First, the outline of the Cu-polyimide substrate fixed on the weak adhesive sheet and kirigami structure were cut using a UV laser cutting machine. The conditions for laser cutting are presented in Appendix A. The surface of the weak adhesive tape was roughened via UV laser processing to reduce the adhesive strength. The Cu-Polyimide substrate was then transferred onto a 0.5 mm thick elastomer substrate placed on the bottom of the mold. After the transfer, unnecessary parts other than wiring and pads were removed from the Cu-polyimide substrate, the mold was filled with uncured elastomer, and then sealed with a lid to keep the thickness constant. Details of the fabrication procedure for mixing and curing the elastomer are provided in the Appendix A. The mold was heated in an oven at 60°C for 1 h to cure, and then cut out of the mold.

In the measurement, a sample prepared using a roll chuck was fixed to a motorized stage. A force gauge

was utilized to measure the load while applying displacement in the extension direction. The average stress ( $\sigma_{\text{average}}$ ) was calculated by dividing the tensile load by sample the cross-sectional area. The distance between the wiring and the pad changes during stretching in the free-end wiring; hence, the distance between the wiring ends is utilized as the wiring length instead of the distance between the chuck areas. The length of the connected area of wiring is also included. Hence, a single-lens reflex camera was utilized to capture videos and images of the sample during stretching, and the video and images were analyzed to obtain the wiring strain. The sample was left slightly slack and the load reset to 0. The measurement start point was set at the point when the load became larger than 0 as the displacement of the stage increased. To synchronize the video taken with the elapsed time of stage displacement and load measurement, the display of a force gauge showing stage displacement and load was placed in the angle of view of the camera, and the point at which the load became larger than 0 N was set as the start point of the video recording. The stage movement speed was maintained constant at 10 mm/min = 0.16 mm/s. In the measurement, the sample was stretched until rupture, and the tensile load against the strain was measured. The tensile stiffness of the sample was determined via the linear approximation of the relationship between strain and tensile load. The breaking strain of the wiring was obtained by analyzing the video. The strain distribution in the wiring was measured by taking an image of the sample being stretched and measuring the vertical projected distance between the middle points of the beams on either side of each slit in the wiring as the amount of aperture. When the amount of aperture was taken for all slits, the sum was equal to the wiring length. The aperture ratio was obtained by dividing the amount of each aperture by the amount of aperture when all slits were equally open. To evaluate the stretchability and electrical connection stability of the wiring with a kirigami structure in the wiring connection area, the wiring length was kept constant at 14 mm, and the length of the wiring connection area without a kirigami structure was varied from 2 mm to 0 mm to evaluate the load and aperture distribution relative to wiring strain. In addition, the sample resistance was measured by repeated stretching at a strain lower than the breaking strain. For cyclic tensile tests, the stage speed was 80 mm/min and the loading and unloading were repeated continuously without stopping. Detailed settings are presented in the Appendix B.

### 4.3.2 Results and Discussion

The relationships between sample strain and  $\sigma_{\text{average}}$  were compared for the different wiring end structures, as shown in Figure 4.10(a). Figure 4.11 shows the optical images of test samples with different



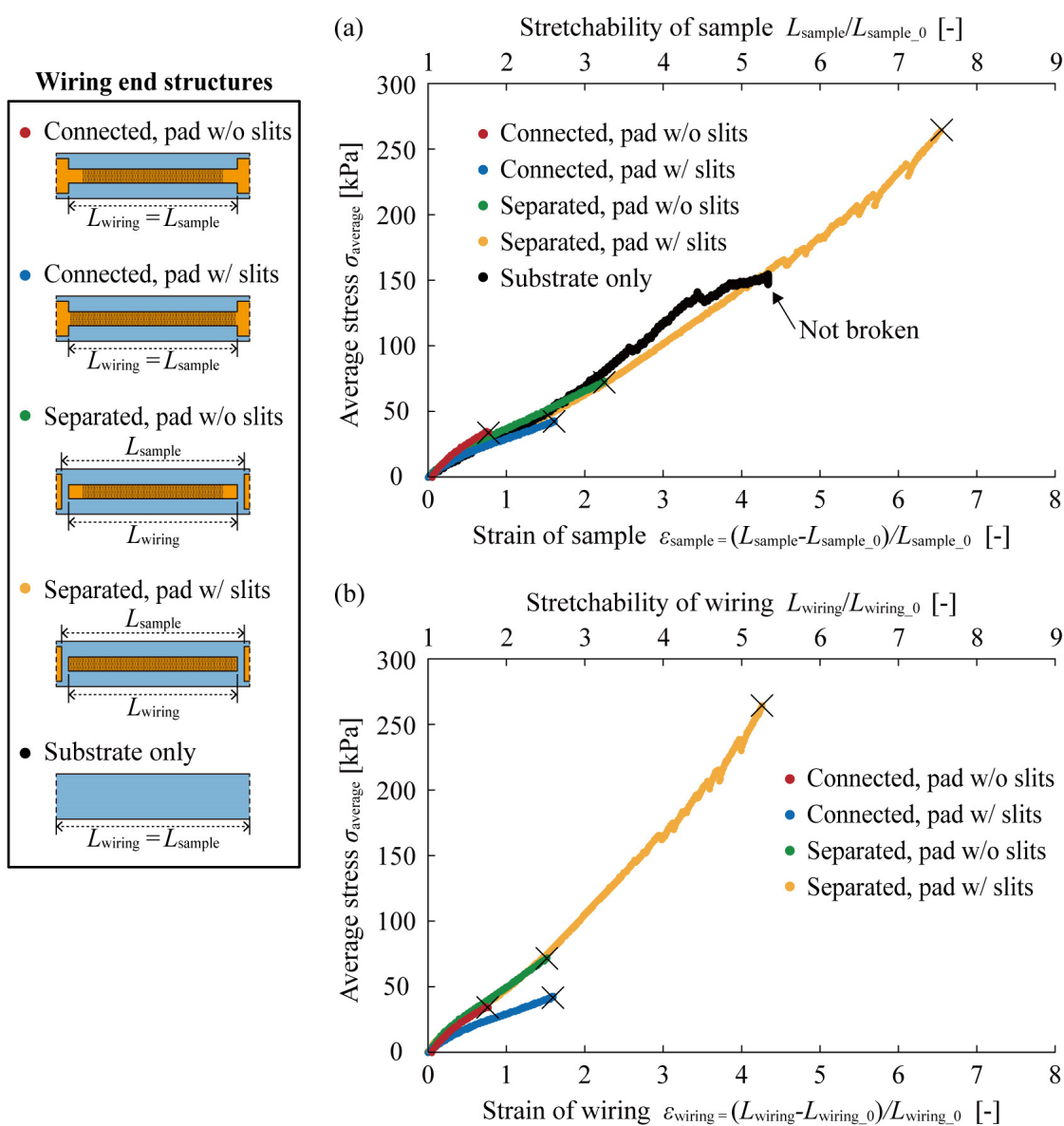


Figure 4.10 Tensile test results for fixed- and free-end wirings without component ( $N = 6$ ) (a) Relationship between (a) sample strain and average stress, (b) wiring strain and average stress.

wiring end structures before and after breakage. When the wiring strain was increased from 0 to 4,  $\sigma_{average}$  increased from 0 kPa to 148 kPa for the sample with elastomer substrate only. For the wiring connected to the gripping substrate, without the kirigami structure on its pads, the tensile load increased from 0 kPa to 32 kPa when the wiring strain was increased from 0 to 0.74. For the wiring connected to the gripping

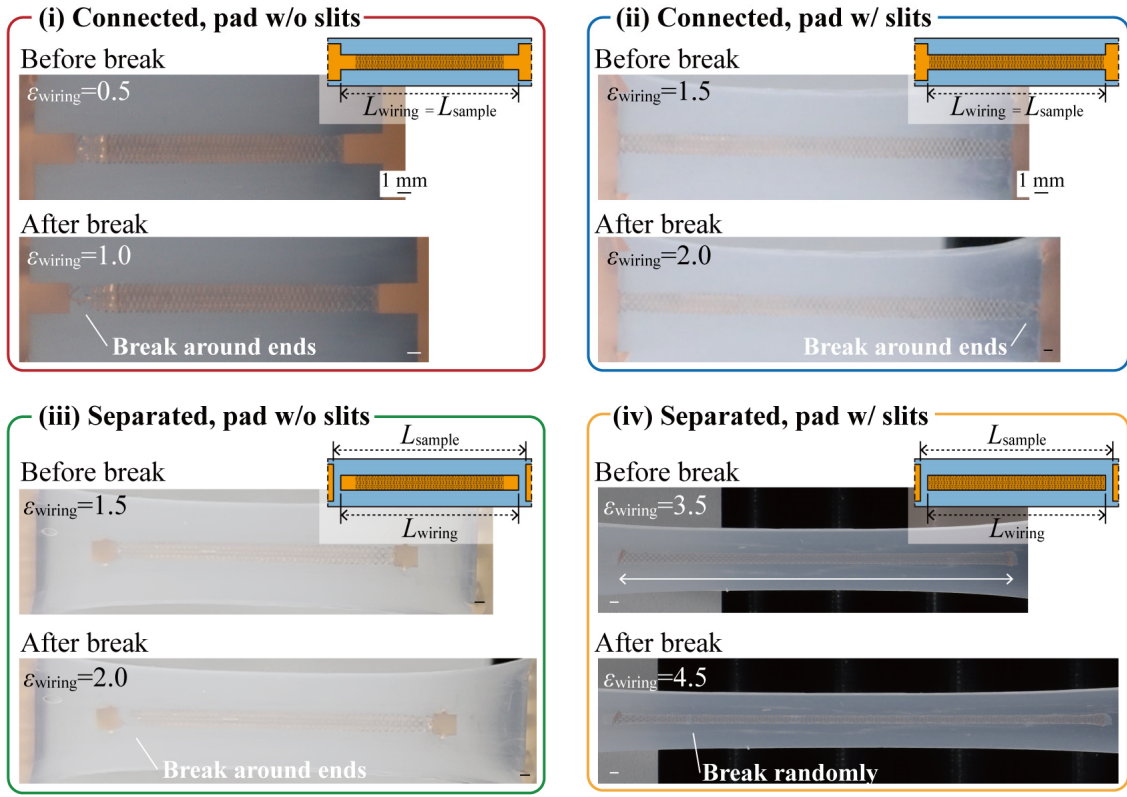


Figure 4.11 Optical images of tensile test samples with different wiring end structures.

substrate, with the kirigami structure on its pads, the tensile load increased from 0 kPa to 45 kPa as the wiring strain increased from 0 to 1.69. For the wiring separated from the gripping substrate, without the kirigami structure on its pads, the tensile load increased from 0 kPa to 70 kPa when the wiring strain was increased from 0 to 1.46. For the wiring separated from the gripping substrate, with the kirigami structure on its pads, the tensile load increased from 0 kPa to 216 kPa as the wiring strain increased from 0 to 3.89. In all cases, the load increased almost linearly within the low strain area; accordingly, the average Young's modulus of the device ( $\underline{E}_{\text{average}}$ ) was obtained. The relationship between wiring strain within 0.02 and  $\sigma_{\text{average}}$  was extrapolated by drawing an approximate straight line with the Y-intercept as 0. The slope of the approximate line [kPa] was  $\underline{E}_{\text{average}}$ .  $\underline{E}_{\text{average}}$  values of the samples with elastomer substrate only were 37 kPa.  $\underline{E}_{\text{average}}$  values for the wiring connected to the gripping substrate, without and with the kirigami structure on its pads, were 50.5 kPa and 46.7 kPa, respectively.  $\underline{E}_{\text{average}}$  values for the wiring separated from the gripping substrate, without and with the kirigami structure on its pads, were 55.2 kPa and 50.2 kPa, respectively. Their tensile test results were overlapped and their  $E_{\text{average}}$  was almost the same. These

results show that the tensile stiffness of the stretchable Cu wiring with the kirigami structure used in this study was the same or lower than that of the elastomer substrate. Thus, the stretch deformation of the elastomer substrate was dominant relative to that of the stretchable Cu wiring.

The breaking wiring strains of the wirings were compared for different wiring end structures, as shown in Figure 4.10(b). Here, the wiring strain did not include the length of separated spaces and differed from the sample strain. Thus, the plots for the wirings separated from the gripping substrates were different in Figure 4.10(a) and (b). The breaking strains for the wiring connected to the gripping substrate, without and with the kirigami structure on its pads, were 0.74 and 1.69, respectively. The breaking strains for the wiring separated from the gripping substrate, without and with the kirigami structure on its pads, were 1.46 and 3.89, respectively. The wiring separated from the gripping substrate, with the kirigami structure on its pads, broke randomly at different locations, whereas the wirings with the other wiring end structures broke near the boundary between the connected area of wiring and other areas. These results indicate that the wiring connected to the gripping substrate, without the kirigami structure, broke due to stress concentration near the connected area caused by the difference in wiring strain. The separation of the wiring from the gripping substrate and the fabrication of the kirigami structures on the pad areas of the wirings can improve stretch tolerance of the wiring 5.2 times by reducing the difference in strain and relieving the stress concentration. Overall, it was determined that the separation of the wirings from the gripping substrates and the installation of a stretchable structure up to the edge of the wiring makes the strain distribution in the wiring uniform, alleviates stress concentration, and improves the stretch tolerance.

The elastic hysteresis of wirings with different end structures was evaluated, as shown in Figure 4.12. As the end structures, the kirigami structure was fabricated in the pad area of the wiring, and the wiring end was separated from the gripping substrate. This cycle test was repeated 10 times. In preliminary experiments, samples were repeatedly stretched 10 times at different strains, and this strain was determined as the wiring strain within the range of no wire breakage. The wiring connected to the gripping substrate, without the kirigami structure on its pads, was stretched to a sample strain of 0.50 and then compressed to  $\sigma_{\text{average}}=0$  kPa. The residual sample strain was  $0.032 \pm 0.007$ , which was 6.3% of the maximum sample strain. The wiring was continuously compressed to negative strain and then stretched to  $\sigma_{\text{average}}=0$  kPa. The residual sample strain was  $0.003 \pm 0.012$ , which was 0.7% of the maximum sample strain. The difference in the stress integrals during stretching and compressing was 911 kPa, which was 17.6% of the stress integral during stretching. The wiring connected to the gripping substrate, without the kirigami structure on its pads, was stretched to a sample strain of 0.52 and then compressed to  $\sigma_{\text{average}}=0$  kPa. The residual

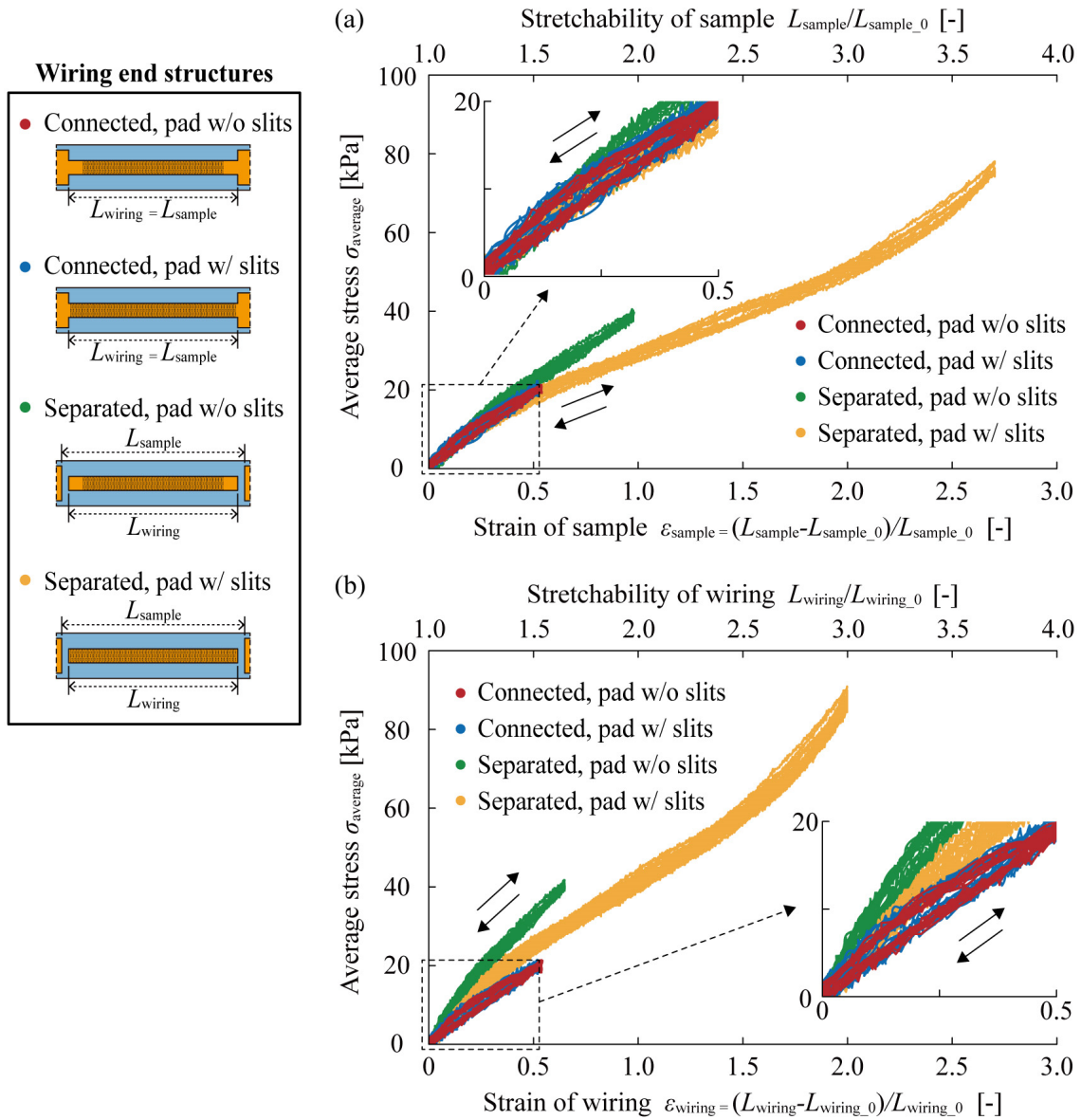


Figure 4.12 Tensile test results from stretching to unloading ( $N = 6$ ). (a) Relationship between (a) sample strain and average stress, (b) wiring strain and average stress.

sample strain was  $0.035 \pm 0.021$ , which was 6.6% of the maximum sample strain. The wiring was continuously compressed to negative strain and then stretched to  $\sigma_{average}=0$  kPa. The residual sample strain was  $0.013 \pm 0.012$  which was 2.4% of the maximum sample strain. The difference in the stress integrals during stretching and compressing was 995 kPa, which was 17.0% of the stress integral during stretching.

The wiring separated from the gripping substrate, without the kirigami structure on its pads, was stretched to a sample strain of 0.98 and then compressed to  $\sigma_{\text{average}}=0$  kPa. The residual sample strain was  $0.020 \pm 0.010$ , which was 2.1% of the maximum sample strain. The wiring was continuously compressed to negative strain and then stretched to  $\sigma_{\text{average}}=0$  kPa. The residual sample strain was  $0.006 \pm 0.09$ , which was 0.6% of the maximum sample strain. The difference in the stress integrals during stretching and compressing was 1476 kPa, which was 6.9% of the stress integral during stretching. The wiring separated from the gripping substrate, with the kirigami structure on its pads, was stretched to a sample strain of 2.55 and then compressed to  $\sigma_{\text{average}}=0$  kPa. The residual sample strain was  $0.012 \pm 0.016$ , which was 0.5% of the maximum sample strain. The wiring was continuously compressed to negative strain and then stretched to  $\sigma_{\text{average}}=0$  kPa. The residual sample strain was  $-0.003 \pm 0.012$ , which was -0.1% of the maximum sample strain. The difference in the stress integrals during stretching and compressing was 5650 kPa, which was 5.4% of the stress integral during stretching. These results show that stretchable metal wiring with kirigami structures embedded in elastomer substrates has high mechanical resilience for all end structures. The difference between the stress integrals during stretching and compression can be attributed mainly to the viscoelastic properties of the elastomer substrate.

#### 4.4 Stretch Tolerance of Wiring with Components

---

In Section 4.3, it was clarified that the separating the wiring from the gripping substrate and fabricating the kirigami structure in the pad areas reduced the wiring strain difference and improves the stretch tolerance of the wiring. However, because electronic components exhibit higher stiffness than the wiring, mounting components on the stretchable Cu wiring may exert an effect on the wiring strain around the components. In addition, the effect of the fabrication of the kirigami structure on the pad areas is unknown, and it may be a trade-off with stretch tolerance. Therefore, the stretch tolerance of the wirings with the components were compared for the different mounting structures. The EIMs of the solder and galinstan and the fabrication of the kirigami structure in the pad areas were studied. Electronic components were mounted on stretchable Cu wiring with a kirigami structure using LM, and the samples were sealed with elastomers. Tensile load and device resistance against wiring strain were measured. The aperture distribution of the kirigami structure was investigated to determine the break points. The effect of the kirigami structure fabricated in the pad areas of wiring on the electrical connection was also investigated. The tolerance of samples mounted with LM to repeated stretching and deformation was evaluated.

#### 4.4.1 Methods

In the previous section, by separating the wiring and pads and making a cutout in the connected area of wiring, the difference in wiring strain is reduced and a highly stretch tolerance of about 400% is achieved. In contrast, when rigid electronic components are mounted on the wiring, the stiffness of the components is significantly higher than the tensile stiffness of the wiring. Hence, there is a concern that the wiring strain near the component will decrease, resulting in a strain difference that will reduce the stretch tolerance. However, the effect of the presence of components on the wiring strain distribution is unknown. Therefore, the stretch tolerance of the wirings with the components were compared for the different mounting structures. The EIMs of the solder and galinstan and the fabrication of the kirigami structure in the pad areas were studied. The study measured tensile load and sample resistance against wiring strain, analyzed the wiring breaking strain and aperture distribution, and compared the stretching tolerance of the sample mounted with LM with that of the sample mounted with conventional soldering. The electrical stability of the sample under repeated stretching was also evaluated.

Figure 4.13 presented schematics and images of a sample for tensile testing to investigate the effect of electronic component and wiring on wiring strain. An SMD is mounted using LM on stretchable metal wiring with a kirigami structure and sealed with elastomer. The SM wiring utilizes a two-layer substrate of Cu and polyimide. The elastomer substrate material is silicone rubber. Chip resistors are adopted as the SMD. Jumper resistors (MCR10EZPJ000, ROHM, Kyoto, Japan)[188] were utilized to reduce the effect on the overall resistance. The component resistance was less than 50 m $\Omega$ . The chip resistors were made of metal-glaze resistors and the electrode surfaces were tin-plated. The stretchable Cu wiring with kirigami structure was 14-mm long and 2-mm wide, with a thickness of 0.008 mm for the Cu layer and 0.025 mm for the Pi layer, as in the previous section. The fixing pad was 13-mm wide, and the distance between the pad and wiring was 1 mm. The elastomer substrate was 15-mm wide and 3-mm thick. The slit pattern of the kirigami structure is presented in the inset. As in the previous section, the cut width was 0.9 mm, the leave-behind width was 0.1 mm, and the cut pitch was 0.1 mm. The  $n_L$  was 69. A circular hole was provided at the edge of the slit. The chip resistor was 2-mm long, 1.2-mm wide, and 0.5-mm thick, and its electrode size was 0.4-mm long and 1.2-mm wide. In addition, 8- $\mu$ l LMs were placed on a 2-mm square connection area and pads at the wiring end. For comparison, a sample mounted with conventional paste solder (SMX-H05A, San Hayato, Tokyo, Japan) heated at 200°C was also prepared. The optical image of the sample is presented in Figure 4.13.

Figure 4.14 illustrates the fabrication procedure of a sample with components mounted on stretching

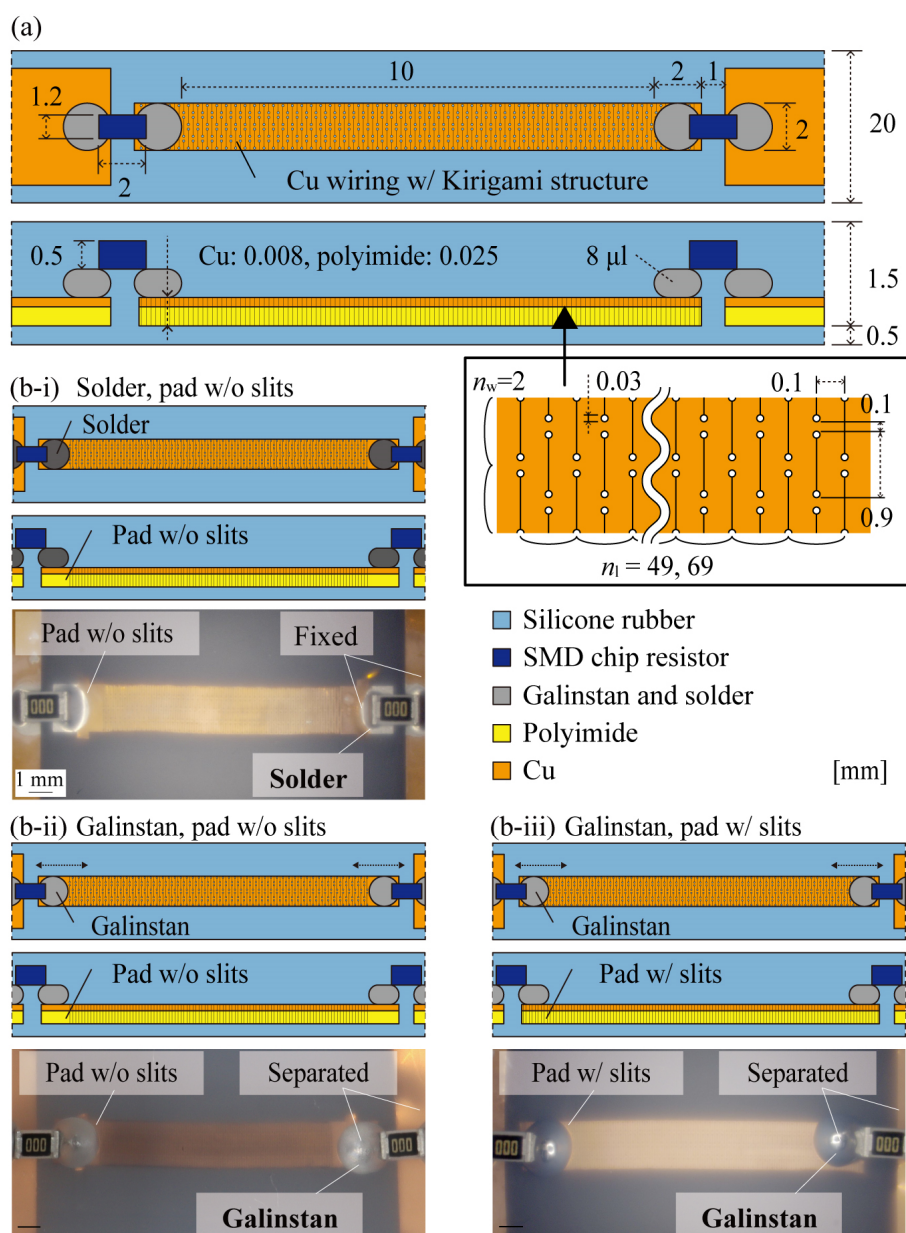


Figure 4.13 Tensile test samples in which chip resistor was mounted on stretchable Cu wiring using solder and galinstan. (a) Schematics and (b) optical images of the sample.

wiring. First, the outline of the Cu-polyimide substrate fixed on the weak adhesive sheet and the paper cut pattern were cut using a UV laser cutting machine. The conditions for laser cutting are presented in Appendix A. The surface of the weak adhesive tape was roughened by a UV laser cutting machine to

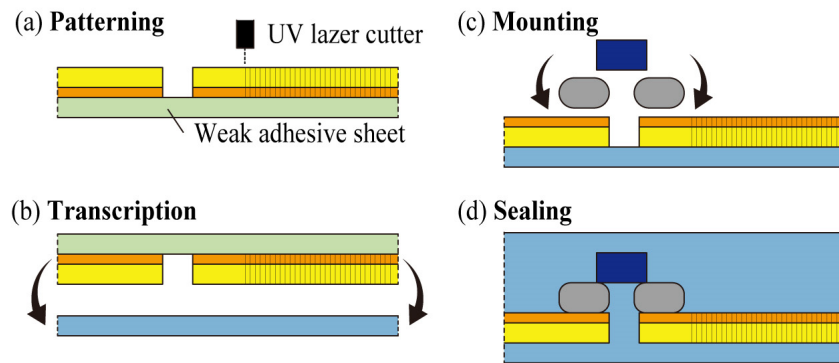


Figure 4.14 Fabrication processes of the sample for tensile test of wiring with component. (a) Cu film was cut using UV razor cutter. (b) Cu film interconnects were placed on an Ecoflex sheet. (c) Solder and galinstan was placed on the pad area of the wiring, and chip resistors were placed on them. (d) Sample was sealed with Ecoflex.

reduce the adhesive strength. The Cu-Polyimide substrate was then transferred onto a 0.5-mm thick elastomer substrate placed on the bottom of the Mold. After transfer, the Cu-polyimide substrate was stripped of all unnecessary parts except for wiring and pads, and the Cu surface was fluxed. Details of the procedure presented for fluxing shown in the Appendix A. Galinstan was placed on the pads and wiring using a dispenser. Chip resistors were mounted on the LM. In the sample with a chip resistor mounted with paste soldering for comparison, after fluxing the Cu substrate, paste solder was stencil printed on a  $1\text{ mm} \times 2.5\text{ mm}$  area of the wiring connected area. A simple mask with a 0.5-mm thick PET substrate was utilized. The stencil was then heated at  $200^\circ\text{C}$  for 1 min to melt and then cured. Subsequently, the uncured elastomer was poured into the mold, and the mold was sealed with a lid to keep the thickness constant. The elastomer was poured slowly and the lid was pressed down slowly to prevent the components from moving when the elastomer was poured. Details of the fabrication procedure for mixing and curing the elastomer are provided in the Appendix A. The elements were heated in an oven at  $60^\circ\text{C}$  for 1 h to cure, and then cut out of the mold.

A sample prepared by a roll chuck was fixed on a motorized stage. A force gauge was utilized to measure the tensile load while applying displacement in the tensile direction. The  $\sigma_{\text{average}}$  was calculated by dividing the tensile load by the sample cross section area. The sample resistance was measured by the four-terminal method using a source meter to evaluate electrical stability and detect breakage. A single-lens reflex camera was utilized to capture videos and images of the sample and analyze the wiring strain; the sample



was also photographed from the backside to examine the deformation of the wiring under the LM. The starting point of measurement was synchronized as in the previous section. The stage movement speed was kept constant at 10 mm/min=0.16 mm/s. In the measurement, the sample was stretched until breaking strain, and the tensile load and sample resistance against the strain were measured. The breaking strain of the wiring was determined from the resistance change. To evaluate the effect of components, the aperture distribution of the wiring was analyzed from the images. Because the measured resistance is the sum of wiring resistance, the mounting area resistance, pad resistance, wiring resistance, and connected area resistance were evaluated separately based on the resistance change of the mounting area in response to EIM strain obtained in the previous section. The resistance change against the strain between components was compared for each mounting method. In addition, the sample resistance was measured by repeated stretching at a strain lower than the breaking strain. For cyclic tensile tests, the stage speed was 80 mm/min and the loading and unloading were repeated continuously without stopping. Detailed settings are presented in the Appendix B.

#### 4.4.2 Results and Discussion

The relationships between sample strain and  $\sigma_{\text{average}}$  were compared for the different wiring end structures, as shown in Figure 4.15 (a). Figure 4.16 shows the optical images of test samples with different wiring end structures before and after breakage. For the wiring mounted using the solder, without the kirigami structure in the pad areas,  $\sigma_{\text{average}}$  increased from 0 kPa to 27 kPa as the wiring strain increased from 0 to 0.53. For the wiring mounted using galinstan, without the kirigami structures in the pad areas,  $\sigma_{\text{average}}$  increased from 0 kPa to 86 kPa as the wiring strain increased from 0 to 1.42. For the wiring mounted using galinstan, with the kirigami structures in the pad areas,  $\sigma_{\text{average}}$  increased from 0 kPa to 158 kPa as the wiring strain increased from 0 to 3.04, and the silicone rubber substrate around the component broke, although the wiring was not broken. The  $E_{\text{average}}$  value of each sample was determined as the tensile load changed almost linearly within low wiring strain for all mounting methods. The relationship between wiring strain within 0.2 and  $\sigma_{\text{average}}$  was extrapolated by drawing an approximate straight line with the Y-intercept as 0. The slope of the approximate line [kPa] is  $\underline{E}_{\text{average}}$ . The  $\underline{E}_{\text{average}}$  values of the samples mounted using the solder was 49 kPa. The  $\underline{E}_{\text{average}}$  values of the samples mounted using the galinstan without and with the kirigami structures in the pad areas were 58 kPa and 52 kPa, respectively. Although there was some variation, the tensile stiffnesses were close to each other. This result was practical because both samples have the same kirigami structure.

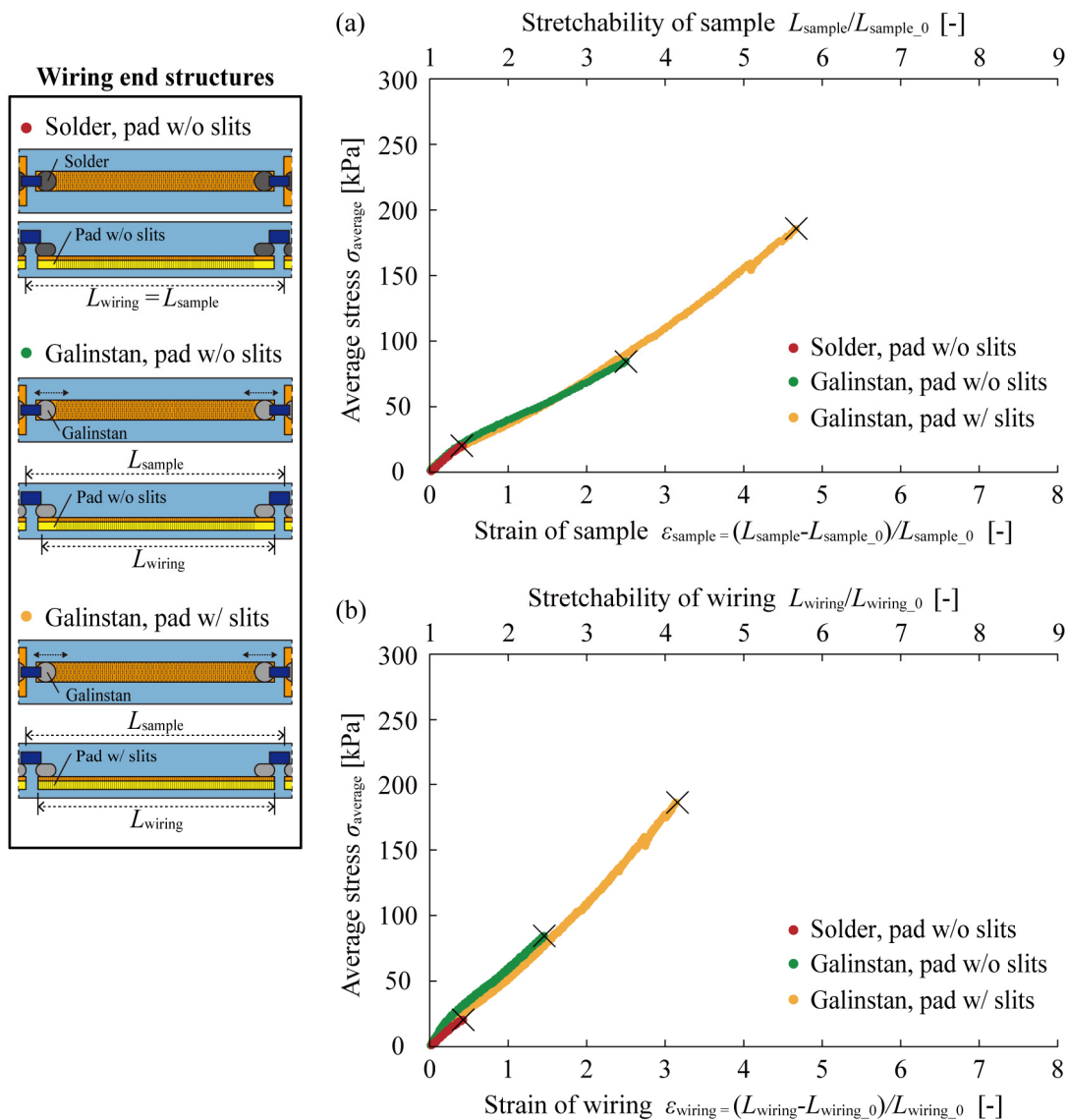


Figure 4.15 Tensile test results for fixed- and free-end wirings with components ( $N = 3$ ).

The breaking wiring strains of the wirings were compared for different wiring end structures, as shown in Figure 4.15(b). The breaking strains for the wiring mounted using the solder, without the kirigami structure in its pads, were 0.53. The breaking strains for the wiring mounted using the galinstan, without and with the kirigami structure in its pads, were 1.42 and 3.04, respectively. The wiring mounted using the galinstan, with the kirigami structure on its pads, the silicone rubber substrate around the component broke, although the wiring did not break. Contrastly, the wirings with the other wiring end structures broke near

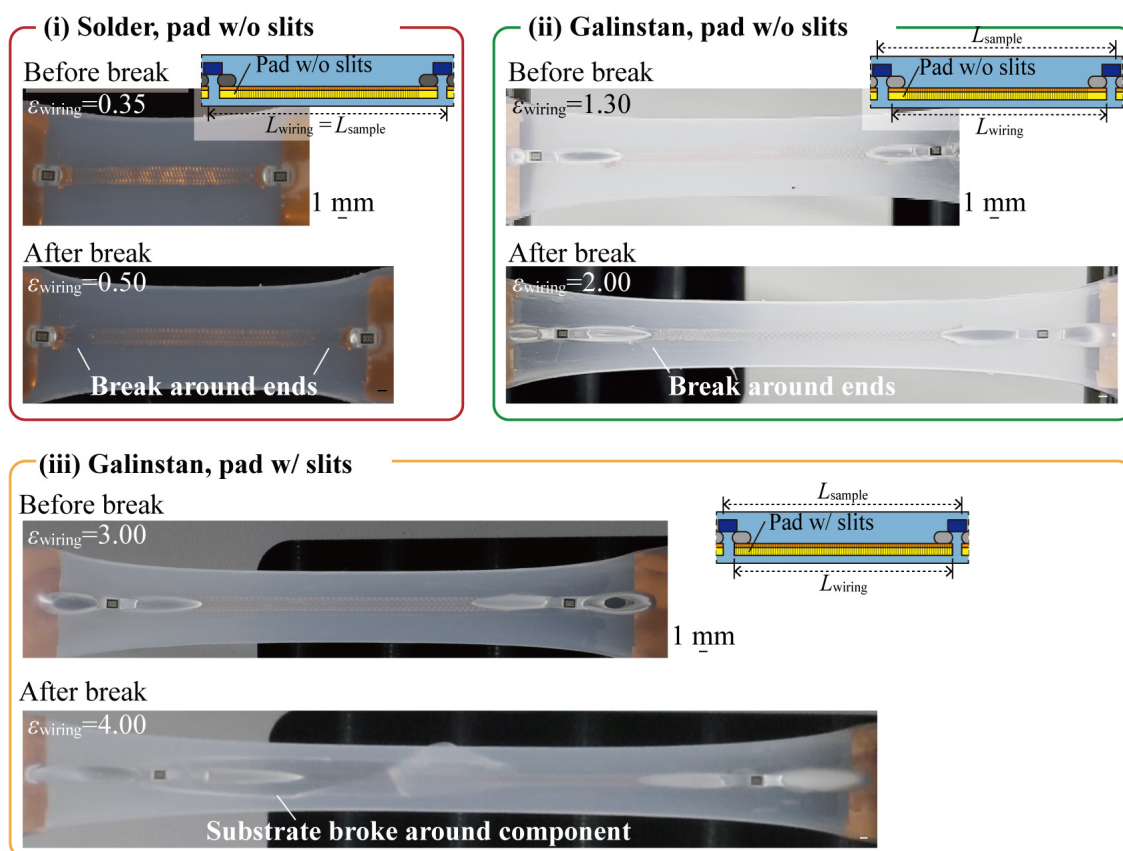


Figure 4.16 Optical images of tensile test samples with different wiring end structures.

the boundary between the connected area of wiring and other areas. These results indicate that the wiring mounted using the solder, without the kirigami structure, broke due to stress concentration near the connected area caused by the difference in wiring strain. The mounting using the galinstan and the fabrication the kirigami structures on the pad areas of the wirings can improve the stretch tolerance of the wiring 5.8 times by reducing the difference in strain and relieving the stress concentration. Overall, it was determined that the mounting using the galinstan and the installation of a stretchable structure up to the edge of the wiring makes the strain distribution in the wiring uniform, alleviates stress concentration, and improves the stretch tolerance.

The elastic hysteresis of wirings with different end structures was evaluated, as shown in Figure 4.17. As the wiring end structures, the kirigami structure was fabricated in the pad area of the wiring, and the chip resistors were mounted on the wiring using the galinstan. This cycle test was repeated 10 times. The wiring mounted using the galinstan, without the kirigami structure in the pad areas, was stretched to a

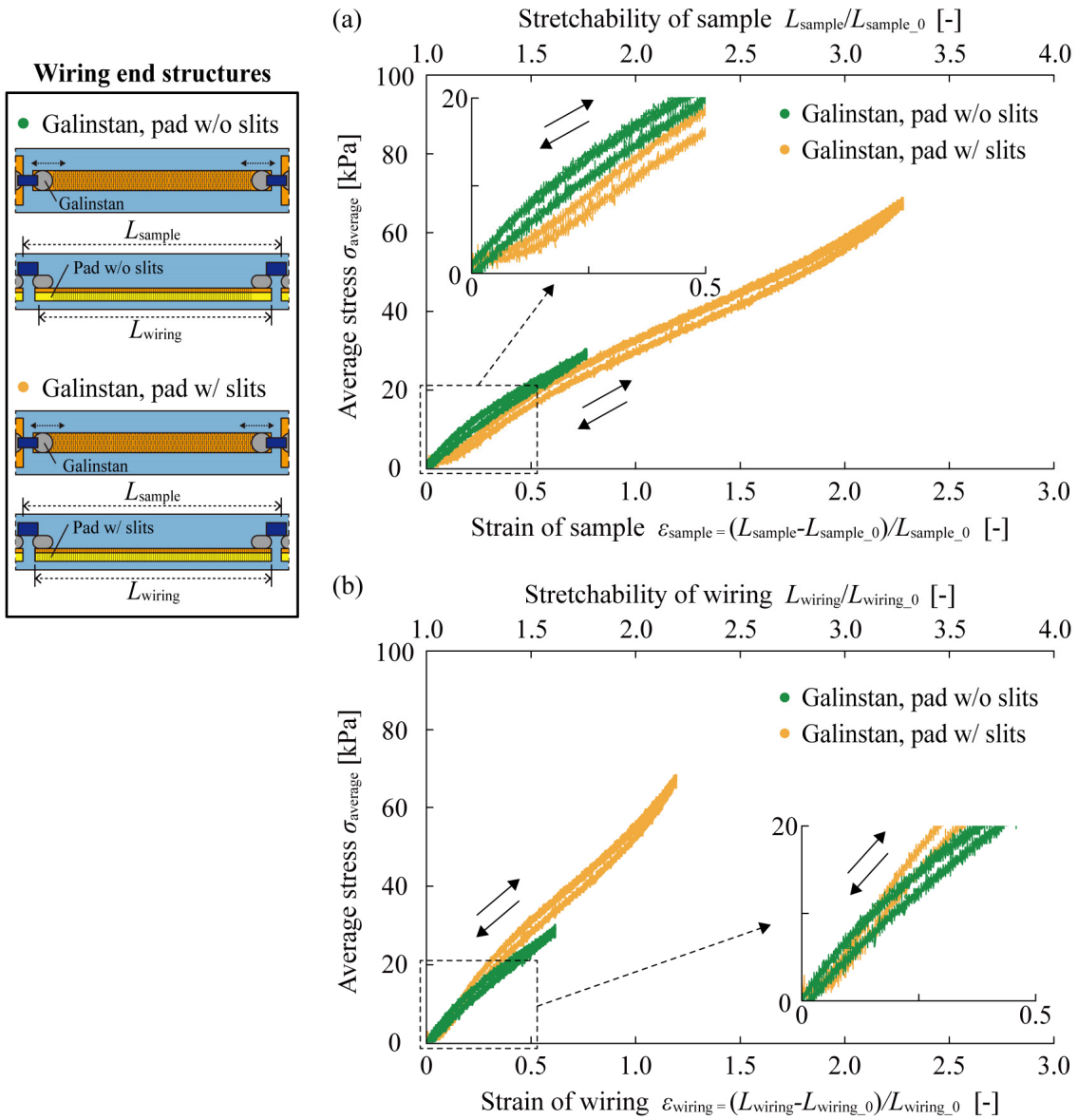


Figure 4.17 Tensile test results from stretching to unloading ( $N = 3$ ). Relationship between (a) sample strain and average stress, (b) wiring strain and average stress.

sample strain of 0.82 and then compressed to  $\sigma_{\text{average}}=0$  kPa. The residual sample strain was  $0.042 \pm 0.004$ , which was 5.1% of the maximum sample strain. The wiring was continuously compressed to negative strain and then stretched to  $\sigma_{\text{average}}=0$  kPa. The residual sample strain was  $0.011 \pm 0.004$ , which was 1.3% of the maximum sample strain. The difference in the stress integrals during stretching and compressing

was 1359 kPa, which was 10.7% of the stress integral during stretching. The wiring mounted using galinstan, with the kirigami structure in the pad areas, was stretched to a sample strain of 2.28 and then compressed to  $\sigma_{\text{average}} = 0$  kPa. The residual sample strain was  $0.053 \pm 0.012$ , which was 2.3% of the maximum sample strain. The wiring was continuously compressed to negative strain and then stretched to  $\sigma_{\text{average}} = 0$  kPa. The residual sample strain was  $-0.007 \pm 0.008$ , which was -0.3% of the maximum sample strain. The difference between the stress integrals during stretching and compressing was 5244 kPa, which was 6.8% of the stress integral during stretching. These results show that stretchable metal wiring with the kirigami structure, on which rigid electronic components are mounted using galinstan, embedded in the elastomer substrate, has high mechanical resilience, regardless of the presence of the kirigami structure at the pad area of the wiring. The difference between the stress integrals during stretching and compression can be attributed to the viscoelastic properties of the elastomer substrate.

The change in the sample resistances against sample and wiring strains for different component mounting methods were investigated, as shown in Figure 4.18. Because the same stretched copper wiring, pads, and chip resistors are utilized, the resistance difference at 0 strain is the resistance of the mounting area. This is the combined resistance of the bulk resistance of the EIM and the  $R_c$  between the EIM, components, and wiring. Regarding solder mounting, as the wiring strain increased from 0 to 0.53, the sample resistance increased from 347.6 m $\Omega$  to 355.5 m $\Omega$ . For the wiring mounted using the galinstan, without the kirigami structure in the pad areas, as the wiring strain increased from 0 to 1.42, the sample resistance increased from 366.4 m $\Omega$  to 385.1 m $\Omega$ . For the wiring mounted using the galinstan, without the kirigami structure in the pad areas, as the wiring strain increased from 0 to 1.42, the sample resistance increased from 366.0 m $\Omega$  to 455.2 m $\Omega$ . This result indicates that fabricating a kirigami structure up to the pad area of wiring makes the stiffness of the wiring uniform, alleviates stress concentration, and further improves the stretch tolerance. Moreover, it is inferred that the change in the  $R_c$  is almost equal because galinstan stretches along with the wiring, and the contact area was maintained. Overall, it was determined that mounting components using LM on wiring with a kirigami structure up to the pad area improved the stretch tolerance of the wiring while maintaining the electrical performance.

The estimated change in the wiring resistance was calculated for the wiring strain, as shown in Figure 4.18(b). The EIM strain for each wiring strain was obtained from the videos and estimated from the relationship between the EIM strain and resistance of the mounting area obtained in Section 4.2. Because the pad resistance is sufficiently lower than the wiring resistance and the resistance of the mounting area, the sample resistance  $R$  is mainly the resultant resistance of the wiring resistance  $R_{\text{wire}}$  and mounting area

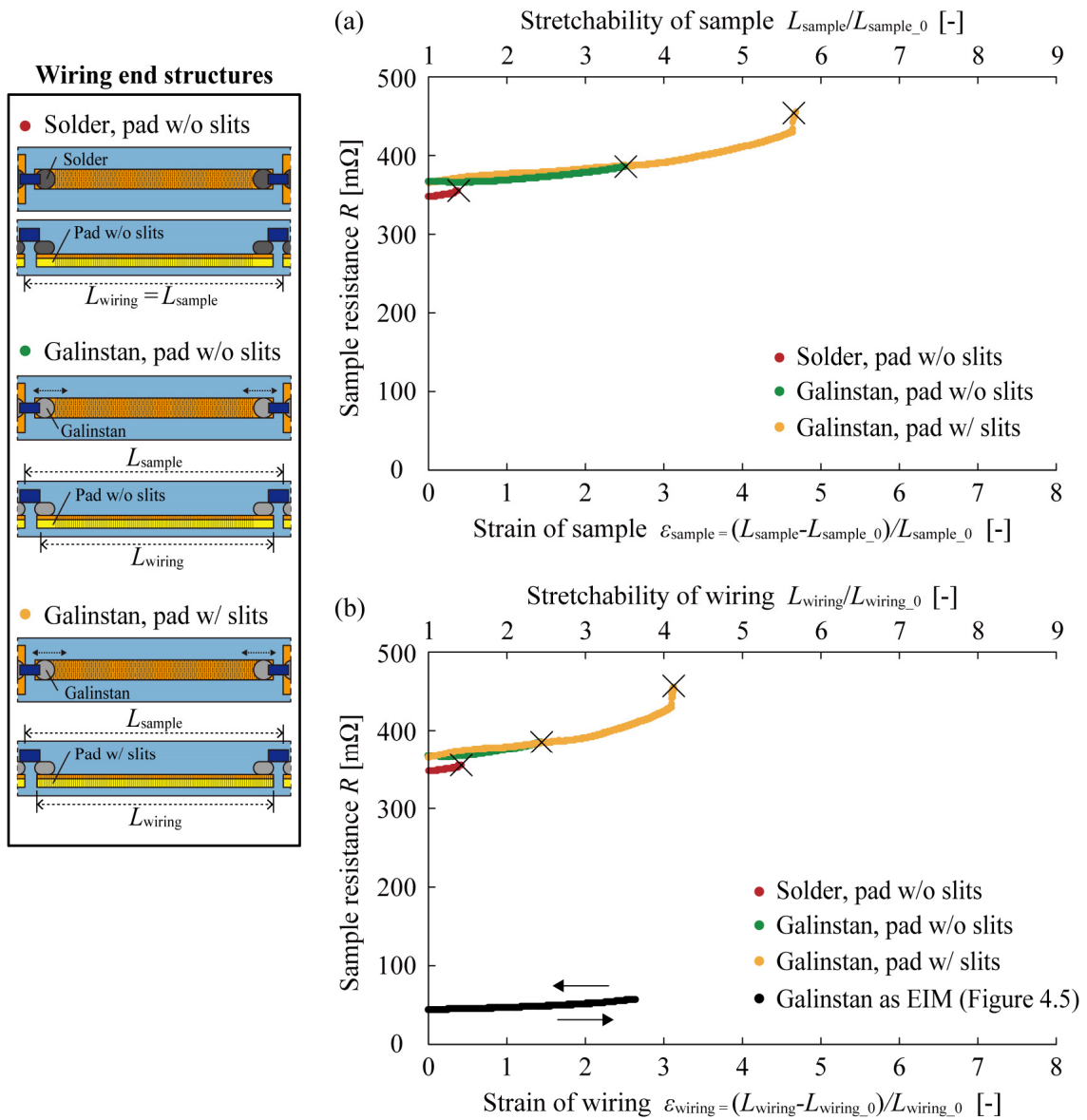


Figure 4.18 Relationship between wiring strain and sample resistance for free- and fixed-end wiring with components ( $N = 3$ ).

resistance  $R_{mount}$ . Therefore, the wiring resistance  $R_{wire}$  was estimated by subtracting the mounting resistance  $R_{mount}$  from the sample resistance  $R$ . At 0 wiring strain,  $R_{mount}$  and  $R_{wire}$  were 44.6 mΩ and 321.4 mΩ, respectively. At 3.04 wiring strain, which is the breaking strain of the elastomer board,  $R_{mount}$  and  $R_{wire}$  were 56.3 mΩ and 398.9 mΩ, respectively. When wiring strain was increased from 0 to 3.04,  $R_{mount}$

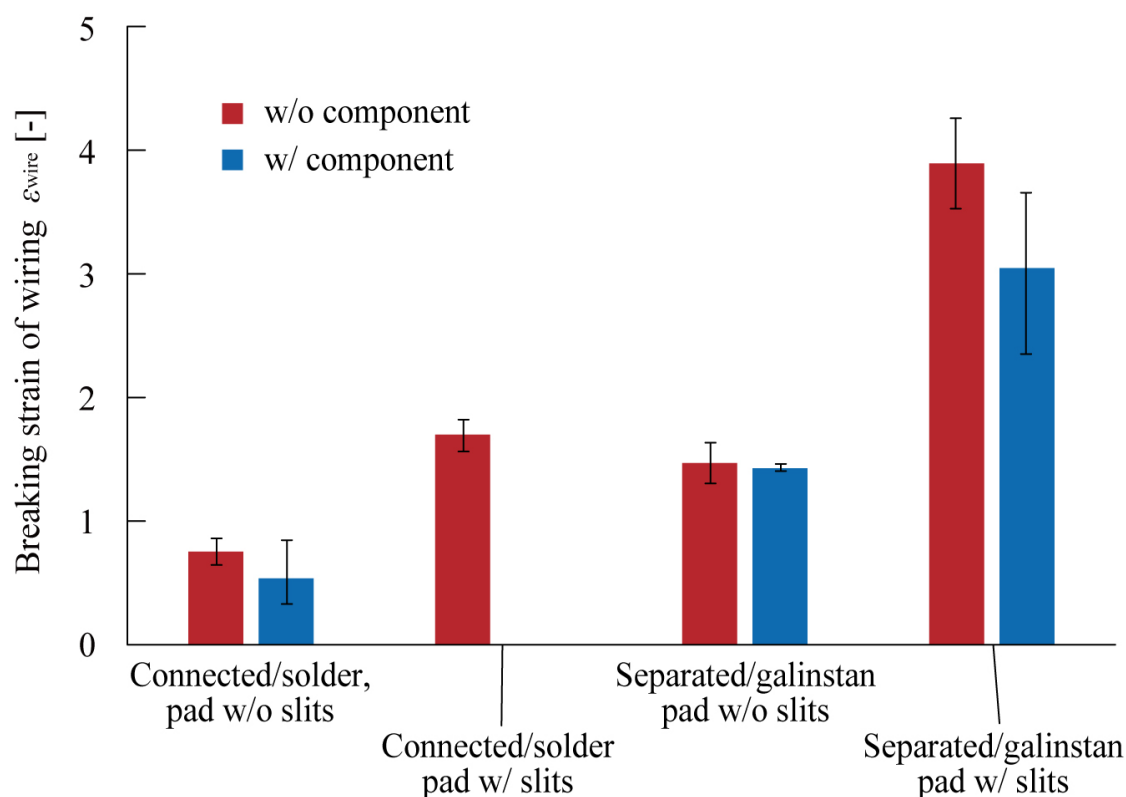


Figure 4.19 Breaking strain of wiring w/o and w/ components.

increased by 11.7 m $\Omega$ , while  $R_{\text{wire}}$  increased by 77.5 m $\Omega$ . The increase in  $R_{\text{wire}}$  was 6.6 times greater than that in  $R_{\text{mount}}$ . These results indicate that the increase in sample resistance during stretching in LM mounting is primarily determined by the wiring resistance, and the effect of the mounting resistance is negligible. For the wiring mounted using galinstan, with kirigami structure in the pad areas, the sample resistance increased by 24% as the wiring strain increased from 0 to 3.04. This result shows the high electrical stability of the device configuration with the components mounted the stretchable metal wirings. In contrast, the resistance of the wiring made of a stretchable conductor, such as conductive elastomers or LMs, increased in proportion to the square of the wiring length.

The breaking strains of the wirings were compared for without and with the electronic components on them, as shown in Figure 4.19. For the wiring separated from the gripping substrate, with the kirigami structure in the pad areas, the wiring broke at a wiring strain of 3.89 in the sample without components. With a component, the wiring did not break; however, the silicone rubber substrate around the component broke at a wiring strain of 3.04. From these results, it is evident that a wiring stretch tolerance of

approximately 3 strain (0.8 times that without components) can be achieved with components, and that further increases in wiring strain will cause the substrate around the component to break due to stress concentration. Overall, when there is a rigid electronic component around the wiring, the stretching deformation of the wiring around the component is suppressed and a strain difference is generated in the wiring, resulting in a lower stretch tolerance than without the component. Nevertheless, the stretchable substrate between the components and wiring mitigates the strain difference, resulting in a higher stretch tolerance than solder mounting.

The electric hysteresis of wirings with different end structures was evaluated, as shown in Figure 4.17. As the wiring end structures, the kirigami structure was fabricated in the pad area of the wiring, and the chip resistors were mounted on the wiring using the galinstan. In preliminary experiments, samples were repeatedly stretched 10 times at different strains, and this strain was determined as the wiring strain within the range of no wire breakage. This cycle test was repeated 10 times. The wiring mounted using the galinstan, without the kirigami structure in the pad areas, was stretched to a sample strain of 0.82, compressed to negative strain, and then stretched to  $\sigma_{\text{average}} = 0$  kPa. The sample resistance increased by 11.1 m $\Omega$ , which was 3.1% of the initial sample resistance. The wiring mounted using galinstan, with the kirigami structure in the pad areas, was stretched to a sample strain of 2.28, compressed to negative strain, and then stretched to  $\sigma_{\text{average}} = 0$  kPa. The sample resistance increased by 39.4 m $\Omega$ , which was 12.1% of the initial sample resistance. The increase in sample resistance in the cyclic tensile test was mainly attributed to the wiring resistance. The resistance change of the LM mounting was 0.4 m $\Omega$  after 100 cycles at a strain of 4 (Figure 4.7). This was less than 3.6% of the increase in sample resistance in this experiment. The increase in the wiring resistance can be attributed to permanent strain and cracks. In a preliminary test, the stretchable Cu wiring with the kirigami structure was stretched to the same strain as that used in this experiment. The wiring did not return to its original shape after unloading. This result indicates that permanent strain was generated in the wiring. In addition, the stretchable Cu wiring with a kirigami structure formed cracks after the cyclic tensile test[107]. Overall, these results indicate that the permanent strain and cracks generated in the wiring by the cyclic stretching increase the wiring resistance. Here, the measurement results of the mechanical hysteresis of the wiring did not show the effect of permanent strain or cracks because the tensile stiffness of the sample is dominated by the elastomer substrate.

The relationship between the number of cycles and sample resistance in repeated tensile tests via the LM mounting was studied Figure 4.21. The increase in resistance at 0 strain of the mounting area due to LM is less than a few percent even after 100 cycles of stretching (Figure 4.7). However, in the previous



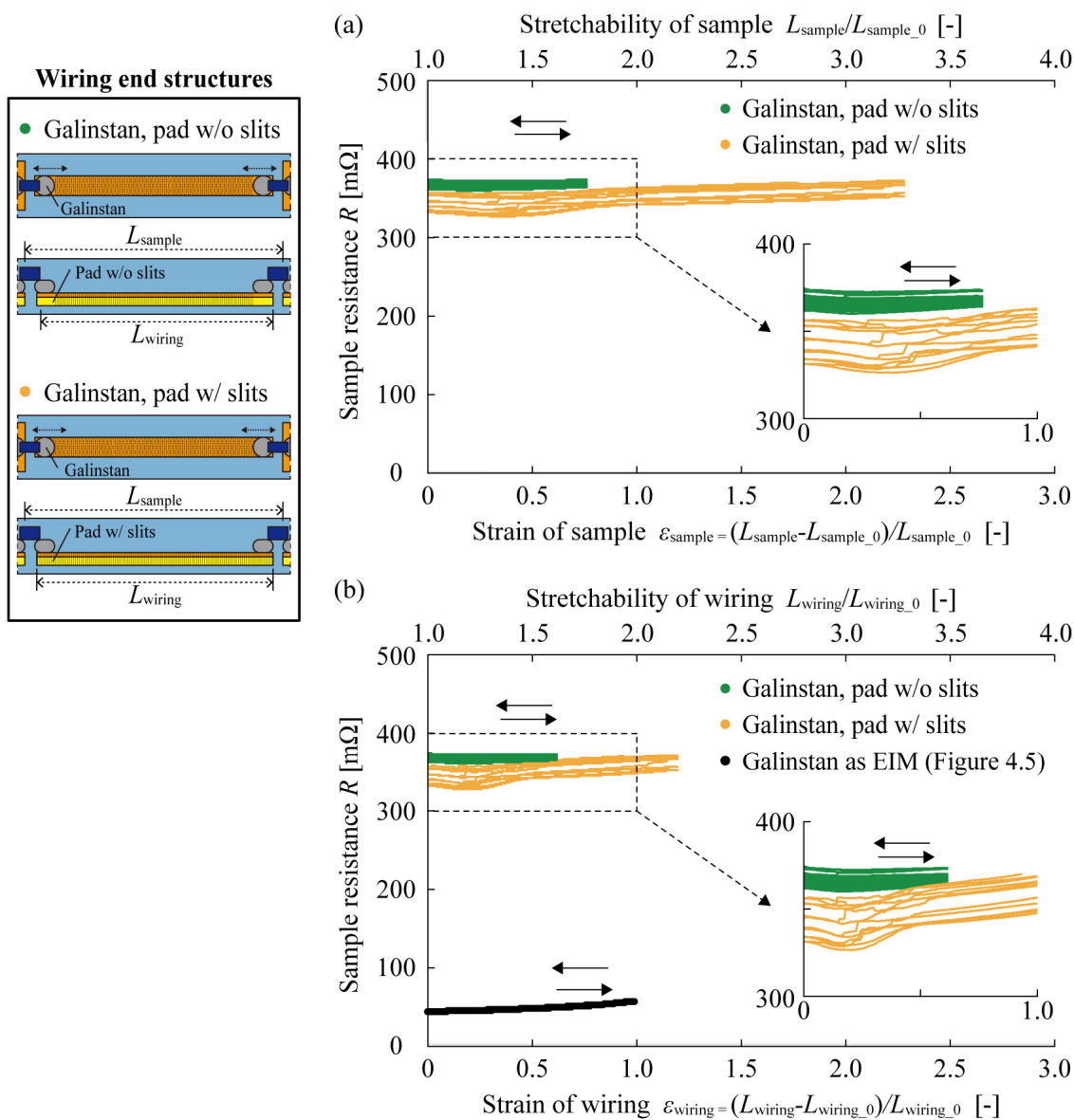


Figure 4.20 Tensile test results from stretching to unloading ( $N = 3$ ). Relationship between (a) sample strain and sample resistance, (b) wiring strain and sample resistance.

section, regarding stretchable wiring with a kirigami structure, the sample resistance at 0% strain increases with increasing number of cycles in repeated stretching due to cracks and other factors. The LM mounting maintained electrical connection up to 463 cycles of stretching at 1 strain and disconnection. The resistance increased by 3.3 times. The LM mounting maintained the electrical connection up to 74 cycles of stretching

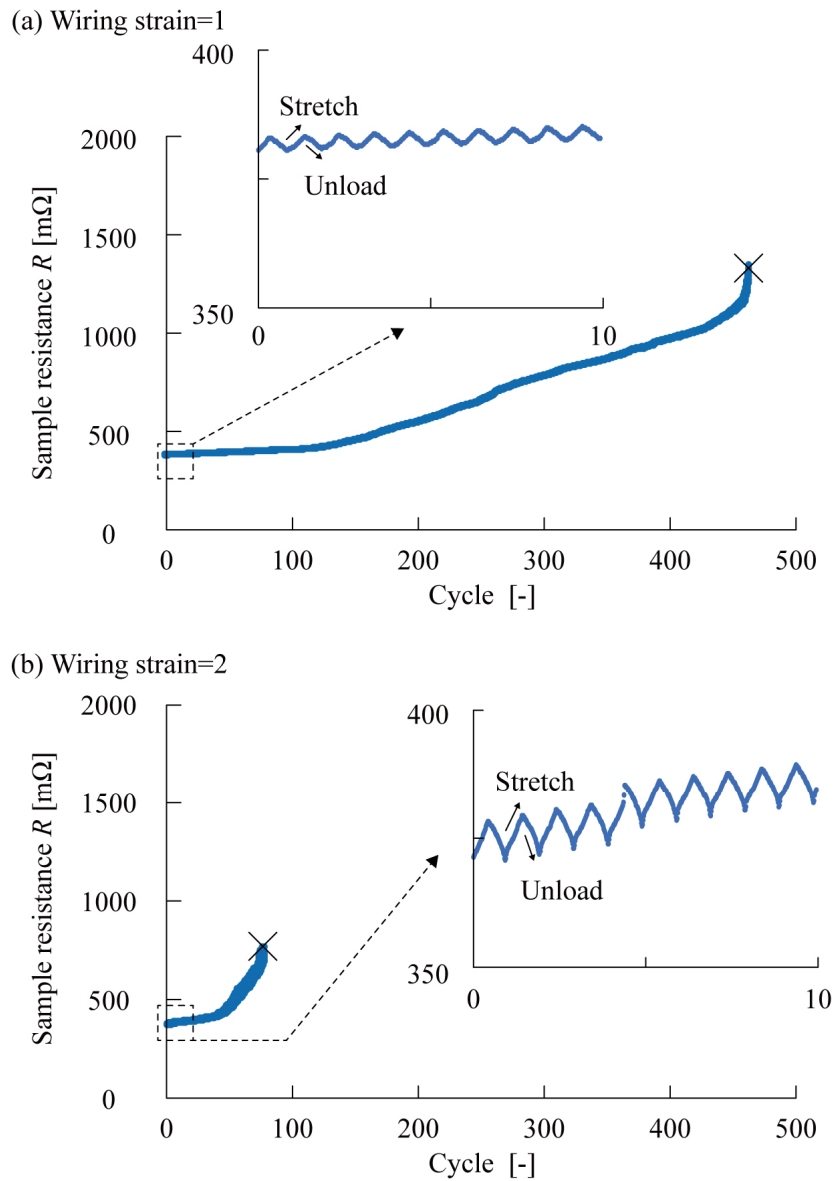


Figure 4.21 Relationship between tensile cycle and sample resistance.

at 2 strain and broke the wire. The resistance increase was 1.9 times. The resistance at 0% strain increased with increasing number of cycles for cyclic stretching with the LM mounting. The resistance of galinstan as EIM returned to that before stretching when unloading. Hence, this result suggests that the increase in the sample resistance during repeated stretching is primarily due to the increase in resistance of the wiring. It was inferred that the LM mounting can significantly enhance the stretchable tolerance of the wiring,

while the wiring with solder mounting breaks due to the difference in strain before the stretch tolerance of the wiring can be extracted.

## 4.5 Demonstration of Stretchable Electronic Devices

---

In Section 4.4, the study investigated the effect of the presence or absence of EC on the wiring strain, and it was determined that the free-edge method without the component provided stretch tolerance of 383.8% wiring strain, while with the component, stretch tolerance of approximately 304.1% wiring strain was achieved; however, further increasing the strain resulted in the breaking strain of the component around the component. Section 4.5 presents the results of this study.

In Section 4.5, the proposed device is presented based on the results obtained in Sections 4.1–4.4. As in the previous section, multiple rigid electronic components were mounted using LM on stretchable metal wiring with a kirigami structure, and devices with elastomer encapsulation were fabricated to evaluate stretch tolerance. To evaluate the electrical performance, a device was utilized with an array of chip resistors to measure the change in resistance under strain. The electrical stability of each component was also evaluated by examining the lighting of each component during stretching using a device with an array of chip LEDs mounted on it.

### 4.5.1 Device Fabrications

Based on the elucidated conditions for improving the stretch tolerance of wiring by LM as EIM, highly stretchable and high-performance stretchable electronic devices were demonstrated. A resistor array and an LED array were mounted on the paper-cut stretched wiring, and the devices were encapsulated with elastomers. A schematic of the stretching electronic device demonstration using LM mounting is presented in Figure 4.22. A stretchable electronic device is fabricated with a highly stretchable surface-mount component mounted on a stretchable copper wiring with a kirigami structure via LM mounting, to demonstrate the high performance and high stretchability of the device. Chip resistors for resistance measurement and chip LEDs for electrical stability evaluation were utilized as surface-mounted components. First, the chip resistor array was stretched to investigate the change in device resistance

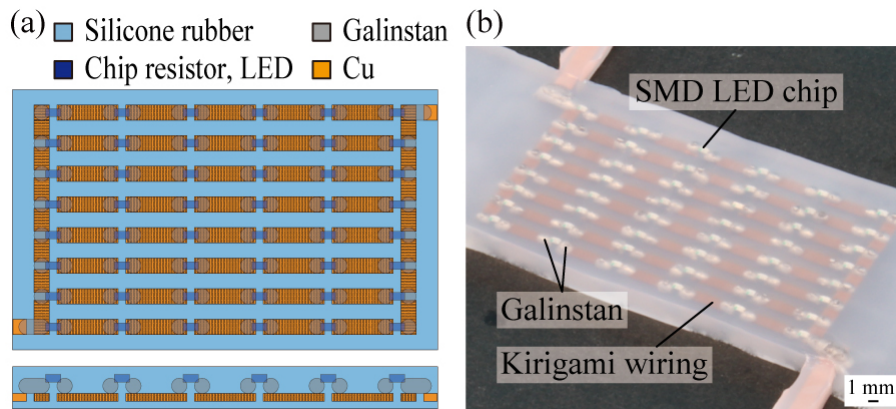


Figure 4.22 Stretchable chip resistors and LEDs array devices. (a) Schematics and (b) optical image of devices.

during stretching and evaluate the stretch tolerance and electrical stability of the LM-mounted stretchable electronic devices. Furthermore, the highly stretchable and high performance of the stretched chip LED array was demonstrated by lighting the LED array while stretching it.

In the circuit diagram of the demonstration device,  $8 \times 6$  electronic components are connected in series, one per line, using stretchable copper wiring with a kirigami structure. Each row is connected in parallel. Although parallel connection is also acceptable from the perspective of low drive voltage, for wiring simplicity, a series-parallel mixture was utilized instead of an all-parallel connection. Pads for connecting to external measurement devices are provided in the upper left, upper right, and lower right of the device. When a chip resistor is mounted, current is applied and voltage is detected to obtain the resistance. When the chip LED was mounted, current was applied.

An optical image of the demonstration device is presented in Figure 4.23. An SMD is mounted using an LM on stretchable metal wiring with a kirigami structure, and the entire device is sealed with an elastomer. The material utilized for the stretchable metal wiring is a two-layer Cu-polyimide substrate. Silicone rubber was utilized as the elastomer substrate material, and galinstan was adopted as the LM material. The same jumper resistors as in the previous section were utilized as chip resistors. Chip LED is blue LED (OSB50805C1C, OptoSupply, Hong Kong, China)[189], as shown in Table 4.6. The stretchable Cu wiring with a kirigami structure is 9-mm long and 2-mm wide, as in the previous section. In addition, a 0.008-mm Cu layer and 0.025-mm polyimide layer were utilized for the Cu-polyimide substrate. The pads were 1.3-mm wide and the distance between the pads and wiring was 1 mm. The elastomer substrate was 15-

Table 4.6 Properties of chip LED used for devices.

Properties	Chip LED	Ref. No.
Purchase	OSB50805C1C, OptoSupply, Hong Kong, China	[189]
Type	Thick film resistors	[189]
Forward current	20 mA	[189]
Forward voltage	5 V	[189]
Chip dimensions	Length 2 mm, Width 1.25 mm, Thickness 1.0 mm	[189]
Electrode dimensions	Length 0.40 mm, Width 1.25 mm	[189]

mm wide and 3-mm thick. The slit pattern of the kirigami structure is presented in the inset. As in the previous section, the slit pattern had a slit width, leave-behind width, and slit pitch of 0.9 mm, 0.1 mm, and 0.1 mm, respectively. The longitudinal period was  $n_L = 69$ . A circular hole was provided at the edge of the slit. The chip resistor was 2-mm long, 1.2-mm wide, and 0.5-mm thick. The chip LED was 2-mm long, 1.25-mm wide, and 1.0-mm thick, with a specified current of 20 mA and voltage of 3.2 V. The electrodes of the chip LEDs were 0.4-mm long and 1.2-mm wide, with 8- $\mu$ l LMs placed on a 2-mm square connection area at the wiring end and on a pad. Both stretching wirings were separated between each component. The pattern of the cutouts is the same as in the previous section. At the intersection of the vertical and horizontal wiring, the three wirings were divided into one and two wirings on either side of the component, and an LM was placed on top of each other, and then two electrodes were placed across the two wirings.

Figure 4.14 illustrates the sample fabrication procedure. First, the outline and kirigami structure of a Cu-polyimide substrate fixed on a weak adhesive sheet were cut using a UV laser cutting machine. The surface of the weak adhesive tape was roughened by a UV laser cutting machine to reduce the adhesive strength. The conditions for laser cutting are presented in Appendix A. The Cu-Polyimide substrate was then transferred onto a 0.5-mm thick elastomer substrate placed on the bottom of the Mold. The Cu surface was fluxed. Galinstan was placed on the pads and wiring end electrodes using a micropipette. Chip resistors were mounted on the LM. The mold was then poured with uncured elastomer. Details of the fabrication procedure are presented in the Appendix A. The mold was cured in an oven at 60°C for 1 h.

A sample prepared by a roll chuck was fixed on a motorized stage. A force gauge was utilized to measure the load while applying displacement in the tensile direction. The resistance of the sample was measured

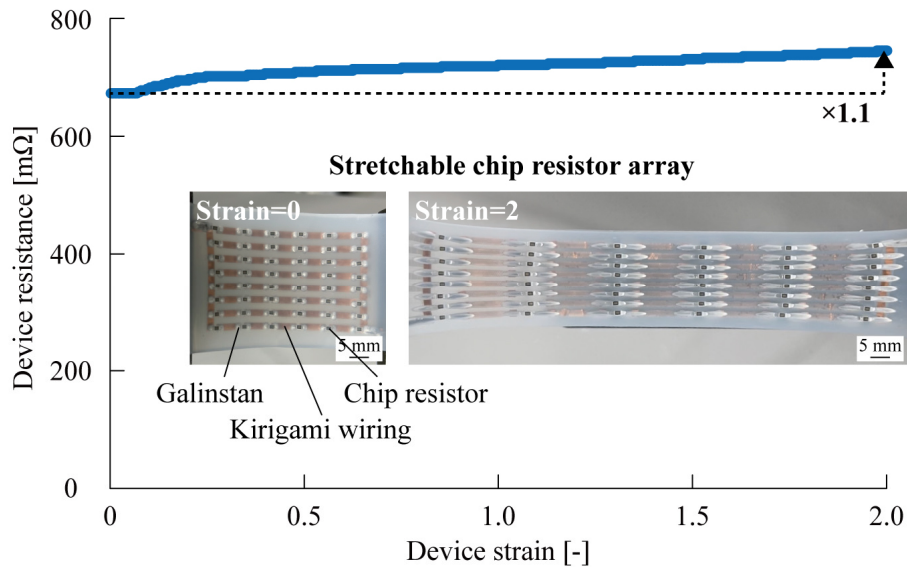


Figure 4.23 Electrical stability of chip resistor arrays for device strain.

by the four-terminal method using a source meter to evaluate electrical stability and detect breakage. The measurement terminals were connected to two connectors on the device. A single-lens reflex camera was utilized to capture the video of the sample during extension, and zero-point alignment and time synchronization of each measurement were performed as in the previous section. The stage movement speed was kept constant at  $10 \text{ mm/min} = 0.16 \text{ mm/s}$ . First, the chip resistor array was pulled to measure the load  $F$  and resistance  $R$  against device strain. The applied current during resistance measurement was  $0.1 \text{ mA}$ . The device strain was calculated by dividing the interstage displacement by the wiring length. The LED array was pulled to check the lighting of each component when the device strain was increased. The applied current was adjusted to  $20 \text{ mA}$  using a source meter. Detailed settings are presented in the Appendix B.

#### 4.5.2 Results and Discussion

Figure 4.23 illustrates the relationship between the device strain and device resistance of the chip resistor array with LM mounting. When device strain was increased from 0% to 200%, device resistance increased from  $640 \text{ m}\Omega$  to  $709 \text{ m}\Omega$ , a 0.11-fold increase. This demonstrates that 200% stretching is feasible for LM-mounted stretchable electronic devices, and that the resistance change during stretching within the device strain = 2 is as low as 10%, thereby demonstrating high electrical stability. The resistance change during

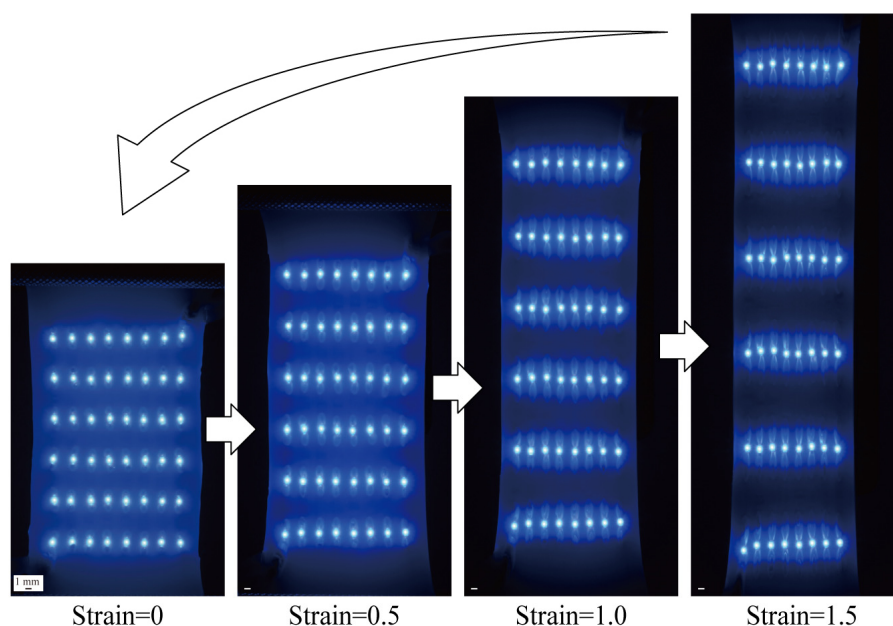


Figure 4.24 Demonstration of stretchable SMD LED chip arrays.

200% expansion/shrinkage was 10%, demonstrating high electrical stability. If a wire is disconnected, the electrical connection is maintained; however, the resistance increases because of the parallel circuit.

Figure 4.24 presents the optical image of the chip LED array as a function of device strain. All components remained lit without disconnection even when the strain was increased from 0% to 150%. Hence, it is clear that the LM mounting maintains stable electrical connection areas even when the device is stretched. This is consistent with the low resistance change during the stretching of the previous device. Overall, in a stretchable electronic device with LM mounting, the wiring breaks during stretching; hence, the stretch tolerance of the device is determined by the stretch tolerance of the wiring. Therefore, this study demonstrated that the device can be stretched until the strain breakage of the wiring, as well as the stability of the electrical connected area of each component. Although the focus tends to be on device stretching, the stretch tolerance of the wiring is critical because the stretchability of the device is determined by the stretchability of the wiring. The component density decreases with the wiring strain for the same device strain. Because the stretching tolerance of a device is determined by the wiring strain, the length ratio of wiring to component is significant. The wiring utilized in this study has a breaking strain of approximately 3, and the length ratio of wiring to component is 5:2 for chip-resistor and chip-LED arrays. Hence, it was demonstrated that the devices can be stretched up to 200% device strain or 2.8 wiring strain. Here, the

higher the component density, the higher the wiring strain for the same device strain, thereby increasing the difficulty of device realization. Considering an electric device that can be stretched to 100% device strain for application to the skin attachment, the proposed method theoretically allows the length ratio of the wiring to the component to be increased up to 1:2.

## 4.6 Conclusions

---

This study presented a method for mounting rigid electronic components such as SMDs on stretchable wirings using a LM for highly stretchable and high-performance electronic devices. Stretchable electronic devices with rigid components mounted on stretchable wiring suffer from breakage around the components due to a stress concentration triggered by significant stiffness and strain difference. To address this challenge, this study proposes the adoption of LMs for mounting to reduce the strain difference by stretching the connected area of the wiring with the component. Stretchable copper wiring with SMD chip resistors mounted using an LM (galinstan) achieved stretch tolerance of 3.0 strain, 5.8 times higher than conventional solder mounting. The study also presented stretchable SMD chip LED arrays. The proposed method improves the stretch tolerance of wiring and provides new opportunities for the development of stretchable electronics.

For stretchable electronic devices with high-performance, rigid electronic components, such as SMD LED chips, and IC chips, mounted on stretchable wiring, the wiring around the components breaks due to the significant strain difference. Hence, a flexible connection between the components and the wiring is critical for reducing the strain difference. In conventional firm connections using solders and conductive adhesives, the connected area of the wiring cannot be stretched; hence, the strain difference is significant. Advanced studies have suppressed wiring breakage using substrates with gradual stiffness distributions; however, the suppression was limited to significant strain differences. In contrast, this study proposes the use of LM for mounting to eliminate strain differences. It was assumed that the wiring was not fixed physically to the components, only connected electrically, and that the connected area of the wiring could be stretched because of the high stretchability of Ga-based LMs.

In Chapter 4, the stretch tolerance of EIMs was studied. Although LM has high stretchability owing to its liquid nature, there is concern about delamination of the LM during stretching because of its high surface tension and poor wettability. Therefore, chip resistors were mounted using galinstan, solder, and flexible conductive adhesive between Cu wirings that did not have stretchability and were encapsulated



with an elastomer. Consequently, the breaking strain of the solder mounting was larger than that of the flexible conductive adhesive, indicating that not only the stretchability of the connecting material but also the bonding force between the connecting material and the components or wiring was critical for the stretch tolerance of the EIMs in stretchable electronic devices. In addition, the LM mounting achieved both high stretchability and bonding force because the resistance change during stretching was caused only by the shape change of the LM, no delamination occurred, and the initial resistance value was restored after unloading. The LM mounting achieved stretch tolerance (wiring strain $>4$ ) that was 12 times higher than that of the solder or conductive paste.

Next, the stretchability of the stretchable metal wire was evaluated. The materials and structures of the wiring have been the focus of attention for stretchable wiring. However, it is thought that even with the same wiring, different wiring end structures can relieve the stress concentration caused by the differences in stiffness and strain. Therefore, the samples with stretchable Cu wiring with the kirigami structure encapsulated in elastomers for different wiring end structures. The separation of the wiring from the gripping substrate and the fabrication of the stretchable structure in the pad areas were compared. As a result, by separating the wiring from the gripping substrate and fabricating the stretching structure to the pad areas, the breakage location changed from the end of wiring to a random location, and the stretchable tolerance improved by 5.2 times compared with that of the wiring connected to the gripping substrate, with the stretchable structure in the pad areas. These results indicate that the stress concentration in the wiring was alleviated, and the stretch tolerance was improved by eliminating the difference in stiffness and strain at the wiring ends.

Furthermore, the effect of the electronic components on stretchable wiring was evaluated. The electronic components were mounted on stretchable Cu wiring with a kirigami structure and encapsulated with elastomers. A stretchable structure was fabricated in the pad areas of the wiring, and solder and galinstan were compared. As a result, the wiring mounted using the solder, without the stretchable structure in the pad areas, broke at the wiring strain, 0.1 times the maximum stretch tolerance of the wiring. In contrast, the wiring mounted using galinstan, without stretchable structures in the pad area broke at the wiring strain, 0.8 times of the maximum stretch tolerance of the wiring. This result indicated that the LM mounting relieved the stress concentration in the wiring, and the stretch tolerance of the wiring was significantly improved. As for the electrical performance, the sample resistance increased only by 1.2 times when the wiring strain=3, demonstrating the low resistance change during stretching. In addition, it was confirmed that the stretchable Cu wiring mounted using galinstan restored the sample resistance after unloading, and

could be repeatedly stretched 463 times at wiring strain=1 and 74 times at wiring strain=2.

Finally, the wiring mounted using galinstan, with the stretchable structures, achieved a stretch tolerance 5.8 times higher than of the solder mounting. The study demonstrated the high stretchability of devices with components mounted using galinstan on stretchable Cu wirings with a kirigami structure. The resistance of the chip resistor arrays increased only 1.1 times under strain=2.0. The SMD LED chip arrays maintained the emission under strain=1.5.

## Chapter 5      Conclusions

### 5.1      Overall Summary

---

This study proposes a novel approach to use LM as an EIM for mounting rigid electronic components on stretchable metal wiring. By clarifying the requirements for a mounting method with low  $R_c$  and developing an  $R_c$  measurement method between LM and SM, a highly stretchable and high-performance electronic device was realized. For stretchable electronic devices using rigid and high-performance SMDs, the connection between the wiring and electronic components is critical, because the stress concentration breaks around the rigid components when the device is stretched. In this study, Ga-based LM was used for mounting to obtain high stretch tolerance and low  $R_c$  because of its liquid nature. However,  $R_c$  may be high owing to the high surface tension and formation of oxide layers on its surface. We evaluated the contact resistance and stretch tolerance of the mounting method using LM to achieve highly stretchable and high-performance electronic devices.

In Chapter 2, the requirements for low  $R_c$  are studied. To evaluate the effect of the physical rupture of the oxide layer and alloying on the  $R_c$  reduction, the contact procedures between the LM and SM were investigated. In the L-S method, SM (S) is brought into contact with LM (L), on which an oxide layer has

been sufficiently formed; in the S-L method, LM is brought into contact by injection after placing the SM, aiming at physically rupturing the oxide layer; in the S-L-V method, vacuum is applied (V) after the injection to physically break down the oxide layer. Comparing the S-L and S-L-V methods, which aim to physically rupture the oxide layer, it was found that the  $R_c$  immediately after contact was reduced to 1/10 that of the L-S method, in which the oxide layer was fully formed. Comparing the S-L and S-L-V methods, which aim to physically rupture the oxide layer, it was found that the  $R_c$  immediately after contact was reduced to 1/10 that of the L-S method, in which the oxide layer was fully formed. Note that the S-L-V method has low reproducibility owing to LM leakage. Thus, in addition to non-heating, the S-L method was used in Chapter 3 for reproducibility, and the L-S method was used in Chapter 4 for simplicity.

In Chapter 3, an  $R_c$  measurement method for LM using the Transfer Length Method (TLM) is proposed by considering the current density distribution. In conventional TLM, it is assumed that the sheet resistance of the metal electrode is negligible for an object (e.g., a semiconductor). The current applied to the outer electrode flows two-dimensionally, and all the current passes through the contact interface. However, because the conductivity of the LM is the same as that of the metal electrode, there is a concern that this assumption may be problematic. This study proposes the application of current to each measurement electrode and compares the measured values with current density distribution analysis using the finite element method. In conventional TLM, the applied current flows two-dimensionally, and the entire applied current passes through the contact interface for objects with high sheet resistance, such as semiconductors. However, for objects with low sheet resistance, such as LM, only 1/10 or less of the applied current passes through the interface, making  $R_c$  measurement impossible. In contrast, in the improved TLM, the applied current flows three-dimensionally, the entire applied current passes through the interface regardless of the sheet resistance ratio, and  $R_c$  of the LM can also be measured. Thus, it is clear that objects with high sheet resistance should be measured with the conventional TLM for simplicity, whereas objects with low sheet resistance, such as LM, must be measured with the improved TLM.

In Chapter 4, the stretch tolerance of the EIM is evaluated. The breaking strain of the solder mounting was greater than that of the flexible conductive adhesive. This result shows that not only the stretchability of the connecting material, but also the bonding force between the EIM and the components or wiring is crucial for the stretch tolerance of the EIM. Furthermore, LM achieved stretch tolerance (strain=4), which was 12 times higher than that of the solder or conductive paste. LM did not delaminate during stretching, and high stretchability and bonding force of the LM were demonstrated. Next, the stretch tolerance of stretchable metal wiring was evaluated for different end structures. By separating the wiring from the

gripping substrate and providing a stretchable structure to the pad areas of the wiring, the stretch tolerance was 6.1 times higher than that of the case where the wiring was not separated from the gripping substrate, and no stretchable structure was provided to the pad area. These results show that the stress concentration in the wiring can be relieved and the stretch tolerance can be improved by eliminating the difference in stiffness and strain at the wiring ends. Furthermore, the stretch tolerance of the wiring for EIMs was evaluated. The electronic components were mounted on stretchable metal wiring. The solder mounted wiring broke at 0.1 times the maximum stretch tolerance of the wiring alone, whereas the LM broke at 0.8 times the maximum stretch tolerance. This result shows that the stress concentration in the wiring is relieved by the LM, and that the stretch tolerance of the metal wiring can be significantly improved. Regarding the electrical performance, the resistance change at strain=3 was 1.2 times, demonstrating a low resistance change. Finally, the stretch tolerance of the stretchable electronic devices was demonstrated. The stretched chip resistor array exhibited a resistance change of 1.1 times at strain=2, whereas the stretched chip LED array remained stable from stretching to unloading even at strain=1.5. The proposed device has a stretchability of more than strain=2, which exceeds the maximum stretchability of the human skin (strain<0.7) and high electrical reliability. This result demonstrates a highly stretchable and high-performance electronic device based on the LM mounting.

In Chapter 5, the conclusion is presented. This thesis tackled the new challenge of using LM as an EIM between metal wiring and rigid electronic components. A novel measurement method for  $R_c$  was developed to elucidate the phenomenon, and a configuration for a stretchable electronic device with high stretchability and performance was proposed. The evaluation results of  $R_c$  show that physically rupturing the oxide layer on the surface of LM and alloying of an electrode surface are effective in reducing the  $R_c$  between LM and a metal electrode. Furthermore, it is shown that TLM, which was previously used for the measurement of  $R_c$  between semiconductors and metal electrodes, is not applicable to the measurement of  $R_c$  between LM and metal wiring, where both materials have high electrical conductivity. A new measurement method was developed to enable measurement by considering the current density distribution and the location of the current application. The evaluation results of stretch tolerance clarify that LM not only has a high stretch tolerance itself but also brings out the performance of stretchable wiring. Thus, LM, which has previously attracted attention as stretchable wirings and sensors, showed significant electrical and mechanical advantages in a new application as an “EIM,” and realized a highly stretchable and high-performance electronic device.

## 5.2 Future Prospect

---

### 5.2.1 Application for Conventional Mounting Methods

This study has given us the possibility of significantly reducing  $R_c$  by physically rupturing the oxide layer of the LM. It is expected that a low  $R_c$  can be obtained in stretchable electronic devices such as wearable and medical devices by mounting electronic components using an LM and physically rupturing the oxide layer of the LM by various physical stimuli. For example, injection, decompression, and vibration are considered effective. This study also found that  $R_c$  decreased over time by alloying. Based on this finding, the author believe that a low  $R_c$  can be obtained immediately after mounting by alloying. A low  $R_c$  can be obtained by coating the electronic components and wiring surfaces with LM alloys. The time required for  $R_c$  to decrease can be significantly shortened by accelerating the alloying by heating. By reducing  $R_c$  with the proposed method, power consumption at the component mounting area and destruction due to thermal expansion caused by heat generation can be suppressed. Because this method can be applied to any type of wiring and components, once established, it is expected to have a large ripple effect industrially. In addition to the stretchable metal wiring with kirigami structure used in this study, it is thought to be applicable to the wiring of various materials and structures. For example, stretchable metal wiring with a serpentine or origami structure and wiring using conductive pastes or polymers. In addition to the chip resistors and LEDs used in this study, various other components can also be mounted. Examples include rigid-sensor components, batteries, microcomputers, and wireless communication modules. The density of electronic components is also critical for high-performance electronic devices. The size of the LM mounting was mainly determined by the LM. The high surface tension of LMs makes fine patterning difficult; however, the development of new LM materials and patterning methods has achieved fine patterning of a few micrometers in recent years. If fine patterning methods are developed in the future, LM mounting can be applied not only to packaged components but also to bare chips without packages.

### 5.2.2 Impacts on Science and Industry

This study is expected to have a significant ripple effect in both the scientific and industrial fields. For scientific and technological impacts, a highly accurate measurement method for  $R_c$  of the LM has been highly evaluated in the scientific field. This study was accepted twice to the most prestigious international conference in the field (*The International Conference on Micro Electro Mechanical Systems (IEEE*

*MEMS*)) and published twice in *ACS Appl. Mater. Interfaces*: an international journal with an impact factor of 10.380. Based on this study, a better understanding of  $R_c$  is expected to make a significant contribution to the fields of materials and interface science. As for the ripple effect in the industrial field, a construction and connector company consulted us and applied LM mounting technology to reinforce the connector part of harnesses used at construction sites. Thus, this study has also been highly evaluated in terms of device applications and is expected to make a significant contribution to the social economy.

### 5.2.3 Development of Proposed Mounting Method

In the future, the applicability and versatility of LM-mounting should be improved by eliminating the encapsulations. The wide use of Ga-based LMs is hindered because encapsulation structures are required for the LMs. The author is considering expanding the range of device configurations by controlling the viscosity and adhesiveness of LM paste and eliminating the encapsulations. Electronic devices that self-repair and reconfigure themselves can be developed using the LMs. The LMs can self-repair and re-conduct once disconnected and can be used in environments where repair and maintenance are difficult, such as in space, underground, and structures. This idea can be expanded to electronic devices that can reconfigure their circuits according to the environment or measurement target by changing the arrangement of LM by external stimuli such as electric or magnetic fields after device fabrication. Furthermore, for sports and medical applications, the comfortability of devices attached to the human skin should be improved. For this purpose, the author is working on stretchable electronic devices using a thin polymer sheet as a flexible substrate. Although sensor devices using thin polymer substrates have excellent properties such as adhesion to biological tissues and self-adhesiveness. However, the stiffness of the substrate is low and easily broken. Robust thin-film electronic devices can be realized by using LM-mounting.

The development of stretchable electronics will realize innovative hardware that connects real and cyber worlds, contributing to resilient societies. Devices that work in real space can be applied to electronic circuit skin on the surface of communicative robots, electronic circuits inside soft robots, and thermoelectric power generation sheets that can be attached to free curved surfaces such as heat pipes. The author also believes that devices that collect data from real space can be applied to biomonitoring devices that measure the body movements of athletes, and sensor sheets that measure surface shear forces when embedded in swimsuits. The application of the proposed mounting method to non-deformable electronic devices is also very wide. For instance, the proposed method can improve the tolerance of conventional

rigid electronic devices, such as automotive electronic devices, against thermal expansion and vibration.



## Appendix A Fabrication Procedures

### Conditions of UV laser cutter for cutting Cu-polyimide substrate (Chapter 2-4)

Parameters	Values
Substrate thickness	Cu: 8 $\mu\text{m}$ , polyimide: 25 $\mu\text{m}$
Velocity	50.00 mm/s
Power	20.00%
Frequency	70.000 kHz
Cycle	2
Spot delay	0.100 ms
Duty cycle	33.0 %

### Conditions of UV laser cutter for cutting Cu substrate (Chapter 4)

Parameters	Values
Substrate thickness	Cu: 30 $\mu\text{m}$
Velocity	50.00 mm/s
Power	20.00%
Frequency	50.000 kHz
Cycle	2
Spot delay	0.100 ms
Duty cycle	25.0 %

### Conditions of UV laser cutter for cutting PET substrate with 0.5 mm thickness (Chapter 4)

Parameters	Values
Substrate thickness	PET: 0.5 mm
Velocity	50.00 mm/s

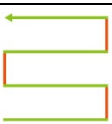
---

*Appendix A Fabrication Procedures*

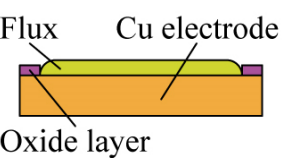

---

Power	20.00%
Frequency	50.000 kHz
Cycle	2
Spot delay	0.100 ms
Duty cycle	25.0 %

**Conditions of UV laser cutter for roughening weak adhesive tape (Chapter 4)**

Parameters	Values
Velocity	1000.00 mm/s
Power	20.00%
Frequency	50.000 kHz
Cycle	1
Spot delay	0.100 ms
Duty cycle	30.0 %
Edge	0.0000
Round pitch	0.0500
Pitch	0.0500
Cycle	2
Start angle	0.0000
Finish angle	90.0000
Style	

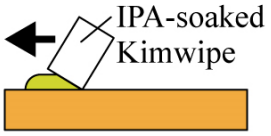

**Procedures for flux treatment (Chapter 2-4)**

Cross sectional view	Procedures	Conditions
	Deposition of flux on the Cu electrode	Leave the Cu electrode for 30 s after deposition of the flux

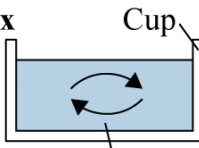
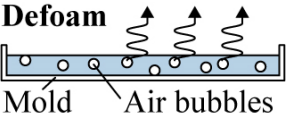

---

*Appendix A Fabrication Procedures*


---

 <p>IPA-soaked Kimwipe</p>	Removal of flux from the Cu electrode	Kimwipe soaked in IPA
	Evaporation of IPA	Leave in the air for 5 min

**Procedures to mix and cure the silicone rubber (Chapter 2-4)**

Cross sectional view	Procedures	Conditions
<p><b>Mix</b></p>  <p>Cup</p> <p>Uncured silicone rubber</p>	Mixing uncured silicone rubber and defoam using an mixer	<ol style="list-style-type: none"> <li>2000 rpm for 30 s to mix</li> <li>2200 rpm for 30 s to defoam</li> </ol>
<p><b>Defoam</b></p>  <p>Mold</p> <p>Air bubbles</p>	Defoam the rubber using an vacuum chamber	-0.09 MPa (gauge pressure) for 10 min
<p><b>Heat</b></p>  <p>Cured silicone rubber</p>	Heating the rubber for curing	60°C of 1 h

## Appendix B Measurement Conditions

### Conditions of resistance measurements using source meter (Chapter 2, 4)

Parameters	Values
Model	2614B and Kickstart, Keithley, OH, US
Source	DC
Mode	Current bias
Current level	1.5 A
Current range	Auto
Limit	5 V
Voltage measurement	Yes
Voltage range	Auto
Minimum range	200 mV
Other measurement	Resistance
Measurement speed	25 NPLC = 2 fps
Sense	4-wire

### Conditions of resistance measurements using ohm meter (Chapter 3)

Parameters	Values
Model	RM3545, Hioki, Nagano, Japan
Range	100 m $\Omega$
Offset voltage correction (OVC)	Yes
Low current	Yes
Speed	Slow 2

**Conditions of resistance measurements using switch main frame (Chapter 3)**

Parameters	Values
Model	SW1002, Hioki, Nagano, Japan
Logging Interval	15 s
Measurement times	10 times
Measurement channel	1–15

**Conditions of resistance measurements using force gauge (Chapter 4)**

Parameters	Values
Force gauge	ZTS-5N and ZTS-200N, IMADA, Aichi, Japan
Motorized stage	FSA-0.5K2, IMADA, Aichi, Japan
Stage speed	10 mm/min for breakage test 80 mm/min for cyclic test
Measurement speed	10 fps

## Appendix C Letters

Letter	Meaning	First appearance page	Letter	Meaning	First appearance page
A, B	Constant	108	$R_c$	Contact resistance	3
$E_{\text{average}}$	Young's modulus of sample	115	$r_c$	$R_c$ in each small region	81
$I$	Applied current	22	$R_c^{\text{Total}}$	Resistance of contact area	22
$i_1, i_2, \dots, i_n$	Current passing through the interface in each small area	81	$R_e$	Electrode resistance	70
$I_i$	Current passing through the interface	23	$r_e$	Electrode resistance in each small region	81
$J_z$	The current density crossing the interface	84	$R_{\text{LM}}$	Resistances of LM	47
$K_\alpha, K_\beta$	Emission lines	60	$R_{\text{max}}$	$R$ at the maximum strain	104
$L_e$	Length of electrode	82	$R_{\text{min}}$	$R$ at 0% strain	104
$L_{\text{LM}}$	Length of LM in the tensile direction	108	$R_{\text{mount}}$	Resistance at the mounted area	125
$l_{\text{LM}}$	Length of LM	50	$R_o$	Object resistance	22
$L_o$	Length of object	22	$r_o$	Object resistance in each small region	81
$l_{\text{SM}}$	Length of SM	50	$R_{\text{she}}$	Sheet resistance of the electrode	24
$L_T$	Transfer length	76	$R_{\text{sho}}$	Sheet resistance	22
$n_L$	Longitudinal period	113	$R_{\text{SM}}$	Resistance of SM	47
$n_w$	Widewise period	113	$R_{\text{wiring}}$	Wiring resistance	125
$p_{\text{t-test}}$	p-value in t-test	50	$S_c$	Contact area	50
$R$	Measured resistance	22	$t_{\text{t-test}}$	t-value in t-test	50
$R_a$	Surface roughness	88	$t$	Lapsed time	57

Letter	Meaning	First appearance page	Letter	Meaning	First appearance page
$T_e$	Thickness of the electrode	84	$\theta$	Diffraction angle	60
$t_{LM}$	Thickness of the LM	50	$\rho_e$	Contact resistivity	24
$T_o$	Thickness of the object	84	$\rho_e$	Volume resistivity of the electrode	84
$t_{SM}$	Thickness of the SM	50	$\rho_{LM}$	Volume resistivity of the LM	50
$V$	Measured voltage	22	$\rho_o$	Volume resistivity of the object	84
$W_e$	Electrode width	84	$\rho_{SM}$	Volume resistivity of the SM	50
$w_{LM}$	Width of LM	50	$\sigma_{average}$	Average strain	114
$W_o$	Object width	84	$\Phi I$	Potentials in the contact area	84
$w_{SM}$	Width of SM	50	$\Phi II$	Potentials in the object	84
$\alpha_{SM}$	Resistance of SM per unit length	50			

## References

- [1] S. Liu, S. N. Reed, M. J. Higgins, M. S. Titus, and R. Kramer-Bottiglio, “Oxide rupture-induced conductivity in liquid metal nanoparticles by laser and thermal sintering,” *Nanoscale*, vol. 11, no. 38, pp. 17615–17629, 2019.
- [2] R. A. Matula, “Electrical resistivity of copper, gold, palladium, and silver,” *J. Phys. Chem. Ref. Data*, vol. 8, no. 4, pp. 1147–1298, 1979.
- [3] G. Li, X. Wu, and D. W. Lee, “Selectively plated stretchable liquid metal wires for transparent electronics,” *Sens. Actuators B Chem.*, vol. 221, pp. 1114–1119, 2015.
- [4] S. Zhu *et al.*, “Ultrastretchable fibers with metallic conductivity using a liquid metal alloy core,” *Adv. Funct. Mater.*, vol. 23, no. 18, pp. 2308–2314, 2013.
- [5] Y. Lu *et al.*, “Transformable liquid-metal nanomedicine,” *Nat. Commun.*, vol. 6, p. 10066, 2015.
- [6] S. Cai *et al.*, “Gallium nitride formation in liquid metal sonication,” *J. Mater. Chem.*, vol. 8, no. 46, pp. 16593–16602, 2020.
- [7] I. D. Joshipura, H. R. Ayers, C. Majidi, and M. D. Dickey, “Methods to pattern liquid metals,” *J. Mater. Chem.*, vol. 3, no. 16, pp. 3834–3841, 2015.
- [8] C. B. Cooper *et al.*, “Stretchable capacitive sensors of torsion, strain, and touch using double helix liquid metal fibers,” *Adv. Funct. Mater.*, vol. 27, no. 20, 1605630, 2017.
- [9] Y. Gao *et al.*, “Wearable microfluidic diaphragm pressure sensor for health and tactile touch monitoring,” *Adv. Mater.*, vol. 29, no. 39, 1701985, 2017.
- [10] J. H. So, J. Thelen, A. Qusba, G. J. Hayes, G. Lazzi, and M. D. Dickey, “Reversibly deformable and mechanically tunable fluidic antennas,” *Adv. Funct. Mater.*, vol. 19, no. 22, pp. 3632–3637, 2009.
- [11] M. Kubo *et al.*, “Stretchable microfluidic radiofrequency antennas,” *Adv. Mater.*, vol. 22, no. 25, pp. 2749–2752, 2010.



- 
- [12] K. Yamagishi, W. Zhou, T. Ching, S. Y. Huang, and M. Hashimoto, “Ultra-deformable and tissue-adhesive liquid metal antennas with high wireless powering efficiency,” *Adv. Mater.*, vol. 33, no. 26, e2008062, 2021.
- [13] A. Zatopa, S. Walker, and Y. Menguc, “Fully soft 3D-printed electroactive fluidic valve for soft hydraulic robots,” *Soft Robotics*, vol. 5, no. 3, pp. 258–271, 2018.
- [14] R. Matsuda, Z. Song, and H. Ota, “Electro-powerless balloon soft actuator with manually driven fluidic circuit,” *Adv. Electron. Mater.*, vol. 9, no. 3, 2201065, 2023.
- [15] D. Tachibana *et al.*, “Ultrafast and highly deformable electromagnetic hydrogel actuators assembled from liquid metal gel fiber,” *Advanced Intelligent Systems*, vol. 4, no. 5, 2100212, 2022.
- [16] N. Ochirkhuyag *et al.*, “Stretchable gas barrier films using liquid metal toward a highly deformable battery,” *ACS Appl. Mater. Interfaces*, vol. 14, no. 42, pp. 48123–48132, 2022.
- [17] Q. Wang, Y. Yu, J. Yang, and J. Liu, “Fast fabrication of flexible functional circuits based on liquid metal dual-trans printing,” *Adv. Mater.*, vol. 27, no. 44, pp. 7109–7116, 2015.
- [18] K. B. Ozutemiz, J. Wissman, O. B. Ozdoganlar, and C. Majidi, “EGaIn–metal interfacing for liquid metal circuitry and microelectronics integration,” *Adv. Mater. Interfaces*, vol. 5, no. 10, 1701596, 2018.
- [19] H. Ota *et al.*, “Application of 3D printing for smart objects with embedded electronic sensors and systems,” *Adv. Mater. Technol.*, vol. 1, no. 1, 1600013, 2016.
- [20] M. Zadan, M. H. Malakooti, and C. Majidi, “Soft and stretchable thermoelectric generators enabled by liquid metal elastomer composites,” *ACS Appl. Mater. Interfaces*, vol. 12, no. 15, pp. 17921–17928, 2020.
- [21] T. Liu, P. Sen, and C.-J. Kim, “Characterization of nontoxic liquid-metal alloy galinstan for applications in microdevices,” *J. Microelectromech. Syst.*, vol. 21, no. 2, pp. 443–450, 2012.
- [22] T. Daeneke *et al.*, “Liquid metals: fundamentals and applications in chemistry,” *Chem. Soc. Rev.*, vol. 47, no. 11, pp. 4073–4111, 2018.
- [23] G. Li, M. Parmar, D. Kim, J. B. Lee, and D. W. Lee, “PDMS based coplanar microfluidic channels for the surface reduction of oxidized Galinstan,” *Lab Chip*, vol. 14, no. 1, pp. 200–209, 2014.
- [24] M. D. Dickey, “Emerging applications of liquid metals featuring surface oxides,” *ACS Appl. Mater. Interfaces*, vol. 6, no. 21, pp. 18369–18379, 2014.

---

*References*

---

- [25] D. Kim, D.-W. Lee, W. Choi, and J.-B. Lee, "A super-lyophobic 3-D PDMS channel as a novel microfluidic platform to manipulate oxidized galinstan," *J. Microelectromech. Syst.*, vol. 22, no. 6, pp. 1267–1275, 2013.
- [26] R. K. Kramer, J. W. Boley, H. A. Stone, J. C. Weaver, and R. J. Wood, "Effect of microtextured surface topography on the wetting behavior of eutectic gallium-indium alloys," *Langmuir*, vol. 30, no. 2, pp. 533–539, 2014.
- [27] G. Li, M. Parmar, and D.-W. Lee, "An oxidized liquid metal-based microfluidic platform for tunable electronic device applications," *Lab Chip*, vol. 15, no. 3, pp. 766–775, 2015.
- [28] S. S. Kadlaskar, J. H. Yoo, Abhijeet, J. B. Lee, and W. Choi, "Cost-effective surface modification for Galinstan® lyophobicity," *J. Colloid Interface Sci.*, vol. 492, pp. 33–40, 2017.
- [29] A. I. Ancharov, T. F. Grigoryeva, A. P. Barinova, and V. V. Boldyrev, "Interaction between copper and gallium," *Russ. Metall. (Met.)*, vol. 2008, no. 6, pp. 475–479, 2008.
- [30] N. Zhang, P. Shen, Y. Cao, R. F. Guo, and Q. C. Jiang, "Electrically induced spreading of EGaIn on Cu substrate in an alkali solution under wetting and non-wetting conditions," *Appl. Surf. Sci.*, vol. 490, pp. 598–603, 2019.
- [31] S. Liu *et al.*, "Properties of CuGa<sub>2</sub> formed between liquid ga and Cu substrates at room temperature," *J. Electron. Mater.*, vol. 49, no. 1, pp. 128–139, 2020.
- [32] C. A. Nijhuis, W. F. Reus, and G. M. Whitesides, "Mechanism of rectification in tunneling junctions based on molecules with asymmetric potential drops," *J. Am. Chem. Soc.*, vol. 132, no. 51, pp. 18386–18401, 2010.
- [33] T. V. Kulikova, V. A. Bykov, K. Y. Shunyaev, and A. B. Shubin, "Thermal properties of CuGa<sub>2</sub> phase in inert atmosphere," *Diffus. Defect Data Pt. A*, vol. 326–328, pp. 227–232, 2012.
- [34] S. K. Lin, C. L. Cho, and H. M. Chang, "Interfacial reactions in Cu/Ga and Cu/Ga/Cu couples," *J. Electron. Mater.*, vol. 43, no. 1, pp. 204–211, 2014.
- [35] J. Tang, X. Zhao, J. Li, R. Guo, Y. Zhou, and J. Liu, "Gallium-based liquid metal amalgams: transitional-state metallic mixtures (TransM<sup>2</sup>ixes) with enhanced and tunable electrical, thermal, and mechanical properties," *ACS Appl. Mater. Interfaces*, vol. 9, no. 41, pp. 35977–35987, 2017.
- [36] J. Tang, X. Zhao, J. Li, Y. Zhou, and J. Liu, "Liquid metal phagocytosis: intermetallic wetting induced particle internalization," *Adv. Sci. Lett.*, vol. 4, no. 5, 2017.
- [37] J. L. Ma, H. X. Dong, and Z. Z. He, "Electrochemically enabled manipulation of gallium-based liquid metals within porous copper," *Materials Horizons*, vol. 5, no. 4, pp. 675–682, 2018.

- 
- [38] Y. Cui *et al.*, “Metallic bond-enabled wetting behavior at the liquid Ga/CuGa<sub>2</sub> interfaces,” *ACS Appl. Mater. Interfaces*, vol. 10, no. 11, pp. 9203–9210, 2018.
- [39] M. I. Ralphs *et al.*, “In situ alloying of thermally conductive polymer composites by combining liquid and solid metal microadditives,” *ACS Appl. Mater. Interfaces*, vol. 10, no. 2, pp. 2083–2092, 2018.
- [40] Y. Liu, M. Pharr, and G. A. Salvatore, “Lab-on-Skin: A review of flexible and stretchable electronics for wearable health monitoring,” *ACS Nano*, vol. 11, no. 10, pp. 9614–9635, 2017.
- [41] S. Bauer, S. Bauer-Gogonea, I. Graz, M. Kaltenbrunner, C. Keplinger, and R. Schwödiauer, “25th anniversary article: A soft future: From robots and sensor skin to energy harvesters,” *Adv. Mater.*, vol. 26, no. 1, pp. 149–162, 2014.
- [42] Y. Zang *et al.*, “25th anniversary article: The evolution of electronic skin (E-Skin): A brief history, design considerations, and recent progress,” *Adv. Mater.*, vol. 2, no. 1, pp. 5997–6038, 2010.
- [43] J. H. Ahn and J. H. Je, “Stretchable electronics: Materials, architectures and integrations,” *J. Phys. D Appl. Phys.*, vol. 45, no. 10, 2012.
- [44] T. Sekitani and T. Someya, “Stretchable, large-area organic electronics,” *Adv. Mater.*, vol. 22, no. 20, pp. 2228–2246, May 2010.
- [45] J. A. Rogers, T. Someya, and Y. Huang, “Materials and mechanics for stretchable electronics,” *Science*, vol. 327, no. 5973, pp. 1603–1607, 2010.
- [46] D.-H. Kim, J. Xiao, J. Song, Y. Huang, and J. A. Rogers, “Stretchable, curvilinear electronics based on inorganic materials,” *Adv. Mater.*, vol. 22, no. 19, pp. 2108–2124, 2010.
- [47] M. Amjadi, Y. J. Yoon, and I. Park, “Ultra-stretchable and skin-mountable strain sensors using carbon nanotubes-Ecoflex nanocomposites,” *Nanotechnology*, vol. 26, no. 37, p. 375501, 2015.
- [48] M. Ahirwar and B. K. Behera, “Prediction of shrinkage behavior of stretch fabrics using machine-learning based artificial neural network,” *Text. Usages Tech.*, vol. 3, no. 1, pp. 88–97, 2023.
- [49] J. Ge *et al.*, “A stretchable electronic fabric artificial skin with pressure-, lateral strain-, and flexion-sensitive properties,” *Adv. Mater.*, vol. 28, no. 4, pp. 722–728, 2016.
- [50] X. He *et al.*, “Highly stretchable, durable, and breathable thermoelectric fabrics for human body energy harvesting and sensing,” *Carbon Energy*, vol. 4, no. 4, pp. 621–632, 2022.
- [51] T. Sun, B. Zhou, Q. Zheng, L. Wang, W. Jiang, and G. J. Snyder, “Stretchable fabric generates electric power from woven thermoelectric fibers,” *Nat. Commun.*, vol. 11, no. 1, p. 572, 2020.

---

*References*

---

- [52] T. Sekitani, U. Zschieschang, H. Klauk, and T. Someya, “Flexible organic transistors and circuits with extreme bending stability,” *Nat. Mater.*, vol. 9, no. 12, pp. 1015–1022, 2010.
- [53] M. Kaltenbrunner *et al.*, “Ultrathin and lightweight organic solar cells with high flexibility,” *Nat. Commun.*, vol. 3, 770, 2012.
- [54] T. Sekitani *et al.*, “Stretchable active-matrix organic light-emitting diode display using printable elastic conductors,” *Nat. Mater.*, vol. 8, no. 6, pp. 494–499, 2009.
- [55] S. Xu *et al.*, “Soft microfluidic assemblies of sensors, circuits, and radios for the skin,” *Science*, vol. 344, no. 6179, pp. 70–74, 2014.
- [56] J. Byun *et al.*, “Electronic skins for soft, compact, reversible assembly of wirelessly activated fully soft robots,” *Sci Robot*, vol. 3, no. 18, 2018.
- [57] H. Cho, Y. Lee, B. Lee, J. Byun, S. Chung, and Y. Hong, “Stretchable strain-tolerant soft printed circuit board: a systematic approach for the design rules of stretchable interconnects,” *J. Soc. Inf. Disp.*, vol. 21, no. 1, pp. 41–47, 2020.
- [58] J. Song, X. Feng, and Y. Huang, “Mechanics and thermal management of stretchable inorganic electronics,” *National Science Review*, vol. 3, no. 1, pp. 128–143, 2016.
- [59] H. Taniyama and E. Iwase, “Design of a kirigami structure with a large uniform deformation region,” *Micromachines*, vol. 12, no. 1, 2021.
- [60] R.-H. Kim *et al.*, “Waterproof AlInGaP optoelectronics on stretchable substrates with applications in biomedicine and robotics,” *Nat. Mater.*, vol. 9, no. 11, pp. 929–937, 2010.
- [61] M. Cai, S. Nie, Y. Du, C. Wang, and J. Song, “Soft elastomers with programmable stiffness as strain-isolating substrates for stretchable electronics,” *ACS Appl. Mater. Interfaces*, vol. 11, no. 15, pp. 14340–14346, 2019.
- [62] G. Cantarella *et al.*, “Design of engineered elastomeric substrate for stretchable active devices and sensors,” *Adv. Funct. Mater.*, vol. 28, no. 30, 1705132, 2018.
- [63] M. Drack, I. Graz, T. Sekitani, T. Someya, M. Kaltenbrunner, and S. Bauer, “An imperceptible plastic electronic wrap,” *Adv. Mater.*, vol. 27, no. 1, pp. 34–40, 2015.
- [64] Y. Lim *et al.*, “Biaxially stretchable, integrated array of high performance microsupercapacitors,” *ACS Nano*, vol. 8, no. 11, pp. 11639–11650, 2014.
- [65] Y. Liu *et al.*, “Stretchable motion memory devices based on mechanical hybrid materials,” *Adv. Mater.*, vol. 29, no. 34, 2017.

- [66] T. Kim, H. Lee, W. Jo, T.-S. Kim, and S. Yoo, "Realizing stretchable OLEDs: A hybrid platform based on rigid island arrays on a stress-relieving bilayer structure," *Adv. Mater. Technol.*, vol. 5, no. 11, 2000494, 2020.
- [67] M. S. Lim *et al.*, "Two-dimensionally stretchable organic light-emitting diode with elastic pillar arrays for stress relief," *Nano Lett.*, vol. 20, no. 3, pp. 1526–1535, 2020.
- [68] S.-W. Jung *et al.*, "Non-volatile organic ferroelectric memory transistors fabricated using rigid polyimide islands on an elastomer substrate," *J. Mater. Chem.*, vol. 4, no. 20, pp. 4485–4490, 2016.
- [69] J.-S. Choi *et al.*, "Stretchable organic thin-film transistors fabricated on wavy-dimensional elastomer substrates using stiff-island structures," *IEEE Electron Device Lett.*, vol. 35, no. 7, pp. 762–764, 2014.
- [70] T. Sekitani, Y. Noguchi, K. Hata, T. Fukushima, T. Aida, and T. Someya, "A rubberlike stretchable active matrix using elastic conductors," *Science*, vol. 321, no. 5895, pp. 1468–1472, 2008.
- [71] N. Matsuhisa, X. Chen, Z. Bao, and T. Someya, "Materials and structural designs of stretchable conductors," *Chem. Soc. Rev.*, vol. 48, no. 11, pp. 2946–2966, 2019.
- [72] C. Keplinger, J.-Y. Sun, C. C. Foo, P. Rothmund, G. M. Whitesides, and Z. Suo, "Stretchable, transparent, ionic conductors," *Science*, vol. 341, no. 6149, pp. 984–987, 2013.
- [73] J.-Y. Sun, C. Keplinger, G. M. Whitesides, and Z. Suo, "Ionic skin," *Adv. Mater.*, vol. 26, no. 45, pp. 7608–7614, 2014.
- [74] K. P. Mineart, Y. Lin, S. C. Desai, A. S. Krishnan, R. J. Spontak, and M. D. Dickey, "Ultrastretchable, cyclable and recyclable 1- and 2-dimensional conductors based on physically cross-linked thermoplastic elastomer gels," *Soft Matter*, vol. 9, no. 32, pp. 7695–7700, 2013.
- [75] J. Kang *et al.*, "Tough and water-insensitive self-healing elastomer for robust electronic skin," *Adv. Mater.*, vol. 30, no. 13, e1706846, 2018.
- [76] M. D. Bartlett, A. Fassler, N. Kazem, E. J. Markvicka, P. Mandal, and C. Majidi, "Stretchable, high-k dielectric elastomers through liquid-metal inclusions," *Adv. Mater.*, vol. 28, no. 19, pp. 3726–3731, 2016.
- [77] M. Vosgueritchian, D. J. Lipomi, and Z. Bao, "Highly conductive and transparent PEDOT:PSS films with a fluorosurfactant for stretchable and flexible transparent electrodes," *Adv. Funct. Mater.*, vol. 22, no. 2, pp. 421–428, 2012.
- [78] S. Savagatrup *et al.*, "Plasticization of PEDOT:PSS by common additives for mechanically robust organic solar cells and wearable sensors," *Adv. Funct. Mater.*, vol. 25, no. 3, pp. 427–436, 2015.

---

*References*

---

- [79] Y. Wang *et al.*, “A highly stretchable, transparent, and conductive polymer,” *Sci Adv*, vol. 3, no. 3, e1602076, 2017.
- [80] V. R. Feig, H. Tran, M. Lee, and Z. Bao, “Mechanically tunable conductive interpenetrating network hydrogels that mimic the elastic moduli of biological tissue,” *Nat. Commun.*, vol. 9, 2740, 2018.
- [81] D. J. Lipomi *et al.*, “Skin-like pressure and strain sensors based on transparent elastic films of carbon nanotubes,” *Nat. Nanotechnol.*, vol. 6, no. 12, pp. 788–792, 2011.
- [82] N. Matsuhisa *et al.*, “Printable elastic conductors by in situ formation of silver nanoparticles from silver flakes,” *Nat. Mater.*, vol. 16, no. 8, pp. 834–840, 2017.
- [83] T. Fukushima *et al.*, “Molecular ordering of organic molten salts triggered by single-walled carbon nanotubes,” *Science*, vol. 300, no. 5628, pp. 2072–2074, 2003.
- [84] R. Ma, B. Kang, S. Cho, M. Choi, and S. Baik, “Extraordinarily high conductivity of stretchable fibers of polyurethane and silver nanoflowers,” *ACS Nano*, vol. 9, no. 11, pp. 10876–10886, 2015.
- [85] N. Matsuhisa *et al.*, “Printable elastic conductors with a high conductivity for electronic textile applications,” *Nat. Commun.*, vol. 6, 7461, 2015.
- [86] W. Dang, V. Vinciguerra, L. Lorenzelli, and R. Dahiya, “Printable stretchable interconnects,” *Flexible and Printed Electronics*, vol. 2, no. 1, 2017.
- [87] W. Guo *et al.*, “Stretchable conductive elastomer for wireless wearable communication applications,” *ACS Appl. Mater. Interfaces*, vol. 7, no. 1, pp. 8567–8575, 2019.
- [88] S. Choi, S. I. Han, D. Kim, T. Hyeon, and D. H. Kim, “High-performance stretchable conductive nanocomposites: Materials, processes, and device applications,” *Chem. Soc. Rev.*, vol. 48, no. 6, pp. 1566–1595, 2019.
- [89] M. K. Blees *et al.*, “Graphene kirigami,” *Nature*, vol. 524, no. 7564, pp. 204–207, 2015.
- [90] T. C. Shyu *et al.*, “A kirigami approach to engineering elasticity in nanocomposites through patterned defects,” *Nat. Mater.*, vol. 14, no. 8, pp. 785–789, 2015.
- [91] D.-H. Kim *et al.*, “Optimized structural designs for stretchable silicon integrated circuits,” *Small*, vol. 5, no. 24, pp. 2841–2847, 2009.
- [92] D. S. Gray, J. Tien, and C. S. Chen, “High-conductivity elastomeric electronics,” *Adv. Mater.*, vol. 16, no. 5, pp. 393–397, 2004.
- [93] G. Lanzara, N. Salowitz, Z. Guo, and F.-K. Chang, “A spider-web-like highly expandable sensor network for multifunctional materials,” *Adv. Mater.*, vol. 22, no. 41, pp. 4643–4648, 2010.

- [94] D.-H. Kim *et al.*, “Epidermal electronics,” *Science*, vol. 333, no. 6044, pp. 838–843, 2011.
- [95] A. Miyamoto *et al.*, “Inflammation-free, gas-permeable, lightweight, stretchable on-skin electronics with nanomeshes,” *Nat. Nanotechnol.*, vol. 12, no. 9, pp. 907–913, 2017.
- [96] T. Someya *et al.*, “Conformable, flexible, large-area networks of pressure and thermal sensors with organic transistor active matrixes,” *Proc. Natl. Acad. Sci. U.S.A.*, vol. 102, no. 35, pp. 12321–12325, 2005.
- [97] Y. Morikawa *et al.*, “Ultrastretchable kirigami bioprobes,” *Adv. Healthc. Mater.*, vol. 7, no. 3, 2018.
- [98] H. Wu *et al.*, “A transparent electrode based on a metal nanotrough network,” *Nat. Nanotechnol.*, vol. 8, no. 6, pp. 421–425, 2013.
- [99] S. P. Lacour, D. Chan, S. Wagner, T. Li, and Z. Suo, “Mechanisms of reversible stretchability of thin metal films on elastomeric substrates,” *Appl. Phys. Lett.*, vol. 88, no. 20, 2006.
- [100] Z. Liu *et al.*, “High-adhesion stretchable electrodes based on nanopile interlocking,” *Adv. Mater.*, vol. 29, no. 2, 2017.
- [101] O. Graudejus, P. Görrn, and S. Wagner, “Controlling the morphology of gold films on poly(dimethylsiloxane),” *ACS Appl. Mater. Interfaces*, vol. 2, no. 7, pp. 1927–1933, 2010.
- [102] X. Yan *et al.*, “Quadruple H-bonding cross-linked supramolecular polymeric materials as substrates for stretchable, antitearing, and self-healable thin film electrodes,” *J. Am. Chem. Soc.*, vol. 140, no. 15, pp. 5280–5289, 2018.
- [103] S. P. Lacour, S. Wagner, Z. Huang, and Z. Suo, “Stretchable gold conductors on elastomeric substrates,” *Appl. Phys. Lett.*, vol. 82, no. 15, pp. 2404–2406, 2003.
- [104] N. Bowden, S. Brittain, A. G. Evans, J. W. Hutchinson, and G. M. Whitesides, “Spontaneous formation of ordered structures in thin films of metals supported on an elastomeric polymer,” *Nature*, vol. 393, no. 6681, pp. 146–149, 1998.
- [105] J. Vanfleteren *et al.*, “Arbitrarily shaped 2.5D circuits using stretchable interconnections and embedding in thermoplastic polymers,” *Procedia Technology*, vol. 15, pp. 208–215, 2014.
- [106] G. Chen *et al.*, “Plasticizing silk protein for on-skin stretchable electrodes,” *Adv. Mater.*, vol. 30, no. 21, 1800129, 2018.
- [107] K. Yamagishi *et al.*, “Elastic kirigami patch for electromyographic analysis of the palm muscle during baseball pitching,” *NPG Asia Materials*, vol. 11, 80, 2019.

---

*References*

---

- [108] S. Chen, J. Chen, X. Zhang, Z.-Y. Li, and J. Li, “Kirigami/origami: unfolding the new regime of advanced 3D microfabrication/nanofabrication with ‘folding,’” *Light: Science & Applications*, vol. 9, 75, 2020.
- [109] Y. Sato, S. Terashima, and E. Iwase, “Origami-type flexible thermoelectric generator fabricated by self-folding,” *Micromachines*, vol. 14, no. 1, 2023.
- [110] A. Eda *et al.*, “Large curvature self-folding method of a thick metal layer for hinged origami/kirigami stretchable electronic devices,” *Micromachines*, vol. 13, no. 6, 2022.
- [111] H. Choi *et al.*, “Highly stretchable and strain-insensitive liquid metal based elastic kirigami electrodes (LM-eKE),” *Adv. Funct. Mater.*, vol. 33, no. 30, 2301388, 2023.
- [112] P. Wang *et al.*, “Stretchable and self-adhesive humidity-sensing patch for multiplexed non-contact sensing,” *ACS Appl. Mater. Interfaces*, vol. 15, no. 32, pp. 38163–39026, 2023.
- [113] J. Byun, E. Oh, B. Lee, S. Kim, S. Lee, and Y. Hong, “A single droplet-printed double-side universal soft electronic platform for highly integrated stretchable hybrid electronics,” *Adv. Funct. Mater.*, vol. 27, no. 36, 1701912, 2017.
- [114] Y. Kim *et al.*, “A modulus-engineered multi-layer polymer film with mechanical robustness for the application to highly deformable substrate platform in stretchable electronics,” *Chem. Eng. J.*, vol. 431, 134074, 2022.
- [115] H. Luan *et al.*, “Design and fabrication of heterogeneous, deformable substrates for the mechanically guided 3D assembly,” *ACS Appl. Mater. Interfaces*, vol. 11, no. 3, pp. 3482–3492, 2019.
- [116] H. Li, Z. Wang, S. Lu, Y. Ma, and X. Feng, “Elastomers with microislands as strain isolating substrates for stretchable electronics,” *Adv. Mater. Technol.*, vol. 4, no. 2, 1800365, 2019.
- [117] M. Cai, W. Hong, S. Nie, C. Wang, and J. Song, “Stretchable electronic skin patch with strain isolation for the simultaneous measurements of surface electromyography and temperature,” *Flex. Print. Electron.*, vol. 7, no. 3, 035002, 2022.
- [118] Z. Wang *et al.*, “Stable epidermal electronic device with strain isolation induced by in situ Joule heating,” *Microsyst Nanoeng*, vol. 7, 56, 2021.
- [119] Y. Liu *et al.*, “Strain-isolation bridge structure to improve stretchability of highly sensitive strain sensors,” *Adv. Mater. Technol.*, vol. 4, no. 9, 1900309, 2019.
- [120] D. P. J. Cotton, A. Popel, I. M. Graz, and S. P. Lacour, “Photopatterning the mechanical properties of polydimethylsiloxane films,” *J. Appl. Phys.*, vol. 109, no. 5, 054905, 2011.



- [121] A. Romeo, Q. Liu, Z. Suo, and S. P. Lacour, “Elastomeric substrates with embedded stiff platforms for stretchable electronics,” *Appl. Phys. Lett.*, vol. 102, no. 13, 131904, 2013.
- [122] I. M. Graz, D. P. J. Cotton, A. Robinson, and S. P. Lacour, “Silicone substrate with in situ strain relief for stretchable thin-film transistors,” *Appl. Phys. Lett.*, vol. 98, no. 12, 124101, 2011.
- [123] S. P. Lacour, S. Wagner, R. J. Narayan, T. Li, and Z. Suo, “Stiff subcircuit islands of diamondlike carbon for stretchable electronics,” *J. Appl. Phys.*, vol. 100, no. 1, 14913, 2006.
- [124] R. Lin, Y. Li, X. Mao, W. Zhou, and R. Liu, “Hybrid 3D printing all-in-one heterogenous rigidity assemblies for soft electronics,” *Adv. Mater. Technol.*, vol. 4, no. 12, 1900614, 2019.
- [125] C. W. Park *et al.*, “Locally-tailored structure of an elastomeric substrate for stretchable circuits,” *Semicond. Sci. Technol.*, vol. 31, no. 2, 025013, 2015.
- [126] N. Rodeheaver *et al.*, “Strain-isolating materials and interfacial physics for soft wearable bioelectronics and wireless, motion artifact-controlled health monitoring,” *Adv. Funct. Mater.*, vol. 31, no. 36, 2104070, 2021.
- [127] L. Zhu, Y. Wang, D. Mei, W. Ding, C. Jiang, and Y. Lu, “Fully elastomeric fingerprint-shaped electronic skin based on tunable patterned graphene/silver nanocomposites,” *ACS Appl. Mater. Interfaces*, vol. 12, no. 28, pp. 31725–31737, 2020.
- [128] J. Zhao *et al.*, “A structured design for highly stretchable electronic skin,” *Adv. Mater. Technol.*, vol. 4, no. 10, 1900492, 2019.
- [129] H. Li, Y. Ma, and Y. Huang, “Material innovation and mechanics design for substrates and encapsulation of flexible electronics: a review,” *Mater Horiz*, vol. 8, no. 2, pp. 383–400, 2021.
- [130] J. Yun, K. Cho, and S. Kim, “Nanoparticle-based flexible inverters with a vertical structure,” *Thin Solid Films*, vol. 539, pp. 256–259, 2013.
- [131] H. Cheng *et al.*, “An analytical model of strain isolation for stretchable and flexible electronics,” *Appl. Phys. Lett.*, vol. 98, no. 6, 2011.
- [132] C. H. Lee *et al.*, “Soft core/shell packages for stretchable electronics,” *Adv. Funct. Mater.*, vol. 25, no. 24, pp. 3698–3704, 2015.
- [133] Y. Ma *et al.*, “Soft elastomers with ionic liquid-filled cavities as strain isolating substrates for wearable electronics,” *Small*, vol. 13, no. 9, 2017.
- [134] T. J. Anderson and I. Ansara, “The Ga-In (gallium-indium) system,” *J. Phase Equilib. Diffus.*, vol. 12, no. 1, pp. 64–72, 1991.

---

*References*

---

- [135] M. D. Dickey, R. C. Chiechi, R. J. Larsen, E. A. Weiss, D. A. Weitz, and G. M. Whitesides, “Eutectic gallium-indium (EGaIn): A liquid metal alloy for the formation of stable structures in microchannels at room temperature,” *Adv. Funct. Mater.*, vol. 18, no. 7, pp. 1097–1104, 2008.
- [136] D. Kim *et al.*, “Recovery of nonwetting characteristics by surface modification of gallium-based liquid metal droplets using hydrochloric acid vapor,” *ACS Appl. Mater. Interfaces*, vol. 5, no. 1, pp. 179–185, 2013.
- [137] M. R. Lorenz, J. F. Woods, and R. J. Gambino, “Some electrical properties of the semiconductor  $\beta\text{Ga}_2\text{O}_3$ ,” *J. Phys. Chem. Solids*, vol. 28, no. 3, pp. 403–404, 1967.
- [138] K. A. Narh, V. P. Dwivedi, J. M. Grow, A. Stana, and W. Y. Shih, “The effect of liquid gallium on the strengths of stainless steel and thermoplastics,” *J. Mater. Sci.*, vol. 33, no. 2, pp. 329–337, 1998.
- [139] Y. G. Deng and J. Liu, “Corrosion development between liquid gallium and four typical metal substrates used in chip cooling device,” *Applied Physics A: Materials Science and Processing*, vol. 95, no. 3, pp. 907–915, 2009.
- [140] P. R. Luebbers and O. K. Chopra, “Compatibility of ITER candidate materials with static gallium,” *Proceedings - Symposium on Fusion Engineering*, vol. 1, pp. 232–235, 1995.
- [141] S. Liu *et al.*, “Effects of Ni and Cu antisite substitution on the phase stability of  $\text{CuGa}_2$  from liquid Ga/Cu-Ni interfacial reaction,” *ACS Appl. Mater. Interfaces*, vol. 11, no. 35, pp. 32523–32532, 2019.
- [142] O. I. Tikhomirova, M. V. Pikunov, L. P. Ruzinov, and I. D. Marchukova, “Interaction of liquid gallium with copper,” *Soviet materials science : a transl. of Fiziko-khimicheskaya mekhanika materialov / Academy of Sciences of the Ukrainian SSR*, vol. 5, no. 6, pp. 586–590, 1972.
- [143] L. B. Freund and S. Suresh, *Thin Film Materials: Stress, Defect Formation and Surface Evolution*. Cambridge University Press, 2004.
- [144] B. A. Gozen, A. Tabatabai, O. B. Ozdoganlar, and C. Majidi, “High-density soft-matter electronics with micron-scale line width,” *Adv. Mater.*, vol. 26, no. 30, pp. 5211–5216, 2014.
- [145] T. Lu, L. Finkenauer, J. Wissman, and C. Majidi, “Rapid prototyping for soft-matter electronics,” *Adv. Funct. Mater.*, vol. 24, no. 22, pp. 3351–3356, 2014.
- [146] J. W. Boley, E. L. White, G. T.-C. Chiu, and R. K. Kramer, “Direct writing of gallium-indium alloy for stretchable electronics,” *Adv. Funct. Mater.*, vol. 24, no. 23, pp. 3501–3507, 2014.
- [147] C. Ladd, J.-H. So, J. Muth, and M. D. Dickey, “3D printing of free standing liquid metal microstructures,” *Adv. Mater.*, vol. 25, no. 36, pp. 5081–5085, 2013.

- [148] N. Lazarus, S. S. Bedair, and I. M. Kierzewski, "Ultrafine pitch stencil printing of liquid metal alloys," *ACS Appl. Mater. Interfaces*, vol. 9, no. 2, pp. 1178–1182, 2017.
- [149] R. K. Kramer, C. Majidi, and R. J. Wood, "Masked deposition of gallium-indium alloys for liquid-embedded elastomer conductors," *Adv. Funct. Mater.*, vol. 23, no. 42, pp. 5292–5296, 2013.
- [150] S. H. Jeong, A. Hagman, K. Hjort, M. Jobs, J. Sundqvist, and Z. Wu, "Liquid alloy printing of microfluidic stretchable electronics," *Lab Chip*, vol. 12, no. 22, pp. 4657–4664, 2012.
- [151] K. Doudrick *et al.*, "Different shades of oxide: from nanoscale wetting mechanisms to contact printing of gallium-based liquid metals," *Langmuir*, vol. 30, no. 23, pp. 6867–6877, 2014.
- [152] D. Kim *et al.*, "Stretchable and bendable carbon nanotube on PDMS super-lyophobic sheet for liquid metal manipulation," *J. Micromech. Microeng.*, vol. 24, no. 5, 055018, 2014.
- [153] A. Fassler and C. Majidi, "3D structures of liquid-phase GaIn alloy embedded in PDMS with freeze casting," *Lab Chip*, vol. 13, no. 22, pp. 4442–4450, 2013.
- [154] M. R. Khan, C. Trlica, and M. D. Dickey, "Recapillarity: Electrochemically controlled capillary withdrawal of a liquid metal alloy from microchannels," *Adv. Funct. Mater.*, vol. 25, no. 5, pp. 671–678, 2015.
- [155] J. Yang, Y. Yang, Z. He, B. Chen, and J. Liu, "A personal desktop liquid-metal printer as a pervasive electronics manufacturing tool for society in the near future," *Proc. Est. Acad. Sci. Eng.*, vol. 1, no. 4, pp. 506–512, 2015.
- [156] B. Yuan, Z.-Z. He, and J. Liu, "Effect of electric field on the wetting behavior of eutectic gallium–indium alloys in aqueous environment," *J. Electron. Mater.*, vol. 47, no. 5, pp. 2782–2790, 2018.
- [157] J. Jeon, J.-B. Lee, S. K. Chung, and D. Kim, "Magnetic liquid metal marble: Characterization of lyophobicity and magnetic manipulation for switching applications," *J. Microelectromech. Syst.*, vol. 25, no. 6, pp. 1050–1057, 2016.
- [158] H. Gui *et al.*, "Spraying printing of liquid metal electronics on various clothes to compose wearable functional device," *Sci. China Tech. Sci.*, vol. 60, no. 2, pp. 306–316, 2017.
- [159] E. Davis and S. Ndao, "On the wetting states of low melting point metal galinstan® on silicon microstructured surfaces," *Adv. Eng. Mater.*, vol. 20, no. 3, 1700829, 2018.
- [160] B. Kim *et al.*, "Interfacing liquid metals with stretchable metal conductors," *ACS Appl. Mater. Interfaces*, vol. 7, no. 15, pp. 7920–7926, 2015.
- [161] T. Kozaki *et al.*, "Liquid-state optoelectronics using liquid metal," *Adv. Electron. Mater.*, vol. 6, no. 3, 1901135, 2020.

---

*References*

---

- [162] H. Ota *et al.*, “Highly deformable liquid-state heterojunction sensors,” *Nat. Commun.*, vol. 5, 5032, 2014.
- [163] M. Takaya *et al.*, “Transformable electrocardiograph using robust liquid-solid heteroconnector,” *ACS Sens*, vol. 6, no. 1, pp. 212–219, 2021.
- [164] S. Harada, T. Arie, S. Akita, and K. Takei, “Highly stable liquid–solid metal contact toward multilayered detachable flexible devices,” *Advanced Electronic Materials*, vol. 1, no. 7, 1500080, 2015.
- [165] P. Ahlberg *et al.*, “Graphene as a diffusion barrier in galinstan-solid metal contacts,” *IEEE Trans. Electron Devices*, vol. 61, no. 8, pp. 2996–3000, 2014.
- [166] T. Sato, K. Yamagishi, M. Hashimoto, and E. Iwase, “Method to reduce the contact resistivity between galinstan and a copper electrode for electrical connection in flexible devices,” *ACS Appl. Mater. Interfaces*, vol. 13, no. 15, pp. 18247–18254, 2021.
- [167] J. B. Andrews *et al.*, “Patterned liquid metal contacts for printed carbon nanotube transistors,” *ACS Nano*, vol. 12, no. 6, pp. 5482–5488, 2018.
- [168] D. K. Schroder, *Semiconductor material and device characterization: Schroder/semiconductor material and device characterization, third edition*, 3rd ed. Chichester, England: Wiley-Blackwell, 2006.
- [169] P. Zhang, Y. Y. Lau, and R. M. Gilgenbach, “Analysis of current crowding in thin film contacts from exact field solution,” *J. Phys. D Appl. Phys.*, vol. 48, no. 47, p. 475501, 2015.
- [170] H. Murrmann and D. Widmann, “Current crowding on metal contacts to planar devices,” *IEEE Trans. Electron Devices*, vol. 16, no. 12, pp. 1022–1024, 1969.
- [171] H. H. Berger, “Models for contacts to planar devices,” *Solid State Electron.*, vol. 15, no. 2, pp. 145–158, 1972.
- [172] D. Peyrou, F. Pennec, H. Achkar, P. Pons, and R. Plana, “Effect of contact force between rough surfaces on real contact area and electrical contact resistance,” *MEMSWAVE Workshop 2007*, hal-00172960, pp. 4, 2007.
- [173] M. Konig, G. Ruhl, A. Gahoi, S. Wittmann, and M. C. Lemme, “Accurate graphene-metal junction characterization,” *IEEE Journal of the Electron Devices Society*, vol. 7, pp. 219–226, 2019.
- [174] S. V. Lozanova and C. S. Roumenin, “A three-point-probe method for measuring resistivity and the Hall coefficient using Hall devices with minimal design complexity,” *Measurement*, vol. 43, no. 3, pp. 385–391, 2010.

- [175] P. N. Vinod, "Specific contact resistance measurements of the screen-printed Ag thick film contacts in the silicon solar cells by three-point probe methodology and TLM method," *J. Mater. Sci.: Mater. Electron.*, vol. 22, no. 9, pp. 1248–1257, 2011.
- [176] Y. Shigetoshi, S. Tsukimoto, H. Takeda, K. Ito, and M. Murakami, "Electrical properties and microstructures of ultraviolet transparent Ga<sub>2</sub>O<sub>3</sub> thin films," *Mater. Sci. Forum*, vol. 561–565, no. PART 2, pp. 1233–1236, 2007.
- [177] S.-Y. Tang *et al.*, "Electrochemically induced actuation of liquid metal marbles," *Nanoscale*, vol. 5, no. 13, pp. 5949–5957, Jul. 2013.
- [178] J. Han, J. Tang, S. A. Idrus-Saidi, M. J. Christoe, A. P. O'Mullane, and K. Kalantar-Zadeh, "Exploring electrochemical extrusion of wires from liquid metals," *ACS Appl. Mater. Interfaces*, vol. 12, no. 27, pp. 31010–31020, 2020.
- [179] Changsha Rich Nonferrous Metals "Galinstan," Aliexpress, [https://richmetals.ja.aliexpress.com/store/group/GaInSn-Galinstan/231282\\_10000000148072.html?spm=a2g0o.store\\_pc\\_groupList.0.0.4f223253sEnrfr](https://richmetals.ja.aliexpress.com/store/group/GaInSn-Galinstan/231282_10000000148072.html?spm=a2g0o.store_pc_groupList.0.0.4f223253sEnrfr), (accessed Apr. 2023).
- [180] Dupont, "Polyimide Films," <https://www.dupont.com/electronics-industrial/polyimide-films.html>, (accessed Apr. 2023).
- [181] Dow, "SYLGARD™ 184 Silicone Elastomer Kit, <https://www.dow.com/ja-jp/pdp.sylgard-184-silicone-elastomer-kit.01064291z.html#overview>, (accessed Apr. 2023).
- [182] KOA, "Jumper resistor" [https://www.koaglobal.com/-/media/Files/KOA\\_Global/EN/product/commonpdf/rk73z.pdf](https://www.koaglobal.com/-/media/Files/KOA_Global/EN/product/commonpdf/rk73z.pdf), (accessed Apr. 2023).
- [183] Y. Guo, G. Liu, H. Jin, Z. Shi, and G. Qiao, "Intermetallic phase formation in diffusion-bonded Cu/Al laminates," *J. Mater. Sci.*, vol. 46, no. 8, pp. 2467–2473, 2011.
- [184] Nilaco, "Copper," [https://shop.nilaco.jp/jp/estimates/?MENU=15&FROM=14&large\\_category=1&middle\\_category=%E9%8A%85&small\\_category=%E7%AE%94](https://shop.nilaco.jp/jp/estimates/?MENU=15&FROM=14&large_category=1&middle_category=%E9%8A%85&small_category=%E7%AE%94), (accessed Apr. 2023).
- [185] Smooth-On, "Ecoflex 00-30," <https://www.smooth-on.com/products/ecoflex-00-30/>, (accessed Apr. 2023).
- [186] Sunhayato, "Special cream solder (SMX-H05A)," <https://shop.sunhayato.co.jp/en/products/smx-h05a>, (accessed Apr. 2023).

---

*References*

---

- [187] Kaken Tec, “Conductive Pastes,” [https://www.kaken-tech.co.jp/products/electronics/conductive\\_paste/tk\\_paste/](https://www.kaken-tech.co.jp/products/electronics/conductive_paste/tk_paste/), (accessed Apr. 2023).
- [188] Rohm, “MCR10EZPJ000 Thick Film Chip Jumper (MCR Series), ” <https://www.rohm.com/products/resistors/standard-chip-resistors/thick-film-chip-resistors/mcr10ezpj000-product>, (accessed Apr. 2023).
- [189] OptoSupply, “Chip LEDs,” <https://www.optosupply.com/product/list.asp?id=60>, (accessed Apr. 2023).

# Achievements

## Journal Articles

- [1] T. Sato and E. Iwase, “High-accuracy contact resistance measurement method for liquid metal by considering current-density distribution in transfer length method measurement,” *ACS Appl. Mater. Interfaces*, vol. 15, no. 37, pp. 44404–44412, Sep. 2023. (Peer reviewed, IF=10.383)
- [2] A. Eda, H. Yasuga, T. Sato, Y. Sato, K. Suto, T. Tachi, K. Tachi, and E. Iwase, “Large curvature self-folding method of a thick metal layer for hinged origami/kirigami stretchable electronic devices,” *Micromachines*, vol. 13, no. 6, 907 (9pp), June 2022. (Peer reviewed, IF=3.523)
- [3] T. Sato, K. Yamagishi, M. Hashimoto, and E. Iwase, “Method to reduce the contact resistivity between galinstan and a copper electrode for electrical connection in flexible devices,” *ACS Appl. Mater. Interfaces*, vol. 13, no. 15, pp. 18247-18254, Apr. 2021. (Peer reviewed, IF=10.383)
- [4] T. Sato, T. Koshi, and E. Iwase, “Resistance change mechanism of electronic component mounting through contact pressure using elastic adhesive,” *Micromachines*, vol. 10, no. 6, 396 (10pp), June 2019. (Peer reviewed, IF=3.523)

## International Conferences

- [5] T. Sato, “Highly-stretchable and high-performance electronic devices by electronic component mounting using liquid metal,” *Proceedings of the 19th IEEE International Conference on Nano/Micro Engineered and Molecular Systems (IEEE NEMS 2024)*, Kyoto, Japan, May 2024. (Invited)
- [6] T. Sato and E. Iwase, “Electronic component mounting with liquid metal for highly stretchable electronic devices,” *Proceedings of the 37th IEEE International Conference on Micro Electro Mechanical Systems (IEEE MEMS 2024)*, 0129, Texas, USA, Jan. 2024. (Poster, Peer reviewed, Acceptance rate: 50%)

---

*Achievements*

---

- [7] Y. Sato, T. Sato, and E. Iwase, “Bilayer self-folding method with high folding force and angle by suppressing delamination of shrink layer,” *Proceedings of the 22nd IEEE International Conference on Solid-State Sensors, Actuators and Microsystems (IEEE TRANSDUCERS 2023)*, 3048, online, June 2023. (Oral, Peer reviewed, Acceptance rate: 10%)
- [8] T. Sato and E. Iwase, “Finite element analysis of current density distribution in transfer length method measurement of galinstan,” *The 5th event of Young Researchers Society for Flexible and Stretchable Electronics*, Yokohama, Kanagawa, May 2023. (Poster)
- [9] T. Sato and E. Iwase, “Highly accurate measurement of contact resistance between galinstan and copper using transfer length method,” *Proceedings of the 36th IEEE International Conference on Micro Electro Mechanical Systems (IEEE MEMS 2023)*, pp. 339-342, Munich, Germany, Jan. 2023. (Poster, Peer reviewed, Acceptance rate: 50%)
- [10] T. Sato and E. Iwase, “Study on measurement of contact resistance between liquid and solid metals using transfer length method,” *Integrated Nanocomposites for Thermal and Kinetic Energy Harvesting (INTAKE) Seminar*, Sendai, Miyagi, Nov. 2022. (Oral, Outstanding presentation award)
- [11] T. Sato and E. Iwase, “Study on measurement method of contact resistance between galinstan and copper electrodes,” *The 4th event of Young Researchers Society for Flexible and Stretchable Electronics*, Yonezawa, Yamagata, July 2022. (Oral)
- [12] T. Sato and E. Iwase, “Study on measurement method of contact resistance between galinstan and copper electrodes,” *The 10th Asia-Pacific Conference of Transducers and Micro-Nano Technology 2022 (APCOT 2022)*, online, May-June 2022. (Oral, Peer reviewed)
- [13] T. Sato, K. Yamagishi, M. Hashimoto, and E. Iwase, “Method to reduce the contact resistivity between galinstan and a copper electrode for electrical connection in flexible devices,” *The 3rd event of Young Researchers Society for Flexible and Stretchable Electronics*, online, Dec. 2021. (Oral)
- [14] T. Sato and E. Iwase, “Stretchable electronic devices with high performance and high stretchability,” *Integrated Nanocomposites for Thermal and Kinetic Energy Harvesting (INTAKE) Seminar*, online, July 2021. (Oral)



- 
- [15] T. Sato, K. Yamagishi, M. Hashimoto, and E. Iwase, “Method to reduce the contact resistivity between galinstan and a copper electrode for electrical connection in flexible devices,” *Proceedings of the 21st IEEE International Conference on Solid-State Sensors, Actuators and Microsystems (IEEE TRANSDUCERS 2021)*, 5004, online, June 2021. (Poster, Peer reviewed, Acceptance rate: 60%)
- [16] T. Sato and E. Iwase, “Electronic component mounting method using liquid metal,” *The 7th Asian Conference on Mechanics of Functional Materials and Structures (ACMFMS2020+I)*, 116, online, Mar. 2021. (Oral)
- [17] T. Sato, K. Yamagishi, M. Hashimoto, and E. Iwase, “Liquid metal as electrical interface material with temporal stability and stretch tolerance,” *Proceedings of the 34th IEEE International Conference on Micro Electro Mechanical Systems (IEEE MEMS 2021)*, pp. 689-692, online, Jan. 2021. (Poster, Peer reviewed, Acceptance rate: 50%)

#### Domestic Conferences

- [18] 佐藤峻, 岩瀬英治, “電流密度分布を考慮した液体金属の高精度接触抵抗計測,” 日本機械学会 第14回マイクロ・ナノ工学シンポジウム, U00160, 熊本, 熊本, Nov. 2023. (ポスター)
- [19] 信田虎太郎, 佐藤峻, 岩瀬英治, “液体金属とエラストマによるスルーホール実装の提案,” 日本機械学会 第14回マイクロ・ナノ工学シンポジウム, U00174, 熊本, 熊本, Nov. 2023. (ポスター)
- [20] 佐藤峻, 岩瀬英治, “液体金属による電子素子実装における応力分布解析,” 日本機械学会 第14回マイクロ・ナノ工学シンポジウム, U00192, 熊本, 熊本, Nov. 2023. (ポスター, 若手優秀講演表彰 (受賞率: 3.6%))
- [21] 佐藤峻, 小此木葵衣, 藤田創, 藤枝俊宣, 岩瀬英治, “高分子超薄膜電子デバイスにおける厚膜電極接続部の形状検討,” 日本機械学会 第14回マイクロ・ナノ工学シンポジウム, U00193, 熊本, 熊本, Nov. 2023. (ポスター)
- [22] 佐藤峻, 岩瀬英治, “高伸縮な電子デバイスのための液体金属を用いた電子素子実装” 早稲田大学 第10回 ZAIKEN Festa, Shinjuku, Tokyo, Oct. 2023. (口頭, 奨励賞受賞)
- [23] 佐藤峻, 岩瀬英治, “Transfer Length Method による液体金属と固体金属間の接触抵抗計測の検討,” 日本機械学会 第13回マイクロ・ナノ工学シンポジウム, 16P2-PN-32, 徳島, 徳島, Nov. 2022. (ポスター)

---

*Achievements*

---

- [24] 羽根田海, 佐藤峻, 岩瀬英治, “折り線を有する切り紙構造による 2 面コーナーリフレクタアレイの製作,” 日本機械学会 第13回マイクロ・ナノ工学シンポジウム, 15P2-PN-30, 徳島, 徳島, Nov. 2022. (ポスター)
- [25] 佐藤峻, 岩瀬英治, “液体金属による電子素子実装,” 切り紙・折り紙に関する合同研究会, 那須, 長野, Sep. 2022 (口頭)
- [26] 佐藤峻, 岩瀬英治, “ガリNSTANと銅電極間の接触抵抗計測方法の検討,” 早稲田大学 第8回 ZAIKEN Festa, online, Dec. 2021. (口頭, 奨励賞受賞)
- [27] 佐藤峻, 岩瀬英治, “Electronic component mounting method using liquid metal,” 拠点形成事業 A. 先端拠点形成型 (令和2年度) IoT 社会を実現するマルチ環境発電材料・デバイス 国際研究拠点形成 Poster presentation, online, Dec. 2020. (ポスター)
- [28] 佐藤峻, 岩瀬英治, “液体金属による電子素子実装手法,” 拠点形成事業 A. 先端拠点形成型 (令和2年度) IoT 社会を実現するマルチ環境発電材料・デバイス 国際研究拠点形成 国内セミナー, online, Nov. 2020. (口頭)
- [29] 佐藤峻, 岩瀬英治, “液体金属における金属配線との接触抵抗計測,” 電気学会 第37回 センサ・マイクロマシンと応用システムシンポジウム, 27P3-SSL-49, online, Oct. 2020. (ポスター)
- [30] 佐藤峻, 山岸健人, 橋本道尚, 岩瀬英治, “液体金属を用いた電子部品実装における接触抵抗の経時変化計測,” 電気学会 マイクロマシン・センサシステム研究会, MSS-20-036, online, July 2020. (口頭)
- [31] 佐藤峻, 山岸健人, 橋本道尚, 岩瀬英治, “液体金属を用いた電子部品実装における電氣的接続の検討,” 日本機械学会 第10回マイクロ・ナノ工学シンポジウム, 20am2-PN3-47, 浜松, 静岡, Nov. 2019. (ポスター)
- [32] 佐藤峻, 古志知也, 岩瀬英治, “押し付け型電子部品実装における弾性体回路基板のヤング率と接触抵抗の関係の評価,” 電気学会 マイクロマシン・センサシステム研究会, MSS-19-030, 横浜, 神奈川, July 2019. (口頭)
- [33] 佐藤峻, 古志知也, 岩瀬英治, “粘着弾性体による押しつけ圧力を利用した非加熱型電子部品実装手法の提案,” 日本機械学会 第9回マイクロ・ナノ工学シンポジウム, 30pm4-PN-58, 札幌, 北海道, Oct.-Nov. 2018. (ポスター)

### Awards

- [34] 佐藤峻, 日本機械学会 第 14 回マイクロ・ナノ工学シンポジウム 若手優秀講演表彰, Nov. 2023. (受賞率 3.6%)
- [35] 佐藤峻, 早稲田大学 第 10 回 ZAIKEN Festa 奨励賞, Oct. 2023.
- [36] 佐藤峻, 早稲田大学-キオクシア連携活動協定, 若手奨励研究, 奨励賞, Mar. 2023.
- [37] T. Sato, JSPS Core-to-Core Program, Integrated Nanocomposites for Thermal and Kinetic Energy Harvesting (INTAKE) Online Seminar, Outstanding presentation award, Nov. 2022.
- [38] 牛奥隆博, Han Yuxuan, 佐藤峻, 萩原佑紀, 木村友紀, 早稲田大学 アーリーバードプログラム 技術賞, Mar. 2022.
- [39] 佐藤峻, 早稲田大学 第 8 回 ZAIKEN Festa 奨励賞, Mar. 2022.
- [40] 佐藤峻, 早稲田大学 基幹理工学研究科 材料科学学術奨励賞, Mar. 2021.

### Grants

- [41] T. Sato, IEEE MEMS 2024, Student Travel Grant, \$500, Jan. 2024.
- [42] 佐藤峻, 総合研究奨励会 若手研究者海外渡航助成, 20 万円, Jan. 2024.
- [43] 佐藤峻, 科学技術振興機構(JST) 戦略的創造研究推進事業(ACT-X) 加速フェーズ, “液体金属実装による強靱なストレッチャブル電子デバイスの創製,” 1,000 万円, Apr. 2024-Mar. 2025. (Acceptance ratio: 23.8% (2021 年度採択者 21 名中 5 名))
- [44] 佐藤峻, 日本学術振興会(JSPS) 特別研究員(PD), “ナノシート基板への液体金属を用いた電子素子実装による高伸縮・高性能な電子デバイス,” 代表者, 450 万円程度, 2024 年 4 月～2027 年 3 月. (採用内定, 採用率: 21.6%)
- [45] 佐藤峻, 早稲田大学 キオクシア研究助成, “剛性分布を有するエラストマ基板へのベアチップ実装,” 50 万円, May 2023-Mar. 2024.
- [46] 佐藤峻, 丸文財団 国際交流助成, 20 万円, Jan. 2023.
- [47] 佐藤峻, 中部電気利用基礎研究振興財団, 国際交流援助, 15 万円, Jan. 2023.
- [48] 佐藤峻, 早稲田大学 キオクシア研究助成, “液体金属によるベアチップ実装手法の提案,” 50 万円, May 2022-Mar. 2023. (奨励賞受賞)
- [49] 佐藤峻, 日本学術振興会(JSPS) 特別研究員(DC2), “液体金属の接触抵抗要因の解明による高伸縮・高性能な伸縮電子デバイスの実現,” 230 万円, Apr. 2022-Mar.2024. (Acceptance ratio: 19%)

---

**Achievements**


---

- [50] **佐藤峻**, 早稲田大学 次世代研究者挑戦的研究プログラム(W-SPRING), “液体金属の接触抵抗要因の解明による高伸縮・高性能な伸縮電子デバイスの実現,” 125 万円, Oct. 2021-Mar. 204. (S 評価採択, 2022 年度以降 DC2 採択のため辞退)
- [51] **佐藤峻**, 科学技術振興機構(JST) 戦略的創造研究推進事業(ACT-X), “液体金属実装による強靱なストレッチャブル電子デバイスの創製,” 600 万円, Oct. 2021-Mar. 204. (Acceptance ratio: 31%)
- [52] **佐藤峻**, 早稲田大学 三菱マテリアル研究助成, “体積抵抗と切り分けた界面抵抗の計測手法の提案,” 40 万円, Jul. 2021-Mar. 2022.
- [53] **佐藤峻**, 早稲田大学 アーリーバードプログラム, “液体金属の接触抵抗要因の解明と低接触抵抗の電子素子実装手法の開発,” 40 万円, May 2021-Mar. 2022. (技術賞受賞)

**Fellowship and scholarship**

- [54] 早稲田大学 日本学術振興会(JSPS) 特別研究員(DC) 採用者支援奨学金, 120 万円, Apr. 2023-Mar.2024.
- [55] 東電記念財団 奨学金, 120 万円, Apr. 2022-Mar.2024.
- [56] 早稲田大学 日本学術振興会(JSPS) 特別研究員(DC) 採用者支援奨学金, 120 万円, Apr. 2022-Mar.2023.
- [57] 日本学術振興会(JSPS) 特別研究員(DC2), 240 万円, Apr. 2022-Mar.2024.
- [58] 早稲田大学 次世代研究者挑戦的研究プログラム(W-SPRING), 300 万円, Oct. 2021-Mar. 204. (S 評価採択, 2022 年度以降 DC2 採択のため辞退)
- [59] 富山文化財団 奨学金, 30 万円, Apl. 2021-Mar. 2022.
- [60] 早稲田大学 大学院博士後期課程若手研究者養成奨学金, 50 万円, Apl. 2021-Mar. 2022.
- [61] 日本学生支援機構(JASSO), 第一種奨学金, 半額免除, Mar. 2021.

**Others**

- [62] 電気学会 第40回センサ・マイクロマシンと応用システムシンポジウムの若手企画にて講演.
- [63] Study with Prof. Yu Shi at University of Chester supported by Integrated Nanocomposites for Thermal and Kinetic Energy Harvesting (INTAKE), JSPS Core-to-Core Program, Dec. 2022-May 2023.
- [64] Study with Associate Prof. Michinao Hashimoto at Singapore University of Technology and Design, supported by Top Global University Project, Aug. 2019-Dec. 2019.



## Acknowledgements

This thesis comprises studies conducted at the Micro and Nano Mechanics Laboratory, Department of Applied Mechanics, Graduate School of Fundamental Science and Engineering, Waseda University. I would like to express my sincere appreciation to those involved in this research. I would like to highlight my deep appreciation for the support from my supervisor Professor Eiji Iwase. This research could not have been established without his help. From him, I learned several things, including characteristics that are necessary for being a professional researcher. In the future, based on these garnered understanding, I would like to contribute to society through my research. I also want to thank Professor Shinsuke Suzuki, Professor Atsushi Hosoi, and Associate Professor Hiroki Ota for their comments and helpful discussions. I could not have drafted this thesis without their help. In addition, I want to thank all members of the Micro and Nano Mechanics Laboratory for their support. They provided me considerable support in the experiments and helped me with the necessary procedures for my research activities. I certainly look forward to their continued success. This research was partially supported by JST ACT-X (Grant Number JPMJAX21K6), JSPS KAKENHI (Grant Number JP22J13665), and the cooperation between Waseda University and Kioxia Corporation. Finally, I would like to express my most sincere thanks to my parents, Osamu and Atsuko, for their ongoing and sacrificial support throughout my life. Finally, I also want to express my deepest gratitude to my wife, Mizuki.

January 2024

Takashi Sato

---

*Acknowledgements*

---